

The Concentration-Mass Relation Across Cosmic Time of Strong Lensing Galaxy Clusters

by

Juan David Remolina González

A dissertation submitted in partial fulfillment
of the requirements for the degree of
Doctor of Philosophy
(Astronomy and Astrophysics)
in the University of Michigan
2021

Doctoral Committee:

Associate Professor Keren Sharon, Chair
Assistant Physicist Lindsey E. Bleem, Argonne National Laboratory
Professor Nuria Calvet
Professor August Evrard
Associate Professor Christopher Miller

Juan David Remolina González

jremolin@umich.edu

ORCID iD: [0000-0002-7868-9827](https://orcid.org/0000-0002-7868-9827)

© Juan David Remolina González 2021

For Cara L. Kyonka

ACKNOWLEDGMENTS

Personal acknowledgements

First, I want to start by thanking my thesis committee members: Keren Sharon, Lindsey Bleem, Nuria Calvet, Gus Evrard, and Chris Miller. I greatly appreciate their feedback and support for the past several years and making this a reality. In particular, I want to thank my research advisor Keren who has been not only my academic advisor but also my mentor, collaborator, and one of my role models. I have learned from her about the universe and life.

Keren's support throughout the past five years has been invaluable. She has always cared about the whole of me. One of the moments I appreciated the most came as the end of my second year of the program was approaching. I told her that I was getting married and that I wanted to find a way to do my work remotely three time zones away in the Pacific Northwest. Keren smiled, responded as follows: "Juan, you would do this to me as I did to my advisor when I was in graduate school", and we started a conversation on the implications of me going remote. Our agreement and expectations were set then and off I went to do remote work nearly as far away as possible from Ann Arbor while still being in the lower 48. Keren also introduced me to her collaborations and other scientists around the world an opportunity that I have cherished. Last, I just want to thank her again for her dedication to help me grow and succeed.

I would also like to thank the Astronomy and Astrophysics Department at University of Michigan in which I have found incredible supportive individuals. A special

mention to the members of *Astronomia en Español*. I want to thank the graduate students whose paths have overlapped with mine. A few particular mentions include Traci Johnson, Kate Napier, Gillen Brown, Tyler Gardner, Paco Holguin, Atom Thanathibodee, Ben Setterholm, Juliette Becker, and Jesse Golden-Marx. I also want to thank the post-docs whom I have create close friendships with over my graduate school: Guillaume Mahler, Anna Niemiec, and Rachel Paterno-Mahler.

Next, I would like to thank Nocona Sanders. We have been on a quite an adventure, from meeting each other about nine years ago in undergrad to today when both of us are about to defend our Ph.Ds. I could not have ask for a more supportive individual with whom to share so much of our paths and lives. I want to thank you for reading so many of my essay, papers, proposals, and more. I am proud of introducing you to the term of accretion, which is most definitely not made up. I can not wait for what the future has in store of the both of us.

A large portion of my time as a graduate student was spent away from Michigan and in the Pacific Northwest. I want to thank my support system in Washington state which has resulted on life long friendships: Kalyn Pearsall, Grady Pearsall, Kayla Fields, Sheldon Fields, Meredith Hodgson, Gordon Hodgson, and Linda Hodgson.

I would like to thank the Kyonka family which I officially joined half way through my graduate school. Curt and Jami, you two have been incredible supportive of me and I can not thank you enough for all you have done for Cara and I. To my siblings in law and nephews thank you for your support and love.

Now, I would like to thank my family. There is not enough words to describe the amount of love and support that you have given me throughout my life. To my parents, Javier Remolina and Claudia González, I am nearing the conclusion of my graduate work as a result of your sacrifice, unconditional love, and dream for a better future for my siblings and I. To Maria and Ana Remolina, I wanted to thank you for being right next to me at every step supporting me along this path.

Last, I want to acknowledge my partner in life and best friend Cara Kyonka. You have been by my side since I started graduate school always with unwavering support for my dreams, passions, and work. Marrying you in the middle of graduate school made a significant positive change on my life and graduate work. I can not thank you enough for being by my side, on my ups and downs. I am very excited for what the future holds for use.

Funding acknowledgements

The projects in this work were supported through a variety of sources. I gratefully acknowledge the support by: the National Science Foundation Graduate Research Fellowship Program under Grant No. DGE 1256260; the Astronomy and Astrophysics Department; and Rackham Conference and Travel Grants. Work at Argonne National Lab is supported by UChicago Argonne LLC, Operator of Argonne National Laboratory. Argonne National Lab, a U.S. Department of Energy Office of Science Laboratory, is operated by UChicago Argonne LLC under contract no. DE-AC02-06CH11357. This research used resources of the Argonne Leadership Computing Facility, which is a DOE Office of Science User Facility supported under Contract DE-AC02-06CH11357. Support for HST program #15307.004 was provided by NASA through a grant from the Space Telescope Science Institute, which is operated by the Associations of Universities for Research in Astronomy, Incorporated, under NASA contract NAS5- 26555.

TABLE OF CONTENTS

DEDICATION	ii
ACKNOWLEDGMENTS	iii
LIST OF TABLES	x
LIST OF FIGURES	xi
LIST OF APPENDICES	xv
ABSTRACT	xvi
CHAPTER	
I. Introduction	1
1.1 Galaxy Clusters	1
1.1.1 Cosmological Probes / Indicators	1
1.1.2 The Mass Distribution of Galaxy Clusters	6
1.1.3 Astronomical Surveys of Galaxy Clusters	11
1.2 Gravitational Lensing	14
1.2.1 Strong Gravitational Lensing Theory	15
1.2.2 Strong Gravitational Lensing by Galaxy Clusters	18
1.2.3 Simulated Strong Gravitational Lensing by Galaxy Clusters	21
1.3 The South Pole Telescope	23
1.3.1 The Thermal Sunyaev Zel'dovich effect	24
1.3.2 South Pole Telescope Galaxy Cluster Sample	28
1.3.3 The SPT Strong Lensing Galaxy Clusters	30
1.4 Dissertation Overview	32
II. Efficient Mass Estimate at the Core of Strong Lensing Galaxy Clusters Using the Einstein Radius	35
2.1 Introduction	36

2.2	Background: Strong Gravitational Lensing	40
2.3	Data: Simulated Lenses	43
2.3.1	The Outer Rim Simulation	43
2.3.2	Simulated SPT-like Strong Lensing Sample	44
2.3.3	Ray Tracing and Density Maps	47
2.4	Methodology	49
2.4.1	Einstein Radius Measurement	49
2.4.2	Inferred Mass	52
2.4.3	Statistical approach to Correctly Represent the Universe	52
2.5	Analysis of Results	55
2.5.1	Possible causes and indicators of the scatter in the $M(< \theta_E)$ mass estimate	59
2.5.2	Results of the Analysis of Systematics	63
2.6	The Effect of Background Source Redshift	66
2.7	Empirical Corrections	68
2.8	Conclusions	74
2.8.1	Application	76

III. Core Mass Estimates in Strong Lensing Galaxy Clusters Using a Single-Halo Lens Model 79

3.1	Introduction	80
3.2	Background: Lens Modeling	84
3.2.1	Detailed Lens Models	84
3.2.2	Single-Halo Models	86
3.3	Simulated Data:	86
3.4	Methodology:	89
3.4.1	Arc Catalog Identification	89
3.4.2	The SHM Procedure	90
3.4.3	Assessment of the SHM Success	90
3.4.4	Aperture Mass Enclosed by the $e\theta_E$	91
3.4.5	Statistics	94
3.5	Analysis of Results:	94
3.5.1	Possible causes of scatter and bias in the M_{SHM} mass estimate	98
3.6	The Effect of the Background Source Redshift and the Lensing Configuration of the Arcs	99
3.6.1	Effects of the Background Source Redshift (z_S) on M_{SHM}	102
3.6.2	Effects of the Lensing Configuration on M_{SHM}	102
3.6.3	Constraining Power of Secondary Lensed Image Systems	104
3.7	Conclusions	105

IV. Core Mass Estimates in Strong Lensing Galaxy Clusters Comparing Detailed Lens Models, Single-Halo Lens Models, and Einstein Radius	108
4.1 Introduction	109
4.2 Observational Data	112
4.2.1 SGAS	113
4.2.2 CLASH	115
4.2.3 HFF	116
4.2.4 RELICS	117
4.3 Lens Modeling And Einstein Radius	127
4.3.1 Detailed Lens Models	127
4.3.2 Single-Halo Lens Models	129
4.3.3 Einstein Radius	130
4.4 Methodology	131
4.4.1 Arc Catalogs	131
4.4.2 BCG Selection	132
4.4.3 Computing $M_{\text{SHM}}(< e\theta_E)$ and $M_{\text{corr}}(< \theta_E)$	132
4.4.4 Statistics	133
4.5 Analysis of Results	135
4.5.1 Mass Enclosed by the Einstein Radius, $M_{\text{corr}}(< \theta_E)$	136
4.5.2 Mass Estimate from Single Halo Lens Models, $M_{\text{SHM}}(< e\theta_E)$	136
4.5.3 Comparison to the Statistical Uncertainty of the Detailed Lens Models	136
4.5.4 Comparison between Observations and Simulations	139
4.6 Summary and Conclusions	141
V. The concentration-Mass Relation of South Pole Telescopes Strong Gravitational Lensing Galaxy Clusters	145
5.1 Introduction	147
5.2 The NFW Density Profile	150
5.3 Simulated Strong Lenses	153
5.4 South Pole Telescope Strong Lensing Cluster Sample	155
5.5 Core Mass Estimates from Strong Lensing Evidence	159
5.5.1 Einstein Radius	161
5.5.2 Single-Halo Lens Models	162
5.6 Methodology	163
5.6.1 Arc Catalogs	163
5.6.2 Computing $M_{\text{corr}}(< \theta_E)$	164
5.6.3 Galaxy Cluster Sample Statistics	164
5.6.4 Fitting the NFW Profile and inferring the Concentration	165
5.6.5 Validation of the Concentration Measurement Method	167

5.6.6	Fitting the concentration-mass Relation	168
5.7	Results	170
5.7.1	The c-M Relation in the Outer Rim SL Cluster Halos	170
5.7.2	The c-M Relation in Mass-Limited Vs. Strong Lensing Selected Samples as Inferred from Simulations	175
5.7.3	The c-M Relation in Observed SL Clusters	176
5.7.4	c-M relation: Comparison Between Simulations and Observations	183
5.8	Summary and Conclusions	183
VI. Future Directions and Conclusions		189
6.1	Summary	189
6.2	Future Work with Strong Lensing South Pole Telescope Galaxy Clusters and the Multi-Year Magellan Spectroscopic Follow-up Program	193
6.3	Future of Strong Lensing Galaxy Clusters in Cosmological Simulations	195
6.4	Future of Strong Lensing Galaxy Clusters in Large Astronomical Surveys	196
APPENDICES		198
D.1	Work as PI of the Spectroscopic Follow-up Program	229
D.2	Observation Records	230
BIBLIOGRAPHY		249

LIST OF TABLES

Table

2.1	Empirical Correction Models.	70
4.1	Strong Lensing Galaxy Clusters.	119
5.1	Results of the c-M Relation for Strong Lensing Galaxy Clusters. . .	174
5.2	SPT SNAP Strong Lensing Galaxy Clusters.	179
A.1	Bias and uncertainty in $M(< \theta_E)$ as a function of ϕ	200
B.1	Strong Lensing Constraints.	202
D.1	Strong Lensing South Pole Telescope Spectroscopic Program Record.	231

LIST OF FIGURES

Figure

1.1	The Last Journey Cosmological Simulation Matter Distribution. . .	3
1.2	Galaxy Cluster Abundance as an Observational Constrain of Cosmo- logical Models.	4
1.3	Galaxy Cluster Radial Density Distribution.	5
1.4	NFW Density, Surface Density, and Average Surface Density Profiles.	9
1.5	Spherical and Projected Enclosed NFW Mass.	10
1.6	Concentration-Mass Relation in Simulations and Observations. . . .	12
1.7	Galaxy Cluster Samples.	13
1.8	LSST Prediction of the Numbers of Strong Gravitational Lensing Galaxy Clusters.	14
1.9	Gravitational Lensing Geometry.	16
1.10	<i>Hubble</i> Frontier Fields (HFF) Galaxy Clusters.	20
1.11	Comparison between a Simulated and Observed Galaxy Cluster. . .	23
1.12	South Pole Telescope (SPT).	24
1.13	SPT Galaxy Cluster Samples.	25
1.14	Cosmic Microwave Background, CMB, and Sunyaev-Zel'dovich effect, SZe, Energy Spectrum.	26
1.15	SPT Observation of the CMB.	27
1.16	Imaging of SPT Strong Lensing Galaxy Clusters.	29

1.17	Strong Lensing SPT Galaxy Clusters.	30
1.18	Magellan Clay Telescope and Its Primary Mirror.	31
2.1	Properties of the Simulated Sample.	46
2.2	Simulated Background Source Redshifts, z_s	48
2.3	Radial Distribution of the Identified Arcs.	50
2.4	Distribution of the Einstein Radius Fitted to the Simulations.	53
2.5	Distribution of the Standard Deviation of the Measured Einstein Radii, $\sigma(\theta_E)$	53
2.6	Example of the Simulated Images to Illustrate our Methodology.	54
2.7	Mass Comparison Between the $M(< \theta_E)$ and $M_{sim}(< \theta_E)$	56
2.8	Ratio of inferred to “true” mass, $M(< \theta_E)/M_{sim}(< \theta_E)$, with respect to θ_E	58
2.9	Examples of the ellipticity (ϵ) of the tangential critical curve (TCC) as a proxy for the cluster deviation from spherical symmetry.	61
2.10	Dynamical State and Deviation from Circular Symmetry.	62
2.11	The fraction of circle covered by the arcs (ϕ) for three examples cases.	63
2.12	Distribution of the fraction of the circle covered by arcs (ϕ) for a given source.	64
2.13	Ratio of Inferred to “True” Mass ($M(< \theta_E)/M_{sim}(< \theta_E)$) Binned by Galaxy Cluster Properties, Background Source, and Lensing Geometry.	65
2.14	The Effect of Source Redshift Uncertainty on the Results.	67
2.15	Empirically Corrected Mass Ratio $M(< \theta_E)/M_{sim}(< \theta_E)$ Binned by θ_E	72
2.16	Empirically-Corrected Inferred Mass Binned by Galaxy Cluster Properties, Background Source, and Lensing Geometry.	73
3.1	Examples of SHM outputs, overplotted on six ray-traced lensing images.	92

3.2	Distribution of Image-Plane Root-Mean-Square (<i>rmsi</i>) of the Lens Models.	93
3.3	Mass Comparison Between the M_{SHM} and M_{SIM}	96
3.4	Comparison between the mass estimates of P-SHMs and F-SHMs. . .	97
3.5	Mass Ratio ($M_{\text{SHM}}/M_{\text{SIM}}$) Binned by the SHM Best Fit Parameters.	100
3.6	Mass Ratio ($M_{\text{SHM}}/M_{\text{SIM}}$) Binned by the Lens-Background-Source System Properties.	101
3.7	Strong Lensing Geometric Configurations of Arcs.	104
4.1	Redshift-Mass ($z_L - M_{500c}$) distribution of the strong lensing galaxy clusters used in our analysis.	114
4.2	Distribution of θ_E and $e\theta_E$ as measured from the two different mass estimate methods.	134
4.3	Mass Comparison Between $M_{\text{corr}}(< \theta_E)$ and M_{DLM}	137
4.4	Mass Comparison Between $M_{\text{SHM}}(< e\theta_E)$ and M_{DLM}	138
4.5	The Scatter of the Efficient Mass Estimate Methods, Compared to the Statistical Uncertainty of the Detailed Lens Models.	140
5.1	Mass-Redshift Distribution of SPT Galaxy Clusters and Simulated Halos.	160
5.2	Einstein Radius Distribution of the SPT SL SNAP sample.	165
5.3	Validation of the Concentration Measurement Methods, using the Outer Rim Simulation.	169
5.4	Posterior Probability Distribution of c-M Fit Parameters for the Simulated and Observed Samples.	172
5.5	c-M Relation Fit to the Simulated and Observed SL Clusters for an Over-density of $\Delta c = 500c$	173
5.6	Comparison of Predicted c-M Relations of Mass-Limited Vs. Strong Lensing Selected Samples.	177

5.7 c-M Relation Comparison Between the Predictions and Observations
for an Over-density of $\Delta c = 500c$ 184

LIST OF APPENDICES

Appendix

- A. Uncertainty Dependence on the Fraction of Circle Covered by Arcs . . . 199
- B. South Pole Telescope Strong Lensing Constraints 201
- C. Analysis of Systematics from the Large Scale SPT Mass 226
- D. Spectroscopic follow-up of SPT Strong Lensing Galaxy Clusters 228

ABSTRACT

We are entering an age of large surveys where hundreds of Strong Lensing (SL) galaxy clusters will be detected, allowing for complete statistical analyses of these sources. Galaxy clusters are prime candidates as cosmic laboratories to learn about the evolution of structure in the Universe, constrain cosmological parameters, and explore the properties of baryonic matter, dark matter, and dark energy. The concentration mass relation of galaxy clusters across cosmic time describes the evolution of matter distribution and test predictions from the Λ Cold Dark Matter (Λ CDM) paradigm using state-of-the-art simulations.

My dissertation describes the combination of the mass at the core from SL and a mass estimate from the outskirts (well established in all wavelengths) of galaxy clusters to constrain the mass distribution and compute the concentration. For this work, we utilize the Outer Rim cosmological simulations to characterize efficient methods to measure the mass at the cores of galaxy clusters and compute the prediction of the concentration-mass relation for strong lensing galaxy clusters.

Two efficient methods to measure the core mass from the strong lensing evidence are the mass enclosed by the Einstein radius and the use of Single-Halo Lens Models (SHM). The mass enclosed by the Einstein radius assumes the projected mass distribution to be spherically symmetric. We establish and apply an empirical correction resulting with a measured scatter of 10.9% and a bias of -0.3% between the mass enclosed by the Einstein radius and the “true” mass from the simulation. The SHM use `Lenstool` to compute a lens model with a single large scale dark matter halo. SHM benefit from a visual inspection to identify and exclude models which fail to

reproduce the lensing configuration. For the SHM that pass the visual inspection, we measure a scatter of 3.3% and bias of 0.3% between the mass estimate and the “true” mass from the simulation. We establish recommendations for applying these two efficient methods to large samples of SL galaxy clusters. Last, we apply these methods to a sample of 67 SL galaxy clusters from the Sloan Giant Arc Survey (SGAS), Cluster Lensing And Supernova with *Hubble* (CLASH), *Hubble* Frontier Fields (HFF), and Reionization Lensing Cluster Survey (RELICS) and compare the mass estimate results to those from the publicly available detailed lens models (DLM). Compared to the DLM, the mass enclosed by the Einstein radius has a scatter of 18.1% with -7.1% bias, while the mass from the SHM has a scatter of 9.0% with 1.0% bias. We conclude, if other uncertainty errors dominate the desired analysis, these two methods become powerful tools particularly when applied to large samples.

For the concentration mass relation work presented in this thesis, we use a sample of 51 strong lensing South Pole Telescope galaxy clusters observed through a Large *Hubble* Space Telescope Snapshot program. This unique sample of strong lensing galaxy clusters spans a broad redshift and mass range. We constrain the concentration mass relation using the simulations and observations to within 9.3% and 5.7%, respectively, find significant evidence at the level of 4.5–sigma for an exponential relation between the mass and the concentration, and cannot make any conclusion to the evolution of the concentration with respect to redshift with this sample. Last, we compare the prediction from the simulation to the observed data and find no tensions with Λ CDM.

CHAPTER I

Introduction

1.1 Galaxy Clusters

Galaxy clusters are the largest gravitational bound structure in the universe, making them ideal cosmological laboratories. Galaxy clusters matter composition is roughly 80% DM and 20% baryonic matter. The baryonic component is further subdivided: $\sim 15\%$ in hot plasma ($10^7 - 10^8\text{K}$) located in the intracluster medium (ICM) and $\sim 5\%$ in stars. As a result, their detection and characterization uses a diversity of observational technique spanning the light spectrum, from the X-ray to the optical to the sub-millimeter. The combination of multi-wavelength observations of galaxy clusters allows for a more comprehensive analyses of the galaxy clusters, their mass components, and their distribution across the range of cluster-centric scales.

1.1.1 Cosmological Probes / Indicators

The matter distribution of the Universe is not random, but rather a complex structure of over-densities and under-densities. The cosmic structure has been named the cosmic web, with filaments leading to knots of high density of matter. Galaxy clusters are harbored at these knots of the cosmic web. Under-dense regions are called voids. An example of the matter distribution from The Last Journey (Heitmann et al., 2021) cosmological simulations is shown in Figure 1.1 representing a large

portion of the Universe. The complex distribution of the cosmic structure is one of the constraints for cosmological models. The current concordance cosmological model is Λ – Cold Dark Matter (Λ – CDM). As part of this cosmological framework the energy density of the Universe is roughly distributed: 70% Dark Energy, 25% Dark Matter, and 5% baryonic matter. Baryons are a composition of an odd number of quarks, most familiar are protons and neutrons making up most of the mass visible in the universe and found at the nucleus of atoms. Dark Matter (DM) is a weakly interacting matter for which properties have been inferred by its gravitational effect (e.g., Zwicky 1933; Mantz et al. 2014), where “Cold” refers to the slow moving property of the matter. Last, Dark Energy is a necessary mathematical term to explain the current accelerated expansion rate of the Universe (e.g., Riess et al. 1998; Perlmutter et al. 1999).

Galaxy Clusters serve as an observational constraint of the matter distribution of the Universe and their abundance can be used to distinguish between different cosmological models. Huterer & Shafer (2018) predict the galaxy cluster abundance for different cosmological models in a simulated survey area of 5,000 deg² of the sky selecting galaxy clusters with a total mass larger than $10^{14} M_{\odot} h^{-1}$, shown in Figure 1.2. The galaxy cluster total mass units are solar masses (M_{\odot}) normalized by h^{-1} , where $h = H(z)/100$ kpc/s/Mpc and $H(z)$ is the expansion rate of the Universe at redshift z . In the figure, the galaxy cluster counts are plotted against cosmological redshift. Each of the curves indicates a different cosmological model and it clearly shows the potential of using galaxy clusters to distinguish between these models. Observational work to complement the simulations and constrain cosmological models, requires the identification of galaxy clusters and a measurement of their mass allowing for a direct comparison between the measurement from observations and predictions from simulations.

In addition to the galaxy cluster abundance, their radial mass distribution allows

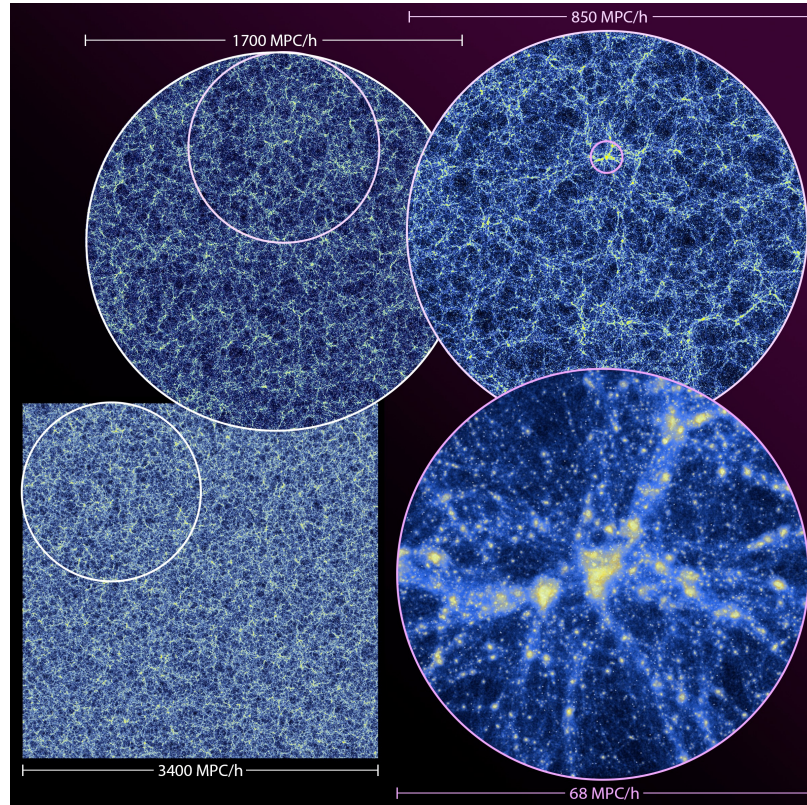


Figure 1.1: **The Last Journey Cosmological Simulation Matter Distribution.** From Heitmann et al. (2021). Visualization of the dark matter distribution at different scales in the cosmological simulation. The large scale structure of matter is called the cosmic web.

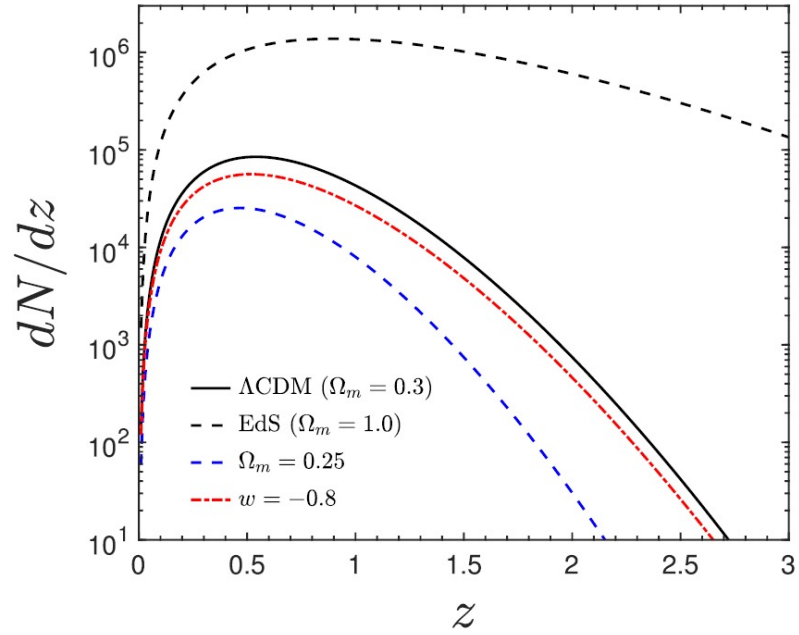


Figure 1.2: **Galaxy Cluster Abundance as an Observational Constraint of Cosmological Models.** From Huterer & Shafer (2018). Predicted galaxy cluster counts, dN/dz , for a survey covering $5,000 \text{ deg}^2$ of the sky with a minimum cluster mass of $10^{14} M_{\odot} h^{-1}$. The y-axis indicates the cosmological redshift. The solid black line represents the fiducial ΛCDM cosmological model and the rest of the curves show different cosmological models.

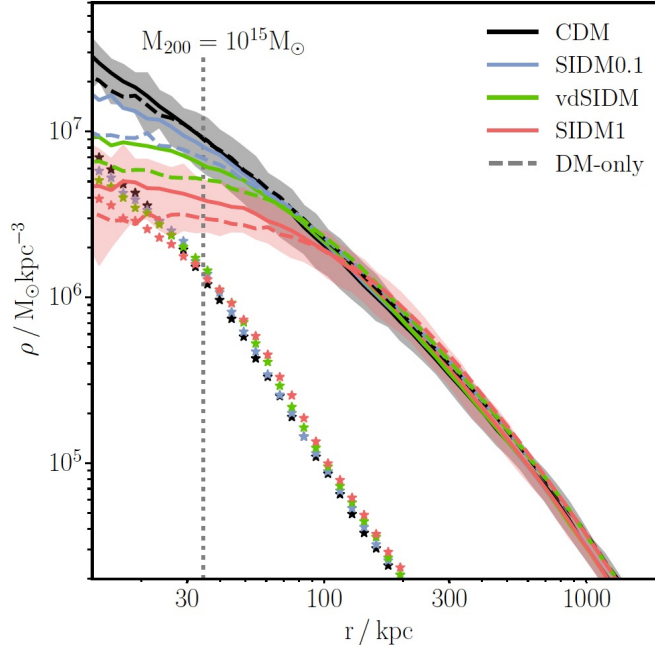


Figure 1.3: **Galaxy Cluster Radial Density Distribution.** From Robertson et al. (2019). Tests of different dark matter properties from the BAHAMAS-SIDM (McCarthy et al., 2017; Robertson et al., 2017) of stacked galaxy cluster radial density profiles at $z = 0$ for a cluster mass $\sim 10^{15} M_{\odot}$. The solid lines represent the radial profile with all matter components, dashed lines represent the dark matter only, and the stars represent the stellar density profile. The vertical dashed line represents the convergence radius meaning the resolution limit from the simulations. Each color indicates a different prescription for dark matter.

for a detailed study of baryonic and Dark Matter properties. Simulations provide us with a prediction of the shape of the density distribution of galaxy clusters for a variety of DM properties, see Figure 1.3 from Robertson et al. (2019). While the density distribution for the different prescriptions for dark matter matches at the very large scales, there are clear distinctions at the cores of galaxy clusters indicating that the use of observational data can be leveraged to distinguish between DM properties. This study highlights the importance of measuring the galaxy cluster mass on a broad range of cluster-centric radial scales from the core to the outskirts of the cluster.

As it has been indicated the galaxy cluster mass is key and provides a connection between the observables and the underlying cosmology (e.g., Evrard et al. 2002). Galaxy cluster mass estimates are dependent on observable astrophysical quantities

making paramount the understanding of systematic errors and assumptions employed in the mass estimation process (e.g., Evrard et al. 2002; Allen et al. 2011; Huterer & Shafer 2018). Also, critical to these works is the use of large samples of galaxy clusters with well characterized selection functions and implicit bias in the observational techniques employed in their detection.

1.1.2 The Mass Distribution of Galaxy Clusters

The radial density profile of galaxies clusters follows a Navarro-Frenk-White (NFW) profile (Navarro et al., 1996, 1997) established using simulations:

$$\rho_{\text{NFW}}(r) = \frac{\rho_s}{(r/r_s)(1+r/r_s)^2}, \quad (1.1)$$

where r_s is the scale radius and ρ_s is the scale density. The scale density can then be defined as $\rho_s(z) = \rho_{\text{crit}}(z)\delta_c$, where $\rho_{\text{crit}}(z)$ is the critical density of the universe and δ_c is the density scaling factor defined further below. The critical density of the universe is as follows:

$$\rho_{\text{crit}}(z) = \frac{3H(z)^2}{8\pi G}, \quad (1.2)$$

where G is the gravitational constant and $H(z)$ is the expansion rate of the Universe at redshift z . The concentration of a galaxy cluster is then established as the ratio of a radius of interest and the scale radius:

$$c_\Delta = \frac{r_\Delta}{r_s}, \quad (1.3)$$

where the radius of interest, r_Δ , is described as the radius for which the averaged enclosed density is Δ times the critical density of the Universe at this redshift:

$$\frac{M_\Delta}{4/3\pi r_\Delta^3} = \rho_{\text{crit}}(z)\Delta, \quad (1.4)$$

and M_Δ is the corresponding enclosed mass within r_Δ . Typical numbers for Δ used in the literature related to galaxy clusters are $\Delta = 2500, 500, 200$ (e.g., r_{200} is the radius for which the averaged enclosed density is 200 times $\rho_{crit}(z)$ and the corresponding mass is M_{200}).

The mass enclosed by a sphere of radius R can be computed using the definition of the NFW density profile:

$$\begin{aligned}
M_{\text{NFW}}(R) &= \int_0^R \int_0^{2\pi} \int_0^\pi \rho_{\text{NFW}}(r) r^2 \sin(\phi) d\phi d\theta dr \\
&= 4\pi \int_0^R \rho_{\text{NFW}}(r) r^2 dr \\
&= 4\pi \rho_{crit}(z) \delta_c r_s^3 \left[\ln \left(1 + \frac{R}{r_s} \right) - \frac{R/r_s}{1 + R/r_s} \right],
\end{aligned} \tag{1.5}$$

and then this mass from the NFW profile, $M_{\text{NFW}}(r_\Delta)$, can be set equal to the mass M_Δ (Equation 1.4) to establish the form of the density scaling factor δ_c and its dependence on Δ , r_Δ , and r_s :

$$\begin{aligned}
M_{\text{NFW}}(r_\Delta) &= M_\Delta \\
4\pi \rho_{crit}(z) \delta_c r_s^3 \left[\ln \left(1 + \frac{r_\Delta}{r_s} \right) - \frac{r_\Delta/r_s}{1 + r_\Delta/r_s} \right] &= \rho_{crit}(z) \Delta \frac{4}{3} \pi r_\Delta^3 \\
\delta_c &= \frac{\Delta}{3} \left(\frac{r_\Delta}{r_s} \right)^3 \left[\ln \left(1 + \frac{r_\Delta}{r_s} \right) - \frac{r_\Delta/r_s}{1 + r_\Delta/r_s} \right]^{-1}.
\end{aligned} \tag{1.6}$$

Substituting Equation 1.6 in the NFW density profile (Equation 1.1) results as follows:

$$\rho_{\text{NFW}}(r) = \frac{\rho_{crit}(z)}{(r/r_s)(1 + r/r_s)^2} \frac{\Delta}{3} \left(\frac{r_\Delta}{r_s} \right)^3 \left[\ln \left(1 + \frac{r_\Delta}{r_s} \right) - \frac{r_\Delta/r_s}{1 + r_\Delta/r_s} \right]^{-1} \tag{1.7}$$

where $\rho_{\text{NFW}}(r)$ is then dependent on the scale radius and several observational parameters: the redshift (z), the radius of interest (r_Δ), and Δ . The NFW profile, ρ_{NFW} , is shown in the *top* panel of Figure 1.4 and the enclosed mass by the sphere, $M_{\text{NFW}}(r)$, in the *top* panel of Figure 1.5. Additional useful forms of the NFW profile include the surface density, $\Sigma_{\text{NFW}}(r)$ (Golse & Kneib, 2002):

$$\Sigma_{\text{NFW}}(r) = 2\rho_{\text{cirt}}(z)\delta_c r_s f(r/r_s), \quad (1.8)$$

where:

$$f(r/r_s) = \begin{cases} \frac{1}{(r/r_s)^2 - 1} \left(1 - \frac{1}{\sqrt{1 - (r/r_s)^2}} \operatorname{arccosh} \frac{1}{r/r_s} \right) & (r/r_s < 1) \\ \frac{1}{3} & (r/r_s = 1) \\ \frac{1}{(r/r_s)^2 - 1} \left(1 - \frac{1}{\sqrt{(r/r_s)^2 - 1}} \operatorname{arccos} \frac{1}{r/r_s} \right) & (r/r_s > 1) \end{cases}$$

and the average enclosed surface density, $\bar{\Sigma}_{\text{NFW}}(r)$:

$$\bar{\Sigma}_{\text{NFW}}(r) = 4\rho_{\text{cirt}}(z)\delta_c r_s \left(\frac{r_s}{r} \right)^2 g(r/r_s), \quad (1.9)$$

where:

$$g(r/r_s) = \begin{cases} \ln \frac{r}{2r_s} + \frac{1}{\sqrt{1 - (r/r_s)^2}} \operatorname{arccosh} \frac{1}{r/r_s} & (r/r_s < 1) \\ 1 + \ln \frac{1}{2} & (r/r_s = 1) \\ \ln \frac{r}{2r_s} + \frac{1}{\sqrt{(r/r_s)^2 - 1}} \operatorname{arccos} \frac{1}{r/r_s} & (r/r_s > 1). \end{cases}$$

Both $\Sigma_{\text{NFW}}(r)$ and $\bar{\Sigma}_{\text{NFW}}(r)$ are plotted on the *middle* and *bottom* panels of Figure 1.4, respectively. The NFW projected enclosed mass, $M_{\text{NFW-2D}}(r) = \pi r^2 \bar{\Sigma}_{\text{NFW}}(r)$, is shown in the *bottom* of Figure 1.5. These figures clearly show that galaxy clusters have a higher density at the core and it decreases towards the outskirts of the galaxy cluster.

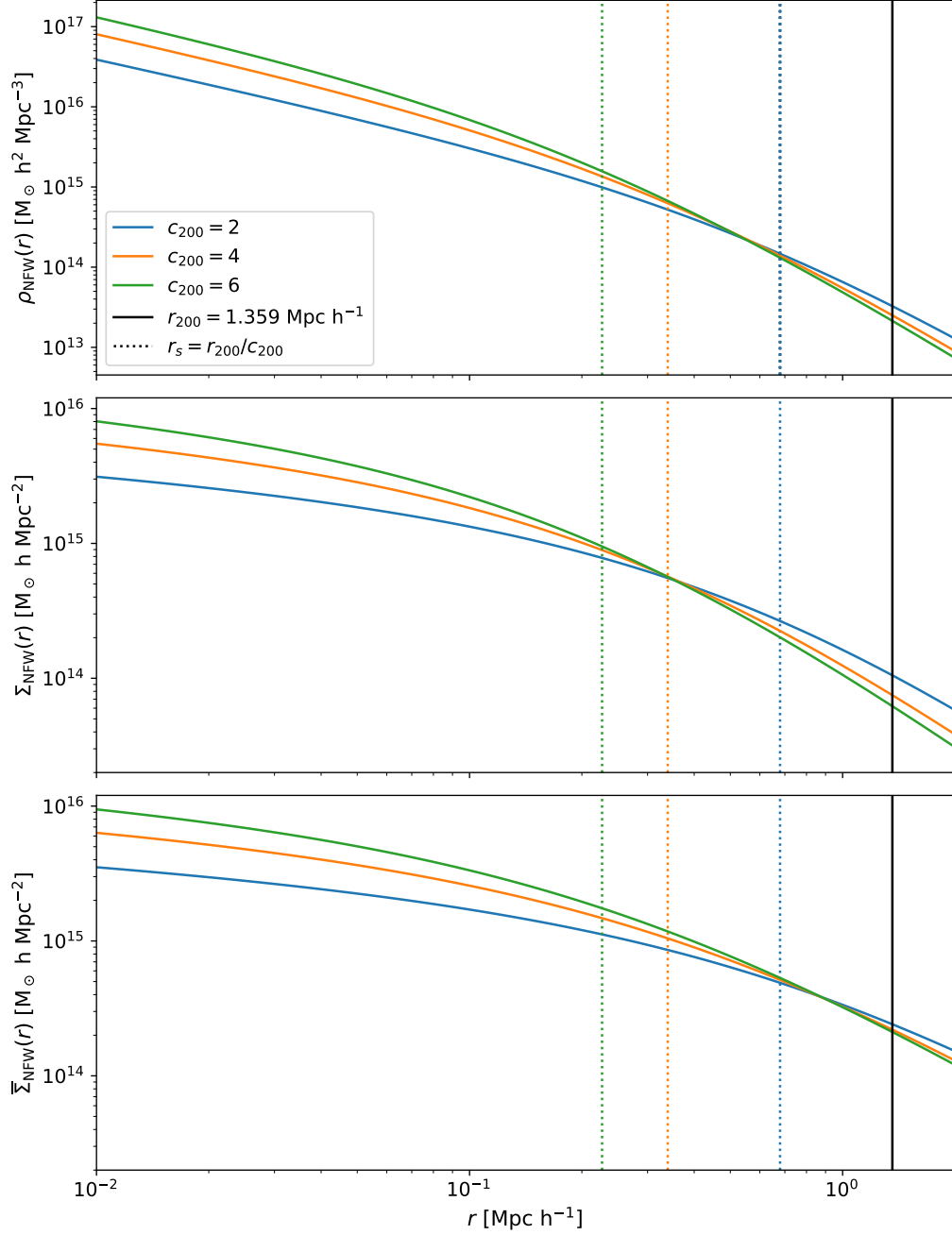


Figure 1.4: **NFW Density, Surface Density, and Average Surface Density Profiles.** The *top* panel shows the NFW mass density radial profile, $\rho_{\text{NFW}}(r)$, the *middle* panel shows the NFW surface density, $\Sigma_{\text{NFW}}(r)$, and the *bottom* panel shows the averaged NFW surface density, $\bar{\Sigma}_{\text{NFW}}(r)$, for a galaxy cluster with a mass of $M_{200} = 1 \times 10^{15} M_{\odot} h^{-1}$ at $z = 0.5$. Each color represents a different concentration, $c_{200} = r_{200}/r_s$, and the dotted vertical lines indicate the location of the scale radius for each case. The solid black line shows the radius of interest, $r_{200} = 1.359 \text{ Mpc } h^{-1}$.

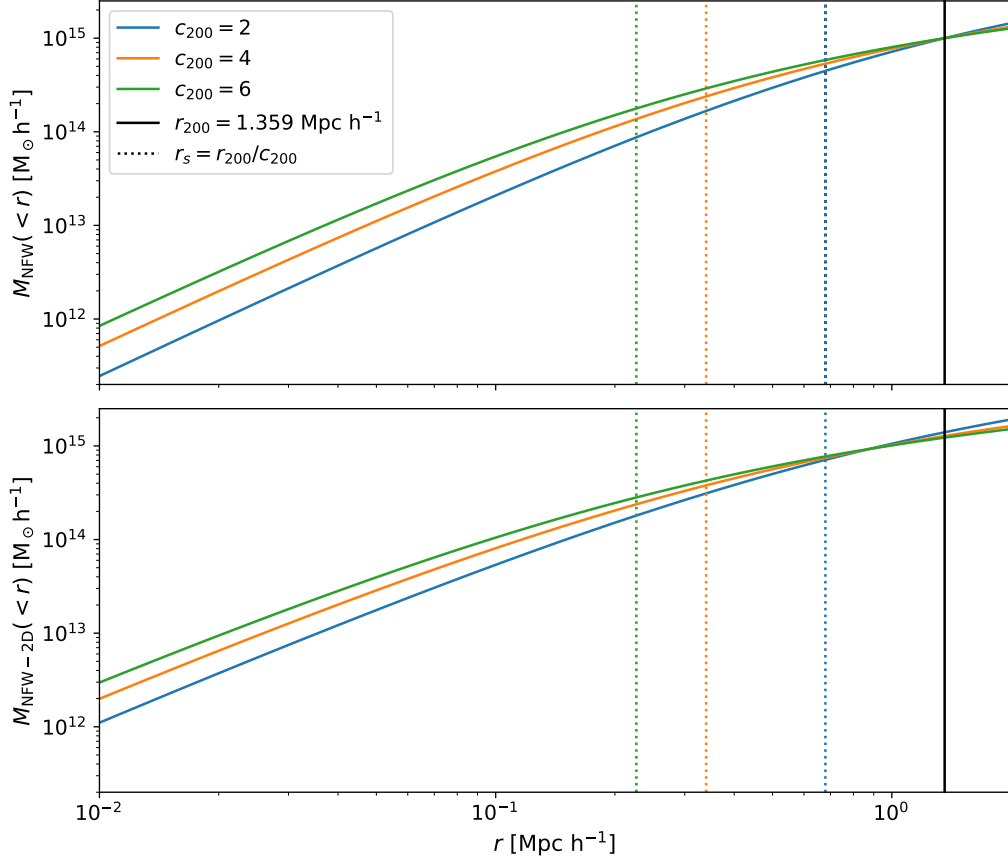


Figure 1.5: **Spherical and Projected Enclosed NFW Mass.** The *top* panel shows the spherical enclosed NFW mass, $M_{\text{NFW}}(< r)$, and the *bottom* panel shows the projected enclosed NFW mass, $M_{\text{NFW-2D}}(< r)$. The conventions of the colors and lines are the same as described in Figure 1.4.

The concentration of galaxy clusters, c_{Δ} , can be directly measured in both simulations (e.g., Duffy et al. 2008; Bhattacharya et al. 2013; Meneghetti et al. 2014; Child et al. 2018) and observations (e.g., Okabe et al. 2010; Oguri et al. 2012; Sereno et al. 2015; Merten et al. 2015), making it feasible to compare predictions and observations. The result of this comparison is informative as the concentration of galaxy clusters provides characterization of the distribution of matter in galaxy clusters and its evolution. A combination of mass estimates from the core and the outskirts of the galaxy cluster serves as leverage when constraining the mass distribution and computing the concentration.

The concentration-mass (c-M) relation represents a connection between the galaxy cluster mass and its mass distribution. In Figure 1.6, from Child et al. (2018), the c-M relation for individual galaxy clusters is shown, where the black line indicates the prediction from simulations and the grey area its uncertainty. The points represent observational measurements. The comparison indicates good agreement between observations and predictions from simulations within errors; however, the sample size is small. A main goal of this thesis work is to increase the number of galaxy clusters for which the concentration is measured spanning a broader galaxy cluster redshift and mass range. The increase in galaxy cluster sample size with a broader mass and redshift coverage will allow for a better population study of the concentration-mass relation through cosmic time.

1.1.3 Astronomical Surveys of Galaxy Clusters

Current and upcoming large astronomical surveys are discovering tens of thousands of galaxy clusters. These surveys use different observational techniques for selection and characterization of clusters, resulting in different selection functions. The use of complementary data in the same sky area also provides a multi-wavelength view of these galaxy clusters and their properties. Galaxy cluster catalogs are

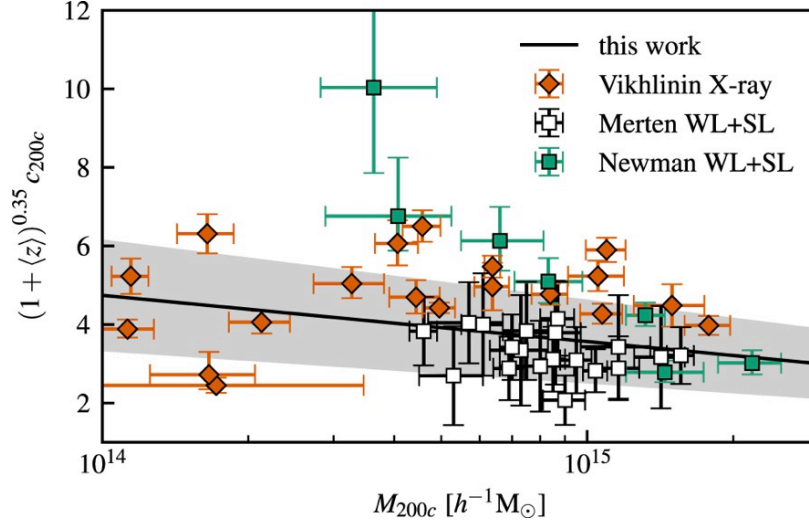


Figure 1.6: **Concentration-Mass Relation in Simulations and Observations.** From Child et al. (2018). Comparison between the prediction of the c - M relation and individual observed galaxy clusters. The y-axis, c_{200c} , is the concentration and M_{200c} is the total mass of the galaxy cluster. The black line is the predicted c - M relation from the individual halos from the Outer Rim cosmological simulations (Heitmann et al., 2019) and the grey shaded region indicates the 1σ . The symbols represent measurements of individual observed galaxy clusters.

drawn from large surveys including the South Pole Telescope (SPT-SZ 2500 deg², Bleem et al. 2015, in the sub-mm wavelength), the Atacama Cosmological Telescope (ACT, Hilton et al. 2018, in the sub-mm wavelength), the Dark Energy Survey (DES, Abbott et al. 2018, in the optical wavelength), the Sloan Digital Sky Survey (SDSS, Rykoff et al. 2014, in the optical wavelength), and ROSAT All-Sky Survey (RASS, Ebeling et al. 1998, in the X-ray wavelength). The future also brings incredible opportunities with surveys like SPT-3G (Benson et al., 2014), the Vera Rubin Observatory Legacy Survey of Space and Time (LSST, LSST Science Collaboration et al. 2009), and eROSITA (Pillepich et al., 2018). In Figure 1.7, we show the Mass-Redshift distribution of galaxy clusters from some of the current large astronomical surveys.

The large samples of galaxy clusters serve as cosmological indicators to constrain cosmological parameters. In addition to the detection and characterization of tens of thousands of galaxy clusters, a portion of these will have gravitational lensing evidence (see Figure 1.8 from LSST Science Collaboration et al. 2017). Strong gravitational

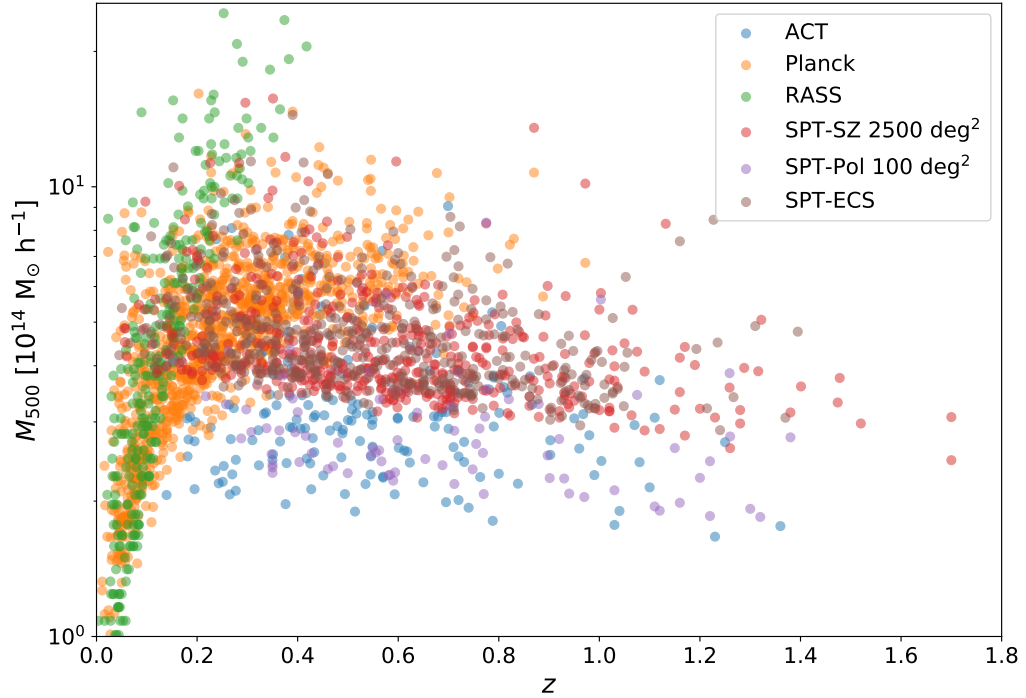


Figure 1.7: **Galaxy Cluster Samples.** The mass - redshift distribution of some large samples of galaxy clusters from different surveys. M_{500} is the mass of an aperture with radius r_{500} for which the average enclosed density is 500 the critical density of the Universe at that redshift. The colors indicate the different parent surveys from which the clusters were identified: Atacama Cosmological Telescope (ACT; Hilton et al. 2018, Planck (Planck Collaboration et al., 2016), Rosat All-Sky-Survey (RASS; Ebeling et al. (1998, 2000)), South Pole Telescope (SPT-SZ 2500 deg²; Bleem et al. 2015, SPT-Pol 100 deg²; Huang et al. 2020, and SPT-ECS; Bleem et al. 2020).

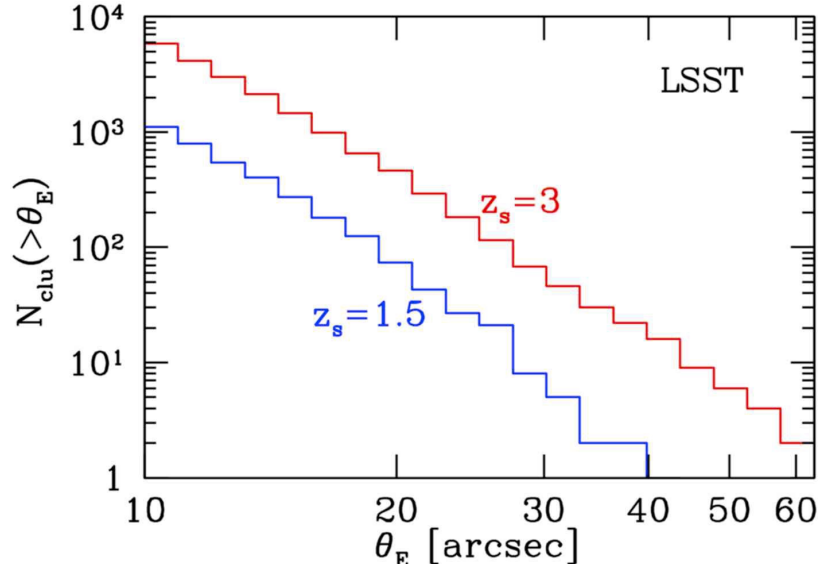


Figure 1.8: **LSST Prediction on the Numbers of Strong Gravitational Lensing Galaxy Clusters.** From LSST Science Collaboration et al. (2017). The estimated number of strong gravitational lenses with large Einstein radius ($\theta_E > 10''$) for galaxy clusters with a total mass $> 10^{14} M_\odot$. The expected number of clusters to be discovered in the survey is $\sim 10^3$.

lensing, defined in the next section, provides a unique opportunity to learn about the galaxy cluster itself and the magnified background universe.

1.2 Gravitational Lensing

Gravitational lensing occurs when light from a source is deflected due to a gravitational potential of a massive object. This results in distorted, magnified, single or multiple images of the background source. Gravitational lensing then provide an opportunity as cosmological telescopes magnifying the background universe. At the same time, the lensing evidence can be used to create a detailed characterization of the lens mass distribution. For further review please see Narayan & Bartelmann (1996); Kochanek (2006).

1.2.1 Strong Gravitational Lensing Theory

Einstein’s General Theory of Relativity (Einstein 1911) describes the motion of light particles through spacetime, traveling at speed c in all reference frames, thus following a geodesic. When the geodesics are solved for the Schwarzschild metric, the deflection of light by a point mass, M , results in the following:

$$\alpha = \frac{4GM}{c^2 b} \quad (1.10)$$

when $GM/c^2 r \ll 1$, where α is the deflection angle and b is the impact parameter (see Figure 1.9). The lensing equation (Equation 1.11) traces the observed image-plane (also referred to as lens-plane) positions of the lensed sources to the source-plane location in the background. When multiple solutions of the lens equation exist, this results in multiple images of the same background source, defining the strong lensing regime. The lensing equation is defined as follows:

$$\begin{aligned} \vec{\beta} &= \vec{\theta} - \vec{\alpha}(\vec{\theta}), \\ \vec{\alpha}(\vec{\theta}) &= \frac{D_{LS}(z_L, z_S)}{D_S(z_S)} \hat{\alpha}(\vec{\theta}), \end{aligned} \quad (1.11)$$

where $\vec{\beta}$ is the lensed source position in the source-plane, $\vec{\theta}$ is the image position in the image-plane, $\vec{\alpha}(\vec{\theta})$ is the deflection angle, $D_{LS}(z_L, z_S)$ is the angular diameter distance between the lens and the source, $D_S(z_S)$ is the angular diameter distance between the observer and the source, z_L is the redshift of the lens, and z_S is the redshift of the source. Due to the large cosmological distance involved between the observer and the lens ($D_L(z_L)$), the lens and the source ($D_{LS}(z_L, z_S)$), and the observer and the source ($D_S(z_S)$), it is common to use the “thin lens approximation” which assumes an instantaneous deflection of the light at the lens-plane. The geometry of the system is shown in Figure 1.9 from Johnson (2018).

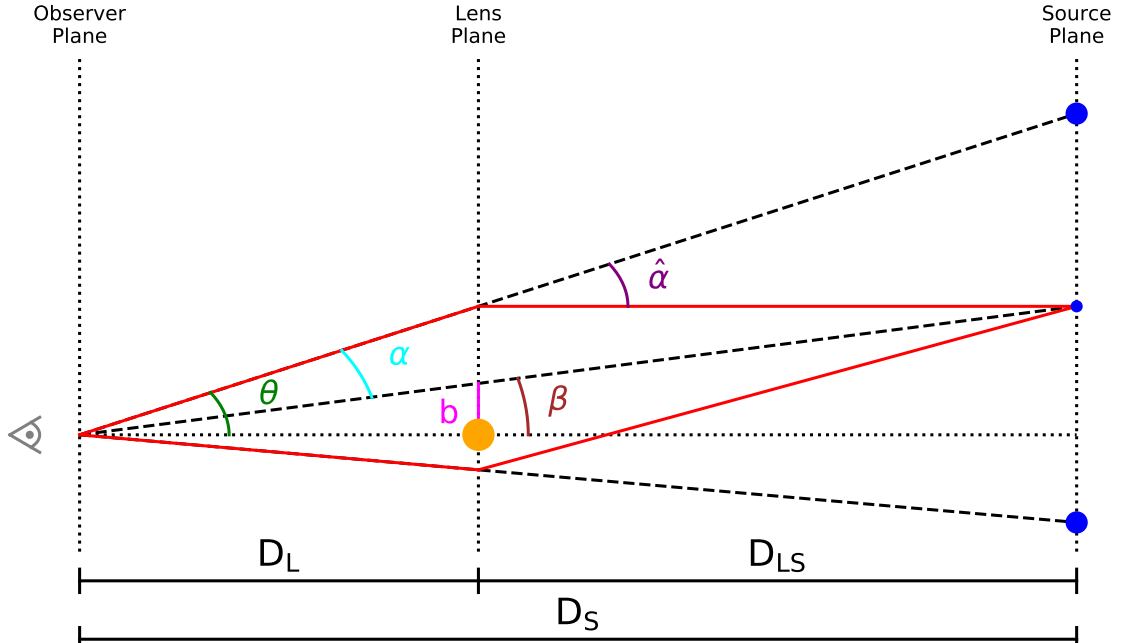


Figure 1.9: **Gravitational Lensing Geometry.** From Johnson (2018). Diagram describing the geometry of the gravitational lensing system including the definition of angles and angular diameter distances utilized in the lensing equation (Equation 1.11).

The magnification, μ , due to the gravitational lens can be computed for the complete field of view as the determinant of the magnification matrix, \mathcal{A} :

$$\mu^{-1} = \det(\mathcal{A}^{-1}) = (1 - \kappa)^2 - \gamma^2, \quad (1.12)$$

where κ is the convergence and γ is the shear. Loci in the image plane where $\mu^{-1} = 0$ formally results in infinite magnification and are called the tangential and radial critical curve, named to indicate the primary direction in which the arcs are magnified. The magnification in the tangential and radial directions are the eigenvectors of \mathcal{A} , defined as follows:

$$\mu_T^{-1} = 1 - \kappa - \gamma \quad (1.13)$$

and

$$\mu_R^{-1} = 1 - \kappa + \gamma. \quad (1.14)$$

Last, we re-write γ and κ as mathematical transformations from the deflection angle, $\alpha(\theta)$:

$$\begin{aligned}\gamma_1 &= \frac{1}{2} \left(\frac{\partial \alpha_1}{\partial \theta_1} - \frac{\partial \alpha_2}{\partial \theta_2} \right), \\ \gamma_2 &= \frac{\partial \alpha_1}{\partial \theta_2} = \frac{\partial \alpha_2}{\partial \theta_1}, \\ \gamma^2 &= \gamma_1^2 + \gamma_2^2,\end{aligned}\tag{1.15}$$

and

$$\kappa = \frac{1}{2} \nabla_{ij} \alpha_{ij} = \frac{\Sigma}{\Sigma_{crit}}\tag{1.16}$$

where Σ is the projected surface mass density and Σ_{crit} is the critical surface mass density defined as follows:

$$\Sigma_{crit}(z_L, z_S) = \frac{c^2}{4\pi G} \frac{D_S(z_S)}{D_{LS}(z_L, z_S) D_L(z_L)}.\tag{1.17}$$

The connection between the mass of the object responsible for the lensing and the deflection angle is clear, with more massive objects resulting in greater deflections and in the case of strong gravitational lensing wide-separation multiply-imaged lensed sources. Fritz Zwicky proposed in his 1937 work “Nebulae as Gravitational Lenses” (Zwicky, 1937) that galaxies could themselves act as lenses and allow for an easier detection of the gravitational lensing effect. It was not until 1979 that the first strong gravitational lens was identified by Walsh et al. (1979) named the “Twin Quasar” and due to the similarity in the redshift and spectral energy distribution of the quasar it was deduced that they had to be two images of the same background object (Chang & Refsdal, 1979; Porcas et al., 1979; Weymann et al., 1979).

1.2.2 Strong Gravitational Lensing by Galaxy Clusters

Galaxy clusters being the largest gravitational bound structures in the Universe, are great candidates as gravitational lenses. The total mass, mass distribution, and concentration properties of the galaxy cluster correlate with its ability to be a strong gravitational lens (e.g., Fox et al. 2021). Studies utilizing strong lensing by galaxy clusters have encompassed a variety of topics including Dark Matter properties (e.g., Bradač et al. 2006; Diego et al. 2018), galaxy cluster concentration (e.g., Oguri et al. 2012; Merten et al. 2015), and constrain cosmological parameters (e.g., Acebron et al. (2017)). When using galaxy clusters as cosmic telescopes to magnify the background universe, strong lensing provides unique opportunities to study in high resolution galaxy properties (e.g., Johnson et al. 2017b; Rigby et al. 2018) at the epoch of cosmic noon ($z \sim 2$, when most of the stars of the Universe were created), and it has allowed for the identification and characterization of high-redshift ($z \sim 5 - 9$) galaxies (e.g., Salmon et al. 2020; Strait et al. 2020).

The unique opportunity created by strong gravitational lensing by galaxy clusters, has resulted in multiple samples with a variety of selection functions and approaches to learn about the Universe. Some of these strong lensing samples include the Sloan Giant Arc Survey (SGAS¹; Hennawi et al. 2008; Sharon et al. 2020) which selected strong gravitational lensing clusters by visually inspecting thousands of color images from the Sloan Digital Sky Survey Data Release 7 (SDSS-DR7; Abazajian et al. 2009) with the main goal of characterizing in detail highly magnified giant arcs; the Cluster Lensing and Supernovae Survey with *Hubble* (CLASH²; Postman et al. 2012), designed to study the dark matter distribution in galaxy clusters, to perform supernova searches, and to detect and characterize high-redshift galaxies; the Reionization Lensing Cluster Survey (RELICS³; Coe et al. 2019), designed primarily to find high-

¹<https://archive.stsci.edu/pub/hlsp/sgas/>

²<https://www.stsci.edu/postman/CLASH/index.html>

³<https://relics.stsci.edu/index.html>

redshift ($z \sim 6 - 8$) lensed galaxy candidates; and the *Hubble* Frontier Fields (HFF⁴; Lotz et al. 2017) with the goal of expanding our understanding of the high-redshift universe and laying the ground work for future observations of the early universe. The HFF program resulted in the second deepest observations with *HST* and the extensive community investment in follow-up has allowed for some of the most detailed studies of strong gravitational lensing galaxy clusters. The HFF galaxy clusters are shown in Figure 1.10 as extraordinary examples of strong gravitational lensing by galaxy clusters. RELICS, CLASH, and particularly HFF have created a unique opportunity to study the systematic and statistical uncertainties of the detailed lens models computed for these galaxy clusters.

Strong gravitational lens models use the positions in the image plane of the multiply-imaged sources and their redshift to constrain the underlying mass distribution and reproduce the observed lensing configuration. There exists a variety of lensing algorithms, which use different techniques and assumptions to model the underlying mass distribution of the lens. In the next few paragraphs, we provide a brief overview of strong gravitational lens models, their uses and limitations.

Detailed lens models are usually grouped into three groups: parametric, non-parametric (“free-form”), and hybrid, based on the parametrization employed to model the mass distribution of the lens. Parametric models utilize a variety of analytical parametric density profiles to describe the mass of the lens. Non-parametric algorithms make no assumption on the functional form of the mass distribution of the lens. Last, hybrid algorithms employ a combination of these two forms. The diversity in algorithms allows for testing a variety of lens properties, including the degree to which the mass distribution is correlated with the observed light distribution. Direct comparisons between the lens models produced for the HFF clusters has revealed great agreement between the different methods (e.g., Remolina González et al. 2018;

⁴<https://outerspace.stsci.edu/display/HPR/HST+Frontier+Fields>

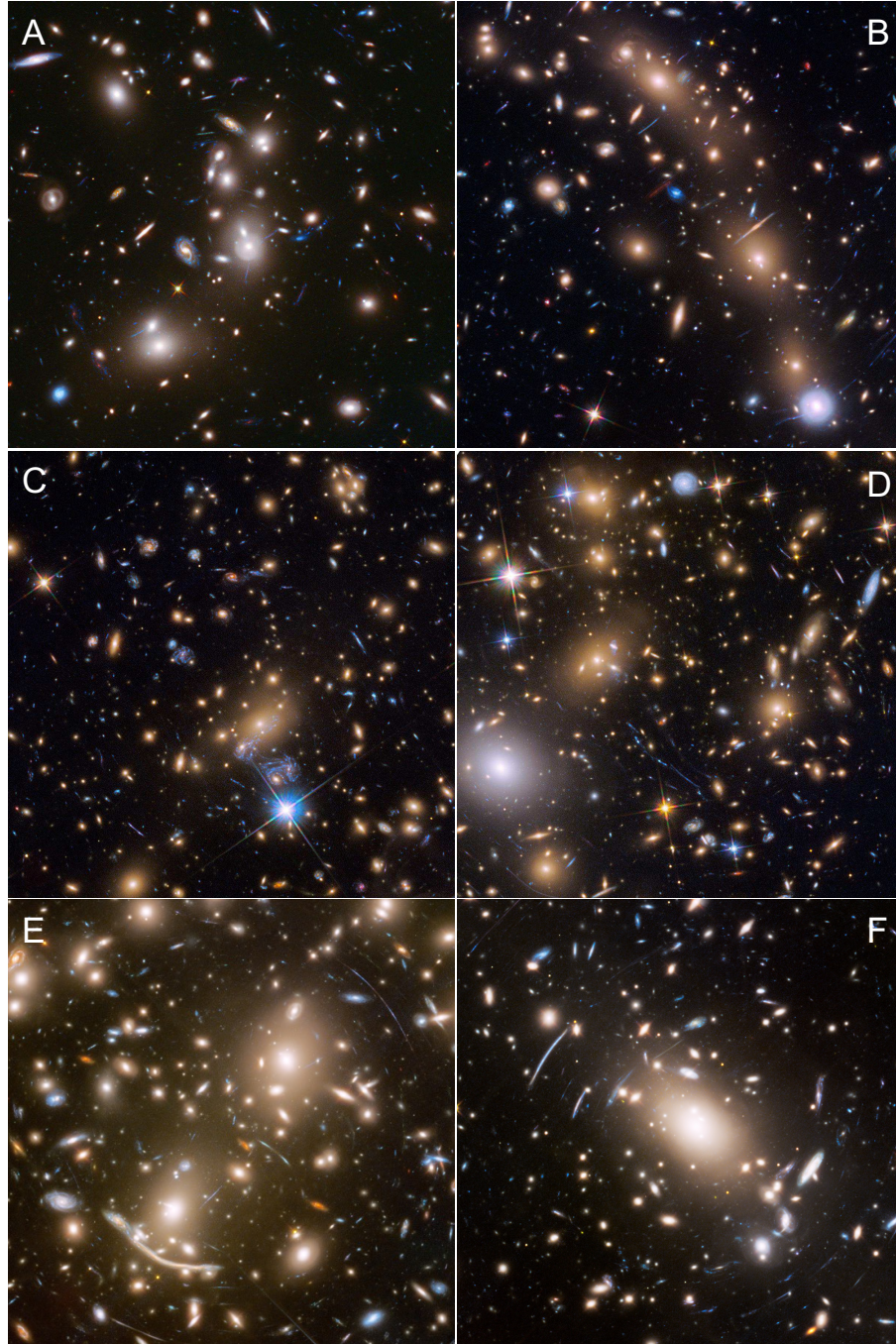


Figure 1.10: *Hubble Frontier Fields (HFF) Galaxy Clusters*. *Hubble* Space Telescope images for the six HFF galaxy clusters utilizing Director’s Discretionary time (Lotz et al., 2017). The galaxy clusters are A) Abell 2744, B) MACS J0416.5–2403, C) MACS J1149.5+2223, D) MACS J0717+3745, E) Abell 370, and F) Abell S1063 (RXC J2248.7–4431). The images for panels A, B, C, and D are taken from Lotz et al. (2017) and represent the full-depth *HST* data. The images of panels E and F use the full depth of the *HST* imaging and are credited to NASA, ESA, and STScI. The field of view for all the images is $1.5' \times 1.5'$. These are some of the best studied strong gravitational lensing galaxy clusters thanks to the extensive community investment on the observations and follow-up.

Raney et al. 2020b) and shown the reliability of the lens model outputs.

The detailed lens models can be highly complex, adding the flexibility required for detailed studies of galaxy cluster properties and their environment, un-correlated structure along the line-of-sight, the background universe, and cosmology. The large number of free-parameters in the detailed lens models require a large quantity of constraints in the form of multiply-imaged lensed sources, whose availability and identification becomes a limiting factor of the modeling process. As part of the modeling process care is needed in the construction and evaluation of the lens models, statistical assessments are utilized to select between lens models (e.g., Lagattuta et al. 2019; Mahler et al. 2019). High-fidelity lens models for clusters with rich strong lensing evidence require an extensive investment from the community including the telescope follow-up, computational resources, and human time. In most cases multiple iterations of the lens models are needed to achieve the final products and models get revised as new observational evidence becomes available (e.g., Sharon et al. 2012; Jauzac et al. 2015). The large investment required is a clear limitation in the lens modeling process, particularly when looking at the future with thousands of galaxy clusters with strong gravitational lensing evidence being discovered.

1.2.3 Simulated Strong Gravitational Lensing by Galaxy Clusters

To complement the assessment of detailed lens models using observations, simulations of strong gravitational lensing by galaxy clusters have been used to characterize the accuracy and precision of the different lensing algorithms. In a lens modeling comparison project by Meneghetti et al. (2017), all HFF lens modeling teams were asked to compute detailed lens models for two simulated strong lensing galaxy clusters created to mimic the observations of a HFF-like galaxy cluster. This work resulted in a direct comparison between the methods, and evaluation of the strengths and weaknesses of each lens modeling team’s approach. Overall, the detailed lens models

recover the mass distribution at the core of the galaxy clusters with high accuracy and precision. The magnification computed from the lens model outputs reveals clear differences between the different lensing algorithms. A large magnification variance of 50% or higher for extreme magnification ($\mu \sim 30$ and higher) and a variance of $\sim 10\% - 30\%$ for regions of high magnification ($\mu \sim 3 - 10$) is reported between the lensing algorithms. Simulations of strong gravitational lensing by galaxy clusters also introduce a unique opportunity to assess other efficient methods to measure the strong lensing cluster core mass by leveraging the strong lensing evidence.

Detailed lens models, while very accurate and precise, are inefficient when applied to large samples of strong lensing galaxy clusters. There is a need to employ other efficient and accurate methods to measure the core mass of galaxy clusters that leverage the strong lensing evidence. Simulated strong lensing by galaxy clusters allow for the assessment of two alternative methods to estimate the mass at the core of galaxy clusters, as described in Chapter II and Chapter III of this dissertation. The assessment of these two methods allow for their application to large samples of strong lensing galaxy cluster and estimate the mass at the cores of strong lensing galaxy clusters with accuracy and precision while taking a fraction of the time and resources than that of a detailed lens model.

Last, cosmological simulations of strong gravitational lensing galaxy clusters are used perform direct comparisons between the simulated and observable Universe. Some of the predictions include number of expected strong lensing galaxy clusters identified in a survey, the distribution of the cluster-centric distance of the multiple-images, and the mass density profile of strong gravitational lenses. An example of a strong lensing simulation by Li et al. (2016) mimicking the observations from a ground base observatory is shown in Figure 1.11. As part of this work our goal is to compare the predictions of the concentration-mass relation of strong gravitational lenses to that of observations and characterize the evolution through cosmic time of

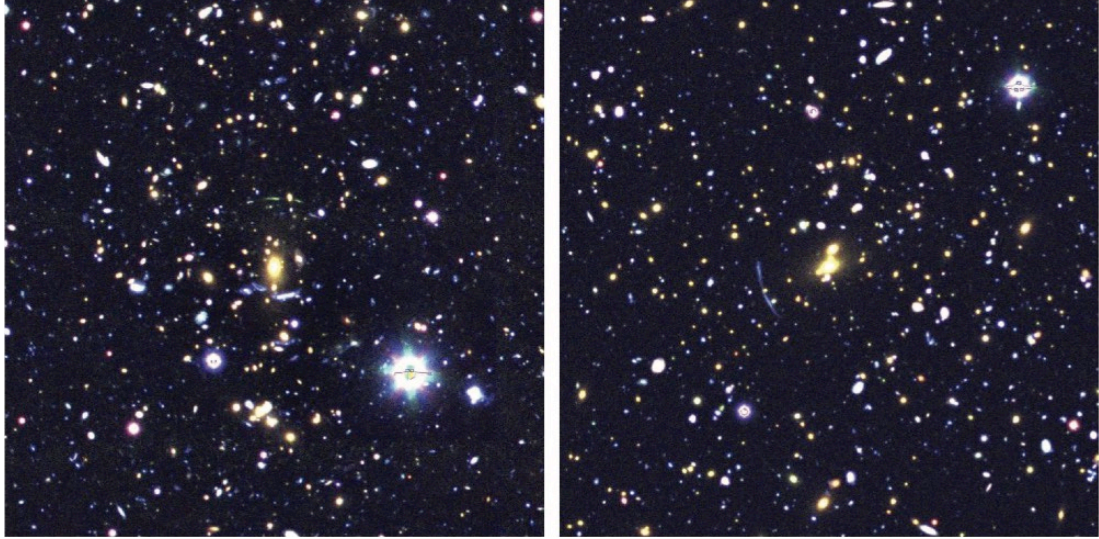


Figure 1.11: **Comparison between a Simulated and Observed Galaxy Cluster.** From Li et al. (2016). *Left* panel shows a South Pole Telescope galaxy cluster, SPT-CLJ0307-5042, observed with the ground-based MegaCam instrument mounted on the Magellan Clay Telescope. The field of view is $3' \times 3'$ and the filters used are g , r , and i . *Right* panel shows a simulated galaxy cluster with strong lensing evidence from the Outer Rim cosmological simulation using the Pipeline for Images of Cosmological Strong lensing (PICS) pipeline (Li et al., 2016) which mimics the observations taken utilizing MegaCam. The performance of the PICS pipeline are illustrated by the similarities between the observed and simulated strong lensing galaxy cluster image including the lensed arc magnification, flexure, galaxy cluster members, interloper sources along the line of sight, bright stars, imaging defects, and the instrument point spread function.

this relation.

1.3 The South Pole Telescope

The South Pole Telescope⁵ (SPT) is a 10-meter microwave, millimeter, and sub-millimeter telescope located at the Amundsen-Scott South Pole research station (see Figure 1.12). The location has an ideal atmospheric environmental conditions enabling high sensitivity at millimeter and sub-millimeter wavelengths. The telescope employs state-of-the-art detectors which have been used to map a portion of the southern sky in the millimeter wavelength. The telescope capabilities and large col-

⁵<https://pole.uchicago.edu/public/Home.html>



Figure 1.12: **South Pole Telescope (SPT)**. Photo credit: Keith Vanderlinde. Image of the 10-meter South Pole Telescope located at the Amundsen-Scott South Pole research station.

laboration effort has resulted in the identification of over a thousand galaxy clusters (see Figure 1.13) using the Sunyaev Zel'dovich effect.

1.3.1 The Thermal Sunyaev Zel'dovich effect

In 1970's Sunyaev and Zel'dovich, proposed that the cosmic microwave background (CMB) could be used to detect galaxy clusters by using the CMB as back-light. The galaxy clusters leave a shadow when observed due to the interaction between the hot cluster gas and the CMB photons. The thermal Sunyaev-Zel'dovich effect (SZe; Sunyaev & Zeldovich 1972) describe an up-scatter in the energy of a CMB photon as it interacts with highly energetic electrons in the hot plasma located in the galaxy cluster intracluster medium. Only $\sim 1\%$ of CMB photons get up-scattered by the galaxy cluster, their energy shifts the CMB spectrum, and the effect can be observed in the maps from the CMB (see Figure 1.14). With advancements in the detectors and the increase in their numbers used to map the CMB, the resolution and precision

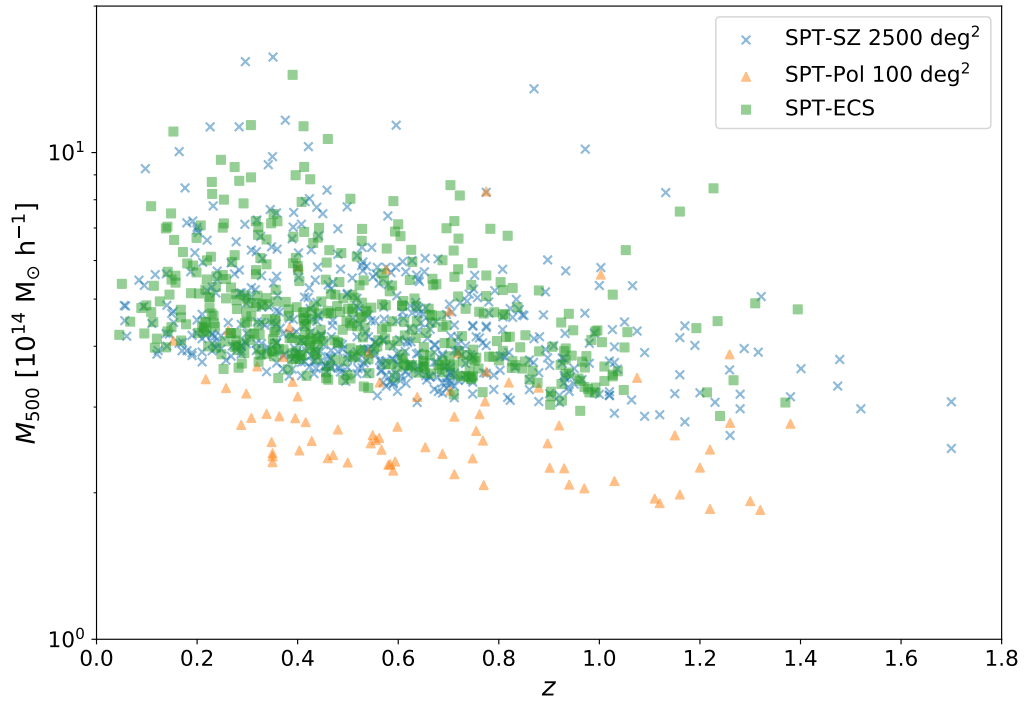


Figure 1.13: **SPT Galaxy Cluster Samples.** Mass redshift distributions for three galaxy cluster samples from the South Pole Telescope: SPT-SZ 2500 deg^2 (Bleem et al., 2015), SPT-Pol 100 deg^2 (Huang et al., 2020), and SPT-ECS (Bleem et al., 2020). A total of over 1,000 galaxy clusters were identified and cataloged in these works.

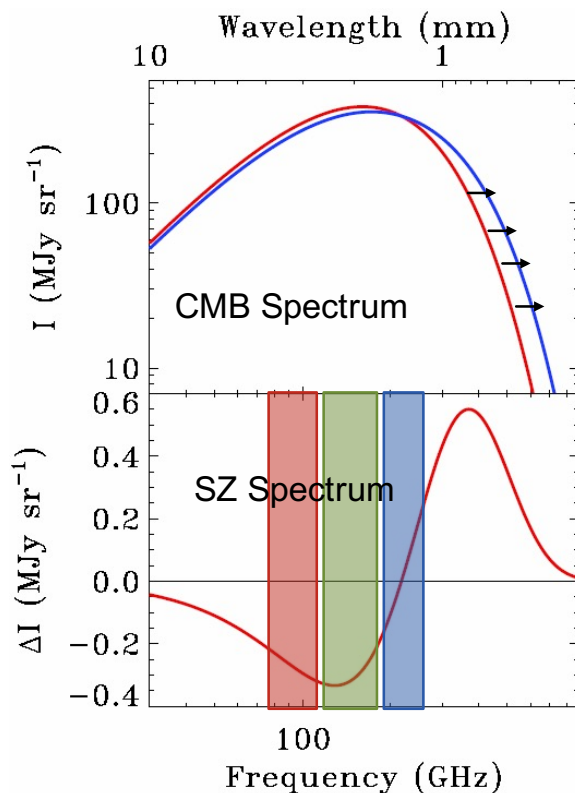


Figure 1.14: **Cosmic Microwave Background, CMB, and Sunyaev-Zel'dovich effect, SZe, Energy Spectrum.** From Bleem 2017 University of Michigan Colloquium obtained by private communication and credited to Tom Crawford and Brad Benson. The *top* panel shows the CMB spectrum in red and the shift due to the upscatter of energy in the CMB photons after interacting with the galaxy cluster hot plasma. The *bottom* panel then shows the difference between the CMB and the SZe spectrum. The 3 regions indicate observing bands that are used to identify sources utilizing the SZe technique.

of the CMB observations have made the SZe a unique method to detect thousands of galaxy clusters from both space- and ground-based observatories like Planck, ACT, and SPT. In Figure 1.15, a 50 deg^2 patch of the sky observed in the 150GHz frequency by SPT is shown. Highlighted in it are different sources of interest particularly the galaxy clusters which can be identified as darker regions where the photon energy has shifted due to its interaction with the galaxy cluster.

SPT is one of the telescopes taking the most advantage of the SZe effect to identify galaxy cluster across cosmic time. In addition to detecting galaxy clusters, the integrated SZe signal correlates well with the galaxy cluster mass at large scales (Motl

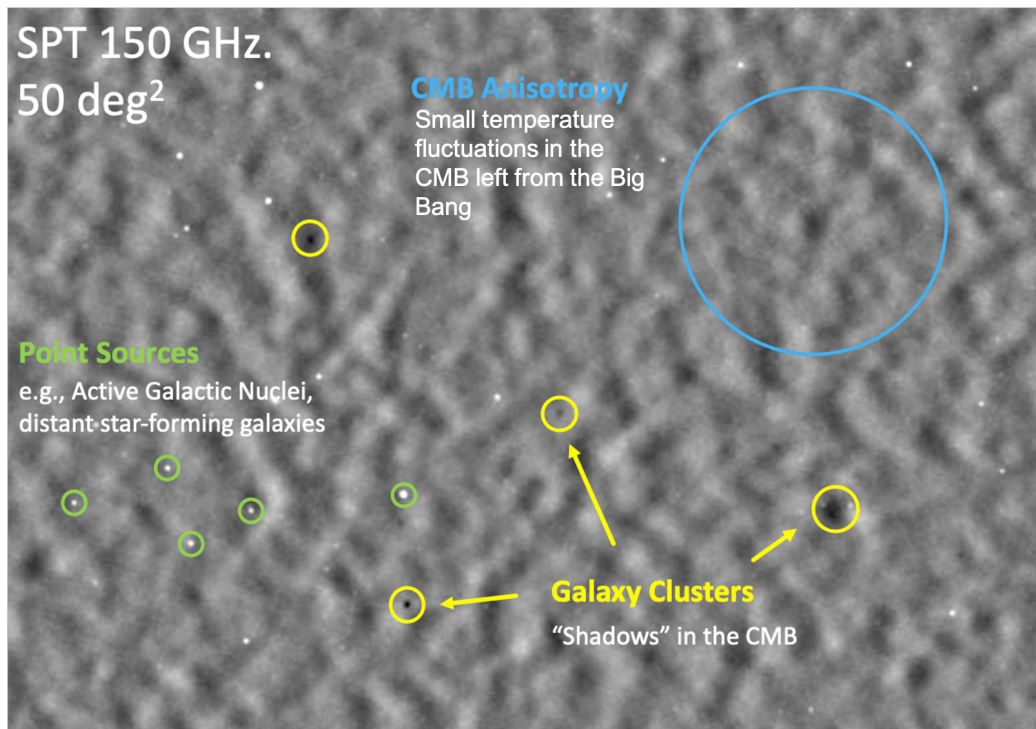


Figure 1.15: **SPT observations of the CMB.** From Bleem 2017 University of Michigan Colloquium obtained by private communication and credited to the SPTpol collaboration. 150 GHz observation of the CMB with SPT. In the image different features are identified. Galaxy clusters appear as shadows in this image.

et al., 2005). The combination of the detection and mass estimate makes the SPT galaxy cluster sample of particular interest for a variety of studies including cosmology, galaxy cluster properties, and their evolution through cosmic time.

1.3.2 South Pole Telescope Galaxy Cluster Sample

The South Pole Telescope galaxy cluster catalogs are of high completeness and purity. Three galaxy cluster catalogs were publicly released⁶ to date. The three galaxy cluster catalogs are: the SPT-SZ 2500deg² with 516 galaxy clusters (Bleem et al., 2015), the SPT Extended Cluster Survey (SPT-ECS) with 448 galaxy clusters, and the SPTpol 100deg² with 79 galaxy clusters for a grand total of 1043 galaxy clusters, shown in Figure 1.13 is their mass and redshift. The SPT galaxy clusters cover a broad range in the mass and redshift space making these cluster samples useful for studies of galaxy cluster properties and their evolution through cosmic time. Of particular interest is the selection function of these samples, which is almost redshift independent and mass limited.

In addition to the large samples of galaxy clusters from SPT, extensive optical imaging and spectroscopic follow-up has been pursued by the collaboration. Space-based optical observations from *HST* for around 200 galaxy clusters (see *top* panels of Figure 1.16 for examples from *HST* GO:15837, PI:Mahler) complements a uniform optical follow-up program undertaken with the ground-based Magellan Telescopes using the Parallel Imager for Southern Cosmology Observations (PISCO) resulting in observations of over 700 galaxy clusters (see *bottom* panels of Figure 1.16 for examples from the PISCO ground-based imaging). This work has allowed for the optical confirmation of the galaxy clusters, estimation of galaxy cluster photometric redshifts, and the identification of strong gravitational lensing evidence.

⁶<https://pole.uchicago.edu/public/data/sptsz-clusters/>

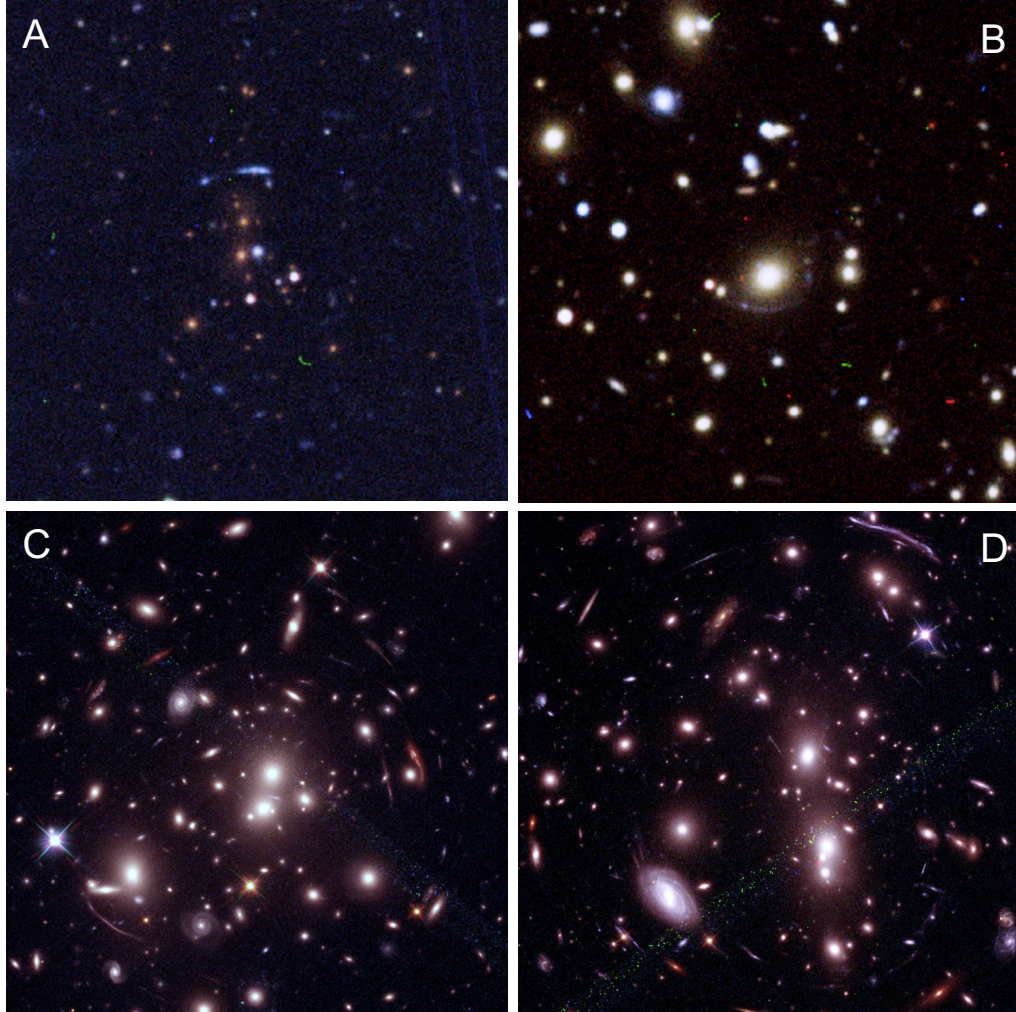


Figure 1.16: **Imaging of SPT Strong Lensing Galaxy Clusters.** *Top* panels are examples of SPT strong lensing galaxy clusters A) SPT-CL 0310-4647 and B) SPT-CL 1141-2127 imaged with the Parallel Imager for Southern Cosmology Observations (PISCO) instrument mounted on the Magellan Telescopes. The color images are created using the g , r , and z filters. The *bottom* panels are examples of SPT strong lensing galaxy cluster C) SPT-CL 0512-3848 and D) SPT-CL 2325-4111 imaged with the *Hubble* Space Telescope (GO:15837, PI: Mahler). The *HST* color images are created using the F140W, F814W, and F606W filters. The field of view for all the images is $1.5' \times 1.5'$.

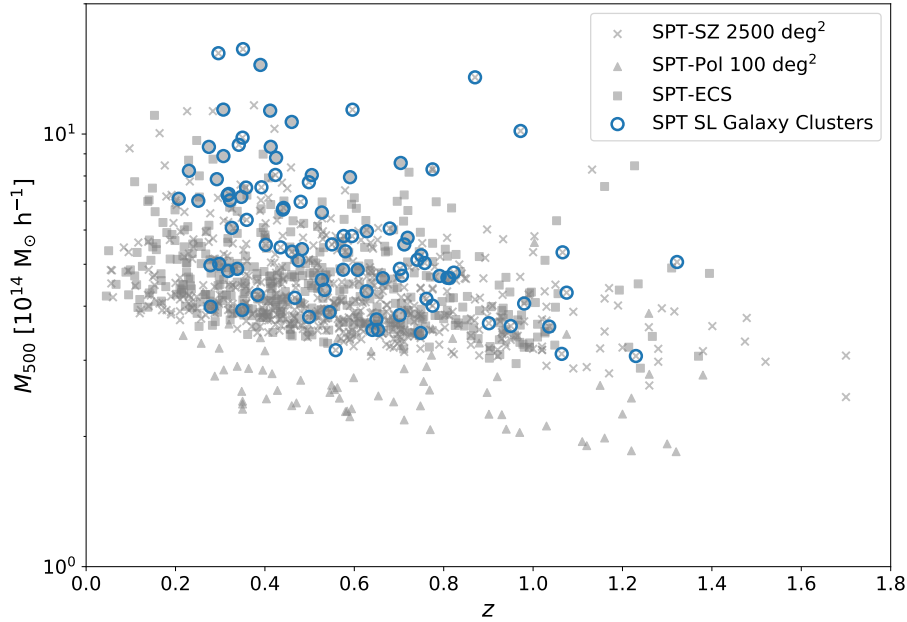


Figure 1.17: **Strong Lensing SPT Galaxy Clusters.** Similar to Figure 1.13, where the blue circles indicate the SPT galaxy clusters for which strong lensing evidence has been identified.

1.3.3 The SPT Strong Lensing Galaxy Clusters

From the extensive optical follow-up by the SPT collaboration a total of 193 galaxy clusters have been identified for having some strong lensing evidence. In Figure 1.17, I show all of the SPT galaxy clusters that have been catalogued and indicate the strong lensing galaxy clusters. The strong lensing galaxy clusters identified by SPT are unique due to the large number of clusters identified and their broad mass and redshift distributions. The identification of the multiply imaged lensed sources serve as important positional constraints for the lens modeling and estimating the mass at the cores of these galaxy clusters. In addition of the arcs locations in the sky, the redshift of the background sources and the lens are needed to estimate the different distance allowing us to constrain the geometry of the system, assuming a cosmology. The most reliable redshifts are measured from spectroscopic observations of sources of interest.

The University of Michigan has been one of the leads in the spectroscopic follow-

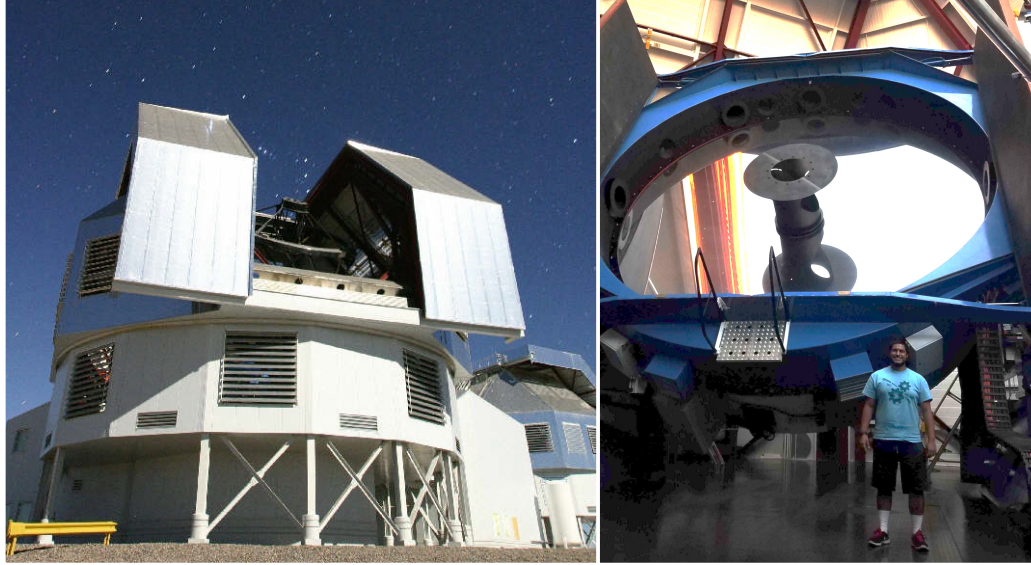


Figure 1.18: **Magellan Clay Telescope and Its Primary Mirror.** The Magellan Clay Telescope in combination with the Low Dispersion Survey Spectrograph (LDSS-3C) instrument are extensively utilized for the spectroscopic follow-up of strong gravitational lensing evidence and clusters (PI: Remolina González). The *left* panel shows the telescope dome and the *right* panel shows the primary 6.5 meter primary mirror.

up of SPT strong lensing galaxy clusters, and I have been the PI of this effort for the past four years (see Appendix D). This program employs the Low Dispersion Survey Spectrograph - 3C (LDSS-3C) mounted on the Magellan Clay Telescope (Figure 1.18 shows on the *left* panel an image of the Magellan Clay Telescope and on the *right* panel an image of the 6.5 meter primary mirror with me standing in-front of it for scale). This instrument's high efficiency, throughput, and broad wavelength coverage is highly compatible for this work. Multi object slit masks provide increased efficiency by targeting multiple objects in the $8.3' \times 6.4'$ field of view. In addition to targeting the strong lensing evidence, the galaxy cluster members are also targeted enabling us to acquire precise spectroscopic redshifts for the galaxy cluster itself. We were able to achieve a success rate of nearly 90% by complementing the LDSS-3C data with spectroscopy in the near infrared (NIR) spectroscopy program from The University of Chicago utilizing the Folded-port InfraRed Echellette (FIRE) instrument on the Magellan Baade Telescope.

The positional information from the optical imaging and the spectroscopic measurements from the spectroscopic follow-up program result in the constraints needed to compute the galaxy cluster core mass. The efficient and accurate methods of the mass enclosed by the Einstein radius (see Chapter II) and the core mass from a Single-Halo Lens Model (see Chapter III) are useful for this work and computing the core mass for a large sample of strong gravitational lensing galaxy clusters. The combination of the core mass estimate from strong lensing and the SZE mass in the outskirts of the cluster serve to constrain the density profile of the galaxy cluster and measure their concentration.

The concentration-mass relation of the SPT strong lensing galaxy clusters will be using the largest sample of strong lensing galaxy clusters with a well-understood selection function, spanning a broad mass and redshift range. The comparison between the simulated predictions and the large sample of strong lensing galaxy clusters identified by SPT is a unique opportunity to explore the concentration-mass relation for a broad range of galaxy cluster masses through cosmic time.

1.4 Dissertation Overview

The goal of this dissertation is to measure the concentration-mass relation across cosmic time. To facilitate this measurement in a large sample of clusters, I developed two fast methods to compute the mass at the core of strong lensing galaxy clusters and assess their efficiency, accuracy, and precision using a cosmological simulation. We demonstrate the application of these two methods in observational data by comparing the mass estimate to that from publicly available detailed lens models, and apply them to a sample drawn from the SPT galaxy clusters. We combine a mass estimate from the core and outskirts of simulated and observed galaxy clusters to constrain the radial, mass, density profile and measure the concentration-mass relation across cosmic time. The dissertation is composed of five chapters.

Chapter II describes the assessment of the mass enclosed by the Einstein radius as a zeroth order efficient method to measure the mass at the cores of strong lensing galaxy clusters. This work utilizes the Outer Rim cosmological simulation for which over a thousand of simulated strong lensing images were created. As part of the assessment, an empirical correction is developed to help debias the mass measurement and a set of recommendations are presented for the application of this method to large samples of observed strong lensing galaxy clusters. This chapter is published in ApJ as Remolina González et al. (2020), ApJ, 902, 44.

Chapter III describes the assessment of the mass enclosed by the effective Einstein radius computed from a Single-Halo Lens Model as a first order efficient method to estimate strong lensing galaxy clusters' core mass. Similar to the work from the previous chapter, the Outer Rim cosmological simulation is used. The Single-Halo Lens Models (SHM) uses the well-established lensing algorithm `Lenstool` (Jullo et al., 2007). The assessment of the SHM performance is undertaken through a quick visual inspection of the lens model outputs and the effect of the strong lensing configuration. This chapter is published in ApJ as Remolina González et al. (2021a), ApJ, 910, 144.

Chapter IV builds on the previous two chapters. In this chapter the two efficient methods are applied to a large sample of 62 observed galaxy clusters from the SGAS, CLASH, HFF, and RELICS samples. For our comparison the publicly available detailed lens models are utilized. This work directly showed the benefit of applying these two methods on large samples of observed strong lensing clusters. This chapter is submitted and under peer-review by ApJ. It is available through the arXiv e-prints as Remolina González et al. (2021b) arXiv:104.03883.

Chapter V describes the measurement of the concentration-mass relation through cosmic time for strong lensing galaxy clusters from the South Pole Telescope. The Outer Rim simulation is utilized to test the modeling procedures and predict the c-M relation for strong lensing clusters. The SPT strong lensing sample is unique for its

large number of clusters, well understood selection function, and broad coverage of the mass and redshift space. We measure the mass at the core of the galaxy clusters using the strong lensing evidence leveraging the methods developed in the previous chapters. We combine it with the SZE mass measured at the outskirts of the cluster to constrain the mass density profile from which the concentration is measured. This chapter is under preparation and will go through the SPT collaboration manuscript review process before being submitted to ApJ.

Chapter VI provides a summary of the main results from the work presented as part of this dissertation. A description of future extensions of this work to include other strong lensing samples. Last a brief discussion of new methods being developed to identify and characterize strong gravitational in the era of large astronomical surveys.

CHAPTER II

Efficient Mass Estimate at the Core of Strong Lensing Galaxy Clusters Using the Einstein Radius

Preface

This chapter has been adapted from a paper of the same title published in the *Astrophysical Journal*, Volume 902, Page 44 (Remolina González et al., 2020), with co-authors K. Sharon, B. Reed, N. Li, G. Mahler, L. E. Bleem, M. D. Gladders, A. Niemiec, A. Acebron, and H. Child. The paper is adapted and partially reproduced here under the non-exclusive rights of republication granted by the American Astronomical Society to the paper authors.

For this project, I utilized already created strong lensing simulations to characterize the accuracy, precision, and sources of uncertainty of a fast method to measure the mass at the core of strong lensing galaxy clusters, the mass enclosed by the Einstein radius. I performed all of the analysis shown with the feedback from the co-authors and the anonymous referee. I produced all of the figures and tables presented in the paper. I wrote nearly the whole text with the feedback and suggestions from the co-authors and the anonymous referee.

Abstract

In the era of large surveys, yielding thousands of galaxy clusters, efficient mass proxies at all scales are necessary in order to fully utilize clusters as cosmological probes. At the cores of strong lensing clusters, the Einstein radius can be turned into a mass estimate. This efficient method has been routinely used in literature, in lieu of detailed mass models; however, its scatter, assumed to be $\sim 30\%$, has not yet been quantified. Here, we assess this method by testing it against ray-traced images of cluster-scale halos from the Outer Rim N-body cosmological simulation. We measure a scatter of 13.9% and a positive bias of 8.8% in $M(< \theta_E)$, with no systematic correlation with total cluster mass, concentration, or lens or source redshifts. We find that increased deviation from spherical symmetry increases the scatter; conversely, where the lens produces arcs that cover a large fraction of its Einstein circle, both the scatter and the bias decrease. While spectroscopic redshifts of the lensed sources are critical for accurate magnifications and time delays, we show that for the purpose of estimating the total enclosed mass, the scatter introduced by source redshift uncertainty is negligible compared to other sources of error. Finally, we derive and apply an empirical correction that eliminates the bias, and reduces the scatter to 10.1% without introducing new correlations with mass, redshifts, or concentration. Our analysis provides the first quantitative assessment of the uncertainties in $M(< \theta_E)$, and enables its effective use as a core mass estimator of strong lensing galaxy clusters.

2.1 Introduction

Located at the knots of the cosmic web, galaxy clusters trace regions of overdensity in the large-scale structure of the universe, making them ideal cosmic laboratories. As cosmological probes (see review articles Allen et al. 2011; Mantz et al. 2014), clusters have been used to study dark energy (e.g., Frieman et al. 2008; Heneka

et al. 2018; Bonilla & Castillo 2018; Huterer & Shafer 2018) and dark matter (e.g., Bradač et al. 2006; Clowe et al. 2006; Bradač et al. 2008a; Diego et al. 2018), constrain cosmological parameters (e.g., Gladders et al. 2007; Dunkley et al. 2009; Rozo et al. 2010; Mantz et al. 2010, 2014; de Haan et al. 2016; Bocquet et al. 2019), measure the baryonic fraction (e.g., Fabian 1991; Allen et al. 2008; Vikhlinin et al. 2009) and the amplitude of the matter power spectrum (e.g., Allen et al. 2003). Crucial to cosmological studies using galaxy clusters is a large well-defined sample with a complete characterization of the selection function of the observations (e.g., Hu 2003; Khedekar & Majumdar 2013).

The mass distribution of galaxy clusters (cluster mass function) provides a connection between the observables and the underlying cosmology, and can constrain structure formation models (e.g., Jenkins et al. 2001; Evrard et al. 2002; Corless & King 2009). The galaxy cluster dynamical and non-linear hierarchical merging growth process (Bertschinger, 1998) introduces variance in the astronomical measurements (Evrard et al., 2002; Allen et al., 2011; Huterer & Shafer, 2018). Understanding the systematic errors and assumptions made when estimating the mass of galaxy clusters is paramount as they depend on observable astrophysical quantities (e.g., Evrard et al. 2002; Huterer & Shafer 2018).

With the advent of recent and upcoming large surveys spanning a broad wavelength range, thousands of strong lensing galaxy clusters will be detected out to redshift of $z \sim 2$ with a high completeness and purity. Examples include the surveys from the South Pole Telescope (SPT-3G, Benson et al. 2014; SPT-SZ 2500 deg², Bleem et al. 2015), Atacama Cosmological Telescope (ACT, Marriage et al. 2011; Hilton et al. 2018), Cerro Chajnantor Atacama Telescope (CCAT, Mittal et al. 2018), Dark Energy Survey (DES, Abbott et al. 2018), Euclid (Laureijs et al., 2011; Boldrin et al., 2012), Vera Rubin Observatory Legacy Survey of Space and Time (LSST, LSST Science Collaboration et al. 2009), ROSAT All-Sky Survey (RASS, Ebeling et al. 1998,

2000), and eROSITA (Pillepich et al., 2018). A thorough characterization of the selection function and bias implicit in the observations and detections is key. In addition, multi-wavelength coverage of some galaxy clusters will allow for an extensive study of their physical components.

Studies of the mass profile of galaxy clusters can provide us with information related to evolution of structure, formation and feedback processes, and dark matter properties. The methods used to estimate the mass of galaxy clusters include X-ray (e.g., Vikhlinin et al. 2009; Ettori et al. 2019; Mantz et al. 2018), Sunyaev-Zel’dovich effect (SZ, Sunyaev & Zeldovich 1972, 1980; e.g., Reichardt et al. 2013; Sifón et al. 2013; Planck Collaboration et al. 2016), richness (e.g., Yee & Ellingson 2003; Koester et al. 2007; Rykoff et al. 2016), dynamics (e.g., Gifford & Miller 2013; Foëx et al. 2017), and gravitational lensing (e.g., Kneib & Natarajan 2011; Hoekstra et al. 2013; Sharon et al. 2015, 2020). Gravitational lensing (weak and strong) is the best technique to probe the total projected (baryonic and dark matter) mass density, independent of assumptions on the dynamical state of the cluster or baryonic physics. At the cores of galaxy clusters, strong gravitational lensing measures mass at the smallest radial scales and most extreme over-densities; when coupled with a mass proxy at a large radii, strong lensing can constrain global properties of the mass profile, including the concentration parameter.

Advances in strong lens (SL) modeling, including better understanding of SL systematics (Johnson & Sharon, 2016), its effects on constraining cosmological parameters (Acebron et al., 2017), magnification (Priewe et al., 2017; Raney et al., 2020b), consequences due to the number of constraints (Mahler et al., 2018), and the use of spectroscopic and photometric redshifts (Cerny et al., 2018), make strong lens modeling a robust technique to study galaxy clusters and the background universe they magnify. A detailed lens model requires extensive follow-up: (1) imaging to identify multiple images and (2) spectroscopy of the lensed images to obtain spectroscopic

redshifts of the sources (e.g., Johnson et al. 2014; Zitrin et al. 2014; Diego et al. 2016; Kawamata et al. 2016; Lotz et al. 2017; Strait et al. 2018; Lagattuta et al. 2019; Sebesta et al. 2019; Sharon et al. 2020). The location of the multiple images and the spectroscopic redshifts are used as constraints when computing the SL models. Typically, a detailed SL model for a rich galaxy cluster can take weeks to finalize, and it is not an automated process. Given the large numbers of strong lensing galaxy clusters expected from coming surveys, an accurate, fast, and well-characterized method of extracting basic strong lensing information is needed.

In this chapter, we evaluate the use of the geometric Einstein radius to estimate the mass at the core of SL galaxy clusters. We determine the uncertainties in the mass estimate, identify its limitations, investigate dependencies on the shape of the projected mass distribution, and find a possible empirical correction to de-bias the mass estimate. We base our analyses on the state-of-the-art, dark matter only, ‘Outer Rim’ simulation (Heitmann et al., 2019). The Outer Rim contains a large sample of massive dark matter halos, and has sufficient mass resolution to enable precise and accurate ray-tracing of the strong lensing due to these halos.

This chapter is organized as follows. In Section 2.2, we describe the lensing formalism, including a detailed description of the assumptions of the Einstein radius method to compute the enclosed mass. In Section 2.3, we summarize the properties of the ‘Outer Rim’ simulation, the halo sample used in our analysis, and the cosmological framework. In Section 2.4, we detail how we measure the Einstein radius from the ray-traced images and compute both the inferred mass enclosed by the Einstein radius and the true mass from the simulation. In Section 2.5, we present our analysis of the mass estimate and the systematics that contribute to the scatter and bias. In Section 2.6, we investigate the effect of not having the redshift information of the background sources (z_S) on the mass estimate. In Section 2.7, we propose an empirical correction to de-bias the mass estimate. Lastly, we present our conclusions and

offer a prescription for applying our findings to real data in Section 2.8.

For consistency with the simulations, we adopt a *WMAP-7* (Komatsu et al., 2011) Flat Λ CDM cosmology in our analysis $\Omega_\Lambda = 0.735$, $\Omega_M = 0.265$, and $h = 0.71$. The large scale masses are reported in terms of M_{Nc} , where M_{Nc} is defined as the mass enclosed within a radius at which the average density is N times the critical density of the universe at the cluster redshift.

2.2 Background: Strong Gravitational Lensing

Gravitational lensing (see Schneider 2006; Kneib & Natarajan 2011 for reviews about gravitational lensing) occurs when photons deviate from their original direction as they travel to the observer through a locally curved space-time near a massive object, as described by Einstein’s General Theory of Relativity. The lensing equation (2.1) traces the image-plane position of images of lensed sources to the source plane location of the background sources. When multiple solutions to the lensing equation exist, multiply-imaged systems are possible, defining the strong lensing regime. The lensing equation is written as:

$$\begin{aligned} \boldsymbol{\beta} &= \boldsymbol{\theta} - \boldsymbol{\alpha}(\boldsymbol{\theta}), \\ \boldsymbol{\alpha}(\boldsymbol{\theta}) &= \frac{D_{\text{LS}}(z_{\text{L}}, z_{\text{S}})}{D_{\text{S}}(z_{\text{S}})} \hat{\boldsymbol{\alpha}}(\boldsymbol{\theta}), \end{aligned} \tag{2.1}$$

where $\boldsymbol{\beta}$ is the position of the lensed source in the source plane, $\boldsymbol{\theta}$ is the image plane location of the images, $\boldsymbol{\alpha}(\boldsymbol{\theta})$ is the deflection angle, $D_{\text{LS}}(z_{\text{L}}, z_{\text{S}})$ is the angular diameter distance between the lens and the source, $D_{\text{S}}(z_{\text{S}})$ is the angular diameter distance between the observer and the source, z_{L} is the redshift of the lens (in our case the redshift of the galaxy cluster), and z_{S} is the redshift of the background source. The deflection angle depends on the gravitational potential of the cluster projected

along the line-of-sight.

The magnification, μ , of a gravitational lens can be expressed as the determinant of the magnification matrix:

$$\mu^{-1} = \det(\mathcal{A}^{-1}) = (1 - \kappa)^2 - \gamma^2, \quad (2.2)$$

where κ is the convergence and γ is the shear. The locations of theoretical infinite magnification in the image plane are called the tangential and radial critical curves, naming the primary direction along which images (arcs) are magnified.

For a circularly symmetric lens with the origin centered at the point of symmetry, the angles $\boldsymbol{\alpha}(\boldsymbol{\theta})$ and $\boldsymbol{\beta}$ are collinear with $\boldsymbol{\theta}$. Then the lens equation (eq. 2.1) becomes one-dimensional, $\beta = \theta - \alpha(\theta)$, and the deflection angle is:

$$\begin{aligned} \alpha(\theta) &= \frac{2}{\theta} \int_0^\theta \theta d\theta \kappa(\theta) \\ &= \frac{4GM(< \theta)}{c^2 \theta} \frac{D_{\text{LS}}(z_{\text{L}}, z_{\text{S}})}{D_{\text{L}}(z_{\text{L}}) D_{\text{S}}(z_{\text{S}})} \\ &= \langle \kappa(\theta) \rangle \theta, \end{aligned} \quad (2.3)$$

where $D_{\text{L}}(z_{\text{L}})$ is the angular diameter distance from the observer to the lens, c is the speed of light, and G is the gravitational constant. We can then substitute the deflection angle into the one-dimensional lens equation:

$$\beta = \theta(1 - \langle \kappa(\theta) \rangle), \quad (2.4)$$

where the critical region, defined as $\langle \kappa(\theta) \rangle = 1$, defines the tangential critical curve. In this circularly symmetric case, $\alpha(\theta) = \theta$, Equation 2.3 becomes

$$\theta^2 = \frac{4GM(< \theta)}{c^2} \frac{D_{LS}(z_L, z_S)}{D_L(z_L)D_S(z_S)}. \quad (2.5)$$

Last, substituting the critical surface density, $\Sigma_{cr}(z_L, z_S)$,

$$\Sigma_{cr}(z_L, z_S) = \frac{c^2}{4\pi G} \frac{D_S(z_S)}{D_L(z_L)D_{LS}(z_L, z_S)}, \quad (2.6)$$

we obtain the expression of the Einstein radius (Narayan & Bartelmann, 1996; Schneider, 2006; Kochanek, 2006; Bartelmann, 2010; Kneib & Natarajan, 2011):

$$\theta_E^2 = \frac{M(< \theta_E)}{\pi \Sigma_{cr}(z_L, z_S) D_L^2(z_L)}. \quad (2.7)$$

Re-arranging Equation 2.7, the total projected mass enclosed by the Einstein radius of a circularly symmetric lens can be computed as:

$$M(< \theta_E) = \Sigma_{cr}(z_L, z_S) \pi [D_L(z_L)\theta_E]^2. \quad (2.8)$$

An Einstein ring results from the exact alignment of the source, lens, and observer, as well as the circular symmetry of the lens. This causes an observed ring-like feature to appear around the lens. However, the three-dimensional mass density distribution of both simulated halos and observed clusters is better described by a triaxial ellipsoid (Wang & White, 2009; Despali et al., 2014; Bonamigo et al., 2015). Complete Einstein rings are not often observed around clusters due to the more complex mass distribution; nevertheless, authors often use the clustercentric projected distance to a giant arc as a proxy for the Einstein radius. The mass calculated using Equation 2.8 is useful for the study of galaxy clusters, since it provides a quick estimate of the mass within the Einstein radius. It was estimated to produce a scatter of $\sim 30\%$ with respect to the true mass enclosed (Bartelmann & Steinmetz, 1996; Schneider, 2006).

This uncertainty was adopted in the literature extensively when estimating the total projected mass enclosed by the Einstein radius (e.g., Allam et al. 2007; Belokurov et al. 2007; Werner et al. 2007; Diehl et al. 2009; Bettinelli et al. 2016; Dahle et al. 2016; Nord et al. 2016), despite limited quantification of its accuracy and precision.

2.3 Data: Simulated Lenses

2.3.1 The Outer Rim Simulation

To assess the accuracy and precision of the enclosed mass inferred from the Einstein radius, we use the state-of-the-art, large-volume, high-mass-resolution, gravity-only, N-body simulation ‘Outer Rim’ (Heitmann et al., 2019) with the HACC framework (Habib et al., 2016) carried out at the Blue Gene/Q (BG/Q) system Mira at Argonne National Laboratory. The cosmology used assumes a Flat- Λ CDM model, with parameters adopted from WMAP-7 (Komatsu et al., 2011), $h = 0.71$ and $\Omega_M = 0.264789$. The size of the simulation box on the side is $L = 3000 \text{ Mpc } h^{-1}$ and it evolves $10,240^3 \approx 1.1$ trillion particles with a mass resolution of $m_p = 1.85 \times 10^9 \text{ M}_\odot h^{-1}$ and a force resolution in co-moving units of $3 \text{ kpc } h^{-1}$.

The large volume of the simulation run allows for many massive halos to be included in the same simulation box, covering the redshift range of interest ($z \sim 0.1 - 0.7$), and the high mass resolution provides excellent projected mass profile distributions of the individual clusters. The large number of massive halos allows for a rigorous statistical analysis, representative of the universe and is sufficient to enable strong lensing computations without the need of re-simulation. In previous simulation efforts when small numbers of massive halos were present in the simulation box, re-simulation of those halos was done to increase the sample to better the statistics (Meneghetti et al., 2008, 2010). The Outer Rim, amongst other applications, was used to study dark matter halo profiles and the concentration-Mass relation (Child

et al., 2018) and to construct realistic strong lensing simulated images (Li et al., 2016).

The majority of the mass in galaxy clusters is in the form of dark matter. Baryons contribute mostly at the core of the galaxy cluster, where the brightest cluster galaxy (BCG) and the hot intra-cluster medium (ICM) reside. Studies have found non-negligible baryonic effects from subhaloes of satellite galaxies as well as the BCG at small θ_E scale (Meneghetti et al., 2003; Wambsganss et al., 2004; Oguri, 2006; Hilbert et al., 2007, 2008; Wambsganss et al., 2008; Oguri & Blandford, 2009). Fully accounting for these baryonic effects awaits for simulations that include baryonic physics in large cosmological boxes.

2.3.2 Simulated SPT-like Strong Lensing Sample

Galaxy cluster halos were identified in the simulation using a friends-of-friends algorithm with a unit-less linking length of $b = 0.168$ (Heitmann et al., 2019). The surface mass density was then computed using a density estimator. Extensive testing by Rangel et al. (2016) showed that the mass resolution is robust enough to compute strong lensing for halos with masses $M_{500} > 2 \times 10^{14} M_{\odot} h^{-1}$. Following an SPT-like selection function, the halos with a mass larger than $M_{500} > 2.1 \times 10^{14} M_{\odot} h^{-1}$ were selected to form the cluster sample.

The simulated halo masses (M_{500} , M_{200}) and concentrations (c_{200}) that we use in this work were calculated by Li et al. (2019) and Child et al. (2018). We adopt the dynamical state values and definitions from Child et al. (2018); a dynamically-relaxed cluster is identified where the distance between the dark matter halo center and the spherical over-density center is smaller than $0.7R_{200}$. When referring to the dynamical state of the galaxy cluster, the center was defined as the center of the potential from all the particles in the simulation corresponding to the particular dark matter halo.

To select SL clusters out of the mass-limited sample, we first compute $\kappa(\theta)$ for a

background source redshift of $z = 2$ for each line of sight. We then identify strong lensing clusters as all lines of sight for which the Einstein radius of the critical region that satisfies $\langle \kappa(\theta) \rangle = 1$ is larger than a few arcseconds. The resulting sample of SPT-like simulated strong lenses includes 74 galaxy cluster halos spanning the redshift range of $z_L \sim 0.16 - 0.67$.

In Figure 2.1, we summarize some of the halo properties of the mass-limited sample and the SL sample. The first three panels show the distributions of redshifts, masses, and concentrations. As can be seen in these panels, the distribution of strong lensing clusters peaks at higher total mass, higher concentration, and lower redshift than the mass-limited sample. Similar trends have been identified in both simulations (Oguri & Hamana, 2011; Giocoli et al., 2014) and observations (Gralla et al., 2011; Oguri et al., 2012).

In the fourth panel, we plot the mass-redshift distribution of the simulated clusters and that of the observed clusters from the SPT-SZ 2500 deg² survey (Bleem et al., 2015).

As can be seen in the right panels of Figure 2.1, the Bleem et al. (2015) strong lensing sample extends to higher cluster redshifts than our simulated sample. The effective redshift cut in the simulated sample is imposed by the selection of cluster-scale lenses by their lensing efficiency for a $z_S = 2$ source plane. On the other hand, the observational SL clusters have been identified using imaging data from various ground- and space-based observatories. We note that while our simulated sample is statistically inconsistent with the full Bleem et al. (2015) strong lensing sample, considering only lenses at $z_L < 0.7$ a Kolmogorov-Smirnov (KS) test does not reject the hypothesis that the simulated and observed SL samples are drawn from the same underlying distribution (KS-statistic 0.264, p-value 0.159). Regardless, the results presented in this work are not dependent on these samples being drawn from the same underlying distribution.

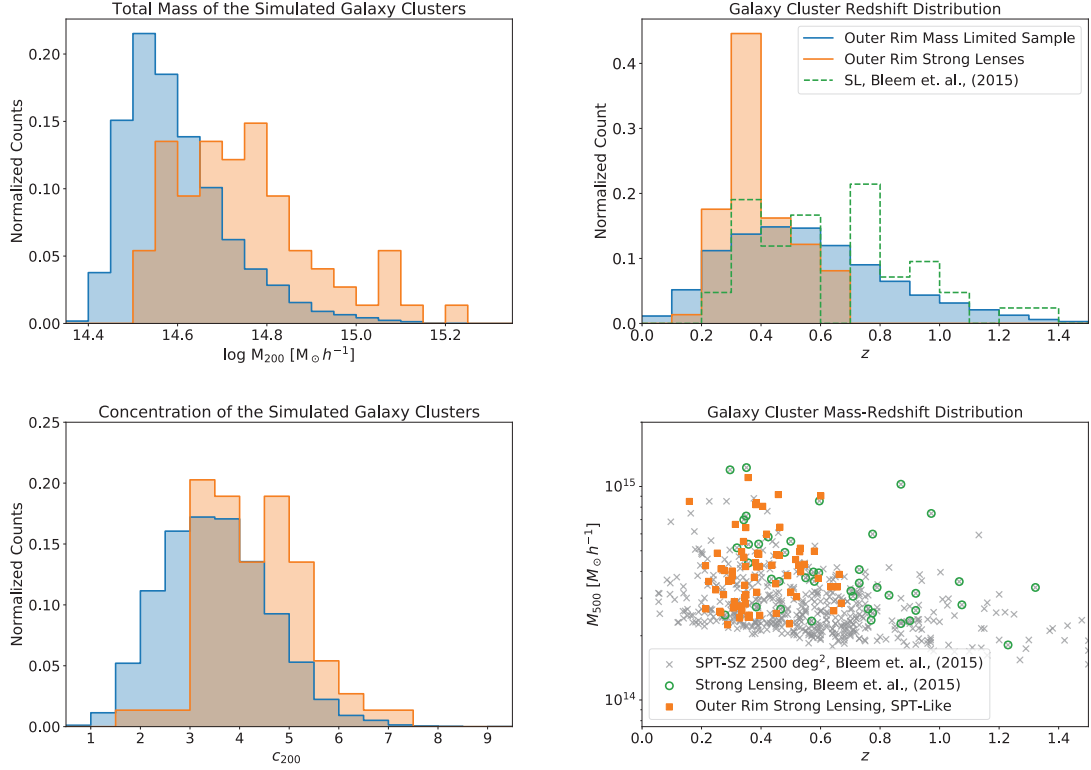


Figure 2.1: **Properties of the Simulated Sample.** *Top-Left*: the total mass (M_{200}), *Top-Right*: redshift (z), and *Bottom-Left*: concentration (c_{200}) distributions of the simulated halos. The mass-limited sample is shown in blue, and strong lenses are in orange. The masses and concentrations were computed by Li et al. (2019) and Child et al. (2018). The counts are normalized by the total number of halos in each sample. *Bottom-Right*: the mass-redshift distribution ($M_{500} - z$). Orange squares indicate the Outer Rim strong lensing cluster halos; grey crosses are observed clusters from the 2500-Square-Degree SPT-SZ Survey (Bleem et al. 2015). The green circles, and the green dotted line in the *Right* panels, are strong lensing galaxy clusters from Bleem et al. (2015), which were identified from very heterogeneous imaging data and are likely not representative of all the strong lenses in the SPT sample.

The redshift range of the simulated SL sample, $z_L \sim 0.16 - 0.67$, is similar to that of the Sloan Giant Arc Survey (SGAS; M. Gladders et al., in preparation; Bayliss et al. 2011a; Sharon et al. 2020), which identified lensing clusters from giant arcs in shallow optical SDSS imaging. Future studies will extend to higher redshifts to complement surveys with samples of galaxy clusters out to $z = 1.75$ such as the SPT-SZ 2500-Square-Degree survey (Bleem et al., 2015).

2.3.3 Ray Tracing and Density Maps

The ray-traced images and the projected mass distributions of the galaxy clusters have a size of 2048×2048 pixels and a resolution of $dx = 0''.09$ per pixel. For more details of the exact procedure to obtain the lensing maps and the ray-traced images, refer to Li et al. (2016). Using the surface density distributions of these clusters, we compute all of the lensing maps, including the deflection angle (α) using Fourier methods, the convergence (κ), the shear (γ), the magnification (μ), and the tangential and radial critical curves.

We draw redshifts for 1024 background sources from a distribution ranging from $z \sim 1.2$ to $z \sim 2.7$, following the observed distribution of Bayliss et al. (2011a) (shown in Figure 2.2). The image plane of each cluster was generated multiple times, resulting in 5 – 24 ray-tracing realizations for each cluster halo. The background sources were randomly placed in areas of high magnification to produce highly magnified (total magnification > 5) arcs easily detected from ground based observations (e.g., Bayliss et al. 2011a; Sharon et al. 2020).

We note that the ray-tracing did not take into account structures along the line-of-sight. Structure along the line-of-sight can boost the total number of lenses observed by increasing the SL cross-section of individual clusters, having a larger effect on the less massive primary lensing halos (Puchwein & Hilbert, 2009; Bayliss et al., 2014; Li et al., 2019). The magnification of the arcs is also affected by the structure

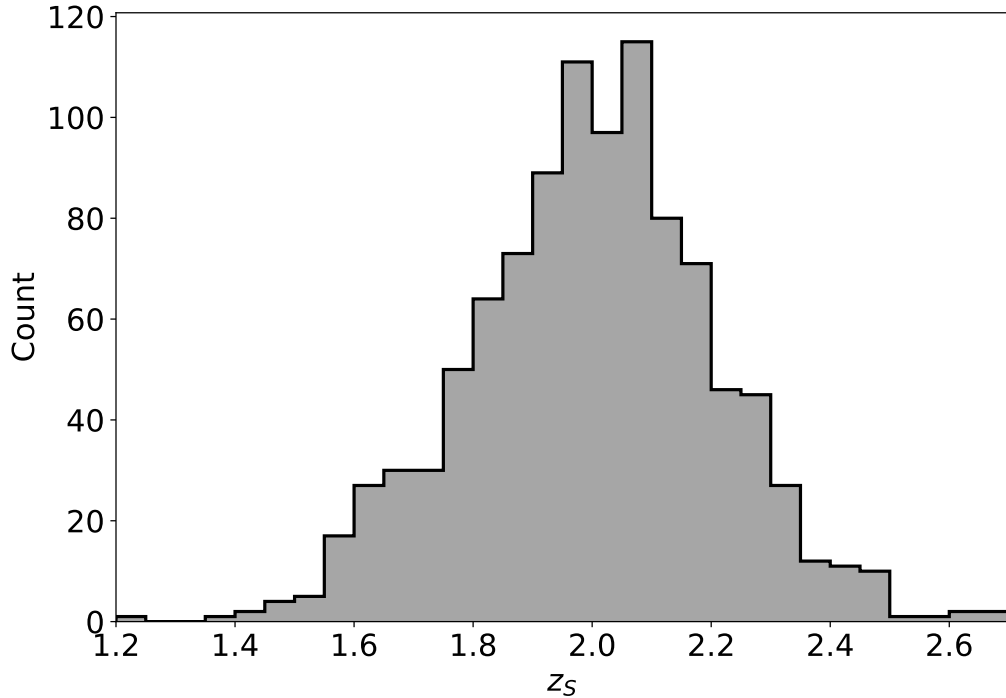


Figure 2.2: **Simulated Background Source Redshifts**, z_s . The distribution is centered at $z = 2$, consistent with the observed redshift distribution of highly magnified giant arcs (Bayliss et al., 2011a).

along the line-of-sight requiring particular care when studying the background source properties (Bayliss et al., 2014; D’Aloisio et al., 2014; Chirivì et al., 2018) and using strong lensing clusters for cosmological studies (Bayliss et al., 2014). A statistical analysis of how the measurement of the core mass is affected by line of sight structure is left for future work.

We use the ray-traced images to compute the mass enclosed by the Einstein radius, and the surface density maps as “true” mass to characterize the efficacy of this mass estimate.

2.4 Methodology

Our methodology attempts to mirror the procedures that would be used in SL analyses of real data. Even in large surveys such as SPT, this includes a significant component of manual inspection and identification of SL evidence. Manual inspection is also required for targeted spectroscopic follow-up.

2.4.1 Einstein Radius Measurement

The first step is to measure an Einstein radius from the positions of the lensed images (arcs). To locate the arcs, we examine each of the ray-traced images by eye to identify sets of multiple images using their morphology and expected lensing geometry, mimicking the process of finding multiply-imaged lensed systems in observational data. If multi-band information is available lens modelers also take advantage of color information of the lensed images, but in this particular case, color information is not available from the ray-traced images.

Using this process, we created a catalog with flags identifying the tangential and radial arcs, corresponding to the tangential and radial critical curves, respectively (see Section 2.2). Identified lensed images whose classification (radial or tangential) is unclear were noted. The radial distribution of the identified arcs is shown in Figure 2.3. We find that the distribution of tangential and radial arcs match our expectations from lensing geometry, the radial arcs are found near the center while the tangential arcs are typically found farther out. The distribution we find is qualitatively consistent with Florian et al. (2016).

Since the Einstein radius is a representation of the tangential critical curve (Bartelmann, 2010; Kneib & Natarajan, 2011), we only include the tangential arcs when finding the Einstein radius. We fit a circle to the tangential arcs as explained below; the radii of the resulting circles shall be our Einstein radii, θ_E .

We explore three alternatives for the centering of the circle; in the first method

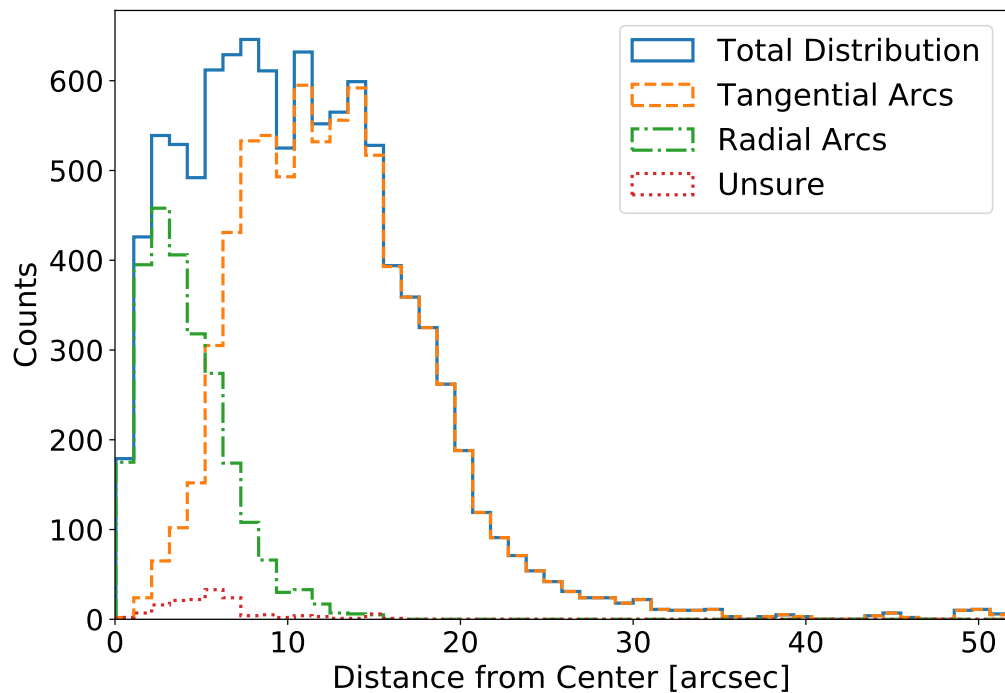


Figure 2.3: **Radial Distribution of the Identified Arcs.** Radial distances are measured with respect to the pixel with the highest projected mass density of the simulated galaxy cluster. We display the distribution of the tangential arcs with an orange dashed line, radial arcs with a green dashed-dotted line, and those images for which we are unsure with a red dotted line. The distribution of the radial and tangential arcs matches our expectation from lensing geometry, having radial arcs closer to the center while tangential arcs are found farther out.

(hereafter *fixed center*) we fix the center of the circle to the point of highest surface density of the projected mass from the simulated halo. Since in observations we do not a priori know where the center of the dark matter halo is located, in the second method we set the center as a free parameter (hereafter *free center*) with a conservative uniform prior of $\pm 13''.5$ from the projected 3-D potential center of the halo. Because the free center requires two more free parameters, the free center minimization was only performed on the cases where 3 or more multiple images were identified as tangential arcs. In the observational realm, the BCG can be, and often is, used as a proxy for the cluster center. The third method (hereafter *fixed center with BCG offset*) mimics fixing the center to an observed BCG. Since the Outer Rim simulation does not include baryonic information, we cannot determine the BCG position directly from it. We therefore turn to studies that investigate the BCG offset from the dark matter center. Harvey et al. (2019) explores the radial offset between the BCG and the dark matter (DM) center as an observable test of self-interacting dark matter (SIDM) models with different dark matter cross-sections. They find that the BCG-DM offset follows a log-normal distribution, with the offsets in the cold dark matter (CDM) case being the smallest ($\mu = 3.8 \pm 0.7$ kpc) and increases with increasing dark matter cross section. We use the distribution of the SIDM model with a DM cross-section of $0.3 \text{ cm}^2/\text{g}$. This value represent a reasonable/conservative upper boundary according to recent analysis (Pardo et al., 2019; Sagunski et al., 2021). Following this rationale, we fix the center of the circle to a point offset from the center of the dark matter halo, with a radial offset drawn from a log-normal distribution with $\mu = 6.1 \pm 0.7$ kpc, in a random direction.

For the fitting procedure, we use an ensemble sampler Markov chain Monte Carlo (MCMC) implemented for python using the libraries `emcee`¹ (Foreman-Mackey et al., 2013) and `lmfit`² (Newville et al., 2014) method to fit a circle to the tangential arcs.

¹Python `emcee` <https://emcee.readthedocs.io/en/stable/>

²Python `lmfit` <https://lmfit.github.io/lmfit-py/index.html>

The fitting method minimizes the distance between the 2-D position of the arcs (visually identified morphological features that can be matched between the multiple images) and the nearest point to it on the circle. We use a uniform prior in the radius fitting parameter of $2''.25 < \theta_E < 45''.0$ for all three of our fitting methods. We note that the cases where only a single arc is identified, the distance between the fixed center and the arc is used to determine the radius of the circle and no scatter is measured.

The distribution of the measured θ_E is shown in Figure 2.4 and the distribution of the standard deviation, $\sigma(\theta_E)$, computed from the covariance matrix of the fit is shown in Figure 2.5. Since the free center fitting procedure is significantly more flexible, the standard deviation on the fitted θ_E for the free center is about 20 times higher compared to that of the fixed center and fix center with BCG offset fit.

2.4.2 Inferred Mass

Taking the Einstein radius from Section 2.4.1 and the corresponding lens and source redshifts (Section 2.3.2), we compute the enclosed projected mass, $M(< \theta_E)$, via Equation 2.8. For our comparison, we use the projected mass distribution from the simulation to measure the true mass enclosed within the same aperture. We refer to this as the “true” mass, $M_{sim}(< \theta_E)$. An example of this procedure is shown in Figure 2.6.

2.4.3 Statistical approach to Correctly Represent the Universe

Our simulated sample consists of a total of 1024 ray tracing realizations through 74 strong lensing galaxy clusters, resulting with 5-24 ray-tracing realizations for each cluster. Each ray-traced simulated realization includes one of the 74 cluster halos and a single background source at a unique redshift. In addition, in some of the realizations multiple distinct structures (clumps) were identified and used to measure

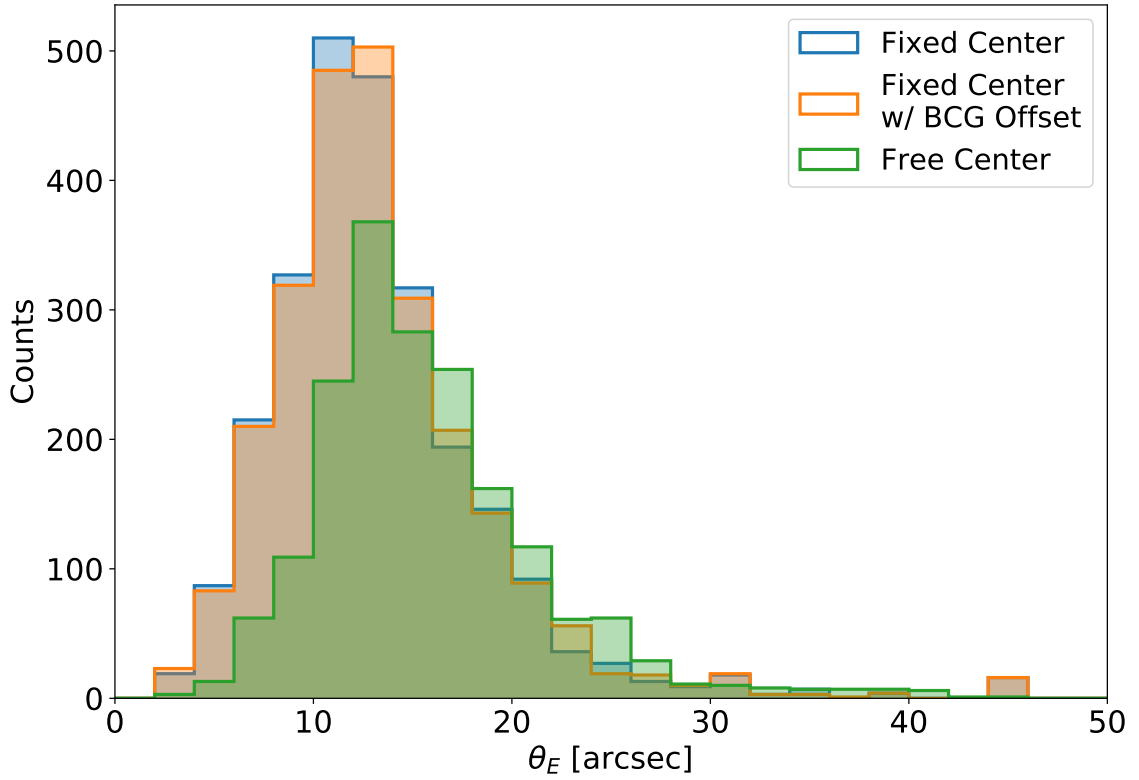


Figure 2.4: **Distribution of the Einstein Radius Fitted to the Simulations.** The fits to the identified tangential arcs utilizing the fixed center (blue), fixed center with BCG offset (orange) and free center (green).

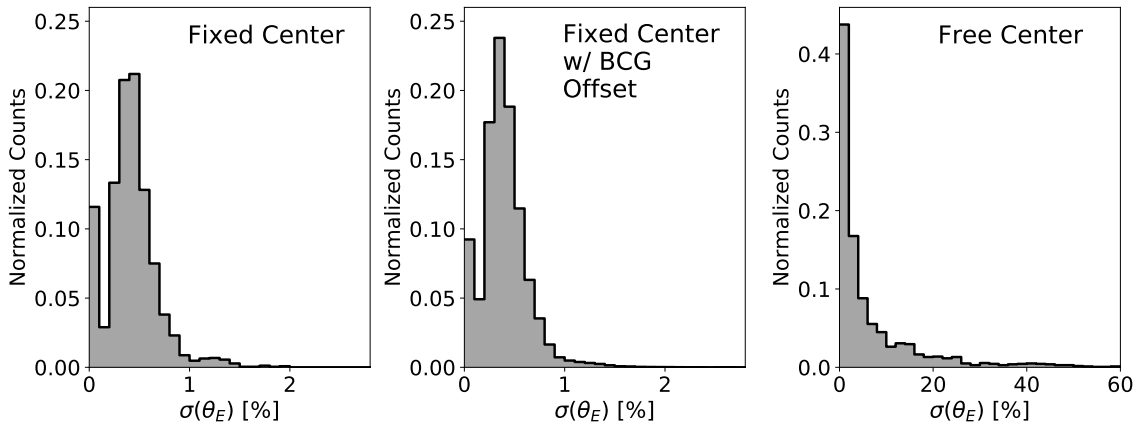


Figure 2.5: **Distribution of the Standard Deviation of the Measured Einstein Radii, $\sigma(\theta_E)$.** $\sigma(\theta_E)$ is measured in units of percentage utilizing the fixed center (*left*), fixed center with BCG offset (*middle*), and free center (*right*). We find that the standard deviation of the free center method is about 20 times higher than that of the fixed center and fixed center with BCG offset methods.

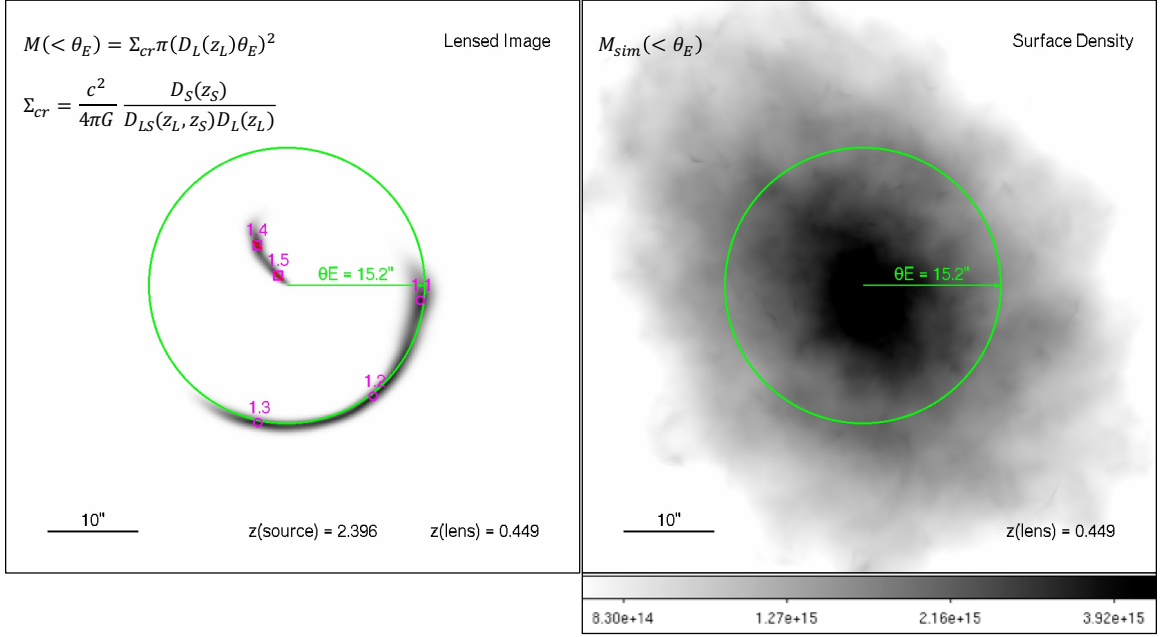


Figure 2.6: **Example of the Simulated Images to Illustrate our Methodology.** *Left:* ray-traced image; the identified lensed images are indicated with magenta symbols, with circles on tangential arcs and squares with a slash through on radial arcs. We fixed the center to the highest surface density point from the projected mass distribution and fit a circle to the tangential arcs of radius of $\theta_E = 15''.2$, shown in green. The mass inferred from the Einstein radius is $M(< \theta_E) = 3.38 \times 10^{13} M_\odot h^{-1}$. *Right:* projected mass density distribution of the simulated galaxy cluster where the green circle is the same aperture from the lensed image. The color-bar is in units of $M_\odot \text{Mpc}^{-2} h$. The “true” projected mass enclosed is $M_{sim}(< \theta_E) = 3.00 \times 10^{13} M_\odot h^{-1}$. We perform our analysis utilizing these two masses, the inferred ($M(< \theta_E)$) and the “true” ($M_{sim}(< \theta_E)$).

more than one Einstein Radius for that particular realization. For this reason the ray-trace realizations and Einstein Radius for a specific galaxy cluster are not independent from each other.

To establish a robust analysis that represents the universe, includes the statistical uncertainty of the fitted Einstein radius, and allows for the application to observational data, we weight each galaxy cluster to equal one. The ray-traced realizations are then evenly weighted by a factor of one over the total number of realizations for the specific cluster, and similarly the Einstein radii were weighted per ray-traced image. For each galaxy cluster, we select, at random, one ray-traced image from that cluster and one Einstein radius measurement for that realization. We then sample the selected Einstein radius using a normal distribution with the mean as the best fit Einstein radius and standard deviation equal to the uncertainty of the fitted Einstein radius. We repeat this process 1,000 times per cluster and use this sample with 74,000 points for our statistical analysis.

2.5 Analysis of Results

In this section, we compare the mass inferred from the Einstein radius ($M(< \theta_E)$) to the true mass ($M_{sim}(< \theta_E)$), measured from the surface density maps within the same aperture (Figure 2.6); measure the scatter of this mass estimate; and explore any dependence on the galaxy cluster properties, as well as observational information available from the ray-traced images.

In Figure 2.7, we show a direct comparison between $M(< \theta_E)$ and $M_{sim}(< \theta_E)$ for the fixed center (left panel), fixed center with BCG offset (middle panel), and free center (right panel) cases. We find that $M(< \theta_E)$ overestimates $M_{sim}(< \theta_E)$ in all cases, especially at large masses.

We measure an overall scatter of 13.9% and bias of 8.8% for the fixed center, scatter of 14.8% and bias of 10.2% for the fixed center with BCG offset, and scatter

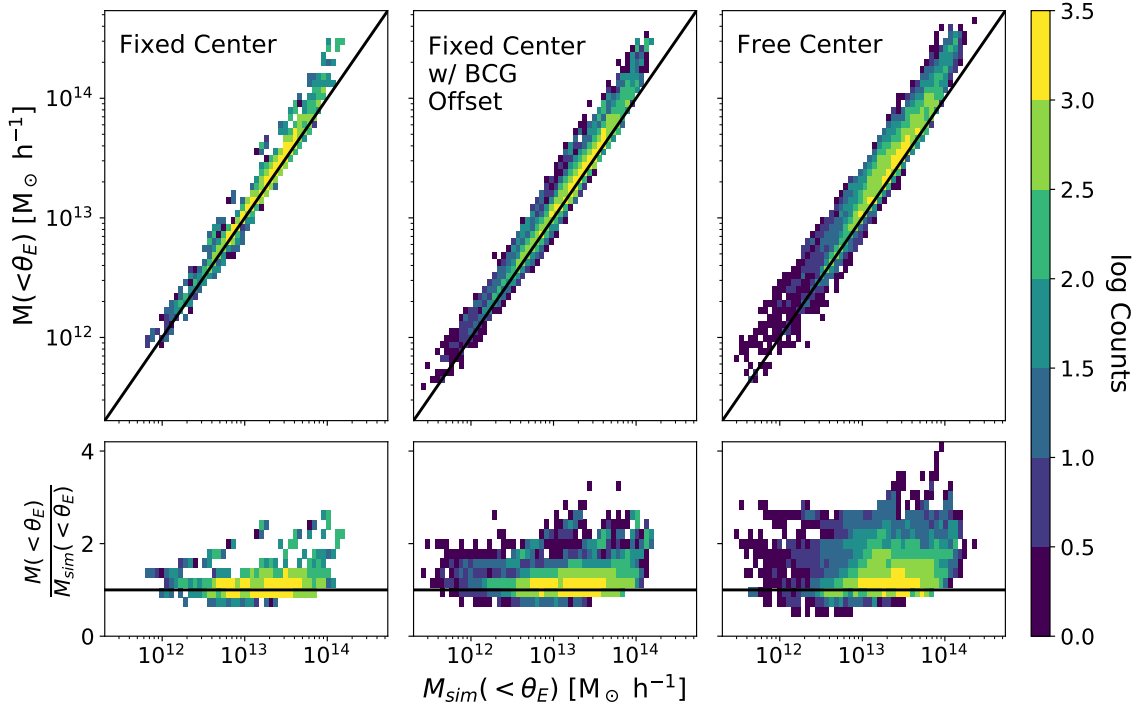


Figure 2.7: **Mass Comparison Between the $M(< \theta_E)$ and $M_{sim}(< \theta_E)$.** The mass comparison for the fixed center (*left*), fixed center with BCG offset (*middle*), and free center (*right*) are shown. $M_{sim}(< \theta_E)$ and $M(< \theta_E)$ are given in units of $M_\odot h^{-1}$ and the solid black line is where $M_{sim}(< \theta_E) = M(< \theta_E)$. The bottom plots show the ratio of the masses, $M(< \theta_E) / M_{sim}(< \theta_E)$. The total number of counts is the 74,000 sampled data points (Section 2.4.3) used in the analysis of the scatter and bias of the $M(< \theta_E)$ compared to $M_{sim}(< \theta_E)$. We find that $M(< \theta_E)$ overestimates $M_{sim}(< \theta_E)$ in all cases, especially at large masses, and the scatter is smallest for the fixed center method and highest for the free center method.

of 27.4% and bias of 20.2% for the free center. The scatter is defined as half the difference between the 84th percentile and the 16th percentile of the distribution and the bias is determined using the median of the distribution. We note that previous estimates of the uncertainty associated with this measurements state $\sim 30\%$ (Bartelmann & Steinmetz, 1996; Schneider, 2006), however, it is unclear how the uncertainty is defined.

Comparing the results of the three methods, we find that the free center method is the least reliable in recovering the true mass. Its measured θ_E statistical uncertainty is 20 times higher than those of the fixed center (Figure 2.5), and the scatter and bias in $M(< \theta_E) / M_{sim}(< \theta_E)$ are significantly higher (Figure 2.7). In addition, the free center method is limited to cases where 3 or more tangential arcs are identified. For these reasons, we do not recommend that the free center method be utilized to measure the Einstein radius and the mass enclosed by the Einstein radius. The fixed center with BCG offset shows that the additional scatter due to the offset between the BCG and dark matter center is small, justifying the use of the observed BCG as the fixed center of the Einstein radius. For the rest of the chapter we are only going to consider the fixed center and the fixed center with BCG offset.

To explore the dependence of this mass estimate on lens properties, we consider the ratio of inferred to true mass, $M(< \theta_E)/M_{sim}(< \theta_E)$, and group the measurements into bins of equal number of points. We plot $M(< \theta_E)/M_{sim}(< \theta_E)$ with respect to the Einstein radius in Figure 2.8. This figure shows clearly that the $M(< \theta_E)$ mass estimate is not randomly scattered about the true mass, and that it overestimates the true mass at all radii. In Section 2.7, we describe an empirical correction to de-bias the measurement of the mass enclosed by the Einstein radius.

In the following sections, we explore possible causes, and identify observable indicators of the scatter and bias of $M(< \theta_E)$.

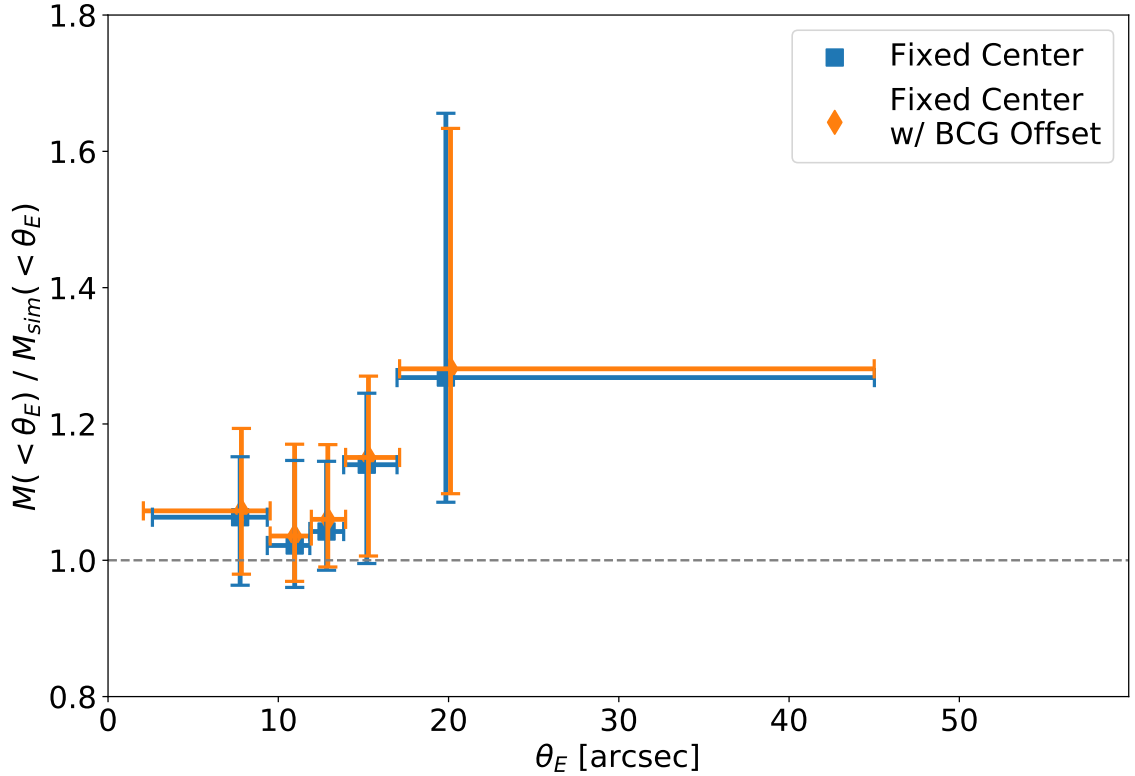


Figure 2.8: **Ratio of inferred to “true” mass, $M(< \theta_E)/M_{sim}(< \theta_E)$, with respect to θ_E .** The fixed center (blue square) and fixed center with BCG offset center (orange diamond), are shown. The symbol marks the median of the distribution of the mass ratio, the horizontal error bars indicate the bin size, and the vertical error bars represent the 16th and 84th percentile. We find a positive bias in all of the bins and that both fixed center and fixed center with BCG offset yield a similar θ_E .

2.5.1 Possible causes and indicators of the scatter in the $M(< \theta_E)$ mass estimate

We explore possible dependence of the scatter and bias on $M(< \theta_E)$ with respect to galaxy cluster properties, background source, and lensing geometry. The galaxy cluster properties used in our analysis include: galaxy cluster redshift (z_L), total mass (M_{200}), concentration (c_{200}), dynamical state, and the shape of the tangential critical curve. The total mass, concentration, and dynamical state information for the simulated cluster sample are adopted from Child et al. (2018). From the background source, we have the redshift information (z_S) and from the lensing geometry, we measure how much of the Einstein circle is covered by the arcs (ϕ), as we explain below.

Lens and Source Redshifts The redshifts of the lens and the source determine the lensing geometry of the system through the angular diameter distances (Equation 2.1). Redshifts can be determined observationally, when spectroscopic or extensive photometric information is available. The redshift distribution of the simulated clusters (z_L) from the Outer Rim and background source redshift (z_S) are shown in Figure 2.1 and Figure 2.2, respectively.

Total Mass and Concentration M_{200} and c_{200} are adopted from Child et al. (2018). The distribution of the simulated galaxy cluster total mass and concentration are shown in the left panels of Figure 2.1. We note that M_{200} and c_{200} are not directly available from the imaging data at the core of the cluster where the strong lensing evidence is present. However, since our aim is to use the core mass to inform the mass-concentration relation, it is important to test whether this mass estimator introduces correlated bias.

Cluster Deviation from Spherical Symmetry Since galaxy clusters do not have a circular projected mass distribution, we expect differences between $M_{sim}(< \theta_E)$ and $M(< \theta_E)$ due to deviations from the assumed circular symmetry. To assess the deviation of the lens from spherical symmetry, we use the tangential critical curves derived from the simulation as a proxy for the shape of the projected mass distribution at the core of the cluster. We sample the tangential critical curves with a few hundred to thousands of points by using the python library `matplotlib.contour`³ setting a contour level at 0 for the inverse magnification due to the tangential critical curve. Using the technique described in Fitzgibbon et al. (1996), we fit an ellipse to each tangential critical curve corresponding to every background source redshift. We then use the resultant ellipticity, defined as $\epsilon = (a^2 - b^2)/(a^2 + b^2)$, where a is the semi-major axis and b is the semi-minor axis. In Figure 2.9, we show three examples of the ellipse fits to the tangential critical curve, over-plotted on the projected mass density distribution. We plot the distribution of ellipticity of the tangential critical curve in Figure 2.10. This characterization of the projected shape of the galaxy cluster is not accessible directly from the observational data prior to a detailed SL model which this method aims to avoid.

Galaxy Cluster Relaxation State We tested whether the relaxation state of the galaxy clusters (see Section 2.3.2 for the simulated sample dynamical state description) can be used as a proxy for the deviation from spherical symmetry. Observationally, this can be determined from X-ray imaging (e.g., Mantz et al. 2015). In Figure 2.10, we plot ϵ separated by the relaxation state of the galaxy cluster. We perform a two sample Kolmogorov-Smirnov test to quantify the difference between the two samples with a confidence level of 99.7%. The KS-statistic is 0.0896 with a p-value of 0.0402. With this test, we cannot reject the null hypothesis that the two samples are drawn from the same continuous distribution. From our KS test and

³Python `matplotlib.contour` https://matplotlib.org/3.1.0/api/contour_api.html

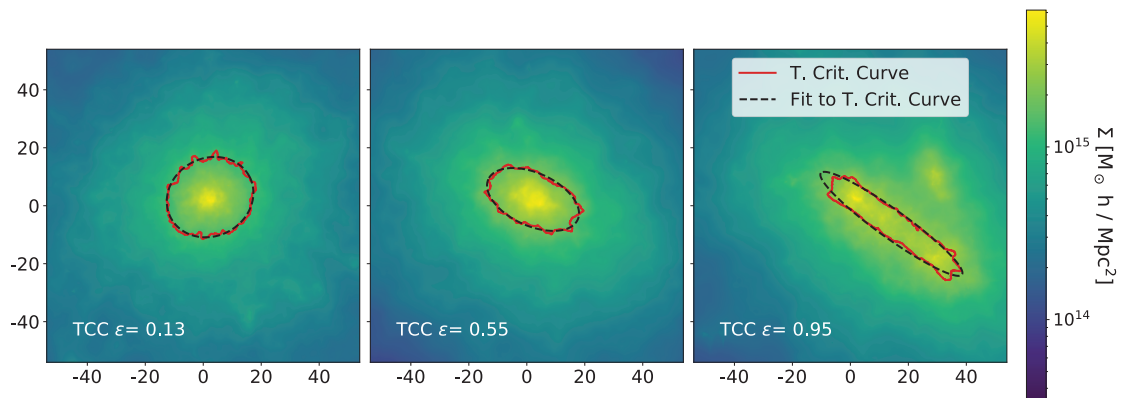


Figure 2.9: **Examples of the ellipticity (ϵ) of the tangential critical curve (TCC) as a proxy for the cluster deviation from spherical symmetry.** We show as example three simulated clusters with different projected ellipticities. The red line is the tangential critical curve for a particular background source redshift z_S . The dashed black line indicates the ellipse fitted to the tangential critical line, from which we compute the ellipticity, ϵ . The lines are plotted over the projected mass distribution of the corresponding simulated galaxy clusters. The x- and y- axes are in units of arcseconds. The color bar indicates the surface density value in units of $M_\odot h / \text{Mpc}^2$.

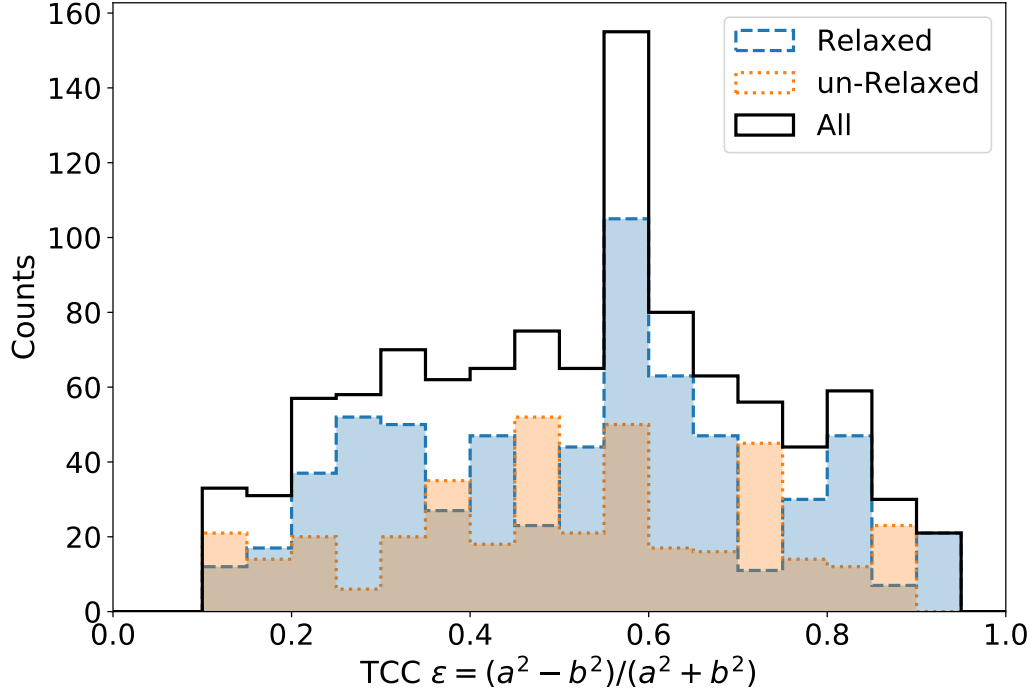


Figure 2.10: **Dynamical State and Deviation from Circular Symmetry.** Distribution of the tangential critical curve (TCC) ellipticity, ϵ . The overall distribution is indicated by the black line and the contributions from the dynamical (relaxed or un-relaxed) state of the simulated galaxy clusters (from Child et al. (2018)) is indicated by the shaded bars. We observe that the dynamical state information is not an indicator of deviations from spherical symmetry of the simulated galaxy cluster.

Figure 2.10, we find no correlation between the dynamical state and ϵ .

The fraction of the Einstein circle covered by arcs of an individual lensed

source ϕ represents the fraction of the Einstein circle that is covered by arcs of a given source. This property is easily accessible from the imaging data. In Figure 2.11, we show three examples of lensed images plotted with their corresponding Einstein circles fitted using the identified tangential arcs for both the fixed center (blue) and an example of one of the realizations of a fixed center with BCG offset (orange). We plot in Figure 2.12 the distribution of ϕ for both the fixed center (blue) and fixed center with BCG offset (orange).

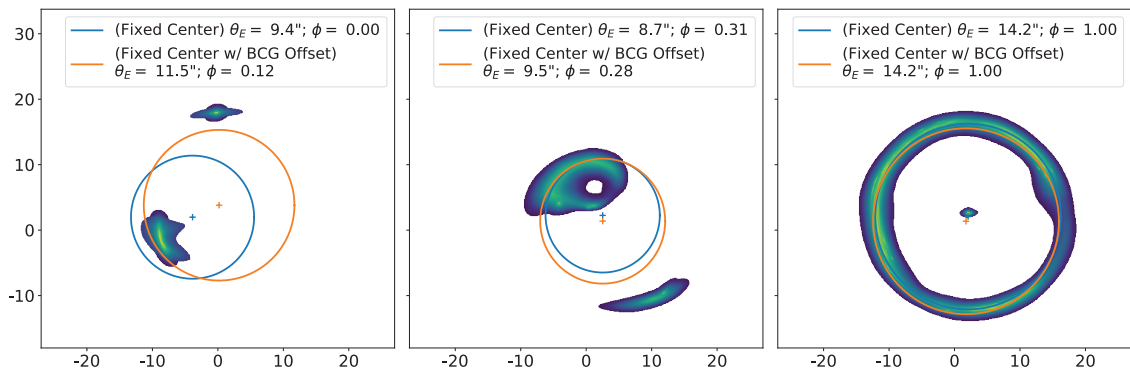


Figure 2.11: **The fraction of circle covered by the arcs (ϕ) for three examples cases.** The Einstein radius fitted to the identified tangential arcs for both the fixed center (blue) and one example of the fixed center with BCG offset (orange) are plotted; the corresponding centers of the circles are indicated by the crosses. The BCG offset was determined by drawing a radial offset between the BCG and dark matter halo from a log-normal distribution with $\mu = 6.1 \pm 0.7$ kpc (Harvey et al., 2019) and an angle from a uniform distribution from 0 to 359 degrees. The fraction of the circle covered by the arcs for the fixed center and fixed center with BCG offset is shown in the legend. The x- and y-axis are in units of arcseconds.

2.5.2 Results of the Analysis of Systematics

We split the measurements of $M(< \theta_E)$ into equal bins of M_{200} , c_{200} , ϵ , z_L , z_S , and ϕ and check whether the bias and scatter in the $M(< \theta_E)$ mass estimate depend on these properties. We find that the scatter and bias of $M(< \theta_E)/M_{sim}(< \theta_E)$ do not depend on four of these properties: the total mass, concentration, cluster redshift, and source redshift, showing flat and uniform progression in panels A–D of Figure 2.13. We also note, we find no difference in the bias and scatter of $M(< \theta_E)/M_{sim}(< \theta_E)$ between the relaxed and un-relaxed clusters nor a correlation between the relaxation state and the bias and scatter of $M(< \theta_E)/M_{sim}(< \theta_E)$.

Conversely, there are strong correlations between the scatter and bias with respect to the ellipticity of the tangential critical curve (ϵ) and the fraction of the circle covered by arcs (ϕ). As can be seen in panel E of Figure 2.13, as ϵ increases both the scatter and bias increase. The dependence on the ellipticity is expected, since one of the main

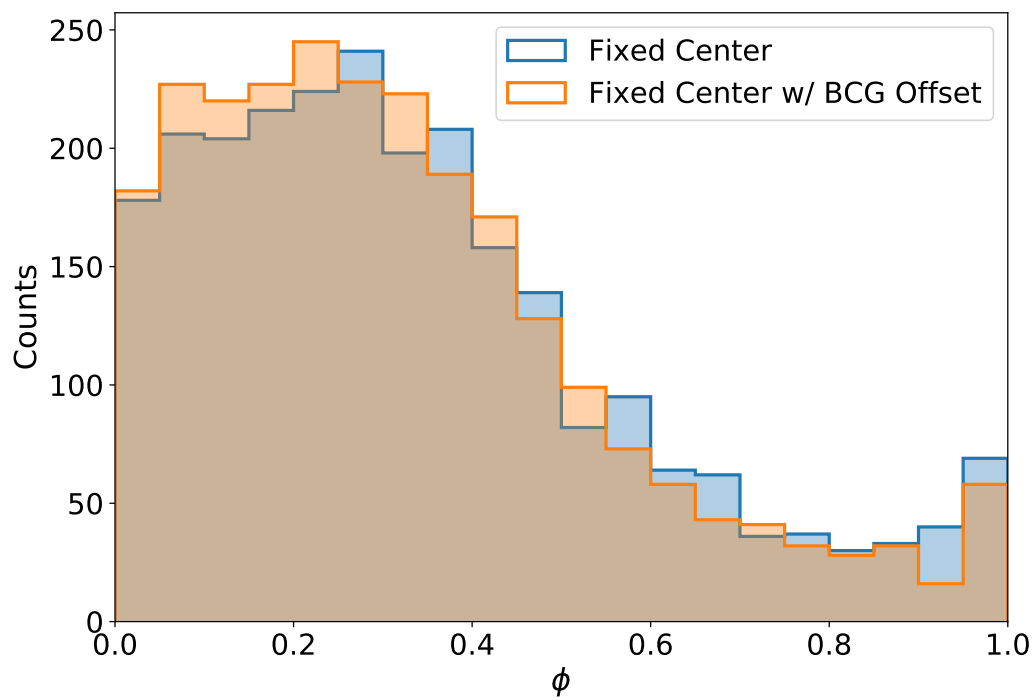


Figure 2.12: Distribution of the fraction of the circle covered by arcs (ϕ) for a given source.

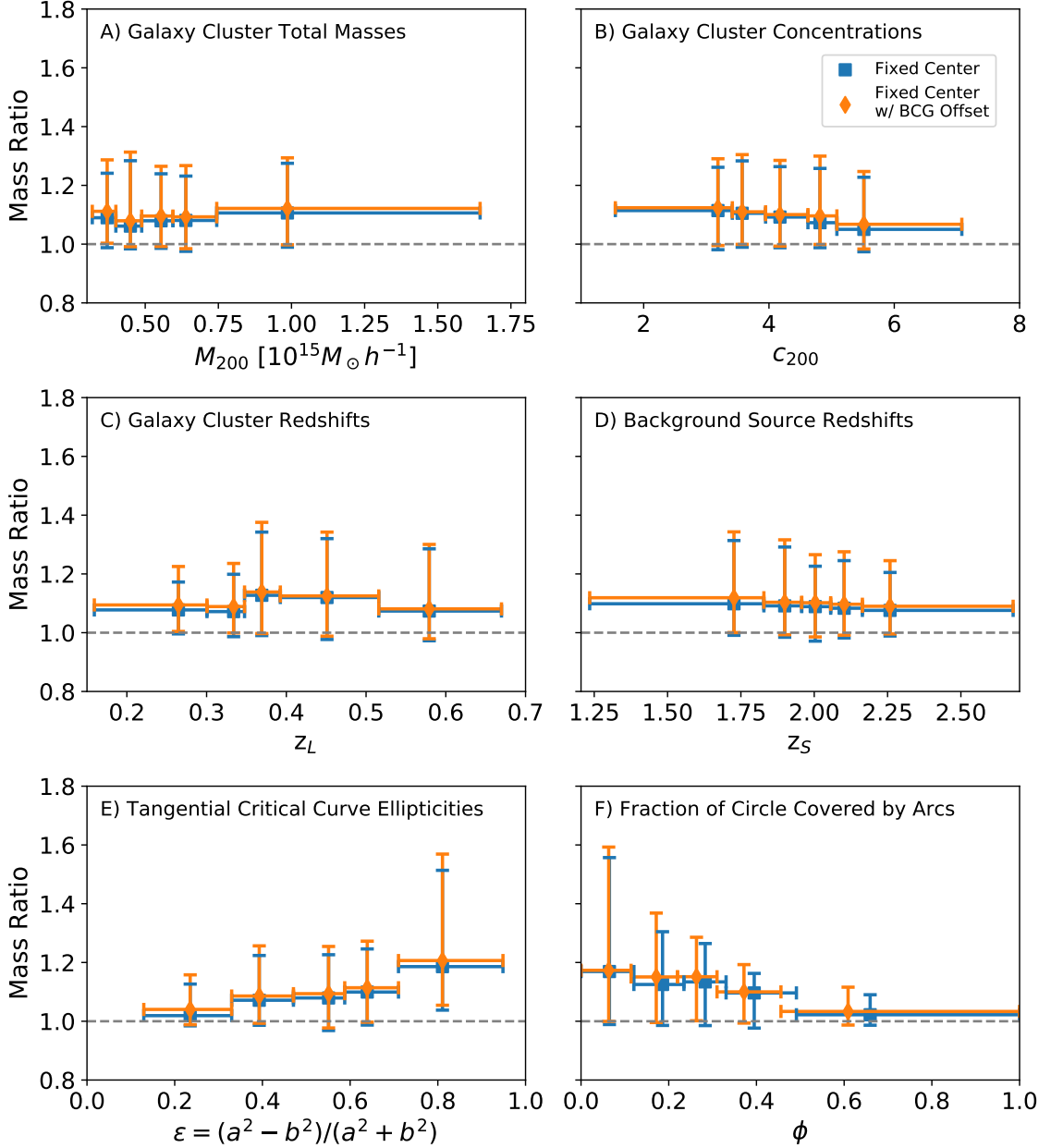


Figure 2.13: **Ratio of Inferred to “True” Mass ($M(< \theta_E)/M_{sim}(< \theta_E)$) Binned by Galaxy Cluster Properties, Background Source, and Lensing Geometry.** Mass ratio binned by total mass (M_{200} , panel A), concentration (c_{200} , panel B), cluster redshift (z_L , panel C), background source redshift (z_S , panel D), tangential critical curve ellipticity (ϵ , panel E), and fraction of circle covered by arcs (ϕ , panel F). We show results for both the fixed center (blue square) and the fixed center with a BCG offset (orange diamond). The symbol marks the median of the distribution, the horizontal and vertical error bars indicate the bin size and scatter (the 16th and 84th percentile of the distribution), respectively. We find that there is a positive bias in all of the bins. We observe a clear trend with ϵ , where both the scatter and bias increase with increasing ϵ , and ϕ , where both the scatter and bias decrease as ϕ increases.

assumptions in the $M(< \theta_E)$ formalism is circular symmetry ($\epsilon = 0.0$). Unfortunately, the measurement of the ellipticity of the tangential critical curve cannot be determined until after a lens model has been computed.

The scatter and bias of $M(< \theta_E)$ decrease with increasing ϕ (Figure 2.13, panel F). This trend matches our expectation; lenses with ϕ closer to 1.0 are typically more circular. Unlike the ellipticity, the fraction of the fitted circle covered by arcs is readily available from the same data used for analysis of observed clusters. It is therefore a useful estimator of lens-dependent uncertainty. For convenience, we tabulate the information displayed in Panel F of Figure 2.13, in Table A.1 in the Appendix.

2.6 The Effect of Background Source Redshift

The redshifts are a piece of information that ideally would be available to the lensing analysis, coming from spectroscopic follow-up (e.g., Sharon et al. 2020) or using photometric redshifts (e.g., Molino et al. 2017; Cerny et al. 2018) from extensive multi-band photometry. However, this may not always be the case, especially considering future large surveys where follow-up may be incomplete. We therefore investigate the additional scatter in the mass estimate due to an unknown source redshift. In this analysis, we assume that we know the underlying distribution of the background source redshifts (Bayliss et al., 2011a).

To evaluate this case, we use the Einstein radius from Section 2.4.1 and the lens redshift from Section 2.3.2, but instead of using the actual source redshifts, we draw 10,000 source redshifts from a normal distribution with $\mu = 2.00$ and $\sigma = 0.2$.

We repeat the analysis in Section 2.5 with this set of drawn background source redshifts. In Figure 2.14, we plot the ratio of the inferred to “true” mass in bins of Einstein radius (left panels) and true background source redshift (right panels). We plot the results for both the fixed center (top panels) and the fixed center with BCG offset (bottom panels). For comparison, we over-plot the results from Section 2.5.2.

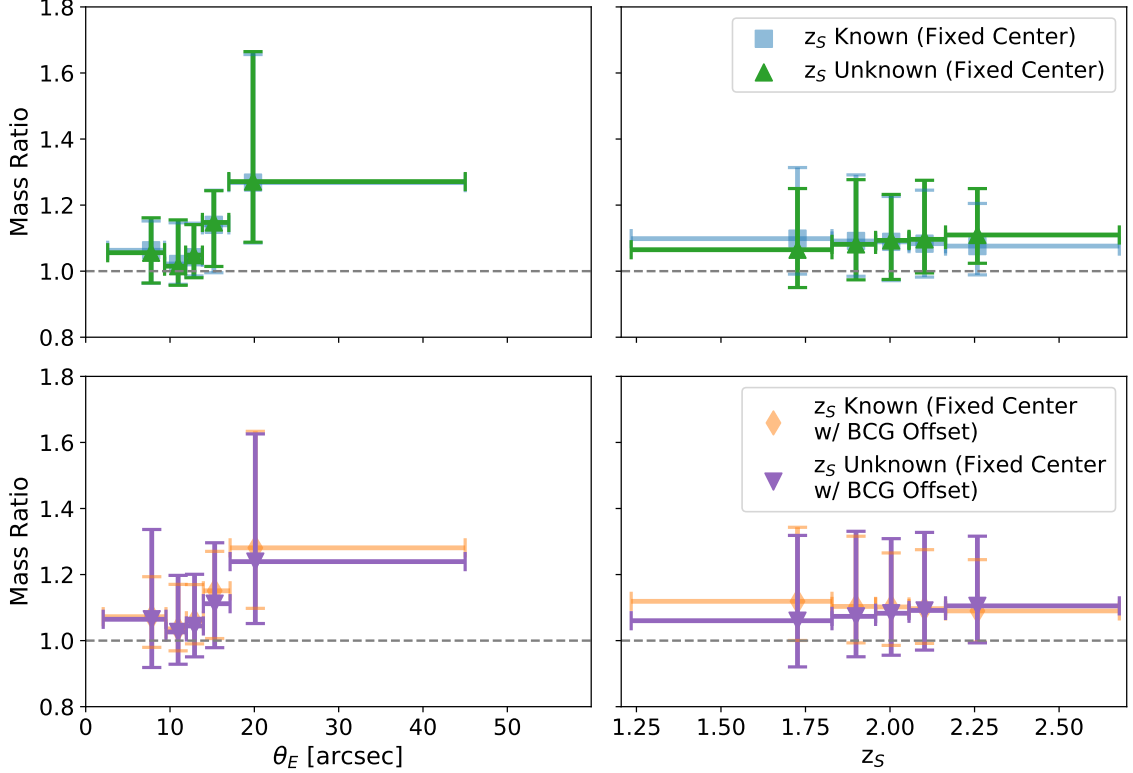


Figure 2.14: **The Effect of Source Redshift Uncertainty on the Results.** The blue square symbols and orange diamonds represent the fixed center and fixed center with BCG offset, and are the same as Figure 2.8 and Figure 2.13, Panel D, respectively. The ratio of the inferred to “true” mass for the unknown source redshift are indicated with up-pointing, green, triangles and down-pointing, magenta, triangles. We find that the uncertainty in source redshift has small effects on the results. As expected, when binned by source redshift (*right*), we find that the inferred mass is low at $z_S < 2.0$ and high at $z_S > 2.0$.

We compute a scatter of 13.8% (18.2%) and bias of 9.0% (8.5%) for the fixed center (fixed center with BCG offset).

As can be seen in the left panel of Figure 2.14 and the scatter and bias of the fixed center, not knowing the exact background redshift and assuming a normal distribution with $\mu = 2.00$ and $\sigma = 0.2$ for typical giant arcs introduces a negligible uncertainty, particularly when compared to the magnitude of the systematics presented in Section 2.5. Split by bins of background source redshift, the scatter remains the same, however, the inferred mass is higher if $z_S > 2$ and lower if $z_S < 2$.

It is important to note that precise source redshifts are critical for most applications of strong lensing (e.g., magnification, time delay, and detailed mass maps). They become negligible in this case because the total enclosed mass is a particularly robust measurement, and the goal is determining the mass of a statistical sample. For mass estimates of individual systems, since the dependence on redshift is straight forward (see Equation 2.8) the uncertainties can be easily determined.

2.7 Empirical Corrections

As can be seen in Figures 2.8 and 2.14, the scatter and bias of this estimator shows dependence on θ_E . We explore the use of an empirical correction to un-bias the mass estimate and reduce the scatter obtained from the Einstein radius method.

We bin the 74,000 data points into 25 bins with equal number of data points per bin, using the Doane’s formula (Doane, 1976) to determine the number of bins for a non-normal distribution. We fit a linear, quadratic, and cubic models to the median of the mass ratio ($M(< \theta_E)/M_{sim}(< \theta_E)$) in each bin and the center of the bin, using the Levenberg-Marquardt algorithm (Levenberg, 1944; Marquardt, 1963). We compute the Bayesian Information Criterion (BIC) for each model (Schwarz, 1978; Liddle, 2007). The results of the fits can be found in Table 2.1 including the scatter and bias of the resulting empirically corrected data. The BIC results for the fixed center (fixed center with BCG offset) are -125.7 (-126.5) for the linear, -152.1 (-157.2) for the quadratic, and -150.7 (-156.9) for the cubic model. Based on this criterion, the quadratic fit, which has the lowest BIC, is clearly preferred over linear and slightly over cubic fits. We therefore use the quadratic fit to determine an empirical correction:

$$\frac{M(< \theta_E)}{M_{sim}(< \theta_E)} = B\theta_E^2 + C\theta_E + D \equiv f(\theta_E), \quad (2.9)$$

where B, C, and D are the fit parameters.

Table 2.1. Empirical Correction Models.

Model	A[arcsec ⁻³]	B[arcsec ⁻²]	C[arcsec ⁻¹]	D	BIC	Scatter	Bias
Fixed Center							
Cubic	$-4.34 \times 10^{-5} \pm 3.36 \times 10^{-5}$	$3.71 \times 10^{-3} \pm 1.73 \times 10^{-3}$	-0.06 ± 0.03	1.29 ± 0.13	-150.7	10.0%	-0.2%
Quadratic	—	$1.49 \times 10^{-3} \pm 2.11 \times 10^{-4}$	$-0.02 \pm 7.05 \times 10^{-3}$	1.14 ± 0.05	-152.1	10.1%	-0.4%
Linear	—	—	$0.02 \pm 2.92 \times 10^{-3}$	0.79 ± 0.04	-125.7	11.4%	-0.5%
Fixed Center w/ BCG Offset							
Cubic	$-4.52 \times 10^{-5} \pm 2.84 \times 10^{-5}$	$3.81 \times 10^{-3} \pm 1.48 \times 10^{-3}$	-0.06 ± 0.02	1.31 ± 0.11	-156.9	10.8%	-0.2%
Quadratic	—	$1.47 \times 10^{-3} \pm 1.84 \times 10^{-4}$	$-0.02 \pm 6.25 \times 10^{-3}$	1.15 ± 0.05	-157.2	10.9%	-0.3%
Linear	—	—	$0.02 \pm 2.84 \times 10^{-3}$	0.81 ± 0.04	-126.5	12.1%	-0.4%

Note. — Model fit results of an empirical correction to un-bias and decrease the scatter of the mass enclosed by the Einstein radius. The last two columns are the scatter and bias of the empirically corrected data. The “fixed center with BCG offset” analysis accounts for the uncertainty added by using the BCG as a proxy for cluster center.

We choose not to include ϕ in our empirical correction because the parameter is dependent on the resolution of the telescope, depth of the observations, and observing conditions. The value of ϕ varies from observation to observation and therefore having a coarser estimate using the binned value in Table A.1 is more appropriate. We correct the measured $M(< \theta_E)$ by dividing it by the corresponding value computed from the parabolic equation evaluated at θ_E :

$$\text{Corrected } M(< \theta_E) = \text{Measured } M(< \theta_E) / f(\theta_E). \quad (2.10)$$

We plot in Figure 2.15 the empirically corrected values of $M(< \theta_E)$ and show the results from Figure 2.8 for reference. With the mass enclosed by the Einstein radius corrected using the empirical correction, the overall scatter (half of the difference between the 84th and the 16th percentile of the distribution) reduces to 10.1% (10.9%) and the bias to -0.4% (-0.3%) for the fixed center (fixed center with BCG offset).

We then perform similar analyses as those in Section 2.5. We explore the systematics in the mass enclosed by the Einstein radius when the empirical correction is applied, and plot the results in Figure 2.16. The blue and orange are the same from Figure 2.13 and are plotted for reference, while the green and red indicate the empirically corrected values.

We observe in Figure 2.16 that overall the measurement of the mass enclosed by the Einstein radius becomes un-biased. The scatter of $M(< \theta_E)$ is reduced in all the bins when compared to the analysis without empirical correction for the total mass, concentration, lens redshift, and background redshift. Using the empirical correction reduces the scatter in the highest-scatter bins, i.e., at high and low Einstein radius, small arc fraction, and large ellipticity of the tangential critical curve.

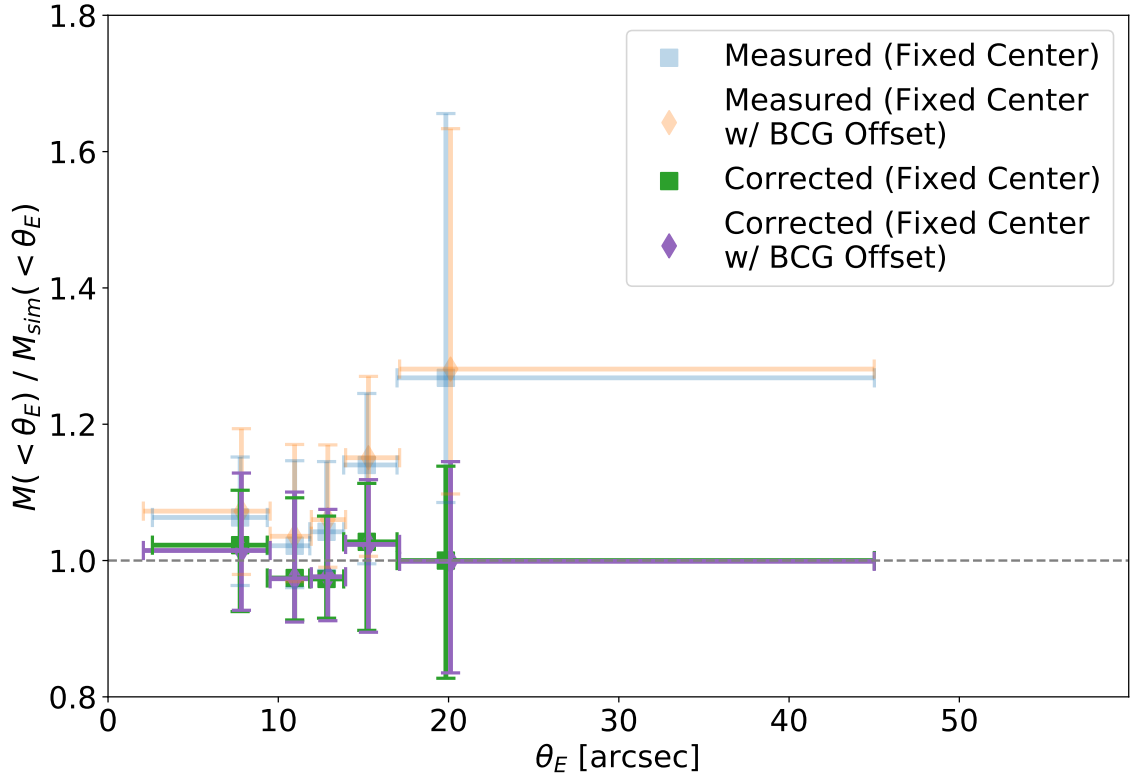


Figure 2.15: **Empirically Corrected Mass Ratio** $M(< \theta_E)/M_{sim}(< \theta_E)$ **Binned by** θ_E . The blue and orange are from the analysis in Figure 2.8, while the green and magenta represent the empirically corrected values, using Equation 2.10. The symbols and error bars are the same as Figure 2.8. We find that using the empirical correction un-biases and reduces the scatter of $M(< \theta_E)$.

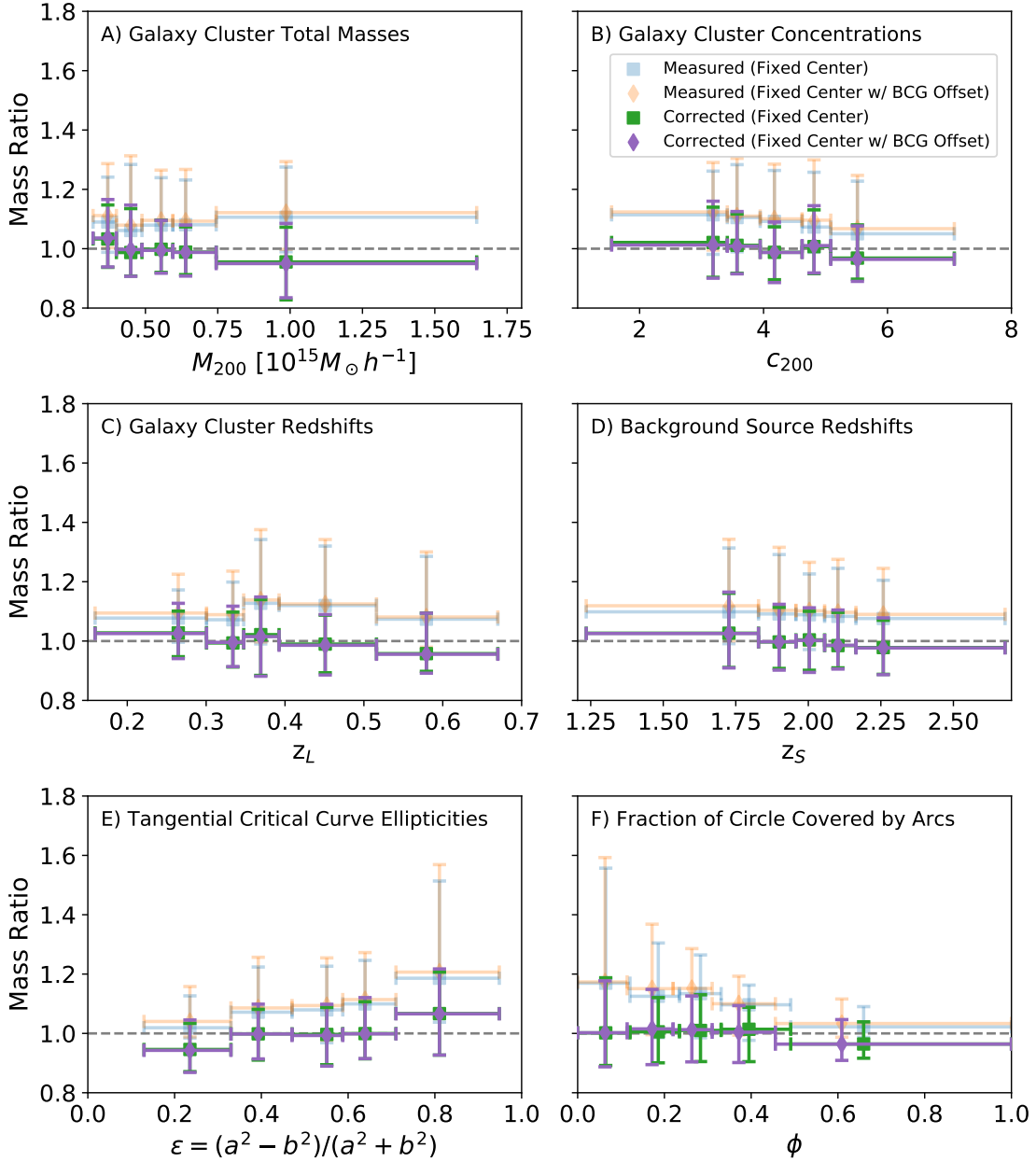


Figure 2.16: **Empirically-Corrected Inferred Mass Binned by Galaxy Cluster Properties, Background Source, and Lensing Geometry.** Same as Figure 2.13, but using Equation 2.10 to empirically correct the mass estimates. The blue and orange points are from the analysis in Figure 2.13, while the green and purple represent the empirically corrected values. We find overall that using the empirical correction un-biases the results and reduces the scatter of $M(< \theta_E)$. The empirical correction does not introduce significant correlation with total cluster mass, concentration, or redshifts. It does not eliminate the trend due to deviation from circular symmetry, as can be seen in Panel E.

2.8 Conclusions

With current and future large surveys discovering tens of thousands of clusters and groups, with thousands expected to show strong lensing features, an efficient method to estimate the masses at the cores of these systems is necessary. The mass enclosed by the Einstein radius is a quick zeroth-order estimate. Studies that use this method quote an uncertainty of $\sim 30\%$ (e.g., Bartelmann & Steinmetz 1996; Schneider 2006), although this uncertainty has not been thoroughly quantified. In this work, we conduct a detailed analysis of the efficacy of the mass enclosed by the Einstein radius as core mass estimator, using the Outer Rim cosmological simulation. When measuring the Einstein radius, we explore three centering assumptions: fixed center, free center, and an observationally-motivated centering that mimics fixing the center to the BCG. We measure the scatter and bias of $M(< \theta_E)$, identify sources of systematic errors, and explore possible indicators available from imaging data at the cores of galaxy clusters. The results of our work are summarized below:

- In the fixed center approach, the center of the circle is fixed to the highest surface density point and a circle is fitted to the tangential arcs. The statistical uncertainty in the measured Einstein radius is small (see Figure 2.5). We measure an overall scatter of 13.9% with a bias of 8.8% in the mass enclosed by the Einstein radius with no correction applied.
- In the free center approach, the center of the circle is a free parameter in the fit. The statistical uncertainty of the Einstein radii fitted with the method is 20 times higher than that of fixed center and the fixed center with BCG offset (see Figure 2.5). With this method, the overall scatter is 27.4% with a bias of 20.2% in the mass enclosed by the Einstein radius with no correction applied. We do not recommend the use of the free center method to measure the mass enclosed by the Einstein radius due to the large scatter in the mass measurement, high

uncertainty in the Einstein radius, and restriction of a minimum of 3 or more identified tangential arcs.

- With the intention to apply this to observational data, we investigate the effect of using the BCG as the fixed center. We move the fixed center from the point of highest density by a random offset, following the log-normal distribution ($\mu = 6.1 \pm 0.7$ kpc) of BCG offsets found by Harvey et al. (2019). This offset increases the scatter to 14.8%, and the bias to 10.2% in the mass enclosed by the Einstein radius when compared to the fixed center method.
- We find that the scatter and bias of $M(< \theta_E)$ with respect to $M_{sim}(< \theta_E)$ does not depend on the total cluster mass, concentration, lens redshift, or source redshift (Figure 2.13).
- We explore how the deviation from circular symmetry affects the measurement of $M(< \theta_E)$. The tangential critical curve ellipticity (ϵ) stems from the deviation from spherical symmetry of the projected mass distribution at the core of the cluster. We find that the bias and scatter correlate with ϵ (Figure 2.13), where larger deviations from circular symmetry lead to a larger bias and scatter of $M(< \theta_E)$ when compared to $M_{sim}(< \theta_E)$.
- The fraction of the circle covered by arcs of a single lensed source (ϕ), can be directly accessed from the imaging data. This observable correlates strongly with the scatter and bias, with both scatter and bias decreasing with an increasing fractional coverage by the arcs (Figure 2.13). ϕ can be used as an observational indicator to estimate the field-specific scatter and bias of $M(< \theta_E)$ (Table A.1).
- Other possible sources of systematic errors exists. While the Outer Rim simulation has a large volume and high mass resolution needed for this work, we are limited by the lack of baryonic information in the simulation and missing

the structure along the line-of-sight in the simulated ray-traced images. For example, the structure along the line-of-sight, particularly in the case of low mass systems, will have an effect on this measurement (Bayliss et al., 2014; Li et al., 2019). We leave this investigation for future work.

- We evaluated the case when the background source redshift measurement is not available, using instead the distribution of the background source redshifts. While an accurate source redshift is critical for several lensing applications (e.g., magnifications, time delays, mass distribution) for the relatively well-constrained enclosed core mass, the scatter introduced by the uncertainty in the background source redshift is negligible compared to that of other systematics (Figure 2.14), if the underlying source redshifts distribution can be accurately estimated. In addition the dependence on the z_s is predictable and matches our expectations, Section 2.6 and Figure 2.14.
- We derive an empirical correction to un-bias and reduce the scatter of the measurement of $M(< \theta_E)$ using a quadratic equation fitted to the mass ratio ($M(< \theta_E)/M_{sim}(< \theta_E)$) with respect to the Einstein radius. The scatter of the empirically corrected masses enclosed by the Einstein radius reduces to 10.1% and 10.9% respectively for fixed center and fixed center with a BCG offset. The empirical correction does not introduce correlation between the inferred mass and other cluster or background source properties, which is important for application of this method in measuring cluster properties such as the concentration-mass relation as a function of redshift.

2.8.1 Application

In this section we provide a recipe for applying the results of this work to observational data, to statistically correct the bias in $M(< \theta_E)$ and estimate its uncertainty.

We note that a more accurate estimate of the field-specific uncertainty can be achieved by using the fraction of the Einstein circle covered by arcs as an indicator of deviation from circular symmetry. We provide instructions for both choices.

1) Starting with a cluster lens field in which lensing evidence has been detected, identify all the secure multiple images (arcs) of the lensed source. Each lensed image should be classified as either tangential or radial. Only the tangential arcs are used to estimate $M(< \theta_E)$.

2) Measure the exact coordinates of a morphological feature (e.g., a bright emission clump) that repeats in each of the arcs.

3) Fit a circle to the list of coordinates. If the cluster has a distinct BCG, we recommend fixing the center of the fitted circle to the position of the BCG. The radius of the fitted circle defines θ_E .

4) Measure ϕ , the fraction of the circle covered by the arcs of a single lensed source, by summing the angles subtended by the extent of the arcs that overlap with the Einstein circle, and dividing the sum by 360° . An example of three cases of different ϕ values is shown in Figure 2.11.

5) Calculate $M(< \theta_E)$, the projected mass density enclosed in θ_E , by evaluating Equation 2.6 and Equation 2.8 for the cluster and source redshifts, and the measured θ_E .

If the spectroscopic redshift of the source is unknown, it can be approximated from photometric redshifts or a probability distribution function of source redshifts. we find that for the purpose of a statistical measurement of the enclosed mass, the increase in uncertainty due to a small error in the source redshift is negligible compared to other sources of uncertainty.

6) Evaluate whether an empirical correction is beneficial: If $\phi \gtrsim 0.5$ (i.e., the arcs of an individual lensed source cover at least half of the Einstein circle), the measured $M(< \theta_E)$ is fairly unbiased and an empirical correction is not necessary. In all other

cases, or if the choice is to not use ϕ as an indicator, proceed to apply the empirical correction as follows.

7) Calculate $f(\theta_E)$, the empirical correction factor, by evaluating Equation 2.9 for θ_E (see Table 2.1 for coefficient values). We recommend using the fixed circle with BCG offset method. For Einstein radii in the range of $\theta_E < 30''0$, we recommend using the quadratic fit. Apply the correction to the measured $M(< \theta_E)$ using Equation 2.10.

8) Determine the uncertainty. The field-specific uncertainty decreases as the fraction of the Einstein circle covered by arcs (ϕ) increases. The numerical values of the scatter as well as the 16th and 84th percentiles (lower and upper limit) for five ϕ bins are tabulated in Table A.1 in Appendix A. If the ϕ estimator is not used, one can assume an overall uncertainty in the corrected $M(< \theta_E)$ of 10.1% (10.9%) for the fixed center (fixed center with BCG offset).

With the characterization of the mass enclosed by the Einstein radius presented in this work — including the application of indicators of the scatter and bias — measuring the mass at the cores of strong lensing galaxy clusters can be performed in large samples in a very efficient manner. The estimation of the mass at the core can be used to determine the mass distribution profile of the galaxy cluster, the concentration parameter (when combined with a mass estimate at larger radius), and provide information about the baryonic and dark matter properties at the core of galaxy clusters.

CHAPTER III

Core Mass Estimates in Strong Lensing Galaxy Clusters Using a Single-Halo Lens Model

Preface

This chapter has been adapted from a paper of the same title published in the *Astrophysical Journal*, Volume 910, Page 144 (Remolina González et al., 2021a), with co-authors K. Sharon, N. Li, G. Mahler, L. E. Bleem, M. D. Gladders, and A. Niemic. The paper is adapted and partially reproduced here under the non-exclusive rights of republication granted by the American Astronomical Society to the paper authors.

For this project, I utilized already created strong lensing simulations to characterize the accuracy, precision, and sources of uncertainty of a fast method to measure the mass at the core of strong lensing galaxy clusters, the mass enclosed by the effective Einstein radius computed from a Sing-Halo Lens Model. I computed 938 Single-Halo Lens Models and visually inspected the outputs of each model. I performed all of the analysis shown with the feedback from the co-authors and the anonymous referee. I produced all of the figures presented in the paper. I wrote nearly the whole text with the feedback and suggestions from the co-authors and the anonymous referee.

Abstract

The core mass of galaxy clusters is an important probe of structure formation. Here, we evaluate the use of a Single-Halo model (SHM) as an efficient method to estimate the strong lensing cluster core mass, testing it with ray-traced images from the ‘Outer Rim’ simulation. Unlike detailed lens models, the SHM represents the cluster mass distribution with a single halo and can be automatically generated from the measured lensing constraints. We find that the projected core mass estimated with this method, M_{SHM} , has a scatter of 8.52% and a bias of 0.90% compared to the “true” mass within the same aperture. Our analysis shows no systematic correlation between the scatter or bias and the lens-source system properties. The bias and scatter can be reduced to 3.26% and 0.34%, respectively, by excluding models that fail a visual inspection test. We find that the SHM success depends on the lensing geometry, with single giant arc configurations accounting for most of the failed cases due to their limiting constraining power. When excluding such cases, we measure a scatter and bias of 3.88% and 0.84%, respectively. Finally, we find that when the source redshift is unknown, the model-predicted redshifts are overestimated, and the M_{SHM} is underestimated by a few percent, highlighting the importance of securing spectroscopic redshifts of background sources. Our analysis provides a quantitative characterization of M_{SHM} , enabling its efficient use as a tool to estimate the strong lensing cluster core masses in the large samples, expected from current and future surveys.

3.1 Introduction

Harbored at the high-density knots of the cosmic web, galaxy clusters trace the large-scale structure formation of the universe, making them valuable cosmological laboratories (see reviews by Allen et al. 2011 and Mantz et al. 2014). Their mass

function, which connects their observational properties to the underlying cosmology (e.g., Jenkins et al. 2001; Evrard et al. 2002; Corless & King 2009; Pratt et al. 2019; Bocquet et al. 2020), is one of the ensemble properties that cluster-based cosmological studies are pursuing. However, the efficacy of cluster-based cosmological studies is sensitive to sample size and selection function (e.g., Hu 2003; Khedekar & Majumdar 2013; Bocquet et al. 2019) and requires a good understanding of the inherent systematic errors in the mass estimate due to the observed astrophysical properties (Evrard et al., 2002; Allen et al., 2011; Huterer & Shafer, 2018). Other cluster properties predicted by cosmological simulations include the radial profiles and concentrations of dark matter halos (Duffy et al. 2008; Meneghetti et al. 2014; Child et al. 2018), and can be directly tested with observations (e.g., Oguri et al. 2012; Merten et al. 2015). An accurate measurement of the mass profile slope of galaxy clusters requires mass proxies that are sensitive to the total cluster mass, as well as mass proxies whose resolution is high enough to probe the innermost hundreds of parsecs.

Gravitational lensing probes the total (dark and baryonic) matter distribution, independent of baryonic physics and cluster dynamical state. Strong gravitational lensing (SL) has the highest resolution at the core of galaxy clusters, where the strong lensing evidence is present; Weak lensing (WL) gives an accurate measurement of the total mass at large cluster-centric radii. By combining the mass estimate from SL at the core with a mass estimate at large scales from WL or other mass proxies, we can constrain the mass distribution profile from the core to the outskirts, and measure profile parameters such as the concentration of the galaxy cluster (e.g., Gralla et al. 2011; Oguri et al. 2012; Merten et al. 2015). Tension between the observations and theoretical expectation of the mass distribution profile of SL galaxy clusters has been reported (e.g., Broadhurst & Barkana 2008; Gonzalez et al. 2012; Meneghetti et al. 2013), however, these studies are limited by small samples and complicated selection functions.

Thousands of SL galaxy clusters are being discovered with current and up-coming large surveys, covering a broad wavelength range, detecting clusters out to $z \sim 2$, and addressing challenges due to small sample sizes. These include cluster surveys based on observations with the South Pole Telescope (SPT; SPT-3G, Benson et al. 2014; SPT-SZ 2500 deg², Bleem et al. 2015; Bocquet et al. 2019; SPT-Pol 100 deg², Huang et al. 2020; SPT-ECS, Bleem et al. 2020), the Atacama Cosmological Telescope (ACT; Marriage et al. 2011; Hilton et al. 2018), the Cerro Chajnantor Atacama Telescope (CCAT; Mittal et al. 2018), Euclid (Laureijs et al., 2011; Amendola et al., 2018), Vera Rubin Observatory Legacy Survey of Space and Time (LSST, LSST Science Collaboration et al. 2017), and eROSITA (Pillepich et al., 2018). We expect that hundreds of the newly discovered clusters will be strong lenses (LSST Science Collaboration et al., 2009). With an order of magnitude increase in sample sizes, an efficient and accurate method will be required in order to measure the mass at the cores of the SL clusters in a timely manner.

Strong lensing-based measurements of the mass distribution at the cores of galaxy clusters typically rely on detailed lensing analyses. A detailed lens model of a cluster with rich strong lensing evidence (e.g., the Frontier Fields; Lotz et al. 2017) can have a high level of complexity requiring a large number of constraints, extensive follow-up observations, computational resources, and multiple iterations to be finalized (e.g., Johnson et al. 2014; Zitrin et al. 2014; Diego et al. 2016; Kawamata et al. 2016; Lotz et al. 2017; Strait et al. 2018; Lagattuta et al. 2019; Sebesta et al. 2019; Raney et al. 2020a). Due to the limited resources and small number of lensing constraints, which is typical for all but the most massive strong lensing clusters (e.g., Sharon et al. 2020), there is a need to investigate efficient methods to estimate the mass at the core of SL galaxy clusters. Remolina González et al. (2020) presented an evaluation of the mass enclosed by the Einstein radius as a zeroth-order method to estimate the mass at the core of galaxy clusters (see Chapter II). The limiting factor when using the Einstein

radius to estimate the core mass is the assumption of spherical symmetry inherent to this method. In this chapter, we investigate a higher complexity first-order method, which is more complex than the mass enclosed by the Einstein radius, but not as expensive as computing a detailed lens model.

The goal of this chapter is to evaluate the use of the Single-Halo model (SHM) as an efficient method to measure the mass at the core of SL galaxy clusters. We measure the scatter and bias in the mass estimate, establish limitations in the use of the SHM, and explore dependence of the scatter on the properties of the model and the lens-source system. We use the state-of-the-art ‘Outer Rim’ simulation run (Heitmann et al., 2019), which facilitates a robust statistical analysis that is representative of the universe.

This chapter is organized as follows. In Section 3.2, we describe the lensing algorithm used in our analysis, `Lenstool`, summarize the procedure employed in detailed lens models, and present the Single-Halo model. In Section 3.3, we describe the ‘Outer Rim’ simulation and detail the simulated sample used in our analysis. In Section 3.4, we describe the identification of constraints for the SHM, compute the SHM, and measure the aperture mass enclosed within the effective Einstein radius, M_{SHM} . In Section 3.5, we measure the bias and scatter of M_{SHM} , in comparison to the true mass. In Section 3.6, we investigate the effects on the SHM of an unknown background source redshift, the lensing geometry of the arc, and addition of a second multiply-imaged source. Last, we present our conclusion and summary of the evaluation of the Single-Halo models as a mass estimate at the core of galaxy clusters in Section 3.7.

In our analysis, we adopt a *WMAP-7* (Komatsu et al., 2011) flat Λ CDM cosmology as in the ‘Outer Rim’ simulation: $\Omega_\Lambda = 0.735$, $\Omega_M = 0.265$, and $h = 0.71$. Masses reported in terms of $M_{\Delta c}$, are defined as the mass enclosed within a radius at which the average density is Δ times the critical density of the universe at the cluster redshift.

3.2 Background: Lens Modeling

Strong lens modeling analyses use the positional and redshift measurements of lensed galaxies (arcs) as constraints to model the underlying mass distribution. We use the publicly available lens modeling algorithm `Lenstool` (Jullo et al., 2007), which has been widely used (e.g., Johnson et al. 2014; Cerny et al. 2018; Paterno-Mahler et al. 2018; Lagattuta et al. 2019; Jauzac et al. 2020; Mahler et al. 2020; Sharon et al. 2020) and its results are similar to other parametric models (Meneghetti et al., 2017; Priewe et al., 2017; Remolina González et al., 2018; Raney et al., 2020b). `Lenstool` uses a Monte Carlo Markov Chain (MCMC) method to explore the parameter space, identify the best fit values, and estimate the statistical uncertainties in the model. To characterize the mass density distribution we use a parameterized dual pseudo-isothermal ellipsoid (dPIE, Elíasdóttir et al. 2007) with seven parameters: position (α and δ), ellipticity ($\epsilon = (a^2 - b^2)/(a^2 + b^2)$), where a and b are the semi-major and semi-minor axis respectively), position angle (θ), velocity dispersion (σ), core radius (R_{core}), and truncating radius (R_{cut}). We fix the truncating radius (R_{cut}) to 1500 kpc, since it is far beyond the lensing region, and cannot be constrained using the strong lensing evidence. We note that this range resembles the splashback radius (e.g., Umetsu & Diemer 2017; Shin et al. 2019). In the next subsections we describe the difference between “detailed” and Single-Halo models, and describe the selection of constraints and priors used for the lens modeling procedure.

3.2.1 Detailed Lens Models

For in-depth description on the commonly used procedures in detailed parametric lens modeling, we refer the reader to Verdugo et al. (2011) and Richard et al. (2011), and examples by Mahler et al. (2018, 2020); Lagattuta et al. (2019); and Sharon et al. (2020). Detailed lens models use the galaxy cluster redshift, and the position and redshift of the arcs as constraints. One or more large cluster-scale profile(s) repre-

sent the dark matter halo(s) of the cluster and correlated structure as needed, and multiple galaxy-scale halos represent the galaxy cluster members mass contribution. The galaxy-scale potentials positional parameters are usually fixed to their observed values and a parameterized mass-luminosity relation is used to set or fit the other parameters. The brightest cluster galaxy (BCG) may be modeled with a separate halo as we do not expect BCGs to follow the same mass-luminosity relation as the rest of the cluster members.

Compared to the Single-Halo models that will be introduced in the next section, detailed lens models can be highly complex. The complexity adds the flexibility needed in order to trace the substructure in the form of multiple dark matter halos, filaments, contributions from cluster-member galaxies, and in some cases uncorrelated structure along the line-of-sight. The versatility of these models has been shown to be a successful tool for studying a broad range of sciences including cosmology, galaxy clusters physics, and the highly magnified background universe (e.g., Johnson et al. 2017b; Acebron et al. 2017; Gonzalez et al. 2020). The flexibility of detailed lens models also means the models are not unique and require care in the construction and evaluation, often multiple statistical assessments to select between models (e.g., Acebron et al. 2017; Paterno-Mahler et al. 2018; Lagattuta et al. 2019; Mahler et al. 2020).

Detailed lens models for galaxy clusters with rich strong lensing evidence require extensive follow-up observations, computational resources, and multiple iterations of the modeling process. The high complexity of the models relies on a large number of free parameters, requiring a large number of constraints, i.e., multiply-imaged lensed galaxies, whose availability becomes a limiting factor in the modeling process.

3.2.2 Single-Halo Models

Single-Halo models are similar to their detailed counterparts and use the same type of constraints. The difference in the SHM modeling procedure is that the lens plane is described by a single cluster-scale dark matter halo, while all secondary halos and contribution from cluster member galaxies are neglected. The small number of parameters requires only a handful of constraints, and the model can be computed quickly and with limited human intervention.

We use the same dPIE halos described above, with six free parameters. We use broad priors in the parameters of the dPIE potential: $-8''.0 < \alpha, \delta < 8''.0$; $0.0 < \epsilon < 0.9$; $0^\circ < \theta < 180^\circ$; $50 \text{ kpc} < R_{core} < 150 \text{ kpc}$; and $500 \text{ km/s} < \sigma < 1500 \text{ km/s}$.

The outputs of the lens models include the projected mass distribution (Σ), convergence (κ), shear (γ), magnification (μ), critical curves, and predicted location of multiple-images. The tangential critical curve (TCC) and radial critical curve (RCC) are the theoretical lines of infinite magnification and name the primary direction along which images (arcs) are magnified. The magnification in the tangential direction is computed as follows: $\mu_t^{-1} = 1 - \kappa - \gamma$. In this analysis, we measure the aperture mass enclosed by the effective Einstein radius ($e\theta_E$), defined as the radius of a circle with the same area as the area enclosed by the tangential critical curves.

3.3 Simulated Data:

To evaluate the SHM method, we use the state-of-the-art, large volume, high-mass-resolution, N-body simulation ‘Outer Rim’ (Heitmann et al., 2019) with the HACC framework (Habib et al., 2016). The simulation was carried out at the Blue Gene/Q system at Argonne National Laboratory. The large size simulation box ($L = 3000 \text{ Mpc h}^{-1}$ on the side) allows for many massive halos in the redshift range of interest

($z \sim 0.1 - 0.7$) with detailed projected mass distribution profiles representative of the universe.

The ‘Outer Rim’ simulation has been used to study the dark matter halo profiles of galaxy groups and clusters (Child et al., 2018), evaluate the effects on lensing due to line-of-sight (LOS) structure (Li et al., 2019), and to construct realistic strong lensing ray-traced simulated images (Li et al., 2016). The simulation does not include the baryonic component; while baryons represent a small portion of the mass content of the galaxy cluster, studies have shown that the baryonic component has non-zero effects on the mass distribution and the lensing potential. For example, the concentration of dark matter halos is higher when baryons are included in the simulation (Meneghetti et al., 2003; Wambsganss et al., 2004; Oguri, 2006; Hilbert et al., 2007, 2008; Wambsganss et al., 2008; Oguri & Blandford, 2009). The light due to the baryonic component is also not depicted in the simulated images, i.e., the diffused light from intracluster medium, and stellar population of cluster member galaxies. Fully accounting for these baryonic effects awaits for simulations that include baryonic physics in large cosmological boxes.

The galaxy cluster halos used in the analysis were identified using a friends-of-friends algorithm with linking length of $b = 0.168$ and the surface density was computed using a density estimator. Rangel et al. (2016) showed that the high mass resolution is robust enough to simulate strong lensing in halos with masses $M_{500c} > 2 \times 10^{14} M_{\odot} h^{-1}$. Following an SPT-like selection function, all halos with $M_{500c} > 2.1 \times 10^{14} M_{\odot} h^{-1}$ were selected. From this sample, the strong lenses are identified as those having an Einstein radius of at least a few arcseconds, as measured from the average convergence $\langle \kappa(\theta) \rangle = 1$.

The sample details are presented in Remolina González et al. (2020), see Chapter II, and summarized here. The sample of simulated SPT-like strong lenses is made of 74 galaxy cluster halos spanning a redshift range of $z \sim 0.16 - 0.67$. The red-

shift range is similar to other strong lensing samples like that of the Sloan Giant Arc Survey (SGAS, Gladders et al, in preparation; Sharon et al. 2020). Future studies will extend the redshift range, $z < 1.75$, to better match surveys like the SPT-SZ 2500-Square-Degree survey (Bleem et al., 2015). We adopt the halo masses (M_{200c}) and concentrations (c_{200c}) that were derived by Child et al. (2018).

The lensed simulated images were created through ray-tracing using the projected mass distribution of the galaxy cluster following the procedure detailed in Li et al. (2016). We draw redshifts for the background sources following the observed distribution of Bayliss et al. (2011a) leading to a simulated source range of $z \sim 1.2$ to $z \sim 2.7$. The image plane of each cluster field is generated 5 to 24 times, each realization using a single redshift and unique background source location. A total of 1024 simulated ray-traced realizations were created from the 74 simulated SL galaxy cluster halos. The simulated images have a resolution of $0''.09$ per pixel and a field of view of 2048×2048 pixels. No additional noise or errors were added, as we use these simulations to investigate the most ideal case rather than creating mock observations that simulate a particular instrument. The background sources were preferentially placed in areas of high magnification, as highly magnified (total magnification > 5) arcs are easily detected from ground based observations. This strategy was chosen in order to mock the selection function of lensing-selected samples, in which lensing clusters were identified based on the appearance of a giant arc in visual inspection of shallow observational data (e.g., Bayliss et al. 2011a; Nord et al. 2016, 2020; Sharon et al. 2020; Khullar et al. 2021). The total magnification is defined as the ratio of the area between the image-plane and source-plane of the lensed image. Only isolated halo ray-tracing is used, no structure along the line-of-sight was included. Structure along the line-of-sight is known to affect the lensing potential (e.g. Bayliss et al. 2014; D’Aloisio et al. 2014; Chirivì et al. 2018; Li et al. 2019). A statistical analysis of the line-of-sight effect and lensing systems without dominant giant arcs is left for future

work.

We use the redshift and observed image plane positions of the arcs as our constraints for the lens models. We compare the model mass we derive from the SHM method to the projected mass density from the simulation.

3.4 Methodology:

Our analysis of the simulated ray-traced lensed images is guided by the procedures used with observational data. The images are inspected one at a time to identify the multiply-imaged morphological features (emission knots) to be used as positional constraints in the lens modeling process. In the case of observational data, visual inspection is also required for spectroscopic follow-up observation of the arcs and cluster members. Here, we assume that the redshifts of the arcs and the clusters have been measured (see Section 3.3, Remolina González et al. 2020, and Chapter II). In this section, we provide a description of the identification of the lensing evidence, compute SHMs, and estimate the mass at the core of the galaxy cluster within the $e\theta_E$.

3.4.1 Arc Catalog Identification

Identical to the procedure described in Remolina González et al. (2020) and Chapter II, we identify the lensing evidence and measure the positional constraints in the simulated lensed images. Lens modelers take advantage of the expected lensing geometry, morphology, and color information to associate sets of multiple-images of the same background source. In our analysis no color information was implemented, so we rely on the morphology and expected lensing geometry for this identification. For each line of sight, we compile a catalog including the positional locations of the arcs (including identified emission knots within each arc) and their redshift. Each identified set of n multiply imaged features contributes $2n - 2$ constraints.

3.4.2 The SHM Procedure

One of the advantages of the SHM is that it can be automatically computed with minimal human intervention. It requires as input the cluster redshift, initial center position (e.g., the BCG), and positions and redshifts of the arcs. The best fit lens model is the one that minimizes the scatter between the observed and model-predicted positions of the arcs in the image-plane. Since the single dPIE halo has six free parameters, the SHM requires a minimum of six lensing constraints. We find that of the 1024 simulated lensed images, 938 have enough constraints for a SHM to be computed. We note that while this requirement is satisfied, it does not guarantee that the lens model will be fully constrained and in some cases may result in unphysical SHMs, as will be discussed in the next section.

3.4.3 Assessment of the SHM Success

A quick visual inspection of the resultant critical curve and model predictions with respect to the lensing evidence can provide a critical quality assessment of the Single-Halo models. We inspect each of the generated models, and find that in some cases the Single-Halo model does not reproduce the lensing configuration, and/or predicts multiple images in areas where no arcs are found. We flag these cases as “Failed Single-Halo Models” (F-SHM); such models would not be trusted in a typical observational analysis and would usually require a more involved lens modeling analysis, or more constraints to improve the fidelity of the models.

We flagged 201 out of our 938 models as F-SHMs, leaving 737 that pass the visual inspection (P-SHM); Figure 3.1 shows representative examples of P-SHMs (top row) and F-SHMs (bottom row). Each of the 74 galaxy clusters still has at least one SHM that passed the visual inspection, with most having 9 or more P-SHMs. We note that due to the construction process of our simulated images, i.e., the background sources were preferentially placed in order to produce highly magnified images, the

SHM success rate we quote here does not represent the expected success rate in the Universe; it is more tuned to resemble the success rate of modeling systems with giant arcs (e.g., Johnson et al. 2017a; Rigby et al. 2018; Sharon et al. 2020; Remolina González et al. 2021a). We use the fail/pass distinction in Section 3.5.

We investigate whether the image-plane root-mean-square (*rmsi*) can be used as a quantitative quality indicator in lieu of a visual inspection. The *rmsi* is often used to determine the goodness of fit of lens models; it measures the scatter between the observed and model-predicted image-plane locations of lensed features, and in most strong lens modeling algorithms it is used in the minimization process. We find that the value of the model *rmsi* is only a weak predictor of the quality of the SHMs. As can be seen in Figure 3.2, while the highest bins of *rmsi* are dominated by F-SHMs, both P-SHMs and F-SHMs span the full range of low *rmsi* bins. This means that a low *rmsi* is not a sufficient indicator of model quality. This finding is consistent with previous studies. In an observational analysis of 37 lensing clusters, Sharon et al. (2020) found that while the *rmsi* serves as a good statistical indicator when comparing different lens models of the exact same system, it is not a good absolute predictor of a lens model quality. Johnson & Sharon (2016) used simulations to study the relationship between the *rmsi*, the number of constraints, and the accuracy in recovering the mass and magnification. They found that as expected, the accuracy of the magnification and mass recovered by the lens models improved with larger numbers of constraints, however, the *rmsi* increases with number of constraints. We therefore do not recommend relying on *rmsi* alone in order to determine which models pass or fail.

3.4.4 Aperture Mass Enclosed by the $e\theta_E$

We use the projected mass distribution (Σ) from the best fit lens model to compute other outputs including the magnification (μ), convergence (κ), and shear (γ). We

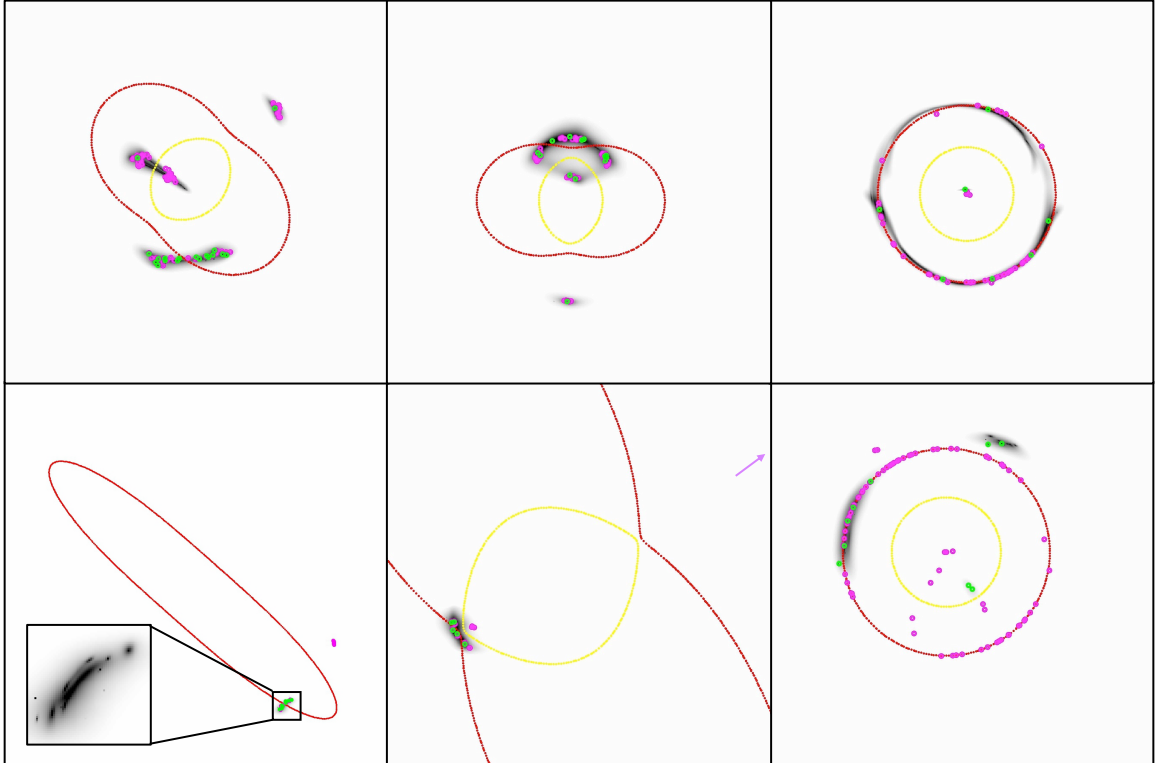


Figure 3.1: **Examples of SHM outputs**, overplotted on six ray-traced lensing images. The tangential and radial critical curves for the redshift of the background source are plotted in red and yellow, respectively. The green circles mark the constraints, and the magenta circles show the model-predicted image locations. Each image is 1.0 arcminute (except the *Bottom-Left*, which is 2.0 arcminutes) on the side and a resolution of $0''.09$ per pixel. *Top row*: representative models that pass the visual inspection test (P-SHM). Each of these models predicts lensed images at their observed locations. *Bottom row*: models that fail to reproduce the lensing geometry (F-SHMs). The primary reason for rejecting these models is as follows: *Bottom-Left*: The lensing configuration, arc curvature, and the unrealistically high ellipticity of the SHM halo suggest that there is a contribution from a secondary mass halo, which cannot be well represented by a single halo model. *Bottom-Middle*: The SHM critical curves are extremely large leading to an unphysical mass distribution for the lensing configuration, also producing projections where no arcs are found outside the shown field of view indicated by the magenta arrow. *Bottom-Right*: The SHM predicts lensed images where no arcs are found.

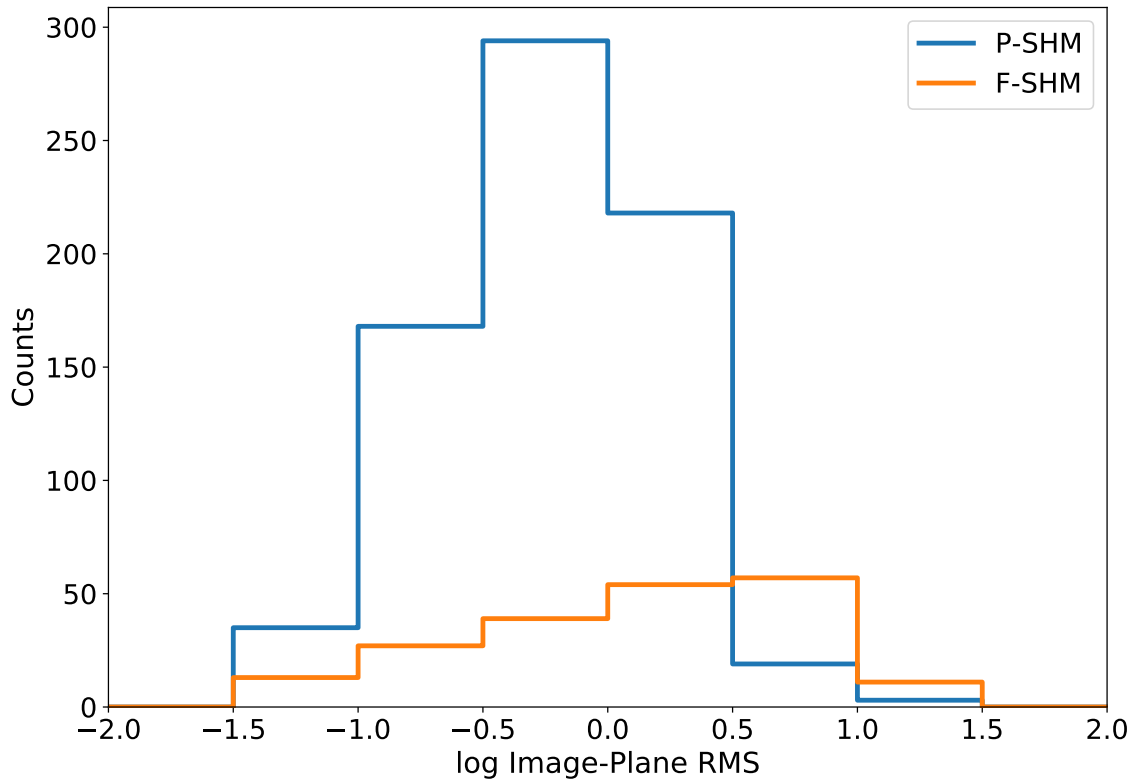


Figure 3.2: **Distribution of Image-Plane Root-Mean-Square ($rmsi$) of the Lens Models.** The distributions of models that passed (P-SHM) or failed (F-SHM) the visual inspection are shown in blue and orange, respectively. The F-SHM distribution is skewed towards higher $rmsi$ values, but both F-SHM and P-SHM can have low $rmsi$ values, making this an insufficient predictor of model quality.

compute the magnification in the tangential direction (μ_t) and determine the location of the TCC ($\mu_t \rightarrow \infty$). Next, we measure the $e\theta_E$ as the radius of the circle with the same area as the area enclosed by the TCC. Last, we measure the aperture mass centered at the center of the modeled dPIE dark matter halo and enclosed by the effective Einstein radius, which we denote M_{SHM} .

3.4.5 Statistics

To establish a robust statistical analysis using our simulated SL sample, we weight each of the 74 SL galaxy cluster equally. We also weight each ray-tracing realization by a factor of one over the total number of realizations with SHMs for each galaxy cluster. Then for every simulated cluster, we randomly select one M_{SHM} representative of a ray-tracing image. We repeat this process 1000 times for each of the 74 simulated clusters for a total of 74,000 mass measurements used in our statistical analysis.

3.5 Analysis of Results:

In this section, we compare the aperture mass enclosed by the effective Einstein radius of the Single-Halo model (M_{SHM}) and the “true” mass enclosed within the same aperture from the simulation (M_{SIM}). We compute the scatter and bias of M_{SHM} versus M_{SIM} and explore whether the M_{SHM} depends on the lens model parameters and the simulated galaxy cluster properties.

For the statistics used in this analysis see Section 3.4.5. The scatter is computed as half the difference between the 84th and 16th percentiles. The bias is computed as

$$\text{bias} = \text{median}(M_{\text{SHM}}/M_{\text{SIM}}) - 1. \quad (3.1)$$

In Figure 3.3, we plot a direct comparison between M_{SHM} and M_{SIM} . We measure an overall scatter of 8.52% about the 1:1 relation between M_{SHM} and M_{SIM} (drawn

in Figure 3.3 to guide the eye), with a positive bias of 0.90%. Interestingly, at the high-mass bin the core mass is highly overestimated; we explain this bias below.

In Figure 3.4, we separate the sample into two bins, according to their pass/fail assessment (see Section 3.4.3). We find that the P-SHMs span a tighter core-mass range compared to the F-SHMs, i.e., SHMs in the high and low mass bins are more likely to fail. In all mass bins the core masses computed from the F-SHM models are less accurate; in particular, the large scatter observed in the high mass bin in Figure 3.3 is due entirely to F-SHM models. Overall, the mass estimate of the P-SHMs has a scatter of 3.26% with a bias of 0.34% compared to the true mass. This result implies that the larger scatter and bias of the whole sample are driven by the failed-SHM lines of sight.

Further investigation of these catastrophic failures highlights the limitation of SHM in recovering some under-constrained lensing configurations. We find that in most of the high-mass, highly overestimated cases, the SHM converges on a solution where the halo is oriented such that the single giant arc forms on a critical curve in the direction of its semi minor axis, rather than in the direction of its semi major axis. An example of such a failed model is shown in the bottom middle panel of Figure 3.1. These models populate the highest core-mass bin in Figure 3.3 since they produce a large $e\theta_E$; and they overestimate the mass since the model converges on a wrong solution, perpendicular to the underlying mass distribution. Fortunately, these cases are easily identified in a visual inspection. In analyses of real data, these cases can be flagged for a more involved analysis beyond the automated SHM. Manually imposing more constrained priors, increasing the complexity of the model, or adding constraints from secondary lensed system may resolve these cases.

All of these indicate that a quick visual inspection of the model outputs is beneficial when estimating the mass at the cores of galaxy clusters, using the SHM method.

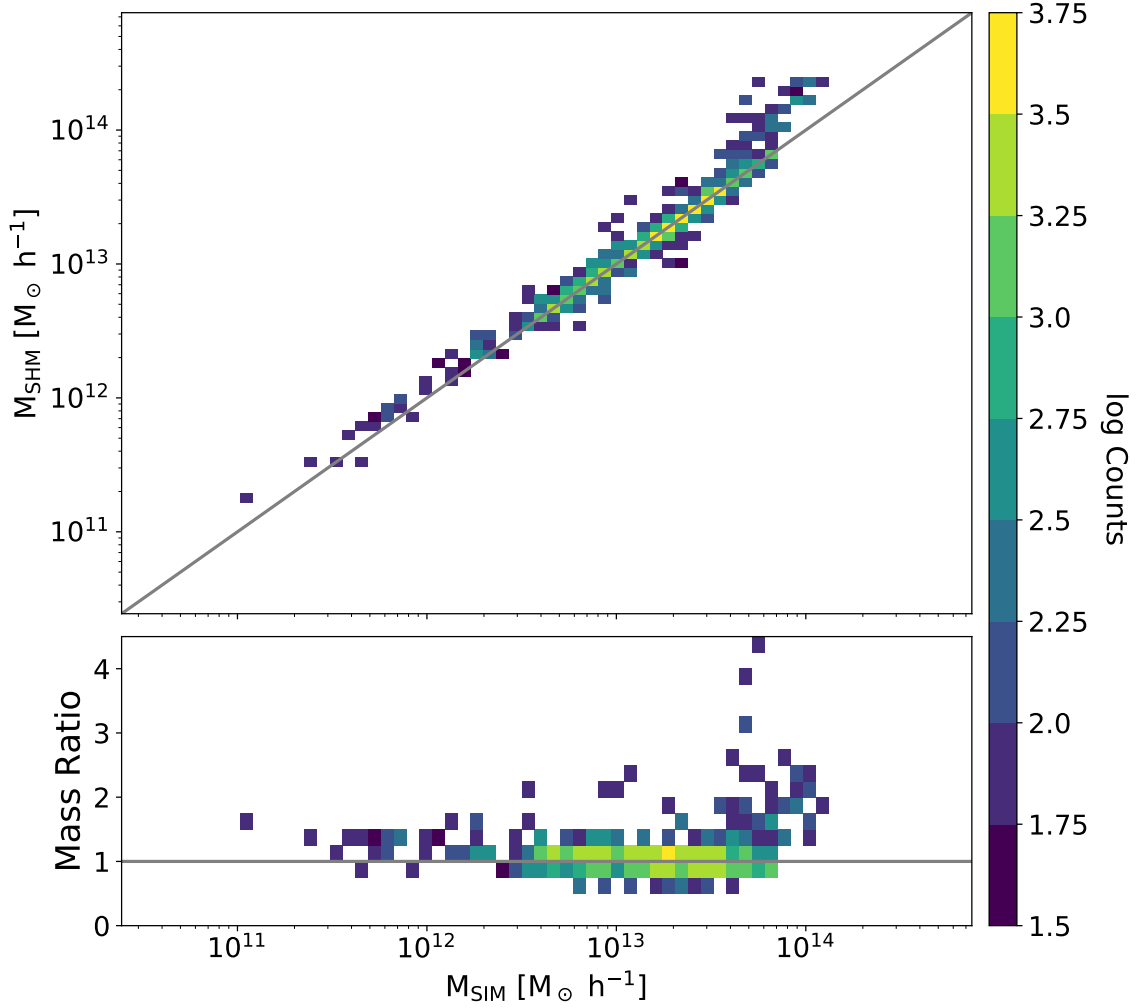


Figure 3.3: **Mass Comparison Between the M_{SHM} and M_{SIM} .** *Top panel:* Direct comparison between the aperture mass enclosed by the $e\theta_E$ (M_{SHM}) and the “true” aperture mass within the same aperture from the simulation surface density (M_{SIM}). The solid gray line is where $M_{\text{SHM}} = M_{\text{SIM}}$, plotted to guide the eye. *Bottom panel:* The mass ratio, $M_{\text{SHM}}/M_{\text{SIM}}$. We find that on average, M_{SHM} overestimates M_{SIM} , especially at the high mass bins (see Section 3.5).

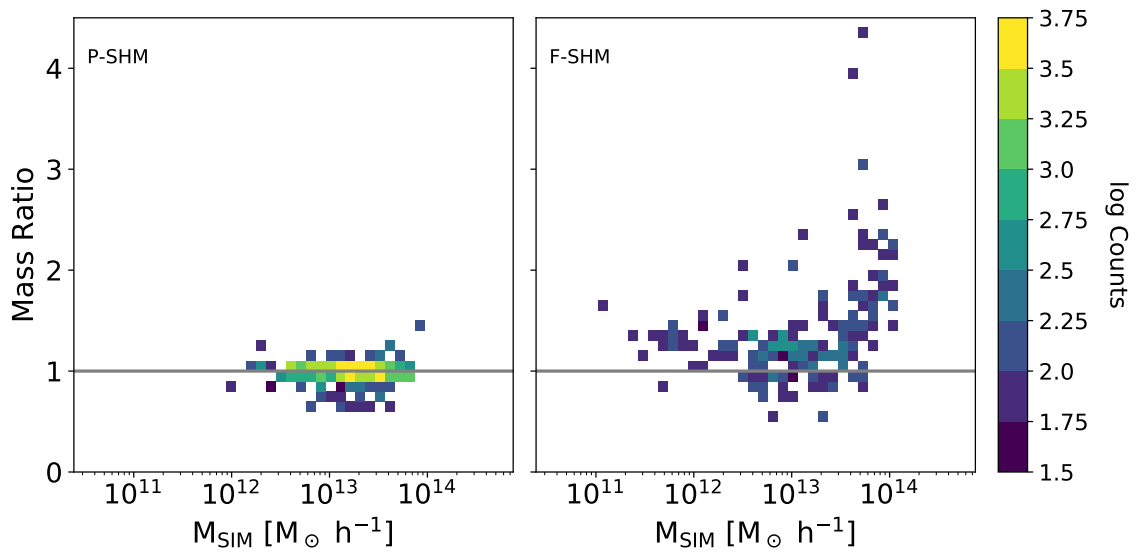


Figure 3.4: **Comparison between the mass estimates of P-SHMs and F-SHMs.** Mass ratio ($M_{\text{SHM}}/M_{\text{SIM}}$) of the SHMs that passed the quick visual inspection (P-SHMs) is plotted in the left panel, and of the ones that Failed (F-SHMs) is plotted in the right panel. The P-SHMs span a somewhat smaller mass range than the F-SHMs. Notably, on average the F-SHMs are biased high, and their spread about the one-to-one line is higher than the P-SHM, indicating that a quick visual inspection of the SHM outputs can easily weed out most of the outliers.

3.5.1 Possible causes of scatter and bias in the M_{SHM} mass estimate

We explore possible dependencies in the scatter and bias of M_{SHM} with respect to M_{SIM} against the SHM best fit parameters (velocity dispersion (σ), ellipticity (ϵ), and core radius (R_{core})). The results are shown in Figure 3.5. When considering the entire sample (including failed SHMs), we find that the scatter is larger at small and large ϵ , $e\theta_E$, and at large values of R_{core} .

For the models that pass the visual inspection, P-SHM (plotted in orange for comparison), we find no trends in the scatter or bias with any of the model parameters. This plot clearly shows the reduction in the scatter and bias in the P-SHMs when compared to all-SHMs.

The large scatter and high occurrence of F-SHM found in the extreme values of the SHM fit parameters – σ , ϵ , and R_{core} – indicate that during the minimization process the best-fit model was found at the edge of the parameter space. These cases require additional human attention, better parameter exploration, and possibly an increase in the flexibility of the model. These interventions are not allowed in the framework of automated SMH, but are common practice in detailed lensing analyses. The increase in the complexity of the model is usually met with a need of additional constraints. It is expected that the SHM will struggle to reproduce dark matter halos with significantly disturbed morphology or mergers, and converge on, e.g., the highest ellipticity allowed, as shown in the bottom-left panel of Figure 3.1.

We also test the results against the image-plane root-mean-square (r_{msi}), in order to determine whether it could serve as a quantitative indicator of model quality (last panel of Figure 3.6). As expected, we find large scatter and bias in the high r_{msi} bin, attributed to F-SHMs. However, we also find that both all-SHMs and the P-SHMs have high scatter in the lowest r_{msi} bin ($r_{\text{msi}} \approx 1''0$). This behavior is consistent with previous studies. For example, Johnson & Sharon (2016) show that a larger number of constraints lead to a better accuracy in recovering the underlying mass

and magnification, while the $rmsi$ becomes worse. The trend of increased scatter with decreased $rmsi$, and the fact that some F-SHM have low $rmsi$, both indicate that the $rmsi$ does not provide a good indicator of model quality. However, high $rmsi$ values may be useful as an initial triage to remove some of the catastrophic failures before visual inspection.

For reference, if excluding models with $\log(rmsi) > 0.5$, the scatter and bias reduce to 4.8% and 0.65%, respectively, better than the overall sample (8.52%, 0.90%), but not as good as the P-SHM sample (3.26%, 0.34%).

Next, we explore whether the scatter and bias depend on properties of the simulated galaxy cluster – total mass (M_{200c}), concentration (c_{200c}), cluster redshift (z_L), and background sources redshift (z_S). The results are shown in Figure 3.6. We find a flat trend in the scatter and bias with respect to all of the cluster and background source properties for both the SHMs (including F-SHMs) and P-SHMs. This exploration of the scatter and bias is crucial for future studies, that may use the M_{SHM} method to measure the core mass and combine it with a large scale mass proxy to measure, e.g., the concentration of an ensemble of galaxy clusters. Based on this result, we conclude that using M_{SHM} to measure core masses will not bias such future work.

3.6 The Effect of the Background Source Redshift and the Lensing Configuration of the Arcs

In this section, we investigate the effect on the Single-Halo model and the aperture mass enclosed by the effective Einstein radius of the SHM due to the background source redshift, lensing configuration of the arcs, and addition of a second lensed image system. Here we do not exclude the F-SHMs from the analysis.

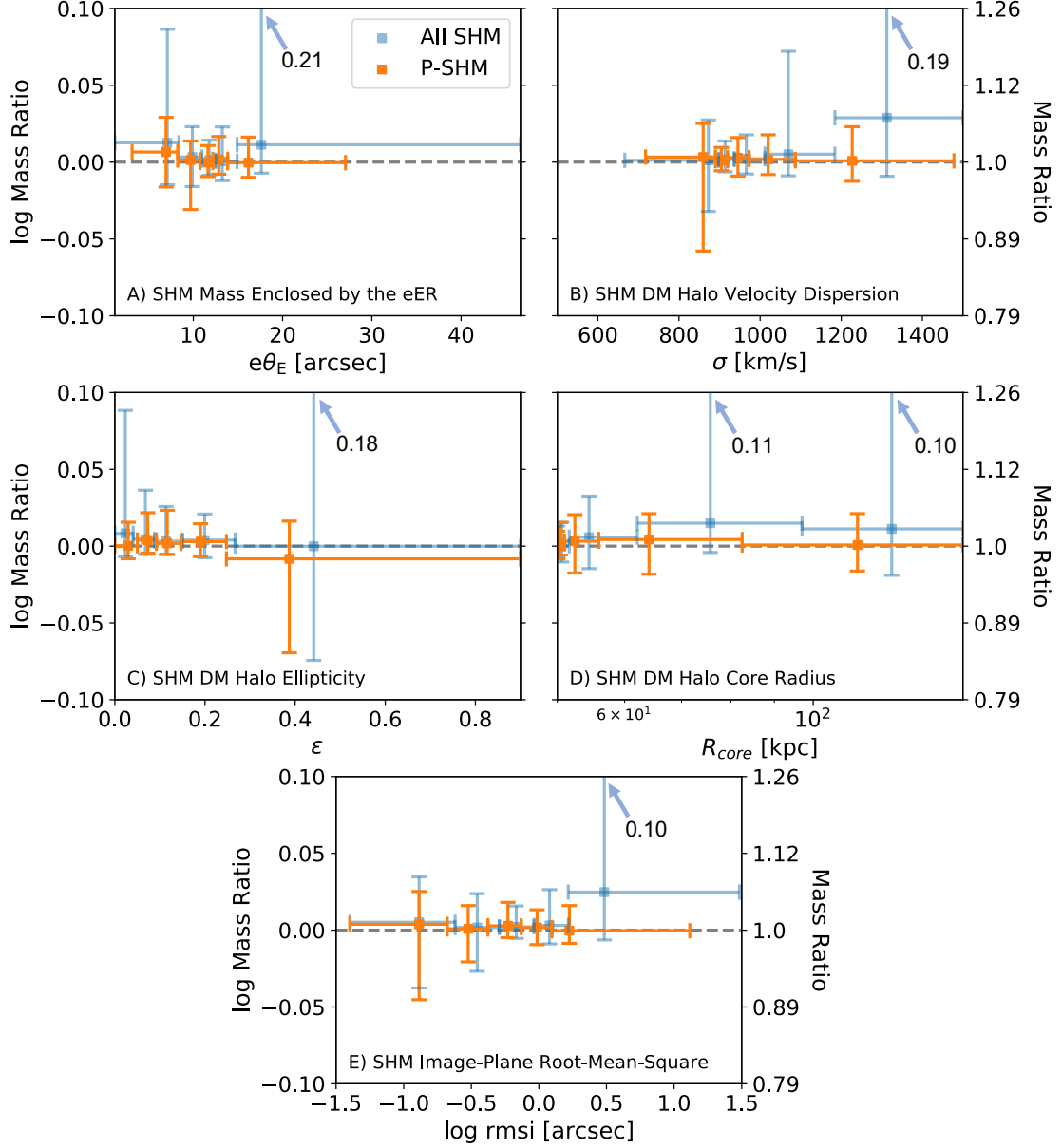


Figure 3.5: **Mass Ratio ($M_{\text{SHM}}/M_{\text{SIM}}$) Binned by the SHM Best Fit Parameters.** Mass ratio, binned by the effective Einstein radius ($e\theta_E$, panel A), dark matter (DM) halo model velocity dispersion (σ , panel B), DM halo model ellipticity (ϵ , panel C), DM halo model core radius (R_{core} , panel D), and the image-plane root-mean-square (rmsi, panel E). The symbol marks the median of the distribution of the mass ratio, the horizontal error bars indicate the bin size (selected such that there is an equal number of SHMs per bin), and the vertical error bars represent the 16th and 84th percentile. We plot the results for all SHMs (blue) and only P-SHMs (orange) for comparison. We find that the P-SHMs have no bias, and a smaller scatter than un-inspected sample (all SHMs). Without eliminating the failed models, the scatter is higher overall; it increases with the extreme (low and high) values of model parameters. See Section 3.5.1 for discussion.

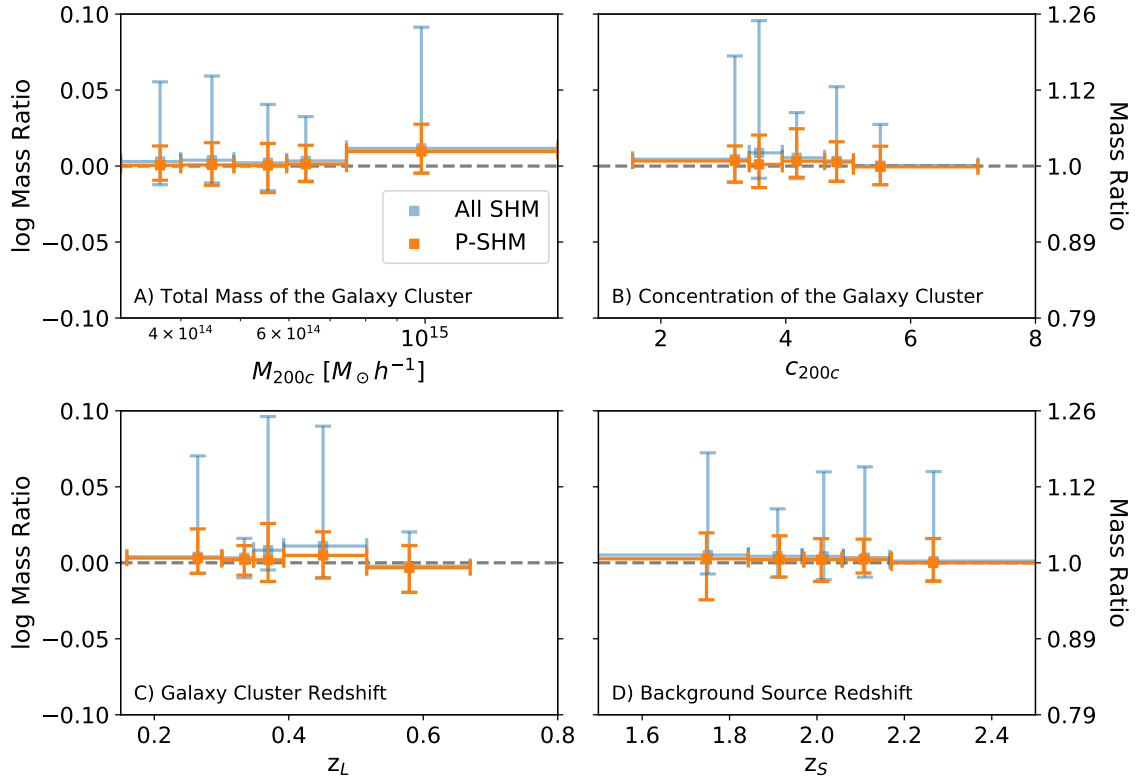


Figure 3.6: **Mass Ratio ($M_{\text{SHM}}/M_{\text{SIM}}$) Binned by the Lens-Background-Source System Properties.** The mass ratio binned by the total mass (M_{200c} , panel A), concentration (c_{200c} , panel B), galaxy cluster redshift (z_L , panel C), and background source redshift (z_S , panel D) are plotted for all SHMs (blue) and the P-SHMs (orange). The symbol marks the median of the distribution of the mass ratio, the horizontal error bars indicate the bin size (equal number of SHMs per bin), and the vertical error bars represent the 16th and 84th percentile. We find no trend in the scatter and bias with respect to any of the simulated cluster and background source properties for neither all SHMs nor P-SHMs.

3.6.1 Effects of the Background Source Redshift (z_s) on M_{SHM}

When a secure spectroscopic redshift of a lensed galaxy is not available, lens modelers often leave the source redshift as a free parameter, sometimes using its photometric redshift as prior. By leaving the background source redshift as a free parameter in our test models, the number of degrees of freedom increases to seven, requiring seven or more constraints. This is satisfied by 895 ray-traced images in our overall simulated sample. We apply a broad uniform prior on the background source redshift, $1 \leq z_s \leq 5$. From the computed models, we find that the model-predicted redshifts are on average 1.9 times higher than the true redshifts. We measure a scatter of 9.85% with a bias of -7.22% on the mass estimate M_{SHM} . The M_{SHM} , when no background source redshift is known, underestimates the true aperture mass enclosed by the effective Einstein radius and the scatter increases. This effect shows the degeneracy between the derived mass and the background source redshift, and highlights the importance of securing spectroscopic redshifts of background sources for the accuracy of lens models.

3.6.2 Effects of the Lensing Configuration on M_{SHM}

We explore the effect of the lensing configuration of the simulated images on the accuracy of the SHMs, as different configurations provide different constraining power. We inspect each of the simulated lensed images and sort them into eight groups of similar lensing geometry. A representative example of each of the groups is shown in Figure 3.7, along with the number of simulated images in each group. Systems in Group A typically have five images: a merging pair forming a tangential arc, a counter image, and a clearly observable pair of radial arcs. Systems in Group B show a single merging tangential arc and a clearly observable pair of radial arcs. Systems in Group C have a similar configuration to group A, without visible radial arcs. Systems in Group D have a single arc similar to group B, but without visible

radial arcs. Systems in Group E, have a tangential arc made of a merging pair and a counter image, but unlike group A only a single radial arc is identified. Group F includes the Einstein ring configuration. Systems in Group G have a set of radial and tangential arcs close to each other and an additional counter image. Group H systems form a merging pair of radial arcs and a single tangential arc.

The SL configuration group that has the most F-SHMs is group D (a single tangential arc); out of the 161 lensed images with this configuration, 117 ($\sim 73\%$) are F-SHMs and 44 ($\sim 27\%$) are P-SHMs. This group accounts for more than half of the 201 total F-SHMs. This lensing configuration, of a single giant arc, provides the least geometrical constraining power, as it leaves regions of the lens plane with no constraints. Since the model is only locally constrained, lensing configurations in which the single halo is oriented approximately perpendicular to the orientation of the underlying mass distribution are allowed; models that have constrains only on one side of the center of mass suffer from high degeneracy between the halo position, its ellipticity, and velocity dispersion. Such low constraining power is also reported in some observed systems with single giant arcs in Sharon et al. (2020). The low constraining power can therefore result in unphysical SHMs and an unreliable measurement of the mass enclosed by the effective Einstein radius. Excluding the 161 single-arc images from the full sample, the scatter and bias reduce to 3.88% and 0.84% respectively, significantly improving upon the scatter of the full sample (scatter: 8.52%, bias: 0.90%), and close to the precision of the P-SHM only sample (scatter: 3.26%, bias: 0.34%).

Some of the challenges inherent to using a single giant arc as the only constraint can be mitigated by obtaining more lensing constraints (see Section 3.6.3), which often requires higher resolution or deeper imaging. Some of these failed cases can be recovered with a more involved analysis, manual inspection of the parameter space, inclusion of physically-motivated priors (such as an upper-limit on the velocity dispersion based cluster richness). As noted in Section 3.5.1, these interventions are









<p>A</p>  <p>171 (165)</p>	<p>B</p>  <p>128 (99)</p>	<p>C</p>  <p>119 (92)</p>	<p>D</p>  <p>161 (44)</p>
<p>E</p>  <p>216 (208)</p>	<p>F</p>  <p>37 (36)</p>	<p>G</p>  <p>72 (68)</p>	<p>H</p>  <p>34 (25)</p>

Figure 3.7: **Strong Lensing Geometric Configurations of Arcs.** Examples of the groups of the simulated SL geometric configurations of the arcs. Each image is 1.0 arcminute on the side. In the bottom left corner of every panel we indicate the total number of simulated images in that group and in parenthesis the number of SHMs that pass visual inspection. See Section 3.6.2 for a description of the different groups.

beyond the framework of the quasi-automated SHM.

3.6.3 Constraining Power of Secondary Lensed Image Systems

Last, we investigate the constraining power of a secondary lensed source system. The SHM benefits from the addition of a lensed system when these new constraints complement the geometrical constraints of the primary image system and the mass distribution. The increase in constraining power at the core of the galaxy cluster benefits lensed systems with a single giant arc (Group D) where the arc coverage is limited to one side of the cluster.

For example, when adding a secondary lensed system (of any non-D group) to failed lens models of group D, 53% of these formerly F-SHM pass the visual inspection and become P-SHM. This behavior illustrates the importance of identifying additional lensed images to help constrain the lens models. On the other hand, about a third of

the failed D models did not benefit from adding a secondary system, even though the SHM produced a passing model when using only that second system as constraints. A further inspection of these failed models indicates that in these particular cases, the lensing geometry of the D arc was so hard for a single-halo model to reproduce that it forced the model to converge on a failed solution. Such configurations will likely require more involved lensing analysis, possibly with higher flexibility in the lens model or imposing user-identified priors beyond the automated SHM process.

3.7 Conclusions

We explore the use of Single-Halo models as an automated tool to efficiently estimate the mass at the core of SL galaxy clusters. The SHM can be automatically computed once the arcs have been identified and background source redshift measured. This method uses the parametric lensing algorithm `Lenstool` with a single dark matter halo, represented by a dPIE. The constraints used are the lens redshift, the positions of the lensed images, and their source redshift. An initial halo center position (e.g. the BCG) is also needed as an input. To characterize the scatter and bias in the estimator, we use ray-traced simulated images from the state-of-the-art Outer Rim simulation. We compute the SHM, measure the aperture mass enclosed by the effective Einstein radius (M_{SHM}), and compare the mass estimate to the mass from the simulation, measured within the same aperture, (M_{SIM}). We conclude the following:

- Considering the entire sample, the scatter of M_{SHM} is 8.52% with a bias of 0.90% compared to the true mass, M_{SIM} .
- A quick visual inspection of the single halo models reveals that some fail to reproduce the lensing configuration or lead to unphysical lens models. Excluding the failed SHMs (F-SHM) reduces the scatter and bias to 3.26% and 0.34%,

respectively.

- We find that the scatter is larger at small and large values of the ellipticity (ϵ) and effective Einstein radius ($e\theta_E$), and large values of the core radius (R_{core}). Excluding the F-SHMs eliminates this trend.
- We find a weak increasing trend in the bias with the SHM velocity dispersion (σ), and a larger scatter at larger σ . Excluding the F-SHMs eliminates this trend.
- We find no significant dependence on the bias and scatter of M_{SHM} with respect to the properties of the lens-source system – total mass, concentration, lens redshift, and source redshift. This exploration is crucial for future studies, that may use the M_{SHM} method to measure the core mass and combine it with a large scale mass proxy to measure, e.g., the concentration of an ensemble of galaxy clusters. Based on this result, we conclude that using M_{SHM} to measure core masses will not bias such future work.
- A high *rmsi* can be used to identify and eliminate some of the worst cases of F-SHM, before the visual inspection; but on its own, it is an insufficient predictor of the SHM model quality.
- When the background source redshift is unknown, lens modelers frequently use priors on the source redshift and set the redshift as a free parameter in the lens model. We use a broad uniform prior on the source redshift and find that the model-predicted redshifts are overestimated, leading to an underestimate of the mass. When the source redshift is unknown the scatter and bias M_{SHM} are 9.85% and -7.22% compared to M_{SIM} respectively. Our analysis affirms the importance of securing spectroscopic redshifts or high-quality photometric redshifts for the lensing constraints, in order to obtain a precise and accurate

mass measurement. This is consistent with findings by e.g., Caminha et al. (2016); Johnson & Sharon (2016).

- The lensing configuration affects the efficacy of the SHM. We find that a single arc configuration (group D) provides the least constraining power and accounts for most of the extreme outliers. Excluding these systems, we compute a scatter and bias on M_{SHM} of 3.88% and 0.84% against M_{SIM} , respectively.
- The addition of a second lensed source helps constrain the lens model and particularly benefits lens models where the geometrical configuration of the arcs has limited constraining power at the core of the SL galaxy clusters (group D). It is therefore most cost-effective to follow-up systems with a single arc with deeper or high resolution imaging, in order to secure additional lensing constraints. However, some lensing configurations may require a more complex lens modeling process than the SHM.

In the future, new tools will expedite the current manual process of strong lensing analysis. Examples include the introduction of convolutional neural networks for identification of strong lensing features (e.g., Petrillo et al. 2017; Jacobs et al. 2019; Cañameras et al. 2020; Huang et al. 2021), and machine learning algorithms to model the mass distribution of strong lenses (e.g., Bom et al. 2019; Pearson et al. 2019). We look forward to the continuous development of these tools as the Single-Halo models introduced in this work will greatly benefit from them.

The evaluation of M_{SHM} presented in this work, facilitates the use of this efficient mass estimate at the core of SL galaxy clusters, and enables an automated measurement of the core mass in the large samples of strong lensing clusters from current and future surveys.

CHAPTER IV

Core Mass Estimates in Strong Lensing Galaxy Clusters Comparing Detailed Lens Models, Single-Halo Lens Models, and Einstein Radius

Preface

This chapter has been adapted from a paper of the same title submitted for peer-review to the *Astrophysical Journal*, and made available through the arXiv (Remolina González et al., 2021a), with co-authors K. Sharon, G. Mahler, C. Fox, C. A. Garcia Diaz, K. Napier, L. E. Bleem, M. D. Gladders, N. Li, and A. Niemic. The paper is adapted and partially reproduced here under the non-exclusive license of republication granted by the arXiv to the paper authors.

For this project, I take the work from the previous two chapters from simulations to observations. I computed the core masses using the mass enclosed by the Einstein radius and the Single-Halo Lens Model for a large sample of 67 observed strong lensing galaxy clusters. I utilized 144 publicly available detailed lens model to compare the mass estimates. I performed all of the analysis shown with the feedback from the co-authors. I produced all of the figures and tables presented in the paper. I wrote nearly the whole text with the feedback and suggestions from the co-authors.

Some of the High Level Science Products (HLSP) presented in this chapter were

obtained from the Mikulski Archive for Space Telescopes (MAST). STScI is operated by the Association of Universities for Research in Astronomy, Inc., under NASA contract NAS5-26555. We thank the HFF, RELICS, CLASH, and SGAS projects for making their lens models publicly available.

Abstract

The core mass of galaxy clusters is both an important anchor of the radial mass distribution profile and probe of structure formation. With thousands of strong lensing galaxy clusters being discovered by current and upcoming surveys, timely, efficient, and accurate core mass estimates are needed. We assess the results of two efficient methods to estimate the core mass of strong lensing clusters: the mass enclosed by the Einstein radius ($M_{corr}(< \theta_E)$; Remolina González et al. 2020; Chapter II), and single-halo lens model ($M_{SHM}(< e\theta_E)$; Remolina González et al. 2021a; Chapter III), against measurements from publicly available detailed lens models (M_{DLM}) of the same clusters. We use publicly available lens models from the Sloan Giant Arc Survey, the Reionization Lensing Cluster Survey, the *Hubble* Frontier Fields, and the Cluster Lensing and Supernova Survey with *Hubble*. We find a scatter of 18.1% (9.0%) with a bias of -7.1% (1.0%) between $M_{corr}(< \theta_E)$ ($M_{SHM}(< e\theta_E)$) and M_{DLM} . Last, we compare the statistical uncertainties measured in this work to those from simulations. This work demonstrates the successful application of these methods to observational data. As the effort to efficiently model the mass distribution of strong lensing galaxy clusters continues, we are in need of fast and reliable methods to advance the field.

4.1 Introduction

Galaxy clusters are harbored at the knots of the cosmic web and trace the large-scale structure of the universe, making them ideal cosmic laboratories (see reviews by

Allen et al. 2011 and Mantz et al. 2014). The galaxy cluster mass function connects the underlying cosmology and the observational properties of galaxy clusters (e.g., Evrard et al. 2002; Pratt et al. 2019; Bocquet et al. 2020). Additional predictions from cosmological simulations include the radial mass distribution of dark matter halos (e.g., Duffy et al. 2008; Meneghetti et al. 2014; Child et al. 2018), which can be directly tested against observations via the concentration measurement (e.g., Oguri et al. 2012; Merten et al. 2015). An accurate account of the cluster mass distribution requires mass estimates that are sensitive at the cores and at the outskirts of the galaxy cluster. Crucial to all cluster-based cosmological studies are the sample size, selection function, and good understanding of the systematic uncertainties of the mass estimates coming from observed astrophysical properties (e.g., Evrard et al. 2002; Khedekar & Majumdar 2013; Huterer & Shafer 2018; Bocquet et al. 2019).

One of the methods to measure the total (dark and baryonic) mass distribution of galaxy clusters is using gravitational lensing. Weak lensing (WL) measures the cluster mass at large cluster-centric radii, while strong lensing (SL) has the highest resolution at the core of the cluster where the SL evidence is present. The combination of the core mass estimates from SL and outskirts mass estimates from WL or other large scale mass proxies can constrain the mass distribution profile of a galaxy cluster, and measure its concentration (e.g., Gralla et al. 2011; Oguri et al. 2012; Merten et al. 2015; Meneghetti et al. 2010). Comparisons between the predicted and observed properties of SL galaxy clusters mass distribution have reported possible tension (e.g., Broadhurst & Barkana 2008; Gonzalez et al. 2012; Meneghetti et al. 2013; Killedar et al. 2018), however these studies have been limited by complicated selection function and small sample sizes.

Current and upcoming large surveys will discover thousands of SL clusters out to $z \sim 2$, using methods that span the wavelength spectrum. Some of these surveys include the South Pole Telescope (SPT; SPT-3G, Benson et al. 2014; SPT-SZ 2500

deg², Bleem et al. 2015), Vera Rubin Observatory Legacy Survey of Space and Time (LSST, LSST Science Collaboration et al. 2017), and eROSITA (Pillepich et al., 2018). These large samples will require a method to timely, effectively, and accurately measure the core mass of SL clusters.

Strong-lensing based mass measurements are typically based on detailed strong lensing models (e.g., Kneib & Natarajan 2011). Detailed lens models for galaxy clusters with rich strong lensing evidence, such as the Frontier Fields clusters (Lotz et al., 2017) but also less extraordinary clusters, allow for the high degree of complexity required to study substructure in the mass distribution of the cluster (e.g., Ebeling et al. 2017; Mahler et al. 2018; Richard et al. 2020). They necessitate extensive follow-up observations, computational resources, and multiple statistical assessments for the best model selection. However, more typical SL clusters have a small number of SL constraints, which limits the utility of detailed lens models (e.g., Smith et al. 2005; Sharon et al. 2020).

The large sample sizes of SL clusters being discovered calls for efficient methods to estimate the mass at the core of galaxy clusters. Remolina González et al. (2020), Chapter II, and Remolina González et al. (2021a), Chapter III, evaluated two methods for efficiently estimating the mass within the core of SL clusters using the Outer Rim cosmological simulation. Remolina González et al. (2020), Chapter II, evaluated the mass estimate derived from the size of the Einstein radius; Remolina González et al. (2021a), Chapter III, assessed results from simplified single-halo lens models. The characterization of uncertainty and bias of these methods established them for the application to large samples of SL galaxy clusters as efficient and accurate galaxy cluster core mass estimators. The two simulation-calibrated methods take orders of magnitude less time and human intervention than detailed lens models.

The goal of this chapter is to test, in real observed clusters, how well these first- and second-order estimates of the core mass compare to detailed lens models. This

chapter is organized as follows. In Section 4.2, we introduce the three strong lensing cluster samples used in our chapter and describe our selection of the detailed lens models. In Section 4.3, we briefly describe the publicly available lensing algorithms used to compute the detailed lens models and summarize the single-halo lens model and Einstein radius methods used as efficient estimates of the mass at the core of galaxy clusters. In Section 4.4, we describe the strong lensing constraints and selection of the brightest cluster galaxy (BCG), and compute the empirically-corrected mass enclosed by the Einstein radius ($M_{corr}(< \theta_E)$) and the aperture mass enclosed by the effective Einstein radius ($M_{SHM}(< e\theta_E)$) from the single-halo lens models that passed a quick visual inspection. In Section 4.5, we measure the scatter and bias of $M_{corr}(< \theta_E)$ and $M_{SHM}(< e\theta_E)$ compared to the mass enclosed by the same aperture in the detailed lens model (M_{DLM}) and explore any possible difference due to the variety of lensing algorithms utilized to compute the detailed lens models. Last in Section 4.6, we present our conclusions and summarize the application of efficient methods to measure the core masses of galaxy clusters.

In our analysis, we adopt a flat Λ CDM cosmology: $\Omega_\Lambda = 0.7$, $\Omega_M = 0.3$, and $H_0 = 70 \text{ km s}^{-1} \text{ Mpc}^{-1}$, which was used by most of the detailed lens models included in our analysis. The GLAFIC detailed lens models of the RELICS clusters follow a Wilkinson Microwave Anisotropy Probe Cosmology (Komatsu et al., 2011): $\Omega_\Lambda = 0.728$, $\Omega_M = 0.272$, and $H_0 = 70.4 \text{ km s}^{-1} \text{ Mpc}^{-1}$. The large scale masses are reported in terms of $M_{\Delta c}$, defined as the mass enclosed within a radius at which the average density is Δ times the critical density of the universe at the cluster redshift.

4.2 Observational Data

For this work, we use the data from four well-established strong lensing surveys of clusters with different selection functions. First, the Sloan Giant Arcs Survey

(SGAS¹; Hennawi et al. 2008; Sharon et al. 2020) which identified highly magnified lensed galaxies in the Sloan Digital Sky Survey (SDSS; Abazajian et al. 2009; Blanton et al. 2017). Second, the Cluster Lensing and Supernova Survey with *Hubble* (CLASH²; Postman et al. 2012), designed to study the dark matter distribution in galaxy clusters, perform supernova searches, and detect and characterize high-redshift lensed galaxy clusters. Third, the *Hubble* Frontier Fields Clusters (HFF³; Lotz et al. 2017) which are some of the best strong lensing clusters, taking advantage of deep imaging and extensive spectroscopic follow-up. Fourth, the Reionization Lensing Cluster Survey (RELICS⁴; Coe et al. 2019), designed primarily to find high-redshift ($z \sim 6 - 8$) lensed galaxy candidates. All four samples base their lensing analyses on multiband *Hubble Space Telescope* (*HST*) imaging. From these samples of lensing galaxy clusters, we only include clusters with spectroscopically confirmed multiply imaged lensed galaxies. Figure 4.1 shows the redshift-mass distribution of the galaxy clusters used in our analysis. The large scale masses, M_{500c} , are taken from Fox et al. (2021), Merten et al. (2015), and references therein.

4.2.1 SGAS

Galaxy clusters were selected for the SGAS survey from the SDSS Data Release 7 (SDSS-DR7; Abazajian et al. 2009) using the cluster red-sequence algorithm by Gladders & Yee (2000). Color images were created from imaging data in g , r , i , and z centered on the detected cluster. The images were visually inspected and scored according to the evidence of strong gravitational lensing. There has been extensive ground- and space-based imaging leading to a multi-wavelength picture of these clusters (e.g., 107 *HST* orbits of the SGAS-*HST*, GO13003 PI:Gladders; Sharon et al. 2020). Spectroscopic follow-up of all the primary strong lensing arcs is complete,

¹<https://archive.stsci.edu/pub/hlsp/sgas/>

²<https://www.stsci.edu/postman/CLASH/index.html>

³<https://outerspace.stsci.edu/display/HPR/HST+Frontier+Fields>

⁴<https://relics.stsci.edu/index.html>

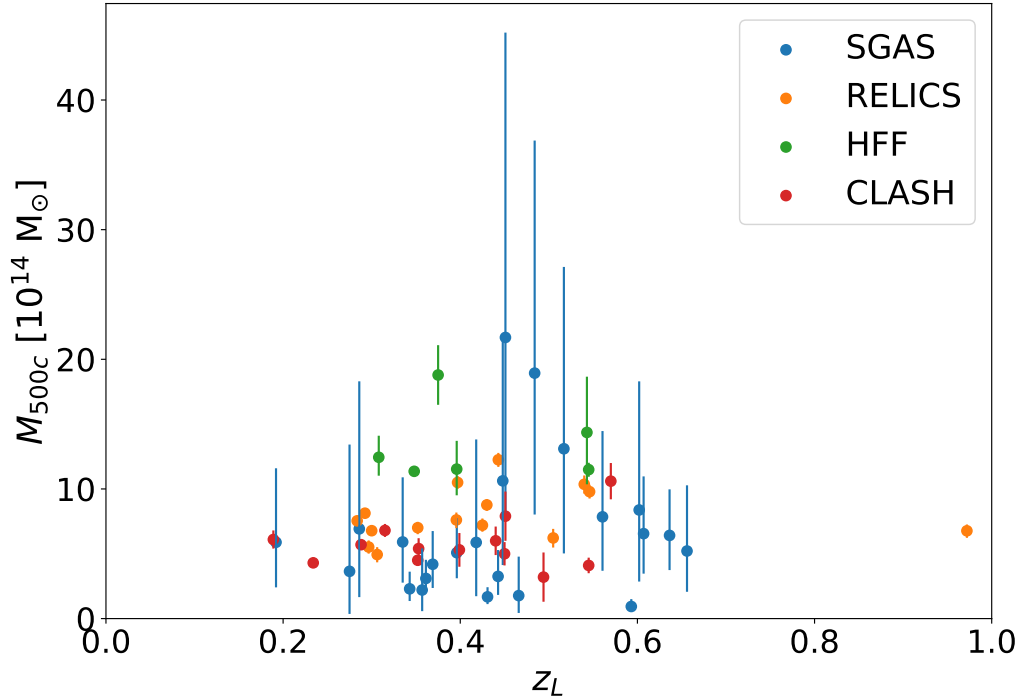


Figure 4.1: Redshift-Mass ($z_L - M_{500c}$) distribution of the strong lensing galaxy clusters used in our analysis.

and additional follow-up campaigns obtained redshifts of secondary arcs to improve the fidelity of the lens models (e.g., Bayliss et al. 2011b; Johnson et al. 2017a; Sharon et al. 2020, and references therein). Several high-impact targets out of this sample of highly magnified arcs have been studied in detail (e.g., Koester et al. 2010; Bayliss et al. 2014; Sharon et al. 2017; Rigby et al. 2018).

The SGAS clusters are unique due to the selection function employed to create the sample, as they were selected uniquely based on the identification of bright strong lensing features. This led to including some clusters with lower masses when compared to the other three samples of galaxy clusters. Sharon et al. (2020) published and released to the community detailed lens models for the 37 SGAS clusters observed as part of *HST*-GO13003. Out of these 37 galaxy clusters with publicly available lens models (Sharon et al., 2020), we only use 31 in this work. Three clusters (SDSS J0004−0103, SDSS J1002+2031, and SDSS J1527+0652) are not in-

cluded due to being poorly constrained (given a classification of C or lower; see Sharon et al. (2020) for more details). Two galaxy clusters (SDSS J1156+1911 and SDSS J1632+3500) lack any spectroscopically confirmed multiply imaged sources. One galaxy cluster (SDSS J2243–0935), has one spectroscopically confirmed flat giant arc, located between two cluster cores, making it unsuitable for the methods used here. In Table 4.1, the list of the SGAS clusters is shown with their corresponding redshift, the right ascension (R.A.) and declination (Decl.) of the selected BCG, and the number of strongly lensed background sources with spectroscopic redshifts that are used as lens modeling constraints.

4.2.2 CLASH

The Cluster Lensing and Supernova Survey with *Hubble* (CLASH; Postman et al. 2012) multi-cycle treasury project observed 25 galaxy clusters for a total of 525 *HST* orbits over a period of nearly three years utilizing 16 *HST* filters. The main science goals included: studying the matter distribution of galaxy clusters, particularly the mass concentration (e.g., Merten et al. 2015); detecting supernovae (e.g., Graur et al. 2014); and detecting and characterizing high-redshift galaxies magnified by the galaxy cluster (e.g., Coe et al. 2013). From the 25 galaxy clusters, 20 are X-ray selected, dynamically relaxed (determined from their circularly symmetric X-ray surface brightness distribution), and massive clusters (X-ray temperatures $T_x > 5$ keV). The majority of these clusters showed strong lensing evidence from ancillary data. The last five galaxy clusters were selected solely for being exceptional strong lenses. Four of the galaxy clusters (Abell S1063, MACS J0416.1–2403, MACS J0717.5+3745, and MACS J1149.5+2223) were later selected for the Hubble Frontier Fields (HFF; see Section 4.2.3) and we only utilize the HFF lens models for these clusters. The community follow-up effort has resulted in the identification of many lensing constraints with measured spectroscopic redshifts for the 13 galaxy clusters included in

this work. Detailed lensing models by Zitrin et al. (2015) and Caminha et al. (2019) have been made publicly available. In Table 4.1, we list the CLASH galaxy clusters utilized in our analysis and their corresponding references.

4.2.3 HFF

The *Hubble* Frontier Fields (HFF; Lotz et al. 2017) project observed six galaxy clusters and adjacent (“parallel”) fields using Director’s discretionary time, obtaining extremely deep multi-band imaging (140 *HST* orbits per cluster for a total of 840 *HST* orbits of Director’s Discretionary Time) with the primary goal of studying the magnified background universe. The clusters were selected for their observability from space- (*HST*, *Spitzer*, and *JWST*) and ground-based observatories, their lensing strength, and the availability of pre-existing ancillary data. These galaxy clusters have become some of the most studied galaxy clusters due to the community investment in extensive multi-wavelength imaging and spectroscopic follow-up, resulting in large numbers of strong lensing constraints identified and used in the detailed lens models (Johnson et al. 2014; Zitrin et al. 2014; Diego et al. 2016; Jauzac et al. 2016; Limousin et al. 2016; Caminha et al. 2017; Karman et al. 2017; Kawamata et al. 2018; Mahler et al. 2018; Strait et al. 2018; Lagattuta et al. 2019; Sebesta et al. 2019; Vega-Ferrero et al. 2019; Raney et al. 2020a; and references therein). The HFF program provides a unique opportunity to study the statistical and systematic uncertainties in the lensing outputs, due to the large number of diverse lensing algorithms that have computed detailed lens models of these clusters (e.g., Meneghetti et al. 2017; Prieue et al. 2017; Remolina González et al. 2018; Raney et al. 2020b compare different aspects of the HFF lens models using different algorithms). In this work, we include the fourth version of the public lens models, which is the most recent release. The clusters and references to the models are listed in Table 4.1.

4.2.4 RELICS

The RELICS program selected 41 galaxy clusters for shallow multi-band observation with *HST* for the primary goal to deliver a large sample of high-redshift ($z \sim 6 - 8$) galaxies (Salmon et al., 2018, 2020; Mainali et al., 2020; Strait et al., 2020). 21 clusters were selected from a subsample of the most massive Planck clusters (using the Sunyaev-Zeldovich effect, Sunyaev & Zeldovich 1970, to estimate their mass; Planck Collaboration et al. 2016). The other 20 clusters were selected based on a prior identification as prominent strong lenses in available imaging data. The reasoning used for this selection is the expectation that the mass of the galaxy cluster relates to its potential to have a large lensing cross-section, leading to an increase in the chance to find high-redshift lensed sources.

The selection function employed for assembling the list of RELICS clusters explores the high-mass parameter space. In addition, the wider and shallower imaging observing strategy (total of 188 *HST* orbits, GO 14096; PI Coe) is a clear example of the challenges confronted by lensing surveys where only the primary and some of the secondary arcs are readily identifiable, leading to a limited number of constraints available for the lens modeling analysis (Acebron et al. 2018, 2019, 2020; Cerny et al. 2018; Cibirka et al. 2018; Paterno-Mahler et al. 2018; Mahler et al. 2019 and references therein). From the 41 galaxy clusters observed, 34 have publicly available detailed lens models and only 17 have publicly available spectroscopically confirmed multiple imaged sources. Following Fox et al. (2021), we inspect the unpublished detailed lens models and include in our analysis only models whose predicted lensed images are within $1''.5$ of the observed lensing evidence, and do not produce critical curves or masses that are not justified by the lensing constraints. In Table 4.1, we present the list of the RELICS clusters used in our analysis with their corresponding lens redshift, R.A. and Decl. of the selected BCG, and the number of background source spectroscopic redshifts that were used to constrain $M_{corr}(< \theta_E)$ and $M_{SHM}(< e\theta_E)$ in

this chapter.

Table 4.1: Strong Lensing Galaxy Clusters.

Galaxy Cluster	z_L	R.A. (J2000)	Decl. (J2000)	Detailed Lens Models	$N(z_S)$	Arcs/Model	Reference
SGAS							
SDSS J0108+0624	0.548	17.17511	6.41210	L	1	a,b	
SDSS J0146-0929	0.447	26.73336	-9.49792	L	2	a,c	
SDSS J0150+2725	0.306	27.50355	27.42676	L	1	a	
SDSS J0333-0651	0.573	53.26940	-6.85635	L	1	a	
SDSS J0851+3331	0.369	132.91194	33.51837	L	3	a,d	
SDSS J0915+3826	0.396	138.91280	38.44952	L	2	a,d,e	
SDSS J0928+2031	0.192	142.01889	20.52919	L	2	a	
SDSS J0952+3434	0.357	148.16761	34.57947	L	1	a,f	
SDSS J0957+0509	0.448	149.41330	5.15885	L	1	a,d	
SDSS J1038+4849	0.431	159.68159	48.82159	L	3	a,d	
SDSS J1050+0017	0.593	162.66637	0.28522	L	3	a,g	

Table 4.1: Strong Lensing Galaxy Clusters (cont'd).

Galaxy Cluster	z_L	R.A. (J2000)	Decl. (J2000)	Detailed Lens Models	$N(z_S)$	Arcs/Model	Reference
SDSS J1055+5547	0.466	163.76917	55.80647	L	2	a,d	
SDSS J1110+6459	0.656	167.57386	64.99664	L	1	a,c,h	
SDSS J1115+1645	0.537	168.76845	16.76058	L	2	a,c,i	
SDSS J1138+2754	0.451	174.53731	27.90854	L	2	a,d	
SDSS J1152+0930	0.517	178.19748	9.50409	L	1	a	
SDSS J1152+3313	0.361	178.00077	33.22827	L	2	a,d	
SDSS J1207+5254	0.275	181.89965	52.91644	L	1	a,f	
SDSS J1209+2640	0.561	182.34877	26.67950	L	2	a,d,j	
SDSS J1329+2243	0.443	202.39391	22.72106	L	1	a,g	
SDSS J1336-0331	0.176	204.00035	-3.52496	L	2	a	
SDSS J1343+4155	0.418	205.88685	41.91763	L	1	a,d,k	
SDSS J1420+3955	0.607	215.16680	39.91859	L	2	a,d	
SDSS J1439+1208	0.427	219.79076	12.14043	L	2	a	
SDSS J1456+5702	0.484	224.00368	57.03898	L	1	a	

Table 4.1: Strong Lensing Galaxy Clusters (cont'd).

Galaxy Cluster	z_L	R.A. (J2000)	Decl. (J2000)	Detailed Lens Models	$N(z_S)$	Arcs/Model	Reference
SDSS J1522+2535	0.602	230.71985	25.59097	L	1	a	
SDSS J1531+3414	0.335	232.79429	34.24031	L	2	a,d	
SDSS J1604+2244	0.286	241.04227	22.73858	L	1	a	
SDSS J1621+0607	0.343	245.38494	6.12197	L	2	a,d	
SDSS J1723+3411	0.442	260.90068	34.19948	L	2	a,f	
SDSS J2111-0114	0.636	317.83062	-1.23984	L	1	a,d	
CLASH							
Abell 383	0.189	42.01409	-3.52938	LTM.v2, NFW.v2	4	l,n,s,t,u	
Abell 611	0.288	120.23673	36.05656	LTM.v2, NFW.v2	2	l,v	
MACS J0329.7-0211	0.450	52.42321	-2.19623	L.v1, LTM.v2, NFW.v2	7	l,m,n	
MACS J0416.1-2403	0.396	64.03808	-24.06750	See HFF	37	See HFF	
MACS J0429.6-0253	0.399	67.40003	-2.88521	L.v1, LTM.v2, NFW.v2	2	l,m	
MACS J0717.5+3745	0.545	109.39855	37.75479	See HFF	8	See HFF	

Table 4.1: Strong Lensing Galaxy Clusters (cont'd).

Galaxy Cluster	z_L	R.A. (J2000)	Decl. (J2000)	Detailed Lens Models	$N(z_S)$	Arcs/Model	Reference
MACS J1115.9+0129	0.353	168.96628	1.49861	L.v1, LTM.v2, NFW.v2	2	1,m,n	
MACS J1149.5+2223	0.543	177.39875	22.39853	See HFF	7	See HFF	
MACS J1206.2-0847	0.440	181.55064	-8.80094	LTM.v2, NFW.v2	4	1,n,w,x	
MACS J1311.0-0310	0.494	197.75751	-3.17770	L.v1, LTM.v2, NFW.v2	1	1,m	
MACS J1423.8+2404	0.545	215.94949	24.07846	LTM.v2, NFW.v2	2	1,y	
MACS J1931.8-2635	0.352	292.95684	-26.57587	L.v1, LTM.v2, NFW.v2	7	1,m	
MACS J2129.7-0741	0.570	322.35879	-7.69105	L.v1, LTM.v2, NFW.v2	11	1,m,o	
MS J2137-2353	0.315	325.06316	-23.66114	LTM.v2, NFW.v2	2	1	
RXC J1347.5-1145	0.451	206.88261	-11.75318	L.v1, LTM.v2, NFW.v2	4	1,m,n,p,q,r	
RXC J2129.7+0005	0.234	322.41649	0.08922	L.v1, LTM.v2, NFW.v2	7	1,m	
RXC J2248.7-4431	0.348	342.18321	-44.53089	See HFF (Abell S1063)	18	See HFF (Abell S1063)	
HFF							
Abell 2744	0.308	3.58626	-30.40017	C.v4, C.v4.1, D.v4	26	z,aa,ag,ah,ak,al,am	

Table 4.1: Strong Lensing Galaxy Clusters (cont'd).

Galaxy Cluster	z_L	R.A. (J2000)	Decl. (J2000)	Detailed Lens Models	$N(z_S)$	Arcs/Model	Reference
Abell 370	0.375	39.97133	-1.58224	D.v4.1, G.v4, K.v4 S.v4c, W.v4	32	z, ag, ai, aj, al, am	
Abell S1063	0.348	342.18321	-44.53089	B.v4, B.v4.1, C.v4 D.v4, D.v4.1, G.v4 K.v4, S.v4, W.v4 W.v4.1	18	z, ab, af, ag, al, am	
MACS J0416.1-2403	0.396	64.03808	-24.06750	D.v4.1, G.v4, K.v4 S.v4, W.v4, W.v4.1 Cam.v4, C.v4, C.v4.1	37	z, ae, ag, al, am	
MACS J0717.5+3745	0.545	109.39855	37.75479	D.v4, D.v4.1, G.v4 K.v4, S.v4c, W.v4 C.v4, C.v4.1, D.v4 D.v4.1, K.v4, S.v4c	8	z, ad, al, am	

Table 4.1: Strong Lensing Galaxy Clusters (cont'd).

Galaxy Cluster	z_L	R.A. (J2000)	Decl. (J2000)	Detailed Lens Models	$N(z_S)$	Arcs/Model	Reference
MACS J1149.5+2223	0.543	177.39875	22.39853	W.v4, W.v4.1 C.v4, C.v4.1, D.v4	7	z,ac,al,am	
				D.v4.1, K.v4, S.v4c W.v4			
RELICS							
Abell 2537	0.297	347.09256	-2.19212	L.v1, G.v2	1	an	
Abell 2813	0.292	10.85271	-20.62822	L.v1	1	au	
Abell 3192	0.425	59.72531	-29.92527	L.v1	2	ao	
Abell S295	0.300	41.35339	-53.02932	LTM.v2	1	ap	
CL J0152.7-1357	0.833	28.18242	-13.95515	L.v1, LTM.v1, G.v2	1	aq	
MACS J0025.4-1222	0.586	6.36415	-12.37303	LTM.v1	1	ap	
MACS J0035.4-2015	0.352	8.85889	-20.26229	L.v1, G.v2	2	au	
MACS J0257.1-2325	0.505	44.28647	-23.43468	L.v1, G.v2	1	au	

Table 4.1: Strong Lensing Galaxy Clusters (cont'd).

Galaxy Cluster	z_L	R.A. (J2000)	Decl. (J2000)	Detailed Lens Models	$N(z_S)$	Arcs/Model	Reference
MACS J0417.5-1154	0.443	64.39454	-11.90885	L.v2, G.v3	2	ar	
MACS J0553.4-3342	0.430	88.33069	-33.70754	L.v1, G.v2	1	au	
MS 1008.1-1224	0.306	152.63455	-12.66469	L.v1	2	au	
PLCK G004.5-19.5	0.540	289.27098	-33.52236	L.v1	5	au	
RXC J0018.5+1626	0.546	4.63992	16.43787	L.v1	2	au	
RXC J0032.1+1808	0.396	8.03914	18.11561	L.v1, LTM.v2, G.v2	1	as	
RXC J0232.2-4420	0.284	38.06804	-44.34669	L.v1	1	au	
RXC J2211.7-0350	0.397	332.94137	-3.82895	L.v1, G.v2	1	an	
SPT-CL J0615-5746	0.972	93.96543	-57.78011	L.v1, LTM.v1	2	at	

Table 4.1: Strong Lensing Galaxy Clusters (cont'd).

Galaxy Cluster	z_L	R.A.	Decl.	Detailed Lens Models	$N(z_S)$	Arcs/Model
		(J2000)	(J2000)			Reference

Strong Lensing Galaxy Clusters Included in this Work. z_L is the lens redshift of the galaxy cluster, R.A. and Decl. are the right ascension and declination of the selected BCG, respectively, and $N(z_S)$ is the number of multiply-imaged lensed background sources with spectroscopic redshifts that are used in this chapter. The Detailed Lens Models lists indicate the name of the lens modeling teams or algorithms, and the versions which are utilized for the comparison in this work. A brief description of the samples can be found in Section 4.2: SGAS (see Section 4.2.1), CLASH (see Section 4.2.2), HFF (see Section 4.2.3), and RELICS (see Section 4.2.4).

Detailed Lens Models used in this work (see also Section 4.2):

SGAS: L = `Lenstool`

CLASH: L = `Lenstool`; LTM = `Light-Traces-Mass`; NFW = `LTM + eNFW`; v1 = version 1; v2 = version 2

HFF: B = `Bradać (SWUnited)`; C = `CATS (Lenstool)`; Cam = `Caminha (Lenstool)`; D = `Diego (WSLAP +)`; G = `Glaflc (GLAFIC)`;

K = `Keeton (GRAVLENS)`; S = `Sharon (Lenstool)`; W = `Williams (GRALE)`; v4 = version 4; v4c = version 4 corrected; v4.1 = version 4.1

RELICS: G = `GLAFIC`; L = `Lenstool`; LTM = `Light-Traces-Mass`; v1 = version 1; v2 = version 2; v3 = version 3

References: a) Sharon et al. (2020); b) Rigby et al. (2018); c) Stark et al. (2013); d) Bayliss et al. (2011a); e) Bayliss et al. (2010); f) Kubo et al. (2010); g) Bayliss et al. (2014); h) Johnson et al. (2017a); i) Bayliss (2012); j) Ofek et al. (2008); k) Diehl et al. (2009); l) Zitrin et al. (2015); m) Caminha et al. (2019); n) CLASH-VLT Rosati et al. (in prep); o) Huang et al. (2016); p) Ravindranath & Ho (2002); q) Bradać et al. (2008b); r) Halkola et al. (2008); s) Smith et al. (2001); t) Newman et al. (2011); u) Richard et al. (2011); v) Newman et al. (2013); w) Ebeling et al. (2009); x) Zitrin et al. (2012); y) Limousin et al. (2010); z) Johnson et al. (2014); aa) Zitrin et al. (2014); ab) Diego et al. (2016); ac) Jauzac et al. (2016); ad) Limousin et al. (2016); ae) Caminha et al. (2017); af) Karman et al. (2017); ag) Kawamata et al. (2018); ah) Mahler et al. (2018); ai) Strait et al. (2018); aj) Lagattuta et al. (2019); ak) Sebesta et al. (2019); al) Vega-Ferrero et al. (2019); am) Raney et al. (2020a); an) Cerny et al. (2018); ao) Hsu et al. (2013); ap) Cibirka et al. (2018); aq) Acebron et al. (2019); ar) Mahler et al. (2019); as) Acebron et al. (2020); at) Paterno-Mahler et al. (2018); au) RELICS public data release (see Section 4.2.4).

4.3 Lens Modeling And Einstein Radius

Strong lens modeling analyses use the positional and redshift measurements of lensed galaxies (arcs) as constraints to model the underlying mass distribution. There is a variety of well-established lensing algorithms that have been used extensively to study both the galaxy cluster and the magnified background universe. Below, we provide a brief description of the lensing algorithms that were employed to compute the publicly available detailed lens models used in our analysis. We also briefly describe the Einstein Radius mass estimate, and single-halo lens models, which were recently evaluated by Remolina González et al. (2020), Chapter II, and Remolina González et al. (2021a), Chapter III, respectively, as methods to quickly and effectively measure the mass at the core of strong lensing galaxy clusters.

4.3.1 Detailed Lens Models

Lensing algorithms are usually grouped into three categories: parametric, non-parametric, and hybrid, based on the parametrization of the modeled mass distribution. Parametric models utilize a combination of parametric functions to describe the mass distribution of the lens plane. Non-parametric or “free-form” algorithms make no assumption on the functional form of the mass distribution. Hybrid models are a combination of these two forms. The degree to which mass is assumed to be correlated with the observed light distribution also varies among the different algorithms.

The parametric models that are used in this work include: GLAFIC (Oguri, 2010; Ishigaki et al., 2015; Kawamata et al., 2016), GRAVLENS (Keeton, 2010; McCully et al., 2014), and `Lenstool` (Kneib et al., 1996; Jullo et al., 2007; Jullo & Kneib, 2009; Niemiec et al., 2020). These algorithms use a variety of analytical mass distributions both for the cluster-scale dark matter halos and the contribution of the galaxy cluster members. Light-Traces-Mass (LTM; Broadhurst et al. 2005; Zitrin et al. 2009, 2015) assigns mass to a parameterized description of the light distribution, and LTM with

elliptical NFW profiles (LTM+eNFW; Zitrin et al. 2009, 2015) combines this approach with analytical mass distributions as the parametric models. The “free-form” algorithms include Strong and Weak Lensing United (SWUnited; Bradač et al. 2006, 2009) which performs an iterative minimization of a non-regular adaptive grid and GRALE (Liesenborgs et al., 2006; Mohammed et al., 2014), which uses a genetic algorithm to iteratively refine the mass distribution on a grid. Last, the hybrid algorithm Weak & Strong Lensing Analysis Package (WSLAP+; Diego et al. 2005, 2007, 2016) is a non-parametric algorithm with the addition of a parametrized distribution for the cluster member contribution. Modeling algorithms also differ by their assumptions on the extent of correlation between light and mass. A variety of techniques are employed to explore the parameter space and determine the model that best reproduces the observed lensing configuration, and determine statistical uncertainties.

Detailed lens models (DLM) can be highly complex, adding the flexibility required for detailed studies of galaxy cluster properties, their surrounding environment, uncorrelated structure along the line-of-sight, the magnified background universe, and cosmology. This high complexity of the models relies on a large number of free parameters, requiring a large number of constraints, i.e., multiply-imaged lensed galaxies, whose availability becomes a limiting factor in the modeling process. The versatility of DLM also means the models are not unique and require care in the construction and evaluation; statistical assessments are employed to select between models (e.g., Acebron et al. 2017; Paterno-Mahler et al. 2018; Lagattuta et al. 2019; Mahler et al. 2019). High-fidelity lens models of galaxy clusters with rich strong lensing evidence require extensive follow-up observations, large investment of computational and human resources, and multiple iterations of the lensing analysis and modeling process to revise the models as new observational evidence becomes available (e.g., Sharon et al. 2012; Johnson et al. 2014; Jauzac et al. 2015).

To determine the statistical uncertainties of the public DLM used in this work,

we use the “range” maps that are provided with them. The “range” maps are the same lensing products as the best-fit products, except they are derived from sets of parameters that sample the parameter space of each model, and provide a handle on how the variation in model parameters affects the lensing-derived projected mass density.

4.3.2 Single-Halo Lens Models

The single-halo lens models (SHM) computed in this analysis follows Remolina González et al. (2021a), Chapter III. We use `Lenstool` to compute the SHM in one lens plane with a single cluster-scale dark matter halo. The mass distribution is parameterized using a dual pseudo-isothermal ellipsoid (dPIE, Elíasdóttir et al. 2007) and no contribution from galaxy cluster members. Of the seven dPIE parameters (α and δ are the R.A. and Decl.; ϵ is the ellipticity; θ is the position angle; r_{core} is the core radius; r_{cut} is the truncation radius; and σ is the effective velocity dispersion), only six are optimized as we set the truncating radius to a fixed 1500 kpc as is typically done in DLM in the literature (note that this projected radius is also similar to the splashback radius; e.g., Umetsu & Diemer 2017; Shin et al. 2019). We use broad priors in the six free parameters of the dPIE potential: $-8''.0 < \alpha, \delta < 8''.0$; $0.0 < \epsilon < 0.9$; $0^\circ < \theta < 180^\circ$; $50 \text{ kpc} < r_{core} < 150 \text{ kpc}$; and $500 \text{ km/s} < \sigma < 1500 \text{ km/s}$. The small number of free parameters calls for only a handful of constraints, with a minimum of 6 constraints required. This can be satisfied with as little as 4 multiple images of the same source, as each identified set of n multiple images contributes $2n - 2$ constraints. With the image identification in hand (see Section 4.4.1), the models can be computed quickly and with limited human intervention. Generally, the SHM can be automatically computed once the cluster redshift, center initial position (e.g., the brightest cluster galaxy - BCG), and position and redshift of the arcs are measured.

Remolina González et al. (2021a), Chapter III, used the lensing products from the SHM best fit model to compute the effective Einstein radius, $e\theta_E$, and measure mass enclosed by this aperture, $M_{\text{SHM}}(< e\theta_E)$. The effective Einstein radius is defined as the radius of a circle with the same area as the area enclosed by the tangential critical curve. Remolina González et al. (2021a), Chapter III, found an overall scatter of 8.5% with a bias of 0.9% in $M_{\text{SHM}}(< e\theta_E)$. When a quick visual inspection is performed and only the models that pass the inspection are used, the scatter and bias of $M_{\text{SHM}}(< e\theta_E)$ improve to 3.3% and 0.3%, respectively. The visual inspection is conducted to identify those single-halo lens models that fail to reproduce the observed lensing configuration and predict arcs in regions where no multiple images are found.

4.3.3 Einstein Radius

The mass enclosed by the Einstein radius, $M(< \theta_E)$, is a quick method to estimate cluster core mass, where strong lensing is detected:

$$M(< \theta_E) = \Sigma_{cr}(z_L, z_S) \pi [D_L(z_L)\theta_E]^2, \quad (4.1)$$

where $\Sigma_{cr}(z_L, z_S)$ is the critical surface density, $D_L(z_L)$ is the angular diameter distance from the observer to the lens, z_L is the lens redshift, z_S is the background source redshift, and θ_E is the Einstein radius, which can be measured from the occurrence of arcs around the center of the lens. The main assumption of this method is that the projected mass distribution of the lens is circularly symmetric (Narayan & Bartelmann, 1996; Schneider, 2006; Kochanek, 2006; Bartelmann, 2010; Kneib & Natarajan, 2011).

Remolina González et al. (2020), Chapter II, quantified the scatter and bias of the mass enclosed by the Einstein radius and introduced empirical corrections based on simulations. The method was calibrated for Einstein radii $\leq 30''$, for different centering assumptions. The corrected mass enclosed by the Einstein radius, $M_{corr}(<$

θ_E), is reported to have no bias, and a scatter of 10.9% for the quadratic (12.1% for the linear) corrected masses. Only the identified tangential arcs are used in this method.

Following the recommendation and procedures established by Remolina González et al. (2020), Chapter II, when applying this method to the observational data we use the BCG of the galaxy cluster as our fixed center.

The projected arc radii in this work extend beyond the calibrated range (see Figure 4.2). We therefore use caution when applying this method to our sample, and investigate different choices in its application at large Einstein radii. We apply the quadratic empirical correction for Einstein radii $\leq 30''$, as recommended by Remolina González et al. (2020), Chapter II, and the linear empirical correction for the rest. In addition to the full sample, we report results for a subsample of $\leq 20''$, which is better represented by the simulated data used by Remolina González et al. (2020), Chapter II, to calibrate the method.

4.4 Methodology

In the following section, we describe the input constraints needed to compute $M(< \theta_E)$ and $M_{\text{SHM}}(< e\theta_E)$. Following the work by Remolina González et al. (2020), Chapter II, and Remolina González et al. (2021a), Chapter III, we compute the core mass for the sample of strong lensing galaxy clusters analysed in this work.

4.4.1 Arc Catalogs

We use the lensing constraints (arcs) that were identified and listed with the public lens models. For this work, we only use constraints with spectroscopic redshifts (reference for the arc catalogs are given in Section 4.2). We inspect the lensed galaxies and determine if they are tangential or radial arcs depending on the direction of their distortion. Only the tangential arcs are used for fitting the Einstein radius, but all of

the arcs are included when computing the single-halo lens models.

4.4.2 BCG Selection

The position of the BCG serves as the initial position for the cluster-scale dark matter halo in the single-halo lens models and as the fixed center in the Einstein radius mass estimate. The BCGs were selected by their magnitude from a cluster member catalog (see Postman et al. 2012 and Fox et al. 2021) and then confirmed by visual inspection.

4.4.3 Computing $M_{\text{SHM}}(< e\theta_E)$ and $M_{\text{corr}}(< \theta_E)$

Using the catalog of the arcs and the selected BCG, we compute the single-halo lens models and measure the Einstein radii of the observed clusters. We compute a SHM for each set (also known as “family”) of multiply-imaged background sources. There are cases where a galaxy cluster has multiple arc families although none of the individual families satisfy the minimum number of 6 constraints needed. We therefore compute one SHM for each cluster that uses all the families as constraints, thus the minimum number of constraints needed is attained (the total number of constraints for a given model is $\Sigma(2n_i - 2)$, where n_i is the number of constraints for background source i). All the SHM are inspected and only the ones that pass the quick visual inspection are used in our analysis. From the total of 67 clusters, 62 (29 SGAS, 15 RELICS, 6 HFF, and 12 CLASH) have enough constraints to compute a SHM, i.e., 6 or more constraints. Following the visual inspection, only 54 (23 SGAS, 13 RELICS, 6 HFF, and 12 CLASH) clusters remain in our analysis.

We plot the distribution of effective Einstein radii measured from the single-halo lens models that pass the visual inspection in Figure 4.2. The distribution of $e\theta_E$ from the SHM generally follows the number of clusters in each survey, as most clusters only have one or two independent SHM that could be computed and pass the visual

inspection. We note that while the depth of the HFF data leads to an unprecedented number of strongly lensed galaxies overall, many of the arc families do not have four or more secure multiple images each. We find that SGAS models occupy the lower end of the effective Einstein radius distribution, followed by RELICS, CLASH, and HFF. The distributions of $e\theta_E$ emphasizes the difference in the selection function of the strong lensing sample, as CLASH, HFF, and RELICS attempted to select clusters with large lensing cross section, to increase the chances of observing magnified high redshift galaxies. The resulting SHM outputs are used to compute $M_{\text{SHM}}(< e\theta_E)$ as described in Section 4.3.2.

Utilizing the same catalog of arcs and BCG positions, we geometrically fit this data with a circle, following Remolina González et al. (2020), Chapter II. We measure at least one Einstein radius per galaxy cluster. We plot the distribution of all θ_E in Figure 4.2. Unlike the SHM case, the $M_{\text{corr}}(< \theta_E)$ can be computed for any number of multiple images of a given lensed source, resulting in a θ_E measurement for each strongly-lensed source with spectroscopic redshift. The deep observations and extensive spectroscopic followup of the 6 HFF clusters resulted in a large number of lensed sources with spectroscopic redshifts, which extend to large cluster-centric radii. In all the other fields, where only a few lensed sources per cluster have spectroscopic redshifts, the number of measurements is driven by the number of clusters in each sample, and the identified sources have smaller cluster-centric distances. The Einstein radius is then used to compute $M_{\text{corr}}(< \theta_E)$ as described in Section 4.3.3.

4.4.4 Statistics

Depending on the number of arcs and arc families available for each method, each cluster enables up to 37 θ_E measurements and up to six SHM measurements. The measurements in each cluster are expected to be correlated, and their distribution can inform the statistical uncertainty. On the other hand, individual clusters are

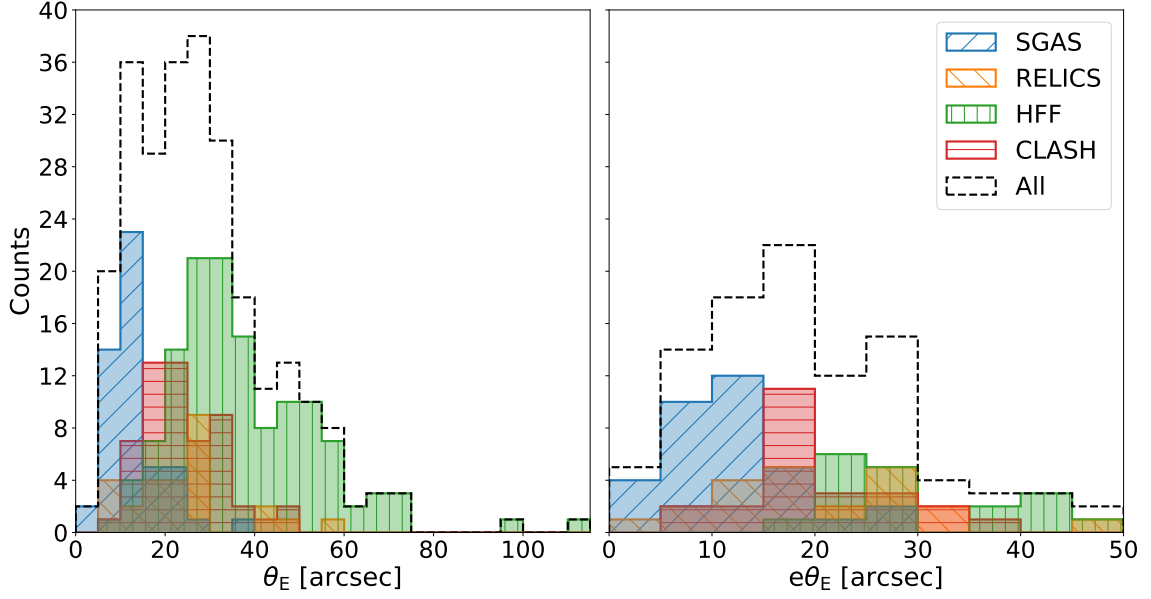


Figure 4.2: **Distribution of θ_E and $e\theta_E$ as measured from the two different mass estimate methods.** The Einstein radius (θ_E ; *Left* panel) is measured from the geometric fit of a circle to the identified tangential arcs of a single background source and the effective Einstein radius ($e\theta_E$; *Right* panel) is measured as the radius of a circle with the same area enclosed by the tangential critical curve of the single-halo lens models that passed the visual inspection. Both θ_E and $e\theta_E$ have units of arcseconds. The black dashed line represents the total counts and the colors denote the counts from the four different surveys of strong lensing galaxy clusters. As expected from the selection functions of these samples, SGAS clusters have lower θ_E and $e\theta_E$, followed by the RELICS, CLASH, and HFF galaxy clusters. The deep observation and extensive followup of the six HFF clusters result in a large number of lensed sources with spectroscopic redshifts, extending to large cluster-centric radii, which is reflected in the distribution of θ_E . SGAS, CLASH (except for those that are also part of HFF), and RELICS have only a few lensed sources per cluster with spectroscopic redshifts, and are found at smaller cluster-centric distances.

independent of each other.

To validate the robustness of our rapid measurements, we follow Remolina González et al. (2020), Chapter II, and Remolina González et al. (2021a), Chapter III, to build a statistical sample for each method (θ_E and SHM) to take into account multiple mass estimates for a single galaxy cluster and set the statistical weight for each cluster equal to one. For each galaxy cluster, we select at random an Einstein radius and a effective Einstein radius from the measured Einstein radii and available single halo lens models that passed visual inspection. For comparison to M_{DLM} , if a cluster has more than one detailed lens model (see Section 4.2), one DLM was selected at random. Then, we sample the selected mass measurement from a normal distribution centered at the best fit and standard deviation equal to the uncertainty. This process is repeated 1,000 times per cluster leading to a sample of 67,000 $M_{\text{corr}}(< \theta_E)$ points, 62,000 points from all SHM, of which 54,000 M_{SHM} points are ones that passed the quick visual inspection.

4.5 Analysis of Results

In the following section, we compare the galaxy cluster core mass measurement between the Einstein radius, $M_{\text{corr}}(< \theta_E)$, and the single halo lens models, $M_{\text{SHM}}(< e\theta_E)$, to the mass enclosed by the respective mass apertures from the detailed lens models. We discuss the difference in the uncertainty measured in this work and the scatter measured from simulations by Remolina González et al. (2020), Chapter II, and Remolina González et al. (2021a), Chapter III. Last, we compare the scatter of two efficient mass methods, $M_{\text{corr}}(< \theta_E)$ and $M_{\text{SHM}}(< e\theta_E)$, to the statistical modeling uncertainty of the detailed lens models. In this work the scatter is defined as half of the difference between the 84th and 16th percentiles. The bias is determined from the median of the distribution.

4.5.1 Mass Enclosed by the Einstein Radius, $M_{corr}(< \theta_E)$

In Figure 4.3, we plot the direct comparison between the corrected mass enclosed by the Einstein radius, $M_{corr}(< \theta_E)$, and the mass enclosed by the same aperture from the best-fit detailed lens model, M_{DLM} , for all clusters. We measure an overall scatter of 18.1% and bias of -7.1% in $M_{corr}(< \theta_E)$ compared to M_{DLM} . We find that the distribution is biased low, particularly at large M_{DLM} values. The observed negative bias is reduced from systems with large Einstein radius ($\theta_E > 20''$). For Einstein radius $< 20''$ the scatter is 14.4% and bias of -4.3% . This bias could be possibly addressed by extending the work of Remolina González et al. (2020), Chapter II, to larger radii, by using simulations that include lower magnification lensed sources at larger cluster-centric distances.

4.5.2 Mass Estimate from Single Halo Lens Models, $M_{SHM}(< e\theta_E)$

We assess the results of the entire SHM sample, and the results of the subsample of models that passed the visual inspection. In Figure 4.4, we plot the direct comparison between the aperture mass enclosed by the effective Einstein radius of the SHM that passed the visual inspection, $M_{SHM}(< e\theta_E)$, and the mass enclosed by the same aperture in the best-fit DLM, M_{DLM} . We measure an overall scatter of 9.0% and a bias of 1.0% between $M_{SHM}(< e\theta_E)$ and M_{DLM} for the SHM that passed the quick visual inspection. For the entire SHM sample, we measure an overall scatter of 12.5% and a bias of 2.4% between the two masses. We find that the visual inspection helps decrease the scatter and bias between $M_{SHM}(< e\theta_E)$ and M_{DLM} .

4.5.3 Comparison to the Statistical Uncertainty of the Detailed Lens Models

To contextualize the scatter of the mass estimates assessed in this chapter, we review it against the uncertainty typically attributed to detailed lens models. We

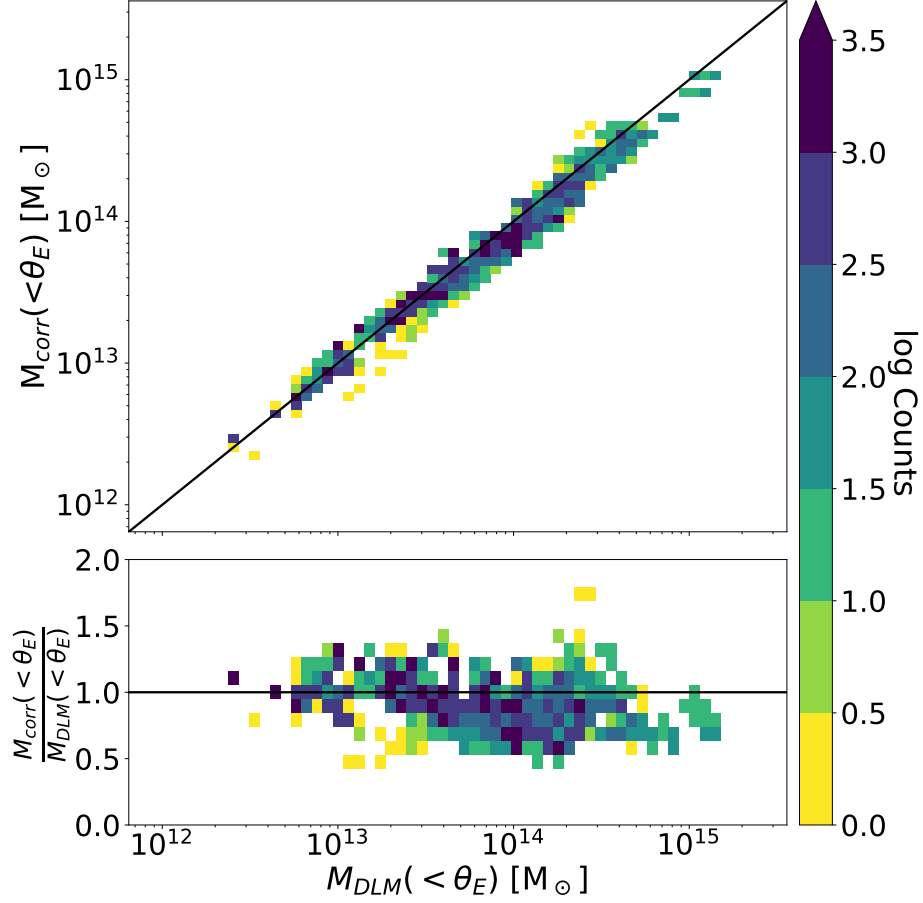


Figure 4.3: **Mass Comparison Between $M_{corr}(< \theta_E)$ and M_{DLM} .** The *top* plot shows the direct mass comparison between the masses and the *bottom* plot is the mass ratio of the measurements. The total number of counts is the 62,000 sampled data points (see Section 4.4.4). The black lines indicate the one-to-one line, where $M_{corr}(< \theta_E)$ equals M_{DLM} . We find that the distribution is biased low particularly at large M_{DLM} .

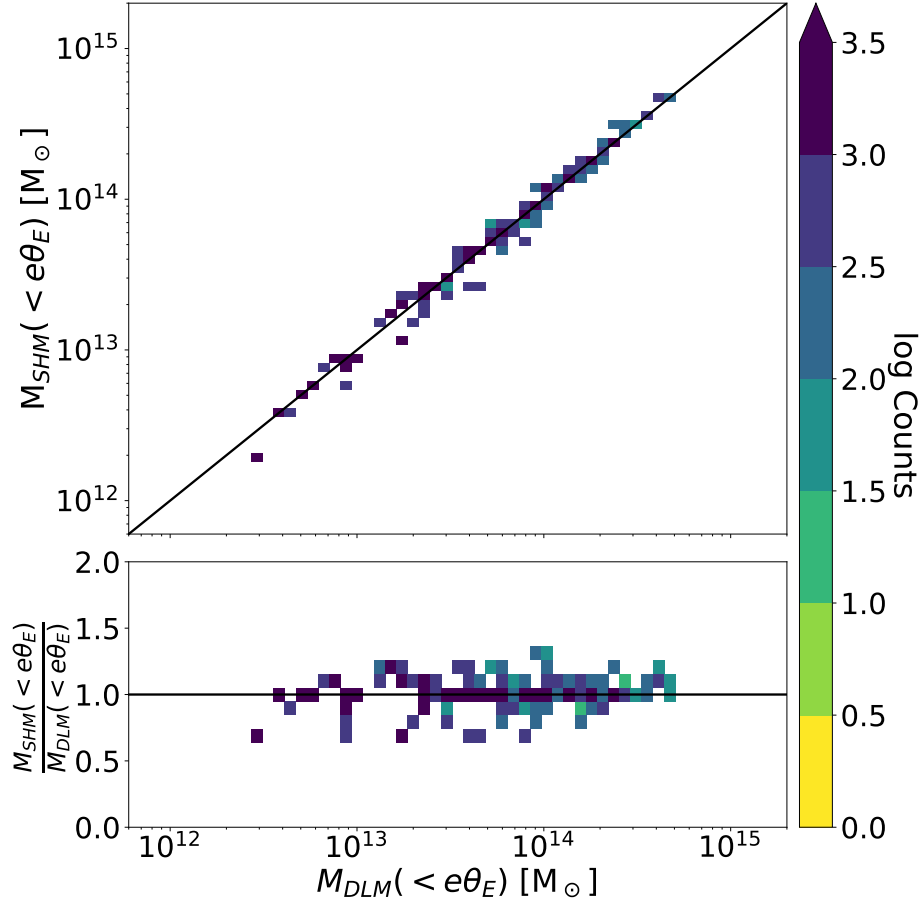


Figure 4.4: **Mass Comparison Between $M_{SHM}(< e\theta_E)$ and M_{DLM} .** The *top* plot shows the direct mass comparison and the *bottom* plot shows the mass ratio. The total number of counts is the 52,000 sampled data points (see Section 4.4.4). The black lines indicate the one-to-one line, where $M_{SHM}(< e\theta_E)$ equals M_{DLM} . We find that $M_{SHM}(< e\theta_E)$ is unbiased compared to M_{DLM} .

plot the overall scatter in the $M_{corr}(< \theta_E)$ and $M_{SHM}(< e\theta_E)$ measurements against the statistical uncertainty of the detailed lens models, $\sigma(M_{DLM})$, normalized by the best-fit DLM in Figure 4.5. The statistical uncertainty of the detailed lens models is computed in the same way as the scatter (see Section 4.5), except the uncertainty of each data point is drawn from the publicly available “range” maps provided by the lensing teams, and represents a statistical sampling of the parameter space, typically using MCMC. The aggregated statistical uncertainty over the entire sample from the detailed lens models is $\sigma(M_{DLM}) = 1.1\%$.

However, the statistical DLM modeling uncertainty is likely underestimated. Comparing models of two simulated clusters that were computed by different DLM algorithms, Meneghetti et al. (2017) conclude that detailed lens models are reliable when recovering the enclosed mass in the inner $100''$ with a scatter of less than 10%. In a recent comparison between DLM algorithms, Raney et al. (2020b) show that while the mass measured by the detailed lens models is reliable, the statistical uncertainty reported by the lensing algorithms underestimates the systematic uncertainty. Raney et al. (2020b) estimate the systematic uncertainty at $\sim 5\%$ for a circularly-averaged mass computed from the most recent versions (v4) of the HFF lens models.

4.5.4 Comparison between Observations and Simulations

Remolina González et al. (2020), Chapter II, and Remolina González et al. (2021a), Chapter III, measured the scatter and bias of $M_{corr}(< \theta_E)$ and $M_{SHM}(< e\theta_E)$ against the “true” mass, from simulations. To compare the scatter found in this work to Remolina González et al. (2020), Chapter II, and Remolina González et al. (2021a), Chapter III, we need to account for the fact that detailed lens models are an observable measurement and while reliable are not the absolute truth. The expected scatter should therefore be a combination of the intrinsic scatter of the mass estimate, as measured from simulations, and the scatter attributed to the DLM measurement.

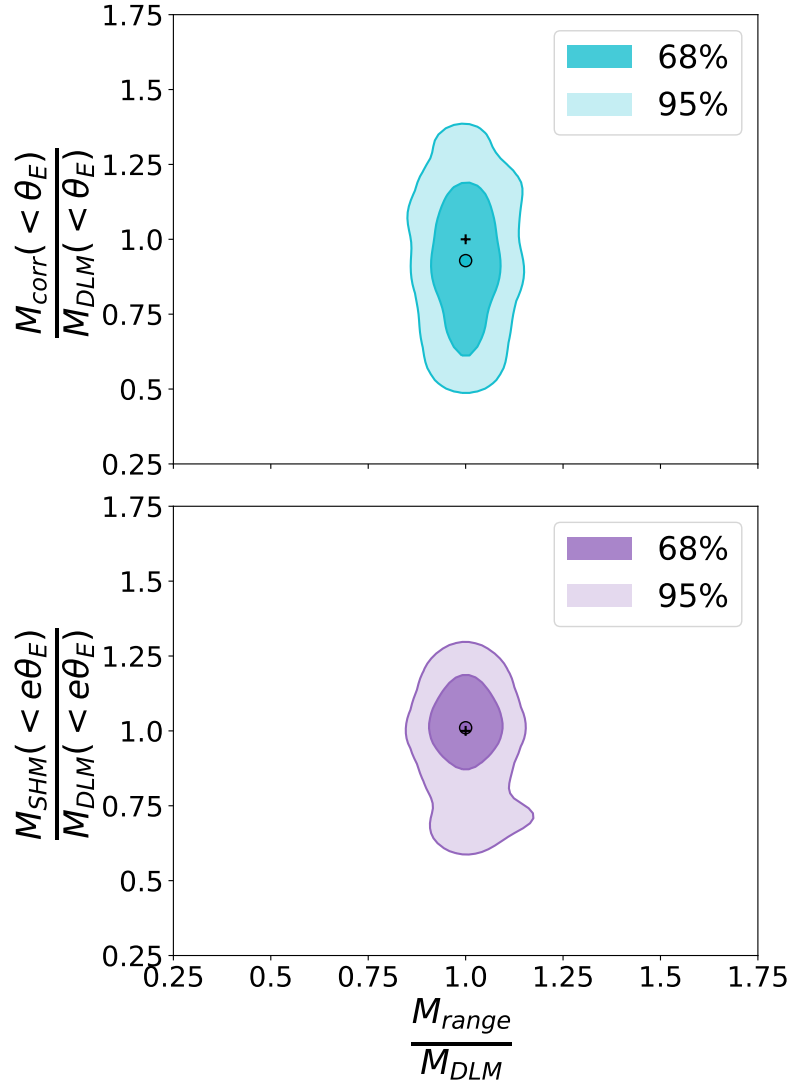


Figure 4.5: **The Scatter of the Efficient Mass Estimate Methods, Compared to the Statistical Uncertainty of the Detailed Lens Models.** We plot the mass ratio between the mass estimate and the best-fit detailed lens model against the statistical scatter of the detailed lens models, M_{range}/M_{DLM} , derived from the publicly available “range” maps and normalized by the best-fit detailed lens model. The crosses stand for the point (1.0,1.0) and the open circles indicate the median of the distributions. Results for $M_{corr}(< \theta_E)$ are shown in the *top* panel, and for $M_{SHM}(< e\theta_E)$ in the *bottom* panel, smoothed by a kernel of 5%. The black cross indicates the location where $M_{corr}(< \theta_E)$ and $M_{SHM}(< e\theta_E)$ equal M_{DLM} .

We note that the scatter between the three mass estimates ($M_{corr}(< \theta_E)$, $M_{SHM}(< e\theta_E)$, and M_{DLM}) may be correlated. To fully characterize the correlations between the masses will require the computation of detailed lens models for a large sample of simulated strong lensing galaxy clusters, which awaits new large cosmological simulations with baryonic information and will require an extensive amount of physical and human resources.

With this in mind, we compute a lower limit in the expected scatter by assuming that the scatter between the masses is un-correlated. We add in quadrature the scatter of $M_{corr}(< \theta_E)$ and $M_{SHM}(< e\theta_E)$ from simulations (10.9% and 3.3%, respectively, from Remolina González et al. 2020, Chapter II, and Remolina González et al. (2021a), Chapter III) with a 5% scatter in M_{DLM} (from Raney et al., 2020b). This results in a expected scatter of 12.0% for $M_{corr}(< \theta_E)$ and 6.0% for $M_{SHM}(< e\theta_E)$ that passed the visual inspection. In both cases, we find that the overall scatter measured in this work (18.1% and 9.0%) is larger than expected. The difference between these scatters highlights some of the limitations in the simulation used by Remolina González et al. (2020), Chapter II, and Remolina González et al. (2021a), Chapter III, to account for the full range of scatter due to, e.g., baryonic effects, uncorrelated mass along the line of sight, and shear from nearby structures.

4.6 Summary and Conclusions

A large number of strong lensing galaxy clusters is expected to be detected in current and upcoming large surveys. Estimating the mass at the core of these galaxy clusters will serve as one of the anchors to the radial mass distribution profile and measurement of the concentration. Detailed lens models to analyze these strong lensing clusters and measure the mass at the core of the galaxy cluster are limited by the small number of constraints available from the identified multiply imaged lensed sources and can take multiple weeks to be finalized. Timely, efficient, and accurate

methods to measure the mass at the core of galaxy clusters in these large samples are needed. Remolina González et al. (2020), Chapter II, assessed an empirically corrected mass enclosed by the Einstein radius ($M_{corr}(< \theta_E)$) and Remolina González et al. (2021a), Chapter III, assessed the aperture mass enclosed by the effective Einstein radius from the single-halo lens models ($M_{SHM}(< e\theta_E)$) using simulated strong lensing images from the Outer Rim (Heitmann et al., 2019). In this work, we applied the two methods to observational data and used the publicly available detailed lens models from the SGAS, CLASH, HFF, and RELICS strong lensing cluster samples to evaluate the efficacy of the methods in measuring the core mass of galaxy cluster. We conclude the following:

- The corrected mass enclosed by the Einstein radius, $M_{corr}(< \theta_E)$, has an overall scatter of 18.1% and bias of -7.1% compared to the detailed lens models. The bias is reduced if large ($\theta_E > 20''$) Einstein radii are excluded. For Einstein radii $< 20''$ the scatter is 14.4% and the bias is -4.3% .
- The SHM aperture mass enclosed by the effective Einstein radius, $M_{SHM}(< e\theta_E)$, when computed over the entire sample, has an overall scatter of 12.5% and bias of 2.4% compared to the DLM. A quick visual inspection of the SHM outputs eliminates the SHM that fail to reproduce the lensing configuration, reducing the scatter to 9.0% and the bias to 1.0%. We find that the quick visual inspection is beneficial in reducing the scatter and bias between $M_{SHM}(< e\theta_E)$ and M_{DLM} , and identify lines of sight that would benefit from a more detailed analysis.
- To compare the overall scatter from $M_{corr}(< \theta_E)$ and $M_{SHM}(< e\theta_E)$ to that of simulations, we need to take into account the uncertainty in the detailed lens models. While we expect correlations between all mass estimates ($M_{corr}(< \theta_E)$, $M_{SHM}(< e\theta_E)$, and M_{DLM}), computing this is out of the scope of this analysis. We choose to compute a lower limit for the expected scatter by adding

in quadrature 5%, which corresponds to the scatter of the mass from the detailed lens models, to the scatter measured in the simulation of 10.9% (3.3%) for $M_{corr}(< \theta_E)$ ($M_{SHM}(< e\theta_E)$ that passed the visual inspection). The resulting expected scatter is 12.0% for the corrected mass enclosed by the Einstein radius and 6.0% for the SMH that passed the visual inspection. The measured scatter in this work for both cases, 18.1% in $M_{corr}(< \theta_E)$ and 9.0% in $M_{SHM}(< e\theta_E)$, is higher than our estimated lower limit of the expected scatter. The difference is then associated with limitations in the simulation used by Remolina González et al. (2020), Chapter II, and Remolina González et al. (2021a), Chapter III, including baryonic effects, line-of-sight structure, and shear due to nearby structures.

- Detailed lens models are considered to be the state of the art in measuring the enclosed projected mass density within the cores of galaxy clusters. While likely underestimated, the relative *statistical* lens modeling uncertainty of detailed lens models, marginalized over the large sample we investigated here, is of order 1.1%. Systematic uncertainties are estimated in the literature (e.g., Meneghetti et al., 2017; Raney et al., 2020b) at the 5–10% level. We show that the precision toll of using the significantly-faster mass estimate methods is only a 9.0% or 18.1% increase over the detailed lens models. We conclude that if other, larger, sources of error dominate the analysis, these fast and efficient mass estimate methods become a powerful tool in analyses of large cluster samples.

Overall, this work demonstrates the successful application of these efficient methods to observational data as currently established, as well as their reliability to estimate the mass at the core of strong gravitational lensing galaxy clusters. We look forward to improvements to these methods benefiting from identification of strong lensing evidence by convolutional neural networks (e.g., Cañameras et al. 2020; Huang et al. 2021; Morgan et al. 2021) and other machine learning algorithms to model the

mass distribution of the SL clusters (e.g., Bom et al. 2019; Pearson et al. 2019).

CHAPTER V

The concentration-Mass Relation of South Pole Telescopes Strong Gravitational Lensing Galaxy Clusters

Preface

This chapter has been adapted from a paper of the same title in preparation with the plans to be submitted for peer-review to the *Astrophysical Journal*, with co-authors K. Sharon, L. E. Bleem, S. W. Allen, L. F. Barrientos, M. Bayliss, B.A. Benson, S. Bocquet, M. Brodwin, R. Canning, M. Florian, C. Fox, M. D. Gladders, S. Habib, K. Heitmann, J. Hlavacek-Larrondo, T. L. Johson, G. Khullar, A. L. King, N. Li, G. Mahler, A. Mantz, O. S. Matthews Acuña, M. McDonald, R. G. Morris, K. Napier, A. Niemiec, E. Noordeh, B. Stalder, A. A. Stark, V. Strazzullo, A. von der Linden and the South Pole Telescope Collaboration. The paper is presented here in progress and ready to go through review by the Clusters Group and full collaboration of the South Pole Telescope.

For this project, I measure the concentration-Mass (c-M) relation for a large sample of South Pole Telescope (SPT) strong lensing galaxy clusters. I used simulations to test the modeling procedures and predict the c-M relation for strong lensing clusters. For the observations, I used a large sample of 51 strong lensing galaxy clusters

identified from a *Hubble* Space Telescope Snapshot program that successfully observed 137 SPT galaxy clusters. This large sample of strong lensing clusters (about twice as large as any previously studied samples) has a well understood selection function and uniform imaging data making it useful for this study. I performed all of the analysis shown with the feedback from the co-authors. I produced all of the figures and tables presented in the paper. I wrote nearly the whole text with the feedback and suggestions from the co-authors.

As part of SPT collaboration work with strong lensing galaxy clusters, I have been the principal investigator of a multi-year spectroscopic follow-up of SPT strong lensing program utilizing the Magellan Telescopes. The results of the program including the spectroscopic redshifts for strong lensing evidence and galaxy cluster members will be presented at a later time by the SPT collaboration. I present a description of the observing program in Appendix D including a summary of the observations.

The work for this chapter is based on observations with the NASA/ESA *Hubble* Space Telescope obtained at the Space Telescope Science Institute, which is operated by the Association of Universities for Research in Astronomy, Incorporated, under NASA contract NAS5 – 26555. These observations are associated with programs GO–15307 and GO-15163. Support for Program GO–15307 was provided through a grant from the STScI under NASA contract NAS5 – 26555. The data used in this chapter are available through the Mikulski Archive for Space Telescopes (MAST). STScI is operated by the Association of Universities for Research in Astronomy, Inc., under NASA contract NAS5-26555.

Abstract

We present the measurement of the concentration-mass relation for a large sample of 51 South Pole Telescope (SPT) strong lensing galaxy clusters, combining the mass at the core from strong lensing and the Sunyaev Zel’dovich inferred mass estimated

by SPT. The SPT strong lensing sample was selected from a uniform *HST* snapshot program. The sample spans a mass range of $3.00 \times 10^{14} M_{\odot} h^{-1} < M_{500c} < 1.00 \times 10^{15} M_{\odot} h^{-1}$ with a median of $5.28 \times 10^{14} M_{\odot} h^{-1}$ and a redshift range of $0.207 < z < 1.150$ with a median of 0.580. We use the Outer Rim simulation and apply our observational selection function to compute the prediction of the concentration-mass relation for SPT-like strong lensing galaxy clusters. We constrain the normalization of the c-M relation to within a 9.3% level in simulations and 5.7% in observations. We find significant evidence at the 4.5-sigma level and higher for a relation between the mass, M_{500c} , and the concentration, c_{500c} . We cannot constrain a possible evolution of the concentration with redshift with these samples. Last, we report an agreement between the predictions from simulations and the observed cluster and find no tensions with Λ CDM.

5.1 Introduction

The concentration-mass (c-M) relation of galaxy clusters can directly compare the predictions from cosmological simulations (e.g., Duffy et al. 2008; Prada et al. 2012; Bhattacharya et al. 2013; Meneghetti et al. 2014; Child et al. 2018 and observational measurements (e.g., Okabe et al. 2010; Oguri et al. 2012; Sereno et al. 2015; Merten et al. 2015). The concentration can be computed from the Navarro, Frenk, and White (NFW; Navarro et al., 1996, 1997) radial mass density profile, and to constrain it requires measurements extending a broad range of cluster radii. Mass measurements extending the broad radial range of galaxy clusters are needed and combinations of various mass estimates have been employed to achieve this work (e.g., Oguri et al. 2012; Merten et al. 2015).

At the cores of galaxy clusters, strong gravitational lensing (SL), provides a highly accurate total (dark and baryonic) mass estimates at the smallest radial scales and largest over-densities. This makes galaxy clusters with strong lensing evidence of

particular interest, as the strong lensing mass estimate at the cluster core (e.g., Sharon et al. 2015; Remolina González et al. 2021a, Chapter III,) can be used to measure c-M, when combined with a large scale mass proxy from weak lensing (e.g., Hoekstra et al. 2013; Merten et al. 2015), X-ray (e.g., Mantz et al. 2018; Ettori et al. 2019), richness (e.g., Koester et al. 2007; Rykoff et al. 2016), dynamical techniques (e.g., Gifford & Miller 2013), or the integrated Sunyaev Zel’dovich effect (SZ, Sunyaev & Zeldovich 1972, 1980; e.g., Planck Collaboration et al. 2016; Bleem et al. 2020). Comparisons between observations and theoretical predictions of c-M in SL galaxy clusters have reported some disagreement (e.g., Broadhurst & Barkana 2008; Gralla et al. 2011; Gonzalez et al. 2012; Meneghetti et al. 2013; Killedar et al. 2018). However, the sample size and selection functions are limitations in these studies.

In this work, we use a large sample of SL galaxy clusters (about twice as large as samples used in previous studies) from the South Pole Telescope (SPT), which has a selection function for galaxy clusters that is almost redshift independent and mass limited (Bleem et al., 2015, 2020; Huang et al., 2020). This unique sample spans a broad range in redshift and total mass. A large *Hubble* Space Telescope (*HST*) Snapshot (SNAP) program has provided uniform imaging of over a hundred galaxy clusters, with 55% of them showing some strong lensing evidence. The large sample requires a fast and accurate method to measure the core mass of galaxy clusters in a timely manner. Remolina González et al. (2020), Chapter II, and Remolina González et al. (2021a), Chapter III, used simulations to assess the use of the mass enclosed by the Einstein radius and the use of Single-Halo Lens Models, respectively, as efficient and accurate mass estimators with recommendations on their application to large samples of strong lensing galaxy clusters. The goal of this chapter is to combine the mass at the core from strong lensing and the SZ mass from SPT to constrain their NFW profile, measure the concentration-mass relation for SPT strong lensing galaxy clusters in the uniformly-imaged sample provided by the *HST* SNAP program, and

compare the observations against predictions from simulations. For the predictions from simulations, we use the Outer Rim cosmological simulation (Heitmann et al., 2019) and adopt the total halo mass, M_{500c} , and concentration, c_{500c} , measured by Child et al. (2018) and Li et al. (2019).

The chapter is organized as follows. In Section 5.2, we describe the NFW density profile and previous comparisons between simulations and observations of the c-M relation. In Section 5.3, we describe the simulations used in the work to establish a prediction for the c-M relation for SPT SL galaxy clusters. In Section 5.4, we describe the SPT SL galaxy cluster sample used in this analysis and the strong lensing evidence identified in these lines of sight. In Section 5.5, we describe the two efficient core mass estimates using the strong lensing evidence, the mass enclosed by the Einstein radius and the Single-Halo Lens Models. In Section 5.6, we describe the selection of strong lensing constraints, the computation of the empirically-corrected mass enclosed by the Einstein radius, the method used to fit the NFW density profile to the mass estimate from strong lensing at the core and the large scale mass from SZ, validate our methods for measuring the concentration using simulations, and describe the fitting procedure for the c-M relation. In Section 5.7, we present the predictions of the c-M relation from the simulated sample of strong lensing galaxy clusters, measure the c-M relation of the observed SPT strong lensing galaxy clusters, and compare our predictions from the simulation to our observations. Last in Section 5.8, we summarize our conclusions.

We adopt a flat Λ CDM cosmology throughout the chapter. For consistency with measurements in the observed and simulated samples, we use $\Omega_\Lambda = 0.7$, $\Omega_M = 0.3$, and $H_0 = 70 \text{ km s}^{-1} \text{ Mpc}^{-1}$ in measurements of the observed sample following the analysis performed to measure the large scale masses from SPT clusters (Williamson et al., 2011; Bleem et al., 2015, 2020; Bocquet et al., 2019; Huang et al., 2020). For the simulations, we adopt the *WMAP*-7 parameters (Komatsu et al., 2011) $\Omega_\Lambda = 0.735$, $\Omega_M = 0.265$, and $h = 0.71$, as was implemented in the Outer Rim simulation

(Heitmann et al., 2019).

The large scale masses are reported in terms of $M_{\Delta c}$, defined as the mass enclosed within a radius at which the average density is Δ times the critical density of the universe, $\rho_{\text{crit}}(z)$, at the cluster redshift, z :

$$M_{\Delta c} = \Delta \rho_{\text{crit}}(z) \times \frac{4}{3} \pi r_{\Delta c}^3, \quad (5.1)$$

where $r_{\Delta c}$ is the radius corresponding to $M_{\Delta c}$.

5.2 The NFW Density Profile

The NFW profile (Navarro et al., 1996, 1997) describes the universal spatial mass distribution of dark matter halos, derived from a functional fit to dark matter halos identified in N-body cosmological simulations. The NFW profile is defined as follows:

$$\rho_{\text{NFW}}(r) = \frac{\rho_{\text{crit}}(z) \delta_c}{\left(\frac{r}{r_s}\right) \left(1 + \frac{r}{r_s}\right)^2}, \quad (5.2)$$

where δ_c is the characteristic dimensionless density parameter and r_s is the scale radius of the halo. The characteristic dimensionless density parameter δ_c takes the following form given $r_{\Delta c}$ (or equivalently $M_{\Delta c}$) which is a useful implementation to aid in the fitting process (see Section 5.6.4):

$$\delta_c = \frac{\Delta}{3} \left(\frac{r_{\Delta c}}{r_s}\right)^3 A(r_{\Delta c})^{-1} \quad (5.3)$$

where

$$A(r_{\Delta c}) = \left[\ln \left(1 + \frac{r_{\Delta c}}{r_s} \right) - \frac{\frac{r_{\Delta c}}{r_s}}{1 + \frac{r_{\Delta c}}{r_s}} \right]. \quad (5.4)$$

The concentration is then defined as the ratio of a radius of interest and the scale radius:

$$c = \frac{r}{r_s}. \quad (5.5)$$

Traditionally the concentration has been measured in relation to $r_{\Delta c}$ for $\Delta = 500$ and 200 resulting with the corresponding concentration $c_{\Delta c}$.

The mass enclosed by a sphere of radius r , is as follows:

$$M_{\text{NFW}}(< r) = 4\pi\rho_{\text{crit}}(z)\delta_c r_s^3 A(r). \quad (5.6)$$

As strong gravitational lensing measures the projected mass distribution, it is convenient to write the average surface density of the NFW profile (Golse & Kneib, 2002):

$$\bar{\Sigma}_{\text{NFW}}(< r) = 4\rho_{\text{crit}}(z)\delta_c r_s \left(\frac{r_s}{r}\right)^2 F\left(\frac{r}{r_s}\right), \quad (5.7)$$

where:

$$F\left(\frac{r}{r_s}\right) = \begin{cases} \ln\left(\frac{r}{2r_s}\right) + \frac{1}{\sqrt{1-\left(\frac{r}{r_s}\right)^2}} \operatorname{arccosh}\left(\frac{r_s}{r}\right) & \left(\frac{r}{r_s} < 1\right) \\ 1 + \ln\left(\frac{1}{2}\right) & \left(\frac{r}{r_s} = 1\right) \\ \ln\left(\frac{r}{2r_s}\right) + \frac{1}{\sqrt{\left(\frac{r}{r_s}\right)^2 - 1}} \operatorname{arccos}\left(\frac{r_s}{r}\right) & \left(\frac{r}{r_s} > 1\right), \end{cases} \quad (5.8)$$

which is then used to compute the projected NFW mass enclosed by radius, r :

$$M_{\text{NFW}}^{\text{proj}}(< r) = \bar{\Sigma}_{\text{NFW}}(< r)\pi r^2. \quad (5.9)$$

A relation between the concentration and the mass has been identified in simulations (e.g., Duffy et al. 2008; Bhattacharya et al. 2013; De Boni et al. 2013; Meneghetti et al. 2014; Child et al. 2018) and observations (e.g., Okabe et al. 2010; Oguri et al. 2012; Merten et al. 2015). We adopt the following form of the concentration-Mass relation:

$$c_{\Delta c}^*(M_{\Delta c}, z) = \alpha \left(\frac{M_{\Delta c}}{M_{\text{pivot}}} \right)^\beta \left(\frac{1 + z_{\text{pivot}}}{1 + z} \right)^\gamma, \quad (5.10)$$

where M_{pivot} is the median mass and z_{pivot} is the median redshift of the halos, α is the normalization parameter, β and γ are the scaling exponents that define the power-law dependence of the concentration on the mass, $M_{\Delta c}$ and the redshift, respectively.

This relation has a scatter of $\sigma(c_{\Delta c}) = c_{\Delta c}/3$ (Duffy et al., 2008; Bhattacharya et al., 2013; Child et al., 2018). In simulations, the c-M relation has been measured using different methods (e.g., Duffy et al. 2008; Prada et al. 2012; Bhattacharya et al. 2013; Meneghetti et al. 2014; Child et al. 2018). Some of disagreements among these results have been found to be largely due to the fitting methods, binning choices, and operational form of the definition of concentration (see Meneghetti et al. 2013; Dutton & Macciò 2014). The shape of the concentration-Mass relation has been debated with a diversity of results coming from simulations including: a power-law dependence for all mass and redshift (e.g., Bhattacharya et al. 2013), a flattening concentration at high mass (e.g., Duffy et al. 2008; Child et al. 2018), an increasing concentration with increasing mass (e.g., Prada et al. 2012). The redshift dependence of the concentration has also been debated with simulations indicating a possible evolution. It is also important to note that different cosmological parameters have an effect on the concentration mass measurement, with high- σ_8 having higher concentrations at a given mass (Child et al., 2018). Last, some of the difference found between the different predictions from simulation have been found to depend on the selection function of the sample of halos, i.e., relaxed halos versus full sample.

Strong lensing galaxy clusters are a unique sample which are not representative of a mass limited sample of galaxy clusters. An example comparison using simulations between a mass limited halo sample and strong lensing halos is shown in Figure 2.1 in Chapter II. When looking particularly at the concentration, *bottom left* panel of the previously mentioned figures, we clearly see that the distribution peak of concentra-

tions of strong lensing clusters is higher than that of the mass limited sample. We also note the difference in the distribution in the mass, with strong lensing clusters generally being more massive, and redshift distribution, which is selection dependent in this particular case. The higher concentration in strong lensing clusters is a selection function as halos with surface densities higher than the critical surface density are required to observe strong gravitational lensing evidence. We expect clear differences in the c-M relation between a mass limited and strong lensing halo sample, with the strong lensing c-M relation having a steeper slope and higher normalization between the concentration and total mass (e.g., Meneghetti et al. 2013).

The over-density of strong lensing galaxy clusters has been reported in observations (e.g., Oguri & Blandford 2009; Gralla et al. 2011). In observations, the c-M relation has been measured in various samples of strong gravitational lensing galaxy clusters (e.g., Oguri & Blandford 2009; Oguri et al. 2012; Okabe et al. 2010; Sereno et al. 2015; Merten et al. 2015). Most of these samples consist of only a handful to a few tens of galaxy clusters, with complicated selection functions, presenting a limitation in the comparison between predictions and observations. In this chapter, we employ the same observational selection function in our predictions from simulations. The use of the same selection function in the simulations and observations allows for a direct comparison of the concentration-mass relation. A large sample spanning a broad mass and redshift range with a well defined selection function is also key of our analysis.

5.3 Simulated Strong Lenses

A comparison between the observed and predicted c-M relation must take into account that SL may be preferentially observed in a biased sub-sample of the cluster population. To account for that, we apply the SNAP program selection function to the catalog of simulated SL clusters from the Outer Rim (Heitmann et al., 2019)

cosmological simulation, to generate a simulated sub-sample that follows a similar selection function as the observed sample.

The Outer Rim is a large box ($L = 3000 \text{ Mpc h}^{-1}$ on the side), high-mass resolution, N-body simulation. The simulation adopts a *WMAP-7* (Komatsu et al., 2011) flat Λ CDM cosmology: $\Omega_\Lambda = 0.735$, $\Omega_M = 0.265$, and $h = 0.71$. The Outer Rim was used by Child et al. (2018) to study the dark matter radial profiles of galaxy cluster-scale and group-scale halos, and measured the c-M relation, using the full 3D particle information. Li et al. (2019) used the simulation to evaluate the effect on lensing due to line-of-sight structure and constructed realistic strong lensing images (Li et al., 2016). For our analysis, we adopt the total halo masses (M_{500c}) and the concentrations (c_{500c}) measured by Child et al. (2018) and Li et al. (2019).

The halos were identified using a friend-of-friends algorithm with a linking length of $b = 0.168$. A density estimator is employed to measure the halo surface density and Rangel et al. (2016) showed that the mass resolution for halos with a mass $M_{500c} > 2.00 \times 10^{14} M_\odot h^{-1}$ is robust for strong lensing studies. Following a SPT-like selection function, all halos with $M_{500c} > 2.10 \times 10^{14} M_\odot h^{-1}$ were selected. From this SPT-like sample, the average convergence was computed and strong lenses are identified where $\langle \kappa \rangle = 1$, and an Einstein radius of a few arcseconds is measured. The simulated SPT-like strong lensing sample is composed of 74 galaxy clusters spanning the redshift range of $z \sim 0.160 - 0.670$. The selection function to identify strong lensing galaxy clusters in the simulation limits the identification of high-redshift ($z > 0.700$) clusters as the lensing efficiency, D_{LS}/D_S , becomes small for increasing lens redshift and a fixed background source redshift of $z_S = 2.000$. For more information of the strong lensing simulated sample we direct the reader to Remolina González et al. (2020), Chapter II, and Remolina González et al. (2021a), Chapter III.

The simulated lensed images were produced following Li et al. (2016). Background source redshifts were drawn from a normal distribution with $\mu = 2.0$ and $\sigma = 0.2$

motivated by the observational analysis of Bayliss et al. (2011a). The image plane for each line of sight was generated 5 to 24 times, each with a unique background source redshift and position. A total of 1024 simulated lensed images were created with a resolution of $0''.09$ and a field of view of 2048×2048 pixels. No additional errors were added to the images as it was created for the most ideal case instead of creating a mock observation of a particular instrument. The background sources were placed in areas of high magnification, as this strategy mocks the selection function of lensing-selected samples (e.g., Bayliss et al., 2011b; Nord et al., 2016, 2020; Sharon et al., 2020; Khullar et al., 2021). The redshift and image plane positions of the multiple images are used to constrain the mass at the core of the galaxy cluster.

5.4 South Pole Telescope Strong Lensing Cluster Sample

The South Pole Telescope observations led to the identification of over 1000 galaxy clusters (Williamson et al., 2011; Bleem et al., 2015, 2020; Huang et al., 2020). These authors made the galaxy cluster catalogs publicly available¹ including their mass estimates M_{500c} . In Figure 5.1, we plot the mass-redshift distribution of the SPT galaxy clusters. The SPT selection function lends itself to galaxy cluster population analyses as it is almost redshift independent and mass limited. This unique sample is of particular interest to evolutionary studies, as we expect galaxy clusters to be less massive at higher redshifts and evolve into more massive descendants at lower redshifts.

The M_{500c} mass estimates reported in the cluster catalogs (Williamson et al., 2011; Bleem et al., 2015, 2020; Huang et al., 2020) and additional work by Bocquet et al. (2019) use a scaling relation to convert from the observed SZ significance to a mass. The observable-mass scaling relation parameters were determined in Bocquet et al. (2019) for a fixed flat Λ CDM cosmology and an observed cluster number count analysis for a sample of SPT-SZ clusters with significance greater than five and redshifts

¹<https://pole.uchicago.edu/public/data/sptsz-clusters/>

greater than 0.25. In Bocquet et al. (2019), an additional mass estimate for galaxy clusters in the SPT-SZ 2500 deg² was performed which marginalized over cosmology and scaling relation. These fully marginalized mass estimates are robust and found to be systematically lower than the un-marginalized mass estimates by about 20%. As the fully marginalized masses are not currently available for the complete sample of SPT galaxy clusters, we use the un-marginalized mass estimates and test the effect of a systematic difference in the large scale masses using simulations, see Appendix C. We expect fully marginalized mass estimates for all of the galaxy clusters shortly, which will enable their use in our analysis.

The large scale mass (M_{500c}) and redshift used in our analysis are taken from Williamson et al. (2011); Bocquet et al. (2019); Bleem et al. (2020); and Huang et al. (2020). The SPT M_{500c} were computed assuming a fixed cosmology and using the best-fit scaling relations for the number count observed in SPT (approach adopted in Bleem et al. 2015 and used in Bocquet et al. 2019; Bleem et al. 2020; Huang et al. 2020). In Table 5.2, we tabulate the galaxy clusters that are used in this analysis, their SPT ID, brightest cluster galaxy (BCG) R.A. and Decl., M_{500c} , and redshift.

A subset of the SPT cluster catalog was uniformly imaged with *HST* as part of a snapshot program in Cycle 25, and extended into Cycle 26 (GO-15307, GO-16017; PI:Gladders). The main goals of this program were to leverage the resolution capabilities of *HST* to study: (1) the evolution of brightest cluster galaxies, (2) strong lensing statistics and the concentration-mass relation of strong lensing clusters, and (3) the active galactic nuclei (AGN) in galaxy cluster members.

HST Snapshot programs execute a fraction of a target list, typically $\sim 30\%$. Targets are selected for implementation by the scheduling algorithm, to fill short time intervals that cannot be allocated to other proposals, thus maximizing the efficiency of the observatory. The SNAP targets were therefore generally drawn at random from a parent pool of clusters, which was constructed as follows.

Clusters were selected from the SPT cluster catalog such that they have an equal co-moving number density at $0.2 < z < 1$. All the clusters at $z \geq 1$ were included, and a lower redshift limit was applied at $z = 0.2$, due to the small volume this redshift bin samples and the extensive data already available for low- z clusters. We applied a redshift-dependent lower limit mass threshold, anchored at $M_{500c} = 4 \times 10^{14} M_{\odot} h^{-1}$ at the median catalog redshift. This threshold selects lower-mass cluster at higher redshifts, to foster evolutionary studies: the less-massive high redshift systems would evolve with cosmic time, to become the high-mass systems of low redshift. A sample of 387 SPT clusters satisfy these criteria. After removing fields which were previously observed by *HST*, the final target list includes 293 clusters.

The execution rate of our SNAP program, 47%, was higher than typical due to the extension of the program into Cycle 25, resulting in successful triggering of 137 targets. The shallow snapshot imaging of each of 137 SPT clusters were obtained with the WFC3-IR camera through the F110W filter, and with the WFC3-UVIS camera through the F200W filter, during a single shortened SNAP orbit. These two filters were selected in order to optimize the throughput, as they provide the broadest UVIS or IR wavelength coverage. The observations were configured to have one of three total exposure lengths (short, medium, or long) depending on cluster redshift, where higher redshift clusters were observed with a longer exposure time. The UVIS data were taken with a 3-point line dither, and post-flash was applied in order to mitigate charge transfer efficiency effects.

The data were reduced as follows. Prior to combining the calibrated single images produced by the Mikulski Archive for Space Telescopes (MAST²) archive , we apply two corrections. The first addresses a visible mismatch in sky levels in the F200LP data between the two WFC3-UVIS chips. We rectify this issue by subtracting the background sky on each chip, with the sky estimated by fitting an iterated Gaussian

²<https://archive.stsci.edu/>

model, sigma-clipped on the high end, to the pixel values. This correction is purely cosmetic with no effect on photometry, and is done to provide the best resulting data for constructing two-band pseudo-color images for further visual examination.

In the IR/F110W data, we correct for the well-known ‘IR blobs’ (See Pirzkal et al. 2010) which overlap in many instances with important target objects (galaxy cluster member galaxies and occasionally lensed arcs) observed in these data. Under normal circumstances, the pixels affected by these features are flagged and not used in final data products; in this program, because the data are minimal (three dithered images only, due to the truncated SNAP orbit length and two filter observations within that orbit) we aim to recover the areas affected by IR blobs by careful flat-fielding. To do so we acquired several hundred additional F110W images of similar integration time from the archive (from program GO-15163), which we then combined with most of the F110W data described here³ using IRAF’s `imcombine` task, tuned to provide robust rejection of the faint wings of object outliers in this large image stack. We then used GALFIT (Peng et al., 2002, 2010) to build a model – using a combination of Sersic profiles – of each identified IR blob across the stacked image. The composite full image of all the fitted blob models is then used to flat-field these features in the F110W data.

Data reduction of the WFC3 imaging with the F200LP and F110W filter – tuned as above – then follows the standard procedures established by STScI, employing the Python3 package `Drizzlepac` (Gonzaga et al., 2012). For astrometric matching of images, sub-exposures taken with the same filter were aligned to the same reference grid, using `tweakreg` operating on tuned catalogs extracted using Source Extractor (Bertin & Arnouts, 1996); the two filters were also astrometrically matched. These exposures were subsequently combined using `astrodrizzle`, using a Gaussian kernel,

³At the time that this calibration was computed, neither GO-15163 nor the program described here were entirely complete, however we do not expect significant change in the IR-blobs over the remaining data not directly used in creating this specialized flat-field.

with nominal cosmic ray rejection, a final `pixfrac`= 1.0 and 0.8 (for the F110W and F200LP, respectively) and pixel scale of $0''.03 \text{ pixel}^{-1}$.

A visual inspection of the 137 galaxy clusters results in the identification of possible lensing evidence in 77 clusters, of which 51 have unambiguous strong lensing evidence. The 51 secure cluster lenses with *HST* SNAP imaging form the sample used in this analysis. They are highlighted in Figure 5.1.

We note that some of the most lensing-rich fields were selected for further analysis beyond this chapter, which may include computation of detailed lens models. As these unpublished detailed lens modeling analyses are still in progress, such models are not included in this work.

Spectroscopic follow up of SPT strong lensing clusters was conducted as part of several multi-year observing programs using the Magellan telescopes (PI: Remolina González, PI: Sharon, and PI: Gladders) and Gemini (PI: Bayliss). The main goal of these programs is to measure redshifts of strongly lensed galaxies and confirm ambiguous strong lensing candidates. A portion of the spectroscopic follow-up work was published in Bayliss et al. (2016) and the rest will be presented in a future publication from the SPT collaboration. The positions and redshifts of the strongly lensed systems are used as constraints in the strong lensing analysis in order to measure the mass at the core of galaxy clusters.

5.5 Core Mass Estimates from Strong Lensing Evidence

The shallow data from the *HST* SNAP programs was sufficient to identify primary strong lensing evidence and a few secondary arcs. While detailed lens models for the most spectacular of these galaxy clusters are being computed, this endeavor is very time consuming and requires significant amount of computational resources and human time. The large sample of SPT strong lensing clusters can take advantage of fast and efficient methods to measure the mass at the core of the galaxy cluster.

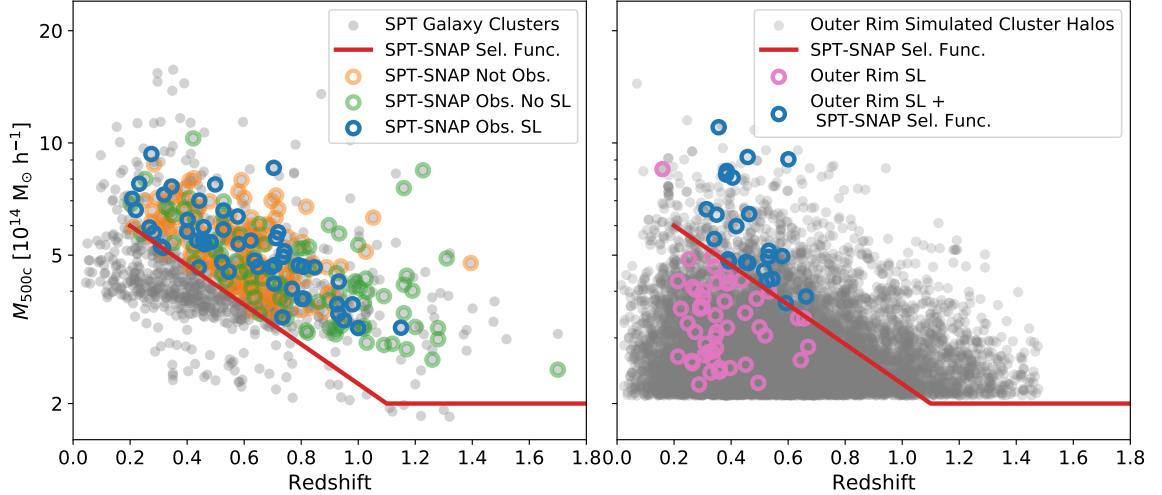


Figure 5.1: **Mass-Redshift Distribution of SPT Galaxy Clusters and Simulated Halos.** The *left* plot shows the Galaxy clusters from the South Pole Telescope. The galaxy cluster data are taken from the publicly available SPT cluster catalogs of the SPT-SZ 2500 deg² (Bleem et al., 2015) with updated masses and redshifts from Bocquet et al. (2019), the SPTpol 100 deg² from Huang et al. (2020), and the SPT-ECS Bleem et al. (2020). The 1043 SPT galaxy clusters are shown in grey. The sub-sample that was selected for the *HST* SNAP program is highlighted in color, blue circles mark clusters with unambiguous identification of strong lensing evidence from the *HST* SNAP program, green circles mark clusters that were observed but show no clear SL evidence, and orange marks targets that were not observed (see Section 5.4). This sample of SPT strong lensing clusters spans a broad range of mass and redshift; the SNAP selection function (the redshift-dependent mass threshold, red line) is motivated by enabling studies across cosmic time. The *right* plot shows the mass and redshift information for the Outer Rim simulated cluster halos. The grey circles indicate all the halos with a mass larger than $2.1 \times 10^{14} M_{\odot} h^{-1}$. The strong lensing halos are indicated in color, where blue marks those that follow the SPT SNAP selection function (red line) and pink the rest.

Remolina González et al. (2020), Chapter II, assessed the use of the mass enclosed by the Einstein radius as a zeroth-order method to measure the mass at the core of large samples of strong lensing galaxy clusters. In Remolina González et al. (2021a), Chapter III, an assessment of a slightly more complex, first-order method, was presented using a Single-Halo Lens Model to measure the mass at the core of SL clusters. We provide a brief description below of the two methods.

5.5.1 Einstein Radius

The mass enclosed by the Einstein radius makes the main assumption that the projected mass distribution of the lens is circularly symmetric (Narayan & Bartelmann, 1996; Schneider, 2006; Kochanek, 2006; Bartelmann, 2010; Kneib & Natarajan, 2011). The equation for the mass enclosed by the Einstein is as follows:

$$M(< \theta_E) = \Sigma_{\text{crit}}(z_L, z_S) \pi [D_L(z_L)\theta_E]^2, \quad (5.11)$$

where $\Sigma_{cr}(z_L, z_S)$ is the critical surface density, $D_L(z_L)$ is the angular diameter distance from the observer to the lens, z_L is the lens redshift, z_S is the background source redshift, and θ_E is the Einstein radius, which is measured between the arcs and the cluster center. Only the tangential arcs are used in this method.

Remolina González et al. (2020), Chapter II, used the Outer Rim strong lensing simulations to characterize the scatter and bias of the mass enclosed by the Einstein radius, introduced an empirical correction, and provided a set of recommendations for applying this method to large samples of observed strong lensing galaxy cluster. As per the recommendations, we use the BCG as our fixed center and the quadratic empirical correction is applied to the Einstein radii $\leq 30''$ for which a scatter of 10.9% and no bias was reported. Following Remolina González et al. (2021b), Chapter IV, who applied and tested this method in a large sample of observed strong lensing galaxy clusters with a wider range of θ_E , we use caution and apply the linear empirical

correction to the strong lensing masses where $\theta_E > 30''$ (see Figure 5.2 for the distribution of observed θ_E in the SPT SL sample) with a scatter of 12.1% as reported by Remolina González et al. (2020), Chapter II. As part of the work with simulations, Remolina González et al. (2020), Chapter II, reported that while the background source redshift is crucial for the magnification, time delays, and substructure analysis, the lack of background source redshifts adds a negligible scatter, compared to others sources of uncertainty. The cluster core mass is relatively well-constrained when assuming a background source redshift distribution.

5.5.2 Single-Halo Lens Models

The Single-Halo Lens Models (SHM; Remolina González et al., 2021a), Chapter III, uses `Lenstool` (Jullo et al., 2007) to compute a lens model with a single, large-scale, dark matter halo with 6 free parameters and no additional mass components. The SHM requires a minimum of 4 multiple images of the same background source, and uses their locations and the source and cluster redshifts as constraints.

Remolina González et al. (2021a), Chapter III, assessed this method against the same simulated data, and measured a lower scatter than the Einstein Radius method of 8.5% (with bias of 0.9%), which further improves to scatter of 3.3% and bias of 0.3% when a visual inspection of the SHM outputs is employed. However, when a background source redshift is not available, the SHM overestimate the background source redshift and underestimate the mass, resulting in a scatter of 9.9% and bias of -7.2% . The analysis by Remolina González et al. (2021a), Chapter III, reiterates the importance of spectroscopic or high-quality photometric redshifts, consistent with other work by e.g., Caminha et al. (2016); Johnson & Sharon (2016).

Which methods can be used to efficiently measure the core mass of the clusters depends on the imaging and spectroscopy information available for the SPT SL clusters, and the chance alignment of background sources which affects the lensing configu-

ration. The Einstein Radius method can be applied to any field for which lensing evidence is identified, with as little as one arc. The SHM method, although more precise, requires a minimum set of constraints – which are not available for all fields – and becomes less accurate when redshift information is lacking. For this analysis, we therefore uniformly apply the Einstein Radius method for measuring the core mass. An alternative approach could be to apply the best method that is practical for each field, i.e., detailed lens model where possible, SHM where enough constraints and spectroscopic redshifts are available, and Einstein Radius otherwise, taking advantage of the growing database of spectroscopic redshifts. We leave such an analysis for future work.

5.6 Methodology

In this section, we describe the procedures to compute the empirically corrected mass enclosed by the Einstein radius, $M_{corr}(< \theta_E)$, following the recommendations by Remolina González et al. (2020), Chapter II. We detail the methodology we use to fit the radial mass profile at the core from strong lensing and the mass at large radial scales from SZ. Last, we describe the fitting procedure of the concentration-mass relation.

5.6.1 Arc Catalogs

The positions and redshifts of the images of strongly-lensed galaxies are used to constrain the core masses of the SL clusters. Lensing evidence was identified through visual inspection in both the simulated sample and the observed sample, using morphology and color information, where available. In several cases a few morphological features (emissions knots) are clearly identified in the multiple images of the same background source, providing additional positional constraints. The catalog of simulated SL evidence is adopted from Remolina González et al. (2020),

Chapter II. The results of the visual inspection of the SPT *HST* SNAP imaging data are listed in Table B.1. The arcs are flagged as radial (R) or tangential (T), which corresponds to the primary direction of distortion. For the mass enclosed by the Einstein radius, only the tangential arcs are to be used.

5.6.2 Computing $M_{corr}(< \theta_E)$

The Einstein radius (θ_E) is measured by geometrically fitting a circle to the identified tangential arcs. We use the position of the BCG as a fixed center, following the procedure recommended by Remolina González et al. (2020), Chapter II. The BCGs were identified by their magnitudes, and confirmed through a visual inspection (see Table 5.2) resulting with sub-arcsecond BCG position accuracy. The distribution of the resulting Einstein radii of the observed sample are shown in Figure 5.2. We refer the reader to Figure 2.4 in Chapter II or Figure 4 of Remolina González et al. (2020) for the distribution of Einstein radii in the simulated sample. The mass enclosed by the Einstein radius is calculated using Equation 5.11. The corrected Einstein radius mass, $M_{corr}(< \theta_E)$, is obtained by applying the quadratic empirical correction for targets with $\theta_E \leq 30''$ and the linear empirical correction otherwise (see Section 5.5 for details). As reported by Remolina González et al. (2020), Chapter II, the lack of background source redshifts adds a negligible amount of scatter compared to other sources of error. For the observed sample, we use the background source redshifts when available and assume a background source redshift of $z_S = 2.0$ for the rest.

5.6.3 Galaxy Cluster Sample Statistics

As each galaxy cluster can have more than one Einstein radius measurement, these measurements are expected to be correlated. We follow the galaxy cluster sampling statistics employed in Remolina González et al. (2020), Chapter II; Remolina González et al. (2021a), Chapter III; and Remolina González et al. (2021b), Chap-

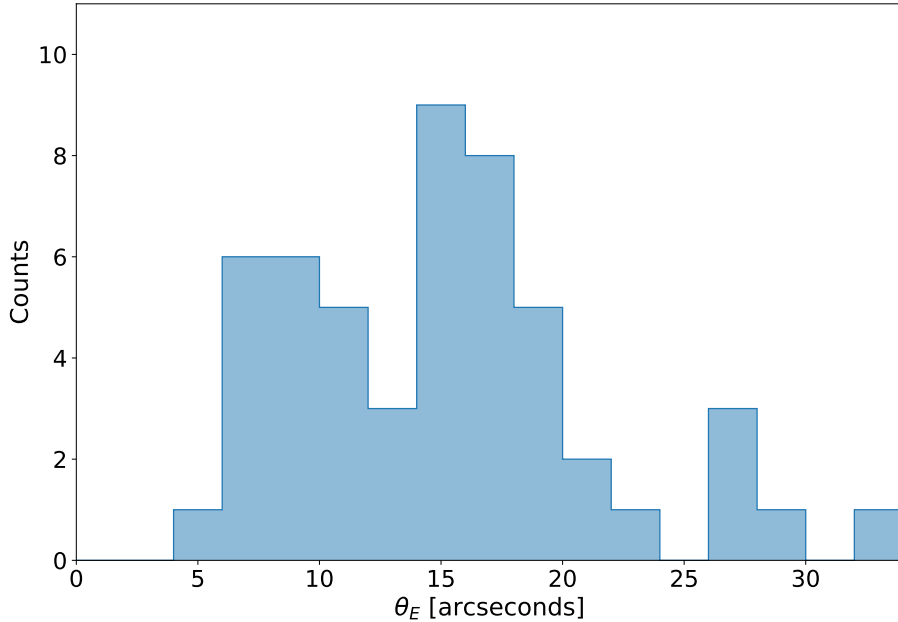


Figure 5.2: **Einstein Radius Distribution of the SPT SL SNAP sample.** The Einstein radius, in units of arcseconds, is measured from a geometric fit of a circle to the identified positions of the strong lensing evidence and the BCG as fixed center.

ter IV. We take into account multiple mass estimates for each galaxy cluster by setting the statistical weight for each cluster to be the same. For each galaxy cluster, we select at random one of the measured Einstein radii for that cluster and take a random sample from a normally distribution with a mean of the measured θ_E and uncertainty from the geometric fit, $\sigma(\theta_E)$. We repeat this process 200 times per galaxy cluster. This process results in 14,800 points for the simulated sample and 10,200 for the observational sample.

5.6.4 Fitting the NFW Profile and inferring the Concentration

To constrain the NFW profile, we combine the mass at the core from strong lensing and the large scale mass estimate from SZ. We utilize the python ensemble sample Markov chain Monte Carlo (MCMC) library `emcee`⁴ (Foreman-Mackey et al., 2013). We express the posterior probability distribution as follows:

⁴Python emcee <https://emcee.readthedocs.io/en/stable/>

$$\begin{aligned}
& p(r_s, M_0 | \theta_E, M_{corr}(< \theta_E), M_{\Delta c}, \Delta c) \propto \\
& p(r_s) \times p(M_0) \times \\
& p(M_{\Delta c} | M_0) \times p(M_{corr}(< \theta_E) | \theta_E, r_s, M_0, \Delta c),
\end{aligned} \tag{5.12}$$

where $p(r_s) \times p(M_0)$ are our priors and $p(M_{\Delta c} | M_0) \times p(M_{corr}(< \theta_E) | \theta_E, r_s, M_0)$ is the likelihood. The prior of the scale radius in units of Mpc h^{-1} :

$$p(r_s) = \begin{cases} \frac{1}{1.1} & (0.1 < r_s < 1.2) \\ 0 & (\text{elsewhere}), \end{cases} \tag{5.13}$$

and for the mass in units of $10^{14} M_{\odot} h^{-1}$:

$$p(M_0) = \begin{cases} \frac{1}{29.1} & (0.9 < M_0 < 30) \\ 0 & (\text{elsewhere}). \end{cases} \tag{5.14}$$

The priors on the mass and scale radius have been selected to be broad, flat, and conservative allowing for a broad range of fit parameter values. The likelihood is then defined as follows:

$$\begin{aligned}
p(M_{\Delta c} | M_0) = & \frac{1}{\sigma(M_{\Delta c}) \sqrt{2\pi}} \times \\
& \exp \left[-\frac{1}{2} \left(\frac{M_{\Delta c} - M_0}{\sigma(M_{\Delta c})} \right)^2 \right],
\end{aligned} \tag{5.15}$$

where $\sigma(M_{\Delta c})$ is the measured uncertainty of $M_{\Delta c}$ and

$$\begin{aligned}
p(M_{corr}(< \theta_E) | \theta_E, r_s, M_0, \Delta c) &= \frac{1}{\sigma(M_{corr}(< \theta_E))\sqrt{2\pi}} \times \\
\exp \left[-\frac{1}{2} \left(\frac{M_{corr}(< \theta_E) - M_{\text{NFW}}^{\text{proj}}(< \theta_E, r_s, M_0, \Delta c)}{\sigma(M_{corr}(< \theta_E))} \right)^2 \right], & \quad (5.16)
\end{aligned}$$

where $\sigma(M_{corr}(< \theta_E))$ is the uncertainty measured in the empirically-corrected mass enclosed by the Einstein radius and $M_{\text{NFW}}^{\text{proj}}$ is the NFW projected mass within θ_E , shown in Equation 5.9. The result of this fit is the scale radius, r_s , and its uncertainty $\sigma(r_s)$. Finally, the concentration is estimated as the ratio of the radius of interest, r_Δ , and the scale radius, r_s (Equation 5.5).

To propagate the uncertainties associated with the profile fit, to the computation of $c_{\Delta c}$ and its uncertainty, we sample 10,000 values of r_s and r_Δ , normally distributed around their respective mean value and width equal to their respective uncertainty. The uncertainty for r_Δ is derived from $\sigma(M_{\Delta c})$. We fit the resulting 10,000 concentration values with a log-normal distribution to measure the mean and standard deviation. This is repeated for each of the 200 realizations of each cluster, and the mean, and standard deviation of the resulting $c_{\Delta c}$ distribution are reported.

5.6.5 Validation of the Concentration Measurement Method

As a validation of the methods we employed here to measure the concentration, we apply the same observationally-motivated methods to the simulated clusters, and compare the resulting ‘‘observed’’ c_{500c} values to those obtained from the full 3D particle information.

We use the catalog of simulated arcs to fit θ_E and compute $M_{corr}(< \theta_E)$ as done in Section 5.6.2, then fit the NFW profile to $M_{corr}(< \theta_E)$ and M_{500c} to derive c_{500c} following the procedures detailed in Section 5.6.4. We assume that the large scale mass has the same uncertainty as the median uncertainty measured from the obser-

vations of all SPT galaxy clusters and reported in the galaxy cluster catalogs (Bleem et al., 2015, 2020; Bocquet et al., 2019; Huang et al., 2020), which is about 20%, i.e., $\sigma(M_{500c}) = 0.2 \times M_{500c}$. In Figure 5.3, we plot the comparison between the “observed” concentrations measured in our analysis for each of the 74 simulated SL cluster halos and the concentrations that were measured for the same halos using the full 3D particle information, taken from Child et al. (2018) and Li et al. (2019). We measure a scatter of 38.0% and a bias of 3.4% between the measured and “true” concentrations, which is expected, as the uncertainty in the concentrations is measured in simulations to be $\sigma(c_{\Delta c}) = c_{\Delta c}/3$.

5.6.6 Fitting the concentration-mass Relation

We fit the concentration-mass relation (Equation 5.10) to the data using the following posterior probability distribution:

$$\begin{aligned}
 p(\alpha, \beta, \gamma | c_{\Delta c}, M_{\Delta c}, z) &\propto \\
 p(\alpha) \times p(\beta) \times p(\gamma) \times & \\
 p(c_{\Delta c} | M_{\Delta c}, z, \alpha, \beta, \gamma), &
 \end{aligned}
 \tag{5.17}$$

where $p(\alpha) \times p(\beta) \times p(\gamma)$ are the priors and $p(c_{\Delta c} | M_{\Delta c}, z, \alpha, \beta, \gamma)$ is the likelihood.

We adopt broad, flat, conservative priors for α , β , and γ as follows:

$$p(\alpha) = \begin{cases} \frac{1}{6} & (0 < \alpha < 6) \\ 0 & (\text{elsewhere}), \end{cases}
 \tag{5.18}$$

$$p(\beta) = \begin{cases} \frac{1}{4} & (-2 < \beta < 2) \\ 0 & (\text{elsewhere}), \end{cases}
 \tag{5.19}$$

and

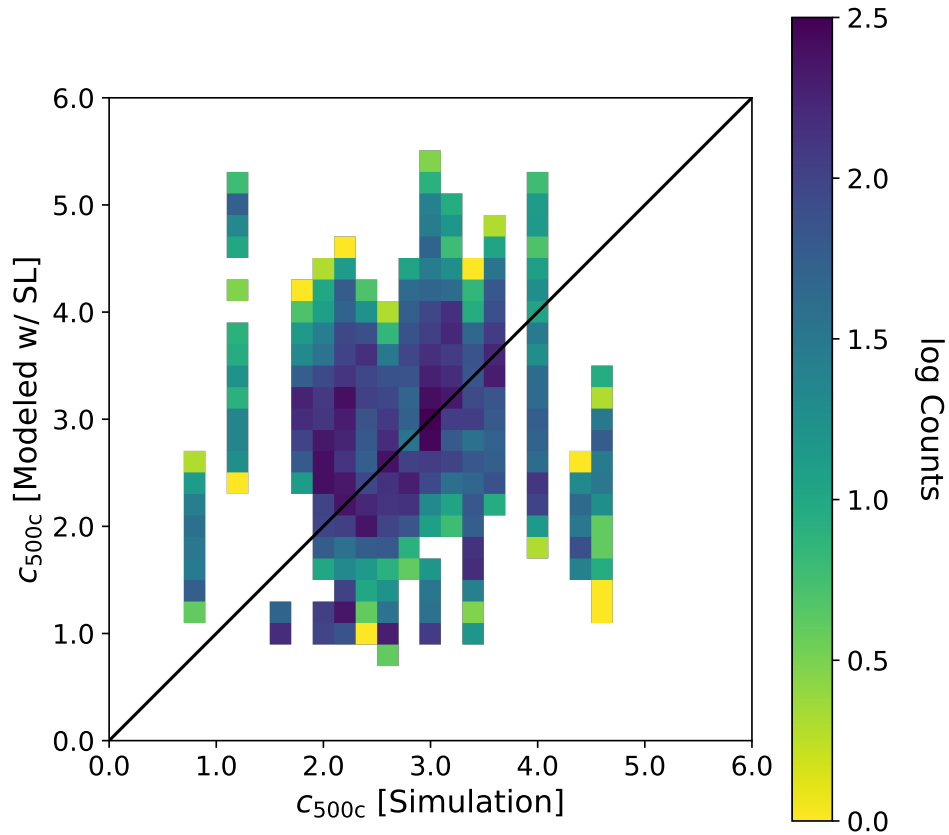


Figure 5.3: **Validation of the Concentration Measurement Methods, using the Outer Rim Simulation.** The concentration measured from the simulation (x-axis) is taken from Child et al. (2018) and Li et al. (2019) and use the full 3D particle information. The concentration modeled using the strong lensing evidence is computed following the procedure outlined in Section 5.6.4. The total number of counts is the 14,800 sampled points (see Section 5.6.3) for the 74 simulated SPT-like strong lensing galaxy clusters. The black line indicates the one-to-one relation.

$$p(\gamma) = \begin{cases} \frac{1}{10} & (-5 < \gamma < 5) \\ 0 & (\text{elsewhere}). \end{cases} \quad (5.20)$$

The likelihood is then defined using a log-normal distribution as follows:

$$p(c_{\Delta c} | M_{\Delta c}, z, \alpha, \beta, \gamma) = \frac{1}{c_{\Delta c} \sqrt{2\pi \ln(1 + \sigma(c_{\Delta c})^2 / c_{\Delta c}^{*2})}} \times \exp \left[-\frac{\left(\ln(c_{\Delta c}) - \ln\left(\frac{c_{\Delta c}^*}{\sqrt{1 + \sigma(c_{\Delta c})^2 / c_{\Delta c}^{*2}}}\right) \right)^2}{2 \ln(1 + \sigma(c_{\Delta c})^2 / c_{\Delta c}^{*2})} \right], \quad (5.21)$$

where $c_{\Delta c}^* = c_{\Delta c}^*(M_{\Delta c}, z, \alpha, \beta, \gamma)$ is the concentration mass relation shown in Equation 5.10 and $\sigma(c_{\Delta c})$ is the uncertainty measured in the concentration. We incorporate the mass uncertainty in our MCMC process by drawing a mass, at every step of the chains, from a random normal distribution with mean of $M_{\Delta c}$ and uncertainty of $\sigma(M_{\Delta c})$.

5.7 Results

In the following section, we present our results of the measurement of the c-M relation. We establish the prediction for the c-M relation using the Outer Rim simulation. We compute the concentration and c-M relation for the 51 SPT SL galaxy clusters. Last, we compare the predictions to the observations.

5.7.1 The c-M Relation in the Outer Rim SL Cluster Halos

We use the Outer Rim N-body simulation to derive a theoretical prediction of the c-M relation, following the procedures outlined in Section 5.6 for both simulated

and observed fields. In order to produce a meaningful prediction, we first apply the same selection function that was used to define the observed sample to the simulated clusters (see Section 5.4). The selection function is designed to have an equal comoving number density at $0.2 < z < 1.0$, all clusters above $z = 1.0$, and a lower limit of $z = 0.2$. With the redshift-dependent mass threshold applied, the simulated sample reduces from 74 to 23 cluster halos and our statistical sample (see Section 5.6.3) reduces from 14,800 to 4,600. Figure 5.1 shows the distribution in mass and redshift of all the Outer Rim cluster halos, the SL-selected halos, and the ones that match the SNAP program selection function. In the *right* panel Figure 5.1, we can see that there are no high- z ($z > 0.700$) strong lensing clusters. The selection function employed to identify the strong lensing clusters is the limiting factor as the lensing efficiency, D_{LS}/ds , becomes smaller for increasing lens redshift and fixed background source redshift at $z = 2.000$.

We compute the concentration-mass relation using c_{500c} and $\sigma(c_{500c})$ as measured in Section 5.6.5, M_{500c} from Li et al. (2019), $\sigma(M_{500c}) = 0.2 \times M_{500c}$, $z_{\text{pivot}} = 0.458$, $M_{\text{pivot}} = 5.14 \times 10^{14} M_{\odot} h^{-1}$, and the lens redshift, z_L , for each of the 23 simulated SL clusters that match the observed selection function. In the *left* panels of Figure 5.4, we show the posterior probability distribution of the c-M fit parameters, α , β , and γ . The median and standard deviations of the fitted parameters, the χ^2 , and p-value are listed in Table 5.1. We perform a Bayesian post-predictive test by using the fitted results to perform a forward model and compare to the observations. We find good agreement between the forward modeled and the observed data and report the median absolute deviation (MAD) in Table 5.1. We constrain the normalization of the c-M relation, α , to within 9.3%. We measure with significant evidence of $4.6 \times \sigma(\beta)$ a relation between the mass and the concentration. Last, we find that γ has a large uncertainty and is consistent with zero, meaning no conclusion can be drawn for a relation between redshift and the concentration from this simulated sub-sample. In

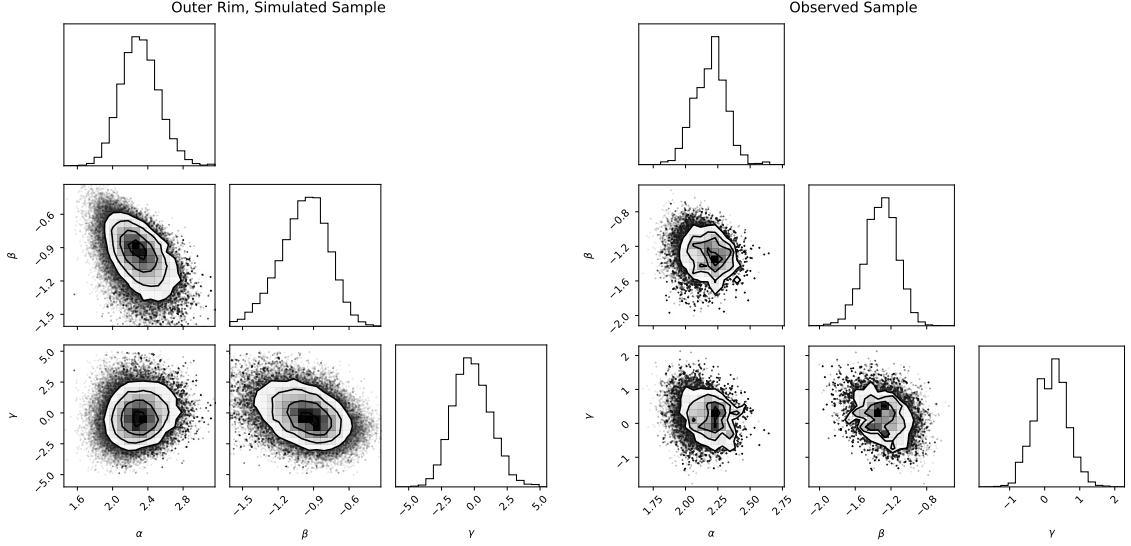


Figure 5.4: **Posterior Probability Distribution of c-M Fit Parameters for the Simulated and Observed Samples.** The fit of the c-M relation (Equation 5.10) at over-density of $\Delta c = 500c$ is computed for the simulated SPT-like halos (*left* panels) that match the *HST* SNAP selection function (see Section 5.4) and the observed (*right* panels). The posterior probability distribution for the c-M relation is defined in Equation 5.17. We report the median and standard deviation of the fit parameters in Table 5.1. We constrain the normalization, α , to within 9.3% and 5.7% for the simulations and observations respectively. We find significant evidence of $4.6 \times \sigma(\beta)$ and $7.2 \times \sigma(\beta)$, respectively, for a relation between the concentration and the mass. Last, γ is consistent with zero with large uncertainty and cannot constrain any possible evolution with redshift with these samples.

the *left* panels in Figure 5.5, we plot the concentration-mass relation for the simulated clusters for the median redshift $z = 0.458$.

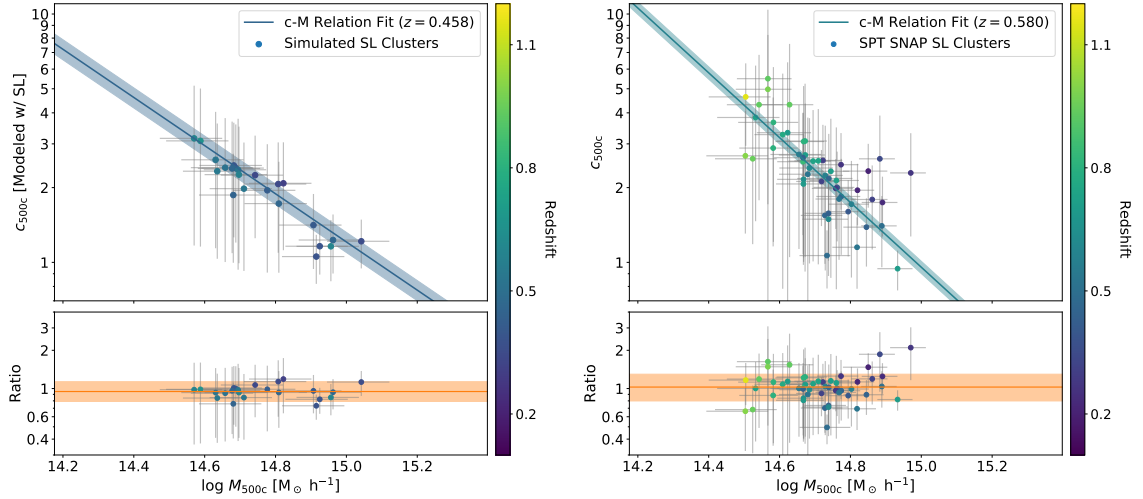


Figure 5.5: **c-M Relation Fit to the Simulated and Observed SL Clusters for an Over-density of $\Delta c = 500c$.** The panels on the *left* are for the simulated halos that match the SNAP program selection function (see Section 5.4) and the *right* are for the observed SL clusters. The *top* plots shows the concentration computed using the combination of strong lensing and a large scale mass. For the simulated halos the mass measurements were computed by Li et al. (2019) and for the observations were measured by SPT (Williamson et al., 2011; Bleem et al., 2015, 2020; Bocquet et al., 2019; Huang et al., 2020). The grey error bars indicate the standard deviation of the measurements (see Section 5.6.5 for a description of the uncertainties). The solid line is the c-M fit plotted for the median redshift of the simulated clusters of $z = 0.458$ and for the observed SL clusters of $z = 0.580$. The shaded regions represent the uncertainty in the normalization fit parameter, α . The colors of the lines, shaded regions, and points indicate their corresponding redshift. The *bottom* plots show the ratio between the measurement and the fit at each cluster or halo redshift. The solid orange line indicates the median ratio and the shaded region indicates the 16th and 84th percentiles of the distribution when taking into account the uncertainty from all three fit parameters (α , β , and γ).

Table 5.1. Results of the c-M Relation for Strong Lensing Galaxy Clusters.

Reference	M_{pivot} $10^{14} M_{\odot} h^{-1}$	z_{pivot}	α median $\pm \sigma(\alpha)$	β median $\pm \sigma(\beta)$	γ median $\pm \sigma(\gamma)$	χ^2	p-value	MAD
Outer Rim SPT-like	5.14	0.458	2.30 ± 0.21	-0.97 ± 0.21	-0.24 ± 1.44	5.27	1.00	0.14
SPT	5.28	0.580	2.20 ± 0.13	-1.30 ± 0.18	0.20 ± 0.46	30.44	0.99	0.30

Note. — c-M relation (Equation 5.10) fit results and pivot parameters for the observed SPT SNAP SL sample, and the strong lensing halos from the Outer Rim simulation that follow the same selection function. The median and standard deviation of the fit parameters (α , β , and γ) are reported. We show the pivot values for the mass, M_{pivot} , and the redshift, z_{pivot} , used in the c-M relations. We list various statistical evaluations of the fits including a Pearson's χ^2 and p-value, and a Bayesian post-predictive test reporting the median absolute deviation (MAD). We report the measurements for the over-density $\Delta c = 500c$.

5.7.2 The c-M Relation in Mass-Limited Vs. Strong Lensing Selected Samples as Inferred from Simulations

In this subsection, we compare and contrast the predicted concentration-Mass relation between mass-limited and strong lensing selected samples. For this comparison, we use the 14,800 and 4,600 statistical points from the Outer Rim strong lensing simulated halos and those that follow the SPT SNAP selection function, respectively. We also include the c-M prediction from Meneghetti et al. (2014) for strong lensing halos. In addition to the strong lensing selected samples, we use three predictions of the c-M relation in literature from simulations by Duffy et al. (2008); De Boni et al. (2013); and Child et al. (2018). All of these works use a similar functional form of the c-M relation as the one adopted in this analysis. In the following paragraphs we provide a brief description of the simulations and identify which reported results are used as comparisons.

Meneghetti et al. (2014) used the MUSIC-2 hydrodynamical simulations to measure the c-M relation of galaxy clusters. Particular to the analysis performed by Meneghetti et al. (2014) is the incorporation of the selection function of The Cluster Lensing and Supernova Survey with *Hubble* (CLASH; Postman et al. 2012). This work included a focus on strong gravitational lensing clusters. We use the reported results for the NFW profile, 2D analysis, and complete sample with a strong gravitational lensing selection.

Duffy et al. (2008) computed the c-M relation using three large, N-body cosmological simulations of various sizes (25, 100, and 400 co-moving Mpc h^{-1}) adopting a WMAP-5. The simulated dark matter halos selected span the redshift range of $z = 0 - 2$ and a mass $M_{200c} = 10^{11} - 10^{15} M_{\odot} h^{-1}$. For our comparison, we use the reported results for the full sample, redshift $z = 0 - 2$, and $\Delta c = 200c$.

De Boni et al. (2013) used hydrodynamical simulations with five different dark energy prescriptions. All clusters with masses above $M_{200c} > 10^{14} M_{\odot} h^{-1}$ and a

selected sub-sample going down to $M_{200c} > 10^{13} M_{\odot} h^{-1}$ are used. The redshift range explored was from $z = 0 - 1$. We use the results reported for the Λ CDM cosmology for the complete sample of clusters.

Child et al. (2018) used the dark matter only Outer Rim simulation (see Section 5.3) to measured the c-M relation for galaxy groups and clusters. The concentrations and masses computed by Child et al. (2018) used the full 3D particle information and are used as a comparison for the simulated SPT-like halo sample in this work (see Section 5.6.5). In this Chapter, we use the reported c-M relation for individual halos, for the complete sample, and with redshift range $0 < z < 1$.

We plot in Figure 5.6 the six different concentration-mass relations. As mention in Section 5.2, we expect to find differences between these c-M relations as they are computed for different selection functions. Particularly important to note is that strong lensing halos are not representative of a mass-limited sample of dark matter halos. In this figure, we highlighted the different samples with blue the mass-limited samples and in orange the strong lensing samples. we note that the selection functions vary significantly in terms of redshift and mass limits, nevertheless, we clearly see difference in the slope of the simulation predicted c-M relations with the strong lensing samples being steeper than the mass-limited samples. The over-concentration of the strong lensing galaxy clusters compared to predictions and mass-limited samples has been reported in the literature (e.g., Oguri & Blandford 2009; Gralla et al. 2011).

5.7.3 The c-M Relation in Observed SL Clusters

We compute the concentration c_{500c} for each of the 10,200 statistically sampled points from the SPT SL galaxy clusters that were observed in the SNAP program. We follow the fitting procedures outlined in Section 5.6.4. The large scale mass, M_{500c} , is taken from the SPT catalogs (see Section 5.4). The uncertainty of the large scale mass, $\sigma(M_{\Delta c})$, was reported for an asymmetric normal distribution with an upper

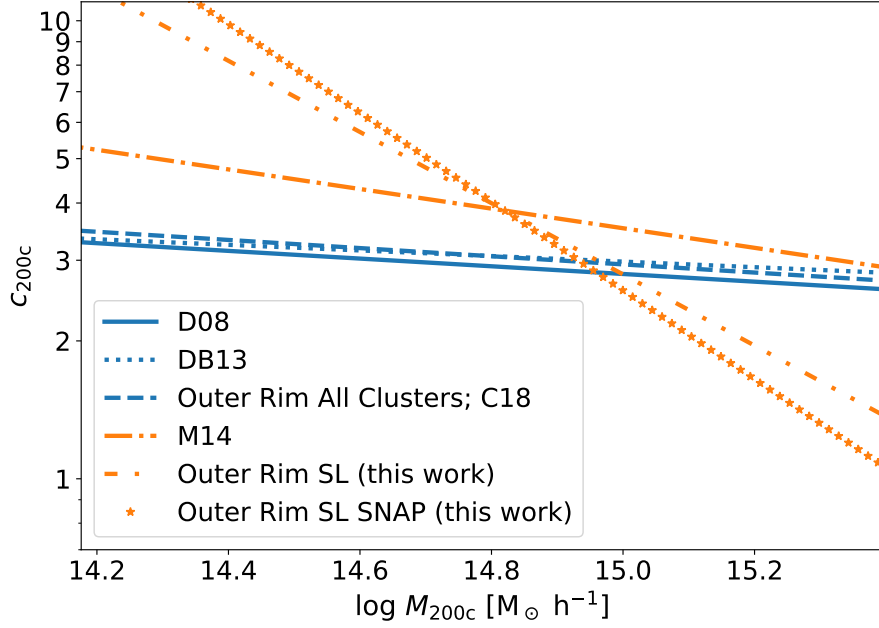


Figure 5.6: **Comparison of Predicted c-M Relations of Mass-Limited Vs. Strong Lensing Selected Samples.** The predicted concentration-Mass relations are shown for $\Delta c = 200c$. In blue, we show the c-M relations for the mass-limited samples and in orange the strong lensing selected samples. D08, DB13, C18, and M14 represent the c-M relations from literature reported by Duffy et al. (2008); De Boni et al. (2013); Child et al. (2018); and Meneghetti et al. (2014). The Outer Rim SL represent all the strong lensing halos identified in the simulation (see Sections 2.3, and 5.3) and the Outer Rim SL SNAP represents the Outer Rim strong lensing halos that follow the observation selection function used for the *HST* SNAP program (see Section 5.4). We note that the selection functions vary significantly in terms of redshift and mass limits, nevertheless, in all cases of strong lensing selected samples the predicted c-M relations are steeper compared those of the mass-limited samples.

and lower error. In Equation 5.15, we therefore use the lower error if $M_0 \leq M_{500c}$ and the upper error if $M_0 > M_{500c}$. The results for the 51 SPT clusters are listed in Table 5.2.

We then proceed to fit the c-M relation following the procedure detailed in Section 5.6.6 using c_{500c} , $\sigma(c_{500c})$, M_{500c} and its asymmetric uncertainty, $z_{\text{pivot}} = 0.580$, $M_{\text{pivot}} = 5.28 \times 10^{14} M_{\odot} h^{-1}$, and the lens redshift, z_L . To incorporate the uncertainty in the masses into our fitting procedure (see Section 5.6.6) we perform this step by drawing a mass from the asymmetric normal distribution. In *right* panels in Figure 5.4, we plot the posterior probability distribution of the c-M parameters and report the median and standard deviation in Table 5.1. With the observational data, we constrain the normalization of the c-M relation, α , to within a 5.7%. We measure a $7.2 \times \sigma(\beta)$ significance of a relation between the mass and concentration. Last, γ has large uncertainties and is consistent with zero, so no conclusion can be made regarding a relation between redshift and concentration from this sample. In the *right* panels in Figure 5.5, we show the concentration-mass relation for the SPT SL cluster sample for a median redshift of $z = 0.580$.

Table 5.2: SPT SNAP Strong Lensing Galaxy Clusters.

SPT ID	R.A. (J2000)	Decl. (J2000)	z_L	M_{500c} ($10^{14} M_\odot h^{-1}$)	c_{500c}	M_{200c} ($10^{14} M_\odot h^{-1}$)	c_{200c}
SPT-CL 0002-5557	0.51575	-55.96764	1.150	$3.20^{+0.56}_{-0.68}$	4.64 ± 1.69	$4.25^{+0.91}_{-1.00}$	6.90 ± 2.40
SPT-CL 0005-3751	1.43962	-37.86826	0.483	$5.42^{+0.89}_{-0.89}$	1.07 ± 0.28	$9.82^{+1.99}_{-1.97}$	1.75 ± 0.42
SPT-CL 0049-2440	12.29560	-24.67860	0.527	$6.59^{+0.86}_{-0.98}$	1.15 ± 0.37	$11.72^{+2.24}_{-2.26}$	1.88 ± 0.55
SPT-CL 0100-5359	15.01969	-53.98683	1.000	$3.19^{+0.51}_{-0.71}$	2.69 ± 1.38	$4.68^{+1.02}_{-1.15}$	4.11 ± 1.99
SPT-CL 0118-5156	19.60321	-51.94148	0.705	$4.20^{+0.69}_{-0.76}$	3.33 ± 3.06	$6.27^{+1.50}_{-1.45}$	5.03 ± 4.33
SPT-CL 0150-4511	27.64706	-45.18675	0.308	$5.28^{+0.71}_{-0.82}$	2.57 ± 1.01	$7.79^{+1.47}_{-1.52}$	3.95 ± 1.45
SPT-CL 0216-2609	34.15122	-26.16275	0.791	$4.70^{+0.72}_{-0.80}$	3.08 ± 2.16	$6.94^{+1.50}_{-1.49}$	4.68 ± 3.09
SPT-CL 0219-4934	34.81437	-49.58168	0.546	$4.52^{+0.70}_{-0.76}$	2.72 ± 1.59	$6.74^{+1.43}_{-1.43}$	4.16 ± 2.28
SPT-CL 0240-5946	40.15991	-59.76362	0.400	$5.79^{+0.69}_{-0.82}$	2.00 ± 0.79	$9.00^{+1.65}_{-1.69}$	3.13 ± 1.15
SPT-CL 0243-4833	40.91207	-48.56091	0.498	$7.74^{+0.79}_{-0.97}$	1.40 ± 0.45	$13.02^{+2.25}_{-2.31}$	2.25 ± 0.66
SPT-CL 0252-2100	43.11358	-21.01422	0.712	$5.56^{+0.71}_{-0.83}$	2.33 ± 1.46	$8.61^{+1.74}_{-1.75}$	3.59 ± 2.11
SPT-CL 0304-5404	46.21924	-54.07045	0.734	$3.41^{+0.57}_{-0.75}$	3.83 ± 2.37	$4.75^{+1.06}_{-1.16}$	5.75 ± 3.37
SPT-CL 0307-6225	46.81905	-62.44479	0.580	$5.36^{+0.64}_{-0.77}$	2.24 ± 1.31	$8.35^{+1.64}_{-1.67}$	3.47 ± 1.90
SPT-CL 0310-4647	47.63554	-46.78564	0.707	$4.70^{+0.65}_{-0.74}$	2.71 ± 1.65	$7.05^{+1.43}_{-1.45}$	4.14 ± 2.38

Table 5.2: SPT SNAP Strong Lensing Galaxy Clusters (cont'd).

SPT ID	R.A. (J2000)	Decl. (J2000)	z_L	M_{500c} ($10^{14} M_\odot h^{-1}$)	c_{500c}	M_{200c} ($10^{14} M_\odot h^{-1}$)	c_{200c}
SPT-CL 0319-2244	49.92001	-22.73908	0.458	$5.94^{+0.78}_{-0.89}$	1.84 ± 0.77	$9.47^{+1.82}_{-1.85}$	2.89 ± 1.12
SPT-CL 0328-2140	52.05659	-21.67204	0.577	$6.35^{+0.76}_{-0.88}$	1.72 ± 0.85	$10.39^{+2.00}_{-2.02}$	2.71 ± 1.24
SPT-CL 0352-2644	58.17660	-26.72820	0.808	$4.65^{+0.66}_{-0.78}$	3.07 ± 2.06	$6.84^{+1.43}_{-1.45}$	4.66 ± 2.95
SPT-CL 0352-5647	58.23964	-56.79771	0.649	$4.65^{+0.63}_{-0.73}$	2.16 ± 1.11	$7.22^{+1.45}_{-1.47}$	3.35 ± 1.61
SPT-CL 0404-4418	61.19185	-44.30015	0.847	$4.64^{+0.62}_{-0.72}$	2.54 ± 1.46	$7.01^{+1.40}_{-1.42}$	3.91 ± 2.11
SPT-CL 0406-4805	61.73024	-48.08249	0.737	$4.95^{+0.61}_{-0.73}$	2.56 ± 1.55	$7.53^{+1.51}_{-1.51}$	3.92 ± 2.23
SPT-CL 0411-2158	62.78063	-21.97577	0.636	$4.84^{+0.80}_{-0.86}$	2.40 ± 1.41	$7.42^{+1.64}_{-1.62}$	3.70 ± 2.03
SPT-CL 0441-4855	70.44957	-48.92332	0.741	$5.12^{+0.62}_{-0.74}$	2.56 ± 1.58	$7.76^{+1.52}_{-1.54}$	3.93 ± 2.27
SPT-CL 0456-4906	74.11899	-49.09963	0.926	$3.69^{+0.61}_{-0.67}$	5.49 ± 4.91	$5.03^{+1.13}_{-1.12}$	8.10 ± 6.90
SPT-CL 0509-5342	77.33917	-53.70350	0.461	$5.35^{+0.64}_{-0.78}$	1.55 ± 0.56	$8.81^{+1.63}_{-1.67}$	2.46 ± 0.82
SPT-CL 0528-5300	82.02223	-52.99816	0.768	$4.06^{+0.60}_{-0.68}$	3.27 ± 2.49	$5.97^{+1.29}_{-1.29}$	4.95 ± 3.54
SPT-CL 0532-3701	83.23193	-37.02680	0.275	$9.34^{+0.96}_{-1.17}$	2.29 ± 1.02	$14.20^{+2.50}_{-2.56}$	3.55 ± 1.48
SPT-CL 0535-4801	83.95500	-48.02644	0.932	$4.25^{+0.71}_{-0.72}$	4.31 ± 3.26	$5.95^{+1.31}_{-1.27}$	6.44 ± 4.63
SPT-CL 0544-3950	86.24155	-39.82857	0.523	$4.78^{+0.73}_{-0.82}$	2.26 ± 1.56	$7.53^{+1.68}_{-1.67}$	3.50 ± 2.25

Table 5.2: SPT SNAP Strong Lensing Galaxy Clusters (cont'd).

SPT ID	R.A. (J2000)	Decl. (J2000)	z_L	M_{500c} ($10^{14} M_\odot h^{-1}$)	C_{500c}	M_{200c} ($10^{14} M_\odot h^{-1}$)	C_{200c}
SPT-CL 0555-6406	88.84556	-64.10371	0.345	$7.64^{+0.78}_{-0.97}$	2.61 ± 1.29	$11.36^{+2.01}_{-2.06}$	4.01 ± 1.86
SPT-CL 0556-5403	89.20193	-54.05814	0.930	$3.48^{+0.58}_{-0.66}$	4.31 ± 2.53	$4.78^{+1.02}_{-1.06}$	6.44 ± 3.60
SPT-CL 0557-4113	89.44749	-41.22416	0.808	$3.83^{+0.67}_{-0.78}$	3.66 ± 2.45	$5.43^{+1.24}_{-1.28}$	5.51 ± 3.49
SPT-CL 0643-4535	100.93248	-45.59659	0.950	$3.34^{+0.57}_{-0.73}$	2.61 ± 1.43	$4.97^{+1.12}_{-1.20}$	4.01 ± 2.06
SPT-CL 0647-5828	101.98022	-58.48075	0.441	$4.64^{+0.72}_{-0.79}$	2.64 ± 1.35	$6.90^{+1.44}_{-1.45}$	4.05 ± 1.95
SPT-CL 0650-4503	102.68311	-45.06605	0.402	$6.22^{+0.71}_{-0.87}$	1.60 ± 0.54	$10.14^{+1.83}_{-1.88}$	2.54 ± 0.80
SPT-CL 1000-3016	150.00634	-30.27612	0.207	$7.09^{+0.94}_{-1.08}$	2.33 ± 0.67	$10.58^{+1.93}_{-2.01}$	3.60 ± 0.97
SPT-CL 1042-2847	160.56411	-28.79316	0.719	$5.76^{+0.91}_{-0.91}$	2.14 ± 1.36	$9.14^{+2.00}_{-1.94}$	3.32 ± 1.96
SPT-CL 1153-2137	178.37008	-21.63190	0.456	$5.48^{+0.91}_{-1.02}$	2.18 ± 1.11	$8.49^{+1.87}_{-1.89}$	3.38 ± 1.61
SPT-CL 2023-5535	305.83677	-55.59737	0.232	$7.77^{+0.79}_{-0.98}$	1.74 ± 0.47	$12.33^{+2.06}_{-2.14}$	2.75 ± 0.69
SPT-CL 2025-5117	306.47298	-51.28642	0.220	$6.61^{+0.76}_{-0.92}$	1.95 ± 0.54	$10.22^{+1.78}_{-1.85}$	3.05 ± 0.79
SPT-CL 2032-5627	308.05854	-56.43684	0.284	$5.74^{+0.67}_{-0.83}$	1.98 ± 0.62	$8.87^{+1.58}_{-1.64}$	3.10 ± 0.90
SPT-CL 2108-4445	317.19779	-44.76834	0.803	$3.82^{+0.67}_{-0.75}$	2.89 ± 1.73	$5.63^{+1.27}_{-1.30}$	4.40 ± 2.47
SPT-CL 2112-4434	318.21757	-44.58255	0.527	$5.86^{+0.69}_{-0.83}$	1.80 ± 0.78	$9.39^{+1.76}_{-1.80}$	2.83 ± 1.13

Table 5.2: SPT SNAP Strong Lensing Galaxy Clusters (cont'd).

SPT ID	R.A. (J2000)	Decl. (J2000)	z_L	M_{500c} ($10^{14} M_\odot h^{-1}$)	c_{500c}	M_{200c} ($10^{14} M_\odot h^{-1}$)	c_{200c}
SPT-CL 2124-6124	321.15750	-61.40781	0.435	$5.47^{+0.66}_{-0.79}$	1.58 ± 0.56	$8.97^{+1.65}_{-1.70}$	2.50 ± 0.82
SPT-CL 2130-6458	322.73405	-64.97796	0.316	$5.23^{+0.66}_{-0.79}$	2.12 ± 0.72	$7.99^{+1.47}_{-1.53}$	3.29 ± 1.04
SPT-CL 2134-4109	323.52544	-41.15859	0.696	$4.65^{+0.67}_{-0.76}$	2.07 ± 1.09	$7.30^{+1.51}_{-1.53}$	3.22 ± 1.58
SPT-CL 2138-6008	324.50338	-60.13158	0.319	$7.27^{+0.76}_{-0.93}$	1.79 ± 0.67	$11.58^{+2.02}_{-2.08}$	2.82 ± 0.97
SPT-CL 2244-3704	341.05410	-37.06673	0.443	$7.00^{+0.82}_{-0.98}$	1.39 ± 0.42	$11.80^{+2.12}_{-2.18}$	2.23 ± 0.62
SPT-CL 2250-4808	342.67555	-48.14311	0.980	$3.69^{+0.61}_{-0.70}$	4.98 ± 3.26	$4.99^{+1.09}_{-1.11}$	7.38 ± 4.62
SPT-CL 2254-4620	343.58547	-46.34677	0.268	$5.94^{+0.71}_{-0.86}$	2.47 ± 0.84	$8.79^{+1.57}_{-1.64}$	3.81 ± 1.21
SPT-CL 2256-2241	344.00971	-22.68499	0.623	$5.47^{+0.74}_{-0.86}$	1.49 ± 0.61	$9.16^{+1.82}_{-1.84}$	2.38 ± 0.90
SPT-CL 2305-2248	346.29417	-22.82015	0.704	$8.57^{+0.87}_{-1.06}$	0.94 ± 0.17	$15.94^{+2.60}_{-2.69}$	1.57 ± 0.26

R.A. and Decl. are the right ascension and declination, respectively, of the selected BCG, z_L is the lens redshift of the galaxy cluster, and M_{500c} is the SZ mass from Williamson et al. (2011); Bleem et al. (2015, 2020); Bocquet et al. (2019); Huang et al. (2020), described in Section 5.4. The mean and standard deviation of the concentration, c_{500c} , were computed in Section 5.6.5. We also report M_{200c} and c_{200c} , which we converted from M_{500c} and c_{500c} using the mass and concentration conversion derived in Hu & Kravtsov (2003); the errors are propagated as in Section 5.6.5.

5.7.4 c-M relation: Comparison Between Simulations and Observations

In this subsection, we compare the results of the concentration-mass relation measured for the observed SNAP SPT SL sample and the simulated strong lensing clusters from the Outer Rim. In Figure 5.7, we plot the concentration-mass relation from the simulations (see Section 5.7.1) for the median redshift of the SPT SL clusters, $z = 0.580$. We perform a Pearson’s χ^2 test with a null hypothesis that the prediction from the simulated c-M relation is a good fit to the measured data from the observed SPT SL sample. The result of the Pearson’s test are $\chi^2 = 40.85$ and p-value of 0.72, indicating that the prediction from simulations represents well the observed data. The *top* panel in Figure 5.7 shows the concentration and mass measurements of the observed SPT SL galaxy clusters, with the color of each data point indicating the cluster redshift. The solid line is not a fit, rather it represents the c-M prediction from Section 5.7.1 for the median redshift of the SNAP SPT SL cluster sample; the shaded region is the one-sigma uncertainty in the predicted normalization parameter. The color of the solid line and shaded region indicate the median redshift. The *bottom* plot shows the ratio between the concentration predicted for each cluster’s mass and redshift by the c-M relation that was derived from the simulations, and the observed concentration. The solid red line indicates the median and the shaded region represents the 14th and 86th percentiles of the ratios.

5.8 Summary and Conclusions

In this work, we measure the concentration-mass relation of strong lensing galaxy clusters in both the Outer Rim simulation and a large sample of strong lensing SPT clusters, uniformly observed by *HST*, with a well-understood selection function. The c-M relation can be used as a direct comparison between predictions from simulations and measurements from observations. The concentration of galaxy clusters is com-

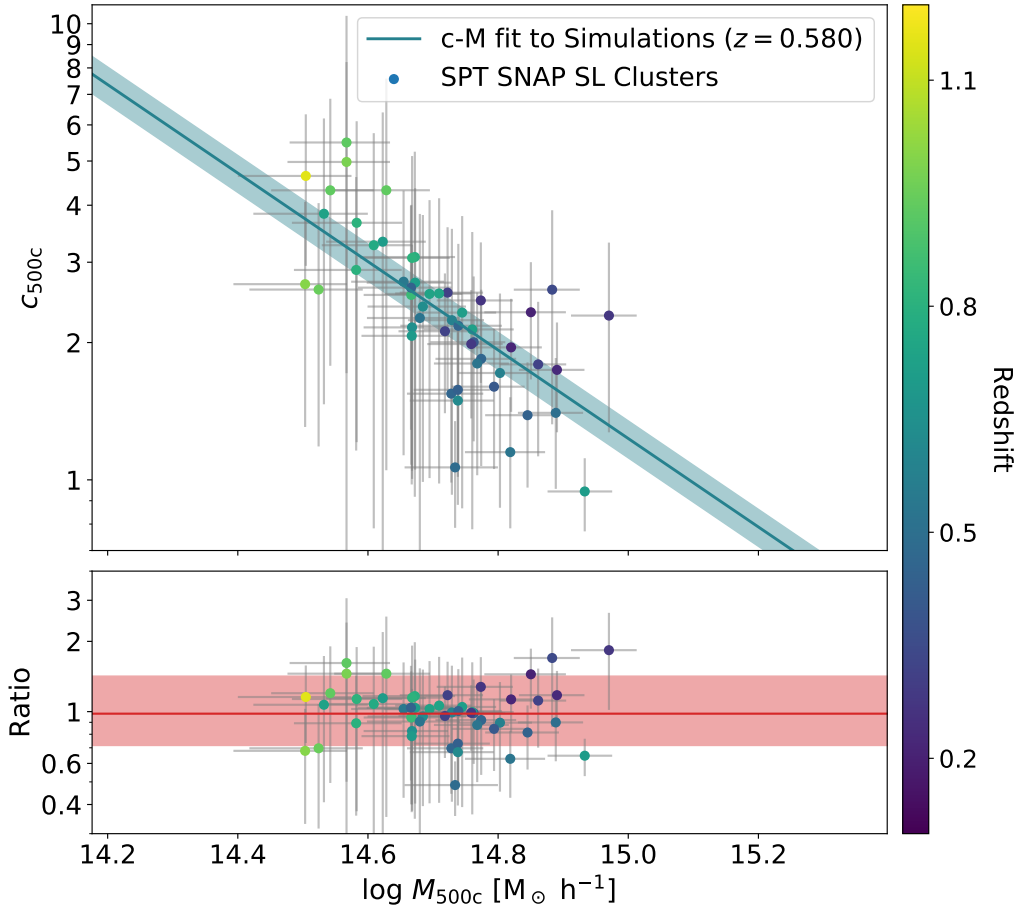


Figure 5.7: **c-M Relation Comparison Between the Predictions and Observations for an Over-density of $\Delta c = 500c$.** This figure follows the structure of the panels in Figure 5.5. In the *top* panel the points represent the observational data, while the line is the c-M relation measured in Section 5.7.1 for the median redshift of the observations. The *bottom* plot shows the ratio between the prediction from simulation and the observational data for the redshift of each SPT galaxy cluster. The solid red line indicates the median of the distribution and the shaded region indicates the 16th and 84th percentiles of the distribution when taking into account the uncertainty from all three (α , β , and γ) fit parameters. We perform a Pearson's χ^2 test resulting on a $\chi^2 = 40.85$ and a p-value of 0.72 meaning that the predictions is a good representation of the observed data.

puted after fitting the cluster’s mass density distribution with an NFW profile. To constrain the NFW profile, we combine a core mass estimate from strong gravitational lensing with a large scale SZ-inferred mass.

The SPT selection function, nearly mass limited and redshift independent, is of particular interest to enable studies of galaxy clusters through cosmic time. SPT has detected over a thousand galaxy cluster and measured their masses using the SZ effect. A large, uniform, optical imaging, *Hubble* Space Telescope Snapshot program observed 137 SPT galaxy clusters from which 51 clusters were identified for their unambiguous strong lensing evidence. This sample of SPT strong lensing galaxy clusters is unique due to its large sample size and broad mass and redshift range.

The SPT data provide a mass measurement at large scale cluster-centric radii from the SZ effect. Here, we compute the mass at the core using the strong lensing evidence. The large sample size of the SPT strong lensing galaxy clusters requires the use of efficient and accurate mass estimates to perform this analysis in a timely manner. Remolina González et al. (2020), Chapter II, used the Outer Rim cosmological simulation to assess the mass enclosed by the Einstein radius as an efficient core mass estimate and developed recommendations for its application to large samples of galaxy clusters. Following the established recommendations, we measure the mass enclosed by the Einstein radius of the galaxy clusters for the large sample of SPT SL clusters.

We used the large box, N-body, Outer Rim cosmological simulation to test our fitting procedures and compute the prediction of the c - M relation. We compare our “observationally motivated” concentration measurements with those from Child et al. (2018), who used the same simulation to measure the concentration-mass relation, from the full 3D particle information. Last, we compare the results from the observed sample to our measurement from the Outer Rim simulation, using the same selection function that defined the observed target list to generate the simulated sample. We

conclude with the following results:

- We perform a visual inspection of 137 SPT galaxy clusters observed through the large *HST* SNAP program. The shallow *HST* imaging allows for the identification of the primary and a few secondary lensed arcs. 51 galaxy clusters (see Table 5.2) were identified for unambiguous strong lensing evidence. The strong lensing evidence is reported in Table B.1. The position information of the lensing evidence is used as constraints to measure the core mass of the galaxy clusters.
- Given the number of available source redshifts and constraints in each cluster, we find that the best fast method for estimating the strong-lensing inferred core mass is the mass enclosed by the Einstein radius, which was assessed by Remolina González et al. (2020), Chapter II, as it requires a minimal number of constraints. In particular, the lack of a background source redshift introduces a negligible amount of uncertainty compared to other sources of error when a background source redshift distribution is assumed. We assume a background source redshift of $z = 2$, typical for giant arcs (Bayliss et al., 2011b).
- Using the Outer Rim simulation, we demonstrate that our method for measuring the concentration, c_{500c} , provides results that are consistent with those measured using the full 3D particle information from Child et al. (2018). We find a scatter of 38.0% and bias of 3.4% between these concentrations, which matches the expectation from literature of $\sigma(c_{\Delta c}) = c_{\Delta c}/3$.
- We fit the c-M relation (Equation 5.10) to the simulated SL clusters and to the observed SPT clusters for an over-density of $\Delta c = 500c$. We constrain the normalization of the c-M relation to within a 9.3% and 5.7%, respectively. We find significant evidence of $4.6 \times \sigma(\beta)$ and $7.2 \times \sigma(\beta)$, respectively, for a relation

between the concentration and the mass. Last, we find that γ has large uncertainties and is consistent with zero in both simulations and observations, so no conclusion can be made regarding the relation between the redshift and concentration from this sample.

- We compare the predicted c-M relation from the simulated halos that match our observational selection function to the observed SPT SNAP clusters. The normalization parameter of the c-M relation, α , of the the simulated sample ($\alpha = 2.30 \pm 0.21$) and observed sample ($\alpha = 2.20 \pm 0.13$) are consistent with each other. We measure a scaling exponent between the mass and the concentration, β , of -0.97 ± 0.21 in the simulations and -1.30 ± 0.18 in the observed sample. These values are consistent to within 1.7 sigma of each other. Last, the exponential scaling between the concentration and the redshift for the simulated and observed sample are -0.24 ± 1.44 and 0.20 ± 0.46 , respectively. These γ values are consistent with each other and consistent with $\gamma = 0$.
- As a comparison tool between the prediction from the simulated sample and the observed SPT SNAP SL clusters, we perform a Pearson's χ^2 test with the null hypothesis that the prediction matches the observed data. We find a $\chi^2 = 40.85$ and a p-value = 0.72, meaning we do not reject our null hypothesis. The direct comparison is shown in Figure 5.7 and the prediction is found to represent the observed data.

The work presented here leverages the use of a large sample of strong lensing galaxy clusters with a broad redshift and mass range to measure the concentration-mass relation across cosmic time. We report an agreement between the c-M predictions from the Outer Rim simulation and the observed clusters, i.e., we find no tensions with Λ CDM. As more strong lensing galaxy clusters are going to be discovered and characterized in large scale surveys, the simulations will need to span a broader redshift

range extending to $z \sim 2$, and larger cosmological volume to improve the statistics of high-mass halos.

CHAPTER VI

Future Directions and Conclusions

This collection of works shows the use of simulations and observations to measure the concentration-Mass relation for a large sample of strong lensing galaxy clusters extending through cosmic time with a well understood selection function. I combined the mass estimates at the core from strong gravitational lensing and outskirts from SZ to model the radial mass distribution of South Pole Telescope strong lensing galaxy clusters and compute their concentration. I presented the assessment of two efficient, accurate, and precise methods to measure the mass at the core of galaxy clusters using the identified strong gravitational lensing evidence. In addition to the assessment, recommendations on the application of these techniques were established for their use on large samples of strong lensing galaxy clusters. I took the assessment and recommendations of these two methods done in simulations and demonstrated their application on a large sample of observed strong lensing galaxy clusters. In this chapter, I summarize the work presented in this thesis and describe future directions of this work as new large astronomical surveys come online.

6.1 Summary

Galaxy clusters, as the largest gravitationally bound objects in the universe, are useful cosmological probes. Of particular interest is their mass distribution from which

we can learn about properties of dark and baryonic matter. The concentration-Mass relation can be directly measured in both state-of-the-art cosmological simulations and observed galaxy clusters, making it useful for comparing theoretical predictions and observations. A combination of mass estimates extending across the galaxy cluster radial scales provides the best constraints. Here, we combined the mass at the core from strong lensing with that at large scales measured by SPT using the SZ effect. Strong gravitational lensing by galaxy clusters provides a unique opportunity to study in detail the core mass distribution of galaxy clusters, as the observed strong lensing evidence is highly-sensitive to the projected mass distribution. With thousands of strong lensing galaxy clusters expected to be identified in current and upcoming large astronomical surveys, fast and efficient methods to measure the mass at the core of strong lensing galaxy clusters are needed. Detailed lens models can be highly complex allowing for the flexibility required for studies of cosmology, the galaxy cluster matter substructure, the uncorrelated structure along the line-of-sight, and the magnified background universe. The versatility of detailed lens models requires a large number of constraints and multiple statistical assessments to evaluate lens models. For a rich strong lensing galaxy cluster, a high-fidelity lens model requires extensive follow-up observations, significant amount of computer resources, modeling iterations, and human time.

In Chapter II, I present the work to assess an efficient and accurate method to measure the mass at the core of strong lensing galaxy clusters. The mass enclosed by the Einstein radius is a zeroth-order technique which assumes the mass distribution of the galaxy cluster is spherically symmetric. As part of this work (Remolina González et al., 2020), we quantify the uncertainty and bias of the mass measurement for three different centering hypothesis. We measure a scatter of 13.9% and bias of 8.8% for the fixed center on the highest surface density position, a scatter of 14.8% and bias of 10.2% for a fixed center with a BCG offset, and a scatter of 27.4% and

bias of 20.2% when letting the center be a free parameter. We characterize the sources of errors including the galaxy cluster total mass, concentration, deviation from spherical symmetry, lens redshift, and background source redshift. We find that the deviation from spherical symmetry projected along the line-of-sight has the most effect on the mass measurement, as expected. In addition, we find that the scatter introduced to this robust mass measurement from a lack of a background redshifts is negligible compared to other systematics when utilizing the underlying background source redshift distribution. We develop an empirical correction to debias the mass estimate and reduce the scatter in the mass estimate to 10.1% in the fixed center and 10.9% in the fixed center with BCG offset. Last, we formulate a set of recommendations for applying this method to large samples of strong lensing galaxy clusters.

Increasing the complexity of the mass estimator, in Chapter III, I present an assessment of the use of Single-Halo Lens Models (SHM) to measure the mass at the core of strong lensing galaxy clusters (Remolina González et al., 2021a). This first-order method uses the lensing algorithm `Lenstool` to model the underlying mass distribution. The SHM use a single, large scale, dark matter halo with no mass contribution added from additional large scale halos, galaxy cluster member galaxies, uncorrelated structure along the line-of-sight, nor shear from structures near the galaxy cluster. The result is a lens model that requires a small number of constraints and is computed in a fraction of the computational time compared to its detailed counterparts. This method benefits from a quick visual inspection of the SHM outputs to identify un-physical lens models which fail to reproduce the strong lensing configuration. The SHM that fail the visual inspection dominate the uncertainty and bias of the measurement and will require additional iterations. When only using the SHM that passed the visual inspection a scatter on the mass estimate of 3.3% and a bias of 0.3% are measured. Last, we find that the lensing configuration has an effect on the SHM,

where the strong lensing images with a single giant arc provide the least constraining power and account for the majority of the SHM that fail the visual inspection.

In Chapter IV, I present the work taking the assessments and recommendations of the mass enclosed by the Einstein radius and the SHM from simulations to observations (Remolina González et al., 2021b). We demonstrate their application on a large sample of 67 observed strong lensing galaxy clusters with 144 publicly available detailed lens models from SGAS, CLASH, HFF, and RELICS. We quantify the uncertainty in the mass estimates between the two efficient methods and the mass from the detailed lens models. Last, we compare the scatter of these two methods from simulations and that measured against the detailed lens models. Overall, detailed lens models are considered to be the state of the art in measuring the mass distribution at the core of strong lensing galaxy cluster. We conclude that if other sources of error dominate the analysis of interest, these two efficient mass estimates become powerful tools for use on large samples of strong lensing galaxy clusters.

In Chapter V, I present the analysis of the concentration-Mass relation of South Pole Telescope strong lensing galaxy clusters. The concentration of galaxy clusters is computed after constraining their radial mass distribution by combining the mass estimates at the core from strong lensing and the outskirts from SZ. We use simulations to test the modeling procedures and predict the concentration-Mass relation for strong lensing galaxy clusters. The large sample of 51 strong lensing clusters from SPT with uniform *HST* SNAP imaging data is of particular interest for this analysis as the sample is about twice as large as previous strong lensing c-M studies, the selection function is well understood, and the sample has a broad coverage of the mass and redshift parameter space. We find significant evidence for a relation between the concentration and mass of the galaxy cluster, constrain the normalization of the c-M relation to within $\sim 5\%$, and find that we cannot constrain a possible evolution of the concentration with redshift with these samples. We find agreement between the

observed c-M relation and the prediction from the Outer Rim N-body simulations, using the same sample selection function in both, i.e., we report no tension with Λ CDM.

6.2 Future Work with Strong Lensing South Pole Telescope Galaxy Clusters and the Multi-Year Magellan Spectroscopic Follow-up Program

As was shown in Chapter V, the strong gravitational lensing galaxy clusters identified from the South Pole Telescope are a unique sample of particular interest for its large number size and well understood selection function. In the work presented in this thesis and the manuscript in preparation, only a sub-sample of all strong lensing SPT clusters is used. The sample used for the analysis comes from a large *HST* SNAP program for which a selection function of the co-moving number density count was constant between $0.2 < z < 1.0$ and mass limited for $z > 1$. The next steps are to increase the sample size of strong lensing clusters used by adding the strong gravitational lensing SPT clusters identified from a complementary ground-based uniform imaging program using the Parallel Imager for Southern Cosmology Observations (PISCO). The SPT PISCO program will identify strong lensing galaxy clusters via a systematic visual inspection of all the lines-of-sight. The SPT SL clusters identified through this method are also expected to include galaxy clusters at lower redshift and mass compared to the SPT *HST* SNAP sample.

Complementary to the uniform imaging programs has been a multi-year spectroscopic follow-up program of SPT strong lensing galaxy clusters (see Appendix D). The data from this program will provide a large amount of spectroscopic redshifts of lensed sources, clusters, and cluster member galaxies. The redshift information of the strong lensing evidence will enable the use of the SHM (Chapter III) for a majority of

the strong lensing clusters resulting with a more accurate mass estimate at the galaxy cluster core compared to the mass enclosed by the Einstein radius (Chapter II). The recommended procedure once the SHM can be computed for the strong lensing clusters is to use a tiered approach where the SHM is computed where possible, otherwise the mass enclosed by the Einstein radius should be used.

Last, detailed lens models are under development for some of the most spectacular strong lensing SPT galaxy clusters (e.g., Mahler et al. in prep). The detailed lens models are going to benefit from the large number of spectroscopic redshifts coming from the spectroscopic follow-up program. The detailed lens models have been shown to provide the most accurate mass estimates of all the methods presented in this thesis (see Chapter IV). When these detailed lens models are available, the suggestions is to use them. This will reveal an additional level to the decision tree of which method to use when measuring the mass at the core of strong lensing galaxy cluster. The recommendation set forth is if a detailed lens model is available, use the detail lens model to measure the core mass; else check if a Single-Halo Lens Model can be computed, if that is the case estimate the core mass using the outputs of the Single-Halo Lens Model; last if neither of the previous options are possible, then use the mass enclosed by the Einstein radius.

We look forward to the maturity and results of the different imaging and spectroscopic programs which will enable additional analyses with large samples of strong lensing galaxy clusters with a well-established selection function.

As noted above, the multi-year spectroscopic follow-up of SPT strong lensing evidence (see Appendix D) has resulted in the observations of over a hundred galaxy clusters. The multi-object slit spectroscopy approach that was employed in this program allowed for the efficient observations of many sources of interest in the field of view including the strong lensing evidence, galaxy cluster members, additional structure along the line-of-sight, and interlopers. The data are currently being processed

and will be primarily used for the precise measurement of spectroscopic redshifts. As part of the processing of the data, a new pipeline is being developed by collaborators to help reduce the effect of artifacts due to the instrument equipment, LDSS3-C, and result in a robust spectral energy distribution. Additional analyses enabled by this rich data set include the confirmation and measurement of spectroscopic redshifts of galaxy clusters, additional mass estimate constraints using dynamical methods, characterize the star formation history of galaxy cluster members through cosmic time, galaxy cluster evolution studies, and identification of structures along the line-of-sight. The legacy this data set will be far reaching with other future analyses across the SPT collaboration and the community relying on these spectroscopic measurements.

6.3 Future of Strong Lensing Galaxy Clusters in Cosmological Simulations

Improvements in the next generation of cosmological simulations will allow for even more detailed studies with strong gravitational lensing by galaxy clusters. Detailed lens models will need simulations to fully quantify their precision and their systematic uncertainties. The two efficient mass estimates at the core of strong lensing galaxy clusters will also benefit the next generation of cosmological simulations which incorporate some baryonic information, and the simulated strong lensing images will require the incorporation of structure along the line-of-sight and shear due to nearby massive structures. These works with the next generation of cosmological simulations have the potential to improve the characterization of the systematic uncertainties on measured properties of strong lensing galaxy clusters.

6.4 Future of Strong Lensing Galaxy Clusters in Large Astronomical Surveys

As emphasized throughout this thesis, current and upcoming large astronomical surveys will discover thousands of strong lensing galaxy clusters. The large numbers present various challenges from the start, including identification and follow-up. New tools under development for the identification of strong gravitational lensing evidence includes the use of convolutional neural networks (CNN). These methods require training with large numbers of images of galaxy clusters with and without strong lensing. Currently, the number of line-of-sight with strong lensing evidence is a small sample, so we are relying on simulated strong lensing images in the training sets for CNN. The hardware and algorithms used by these techniques are also under investigation to identify the best combination for the identification task. The advantage of a fully trained CNN is when deployed it can look at pre-processed images taken from the telescope in real-time and evaluate if there is strong lensing evidence in the field of view. This automated tool is set to revolutionize current standard methods of identification of strong gravitational lenses by human visual inspections of tens of thousands of images (e.g., Petrillo et al. 2017; Jacobs et al. 2019; Cañameras et al. 2020).

The vast majority of the strong lensing galaxy clusters that will be identified are not going to be extraordinary gravitational lenses like the *Hubble* Frontier Fields. Depending on the imaging depth and resolution only the primary and possibly a few secondary lensed images will be identified based on the morphology and color (e.g., Sharon et al. 2020). The small number of constraints identified from the visual inspection will be a limitation for detailed lens models. Additionally the identification, follow-up and confirmation of strong lensing candidates with spectroscopic observations will require an extensive commitment by the astronomical community.

Spectroscopic observations of strong lensing with some of the largest ground base telescopes requires hours of integration per target and this does not guarantee a spectroscopic redshift measurement as the target might be too faint, not have bright spectroscopic features in its spectral energy distribution, or the emission lines lay outside its wavelength coverage. As the large astronomical surveys identifying strong lensing are imaging based, photometric redshifts could be measured although they are more uncertain and prone to catastrophic failures requiring care when being used as constraints (e.g., Cerny et al. 2018).

The two efficient methods to measure the mass at the core of strong lensing galaxy clusters presented in this thesis can be used in combination with these new tools. For example, the CNN can identify that an image has strong gravitational lensing and extract the locations of the strong lensing evidence. These positions can then be used as the constraints of the mass enclosed by the Einstein radius assuming a previously established background source redshift distribution. Other techniques of modeling the mass distribution of strong lensing galaxy clusters utilizing machine learning (e.g., Bom et al. 2019; Pearson et al. 2019) are being investigated as well. Last, while these tools are meant to help with the large numbers of strong lensing clusters, detailed lens models will continue to be needed to study complex and rich strong lensing galaxy clusters. The analysis of strong gravitational lensing continues to demonstrate the incredible potential to learn about cosmology, the lens, and the magnified background Universe.

APPENDICES

APPENDIX A

Uncertainty Dependence on the Fraction of Circle Covered by Arcs

Appendix of Chapter II

In this appendix we give numerical values of the field-specific uncertainty, which depends on the deviation from circular symmetry, as indicated by the fraction of the circle covered by arcs (ϕ). For the statistics used in our analysis see §2.4.3. The scatter is defined as half the difference between the 84th percentile (upper) and the 16th percentile (lower) of the distribution and we compute the bias using the median of the distribution. For convenience, we tabulate the numerical values that are plotted in Figure 2.16 in Table A.1.

Table A.1. Bias and uncertainty in $M(< \theta_E)$ as a function of ϕ .

	ϕ bin median [min — max]	$M(< \theta_E)/M_{sim}(< \theta_E)$	
		Measured median [lower — upper]	Corrected median [lower — upper]
Fixed Center	0.06 [0.00 — 0.12]	1.17 [0.99 — 1.56]	1.00 [0.89 — 1.19]
	0.19 [0.12 — 0.23]	1.13 [0.99 — 1.30]	1.01 [0.90 — 1.12]
	0.28 [0.23 — 0.33]	1.13 [0.99 — 1.26]	1.01 [0.91 — 1.13]
	0.39 [0.33 — 0.49]	1.10 [0.98 — 1.16]	1.01 [0.90 — 1.09]
	0.66 [0.49 — 1.00]	1.02 [0.99 — 1.09]	0.96 [0.92 — 1.04]
Fixed Center w/ BCG Offset	0.06 [0.00 — 0.11]	1.17 [1.00 — 1.59]	1.00 [0.89 — 1.18]
	0.17 [0.11 — 0.22]	1.15 [1.00 — 1.37]	1.02 [0.89 — 1.15]
	0.26 [0.22 — 0.31]	1.15 [1.00 — 1.29]	1.01 [0.90 — 1.13]
	0.37 [0.31 — 0.46]	1.10 [0.99 — 1.19]	1.00 [0.90 — 1.09]
	0.61 [0.46 — 1.00]	1.03 [0.99 — 1.12]	0.96 [0.91 — 1.05]

Note. — A quantitative form of the information displayed in Panel F of Figure 2.13 and Figure 2.16. The median and boundaries of the bins of ϕ are tabulated in the first column; the next columns tabulate the median, lower 16th percentile, and the upper 84th percentile of $M(< \theta_E)/M_{sim}(< \theta_E)$, for the measured results (Figure 2.13) and corrected results (Figure 2.16).

APPENDIX B

South Pole Telescope Strong Lensing Constraints

Appendix of Chapter V

In Table B.1, we show the strong lensing constraints identified in the visual inspection of the *HST* imaging (*HST* SNAP 15307 and *HST* SNAP 16017 programs). The multiple-images R.A. and Decl. are indicated. the Flag (T or R) identified which multiple-images are primarily distorted in the tangential or radial direction respectively. The spectroscopic background source redshifts and references are also shown.

Table B.1: Strong Lensing Constraints.

SPT ID	Arc ID	R.A. (J2000)	Decl. (J2000)	Flag T or R	z_s	Reference
SPT-CL 0002-5557	1.1	0.51075	-55.96528	T	...	
	1.2	0.50884	-55.96648	T	...	
	1.3	0.50889	-55.96910	T	...	
SPT-CL 0005-3751	1.1	1.44341	-37.86753	T	...	
	1.2	1.43907	-37.86788	T	...	
	1.3	1.43720	-37.86824	T	...	
	2.1	1.44227	-37.86879	T	...	
	2.2	1.44053	-37.86959	T	...	
	3.1	1.44072	-37.86835	T	...	
	3.2	1.43982	-37.86877	T	...	
	3.3	1.43829	-37.86852	T	...	
	SPT-CL 0049-2440	1.1	12.30667	-24.67868	T	...
1.2		12.30459	-24.67374	T	...	
1.3		12.29331	-24.66919	T	...	

Table B.1: Strong Lensing Constraints (cont'd).

SPT ID	Arc ID	R.A. (J2000)	Decl. (J2000)	Flag T or R	z_s	Reference
	2.1	12.29756	-24.66902	T	...	
	2.2	12.29688	-24.66898	T	...	
	2.3	12.29671	-24.66893	T	...	
	3.1	12.29119	-24.68067	R	...	
	3.2	12.29088	-24.68074	R	...	
	4.1	12.29836	-24.68124	R	...	
	4.2	12.29813	-24.68120	R	...	
	5.1	12.29041	-24.67646	T	...	
	5.2	12.30448	-24.67694	T	...	
	6.1	12.28730	-24.67846	T	...	
	6.2	12.28683	-24.67936	T	...	
	6.3	12.28697	-24.68085	T	...	
	7.1	12.30188	-24.68182	T	...	
	7.2	12.30108	-24.68246	T	...	

Table B.1: Strong Lensing Constraints (cont'd).

SPT ID	Arc ID	R.A. (J2000)	Decl. (J2000)	Flag	z_s	Reference
SPT-CL 0100-5359	1.1	15.01640	-53.98581	T	...	
	1.2	15.01658	-53.98726	T	...	
	1.3	15.01720	-53.98819	T	...	
SPT-CL 0118-5156	1.1	19.59222	-51.94438	T	...	
	2.1	19.60396	-51.94116	R	...	
SPT-CL 0150-4511	1.1	27.64005	-45.18728	T	...	
	2.1	27.65500	-45.18622	T	...	
	3.1	27.65392	-45.18647	T	...	
	4.1	27.65139	-45.18552	T	...	
	5.1	27.65291	-45.18895	T	...	
SPT-CL 0216-2609	1.1	34.15050	-26.16758	T	...	
	1.2	34.14834	-26.16645	T	...	
SPT-CL 0219-4934	1.1	34.81493	-49.57701	T	...	
SPT-CL 0240-5946	1.1	40.16635	-59.76455	T	...	

Table B.1: Strong Lensing Constraints (cont'd).

SPT ID	Arc ID	R.A. (J2000)	Decl. (J2000)	Flag T or R	z_s	Reference
	1.2	40.16182	-59.76552	T	...	
	1.3	40.15268	-59.76533	T	...	
	2.1	40.16619	-59.76452	T	...	
	2.2	40.16201	-59.76544	T	...	
	2.3	40.15253	-59.76529	T	...	
	3.1	40.16600	-59.76463	T	...	
	3.2	40.16234	-59.76552	T	...	
	3.3	40.15245	-59.76538	T	...	
	4.1	40.16666	-59.76405	T	...	
	4.2	40.16098	-59.76517	T	...	
	4.3	40.15276	-59.76481	T	...	
	5.1	40.16005	-59.76994	T	...	
	5.2	40.15934	-59.76999	T	...	
	6.1	40.15670	-59.77046	T	...	

Table B.1: Strong Lensing Constraints (cont'd).

SPT ID	Arc ID	R.A. (J2000)	Decl. (J2000)	Flag T or R	z_s	Reference
	6.2	40.16025	-59.77027	T	...	
	7.1	40.16006	-59.76325	R	...	
SPT-CL 0243-4833	1.1	40.90776	-48.55780	T	...	
	1.2	40.90636	-48.55911	T	...	
	1.3	40.90601	-48.56017	T	...	
	2.1	40.92389	-48.56364	T	...	
SPT-CL 0252-2100	1.1	43.11029	-21.01284	T	...	
	1.2	43.11060	-21.01385	T	...	
	1.3	43.11368	-21.01678	T	...	
	2.1	43.11078	-21.01375	T	...	
	2.2	43.11095	-21.01435	T	...	
	3.1	43.11875	-21.01227	T	...	
	3.2	43.11858	-21.01137	T	...	
	3.3	43.11453	-21.00703	T	...	

Table B.1: Strong Lensing Constraints (cont'd).

SPT ID	Arc ID	R.A. (J2000)	Decl. (J2000)	Flag T or R	z_s	Reference
	4.1	43.12123	-21.00759	T	...	
	4.2	43.11987	-21.00636	T	...	
	5.1	43.11854	-21.00700	T	...	
	5.2	43.11821	-21.00673	T	...	
	6.1	43.10969	-21.01091	T	...	
	6.2	43.11189	-21.01555	T	...	
	6.3	43.11742	-21.01767	T	...	
SPT-CL 0304-5404	1.1	46.21993	-54.06616	T	...	
	1.2	46.21911	-54.06611	T	...	
SPT-CL 0307-6225	1.1	46.82148	-62.44127	T	...	
	2.1	46.81350	-62.45538	T	...	
SPT-CL 0310-4647	1.1	47.63405	-46.78145	T	1.99	Bayliss et al. (2016)
	1.2	47.63458	-46.78141	T	1.99	Bayliss et al. (2016)
	1.3	47.63822	-46.78199	T	1.99	Bayliss et al. (2016)

Table B.1: Strong Lensing Constraints (cont'd).

SPT ID	Arc ID	R.A. (J2000)	Decl. (J2000)	Flag T or R	z_s	Reference
SPT-CL 0319-2244	1.1	49.91846	-22.73534	T	...	
	1.2	49.92071	-22.73620	T	...	
	1.3	49.92505	-22.73951	T	...	
	2.1	49.91847	-22.73582	T	...	
	2.2	49.92033	-22.73639	T	...	
	2.3	49.92508	-22.74006	T	...	
SPT-CL 0328-2140	3.1	49.91875	-22.73616	T	...	
	3.2	49.91982	-22.73642	T	...	
	3.3	49.92514	-22.74032	T	...	
	1.1	52.05885	-21.67800	T	...	
	1.2	52.05693	-21.67789	T	...	
	1.3	52.05547	-21.67775	T	...	
SPT-CL 0328-2140	1.4	52.05382	-21.67751	T	...	
	2.1	52.05973	-21.67779	T	...	

Table B.1: Strong Lensing Constraints (cont'd).

SPT ID	Arc ID	R.A. (J2000)	Decl. (J2000)	Flag T or R	z_s	Reference
	2.2	52.05631	-21.67778	T	...	
	2.3	52.05599	-21.67775	T	...	
	2.4	52.05309	-21.67732	T	...	
	3.1	52.06030	-21.66877	T	...	
	3.2	52.05941	-21.66803	T	...	
	3.3	52.05274	-21.66734	T	...	
	4.1	52.06042	-21.66907	T	...	
	4.2	52.05920	-21.66804	T	...	
	4.3	52.05261	-21.66749	T	...	
	4.4	52.05193	-21.66799	T	...	
	4.5	52.05183	-21.66800	T	...	
	5.1	52.05979	-21.66861	T	...	
	5.2	52.05965	-21.66847	T	...	
	5.3	52.05242	-21.66749	T	...	

Table B.1: Strong Lensing Constraints (cont'd).

SPT ID	Arc ID	R.A. (J2000)	Decl. (J2000)	Flag T or R	z_s	Reference
	5.4	52.05207	-21.66787	T	...	
	5.5	52.05151	-21.66804	T	...	
	5.6	52.05184	-21.66755	T	...	
SPT-CL 0352-2644	1.1	58.18096	-26.72601	T	...	
	1.2	58.18186	-26.72884	T	...	
	2.1	58.17357	-26.72720	T	...	
	2.2	58.17349	-26.72743	T	...	
	2.3	58.17671	-26.73375	T	...	
SPT-CL 0352-5647	1.1	58.24510	-56.79677	T	...	
SPT-CL 0404-4418	1.1	61.19650	-44.30194	T	...	
	1.2	61.19252	-44.30332	T	...	
	1.3	61.19227	-44.30341	T	...	
	2.1	61.19630	-44.30186	T	...	
	2.2	61.19287	-44.30302	T	...	

Table B.1: Strong Lensing Constraints (cont'd).

SPT ID	Arc ID	R.A. (J2000)	Decl. (J2000)	Flag T or R	z_s	Reference
	2.3	61.19183	-44.30345	T	...	
	3.1	61.19709	-44.30128	T	...	
	3.2	61.19335	-44.30252	T	...	
	3.3	61.18968	-44.30382	T	...	
SPT-CL 0406-4805	1.1	61.72834	-48.08201	T	...	
	1.2	61.72819	-48.08228	T	...	
	1.3	61.72885	-48.08240	R	...	
	2.1	61.72806	-48.07564	T	...	
	3.1	61.73373	-48.07582	T	...	
SPT-CL 0411-2158	1.1	62.78231	-21.97359	T	...	
	2.1	62.78078	-21.98102	T	...	
SPT-CL 0441-4855	1.1	70.44681	-48.92744	T	...	
	1.2	70.44552	-48.92703	T	...	
	1.3	70.44388	-48.92572	T	...	

Table B.1: Strong Lensing Constraints (cont'd).

SPT ID	Arc ID	R.A. (J2000)	Decl. (J2000)	Flag T or R	z_s	Reference
	1.4	70.44365	-48.92543	T	...	
	2.1	70.44790	-48.92753	T	...	
	2.2	70.44425	-48.92621	T	...	
	2.3	70.44329	-48.92475	T	...	
	3.1	70.43952	-48.92096	T	...	
	4.1	70.45028	-48.91714	T	...	
SPT-CL 0456-4906	1.1	74.11842	-49.09501	T	...	
	1.2	74.11735	-49.09517	T	...	
	1.3	74.12917	-49.10011	T	...	
	2.1	74.11037	-49.10637	T	...	
	2.2	74.10984	-49.10611	T	...	
	3.1	74.11630	-49.10586	T	...	
	3.2	74.11765	-49.10615	T	...	
	4.1	74.12825	-49.10350	T	...	

Table B.1: Strong Lensing Constraints (cont'd).

SPT ID	Arc ID	R.A. (J2000)	Decl. (J2000)	Flag T or R	z_s	Reference
	4.2	74.12315	-49.09593	T	...	
SPT-CL 0509-5342	1.1	77.33591	-53.70192	T	...	
	1.2	77.33534	-53.70261	T	...	
	1.3	77.33561	-53.70545	T	...	
	1.4	77.33927	-53.70360	R	...	
	2.1	77.33803	-53.70190	T	...	
	2.2	77.33672	-53.70344	T	...	
	2.3	77.33736	-53.70516	T	...	
SPT-CL 0528-5300	1.1	82.01380	-52.99703	T	2.29	This Work
	1.2	82.02020	-52.99341	T	2.29	This Work
	2.1	82.03047	-52.99411	T	...	
	3.1	82.02436	-53.00185	T	...	
SPT-CL 0532-3701	1.1	83.23272	-37.01980	T	...	
	1.2	83.22700	-37.02650	T	...	

Table B.1: Strong Lensing Constraints (cont'd).

SPT ID	Arc ID	R.A. (J2000)	Decl. (J2000)	Flag T or R	z_s	Reference
	1.3	83.23043	-37.03544	T	...	
	2.1	83.21752	-37.02417	T	...	
	2.2	83.21714	-37.02521	T	...	
	3.1	83.24113	-37.03560	T	...	
	3.2	83.23908	-37.03671	T	...	
SPT-CL 0535-4801	1.1	83.94958	-48.02999	T	...	
	1.2	83.94940	-48.02988	T	...	
SPT-CL 0544-3950	1.1	86.24791	-39.82166	T	...	
	1.2	86.25240	-39.82581	T	...	
	2.1	86.24426	-39.82143	T	...	
	2.2	86.24868	-39.82418	T	...	
	2.3	86.24941	-39.82511	T	...	
SPT-CL 0555-6406	1.1	88.86349	-64.11064	T	...	
	1.2	88.86561	-64.10721	T	...	

Table B.1: Strong Lensing Constraints (cont'd).

SPT ID	Arc ID	R.A. (J2000)	Decl. (J2000)	Flag T or R	z_s	Reference
	1.3	88.85945	-64.09598	T	...	
	2.1	88.83652	-64.10128	T	...	
	2.2	88.83613	-64.10234	T	...	
	3.1	88.83193	-64.10947	T	...	
	3.2	88.83239	-64.10995	T	...	
	4.1	88.86844	-64.10630	T	...	
SPT-CL 0556-5403	1.1	89.20727	-54.06095	T	...	
	1.2	89.20618	-54.06139	T	...	
SPT-CL 0557-4113	1.1	89.44262	-41.22175	T	...	
	1.2	89.44243	-41.22222	T	...	
	1.3	89.44219	-41.22263	T	...	
	1.4	89.44193	-41.22372	T	...	
SPT-CL 0643-4535	1.1	100.93018	-45.59800	T	...	
	1.2	100.93012	-45.59793	T	...	

Table B.1: Strong Lensing Constraints (cont'd).

SPT ID	Arc ID	R.A. (J2000)	Decl. (J2000)	Flag T or R	z_s	Reference
	1.3	100.93003	-45.59782	T	...	
	1.4	100.92989	-45.59768	T	...	
SPT-CL 0647-5828	1.1	101.98579	-58.47692	T	...	
	1.2	101.97975	-58.47633	T	...	
	1.3	101.97158	-58.47907	T	...	
	1.4	101.98124	-58.48239	R	...	
	2.1	101.98344	-58.47655	T	...	
	2.2	101.98274	-58.47647	T	...	
	2.3	101.97109	-58.47926	T	...	
	2.4	101.98149	-58.48229	R	...	
SPT-CL 0650-4503	1.1	102.68519	-45.06822	T	...	
	1.2	102.68299	-45.06844	T	...	
	1.3	102.67982	-45.06773	T	...	
SPT-CL 1000-3016	1.1	150.01062	-30.27426	T	...	

Table B.1: Strong Lensing Constraints (cont'd).

SPT ID	Arc ID	R.A. (J2000)	Decl. (J2000)	Flag T or R	z_s	Reference
	1.2	150.00837	-30.27778	T	...	
	1.3	150.00480	-30.27995	T	...	
	2.1	150.01057	-30.27418	T	...	
	2.2	150.00829	-30.27773	T	...	
	2.3	150.00472	-30.27988	T	...	
	3.1	150.01084	-30.27313	T	...	
	3.2	150.00723	-30.27797	T	...	
	3.3	150.00483	-30.27920	T	...	
	4.1	150.00549	-30.27377	T	...	
	4.2	150.00490	-30.27419	T	...	
	4.3	150.00306	-30.27661	T	...	
SPT-CL 1042-2847	1.1	160.57174	-28.79423	T	...	
	1.2	160.57148	-28.79540	T	...	
	2.1	160.56789	-28.79236	T	...	

Table B.1: Strong Lensing Constraints (cont'd).

SPT ID	Arc ID	R.A. (J2000)	Decl. (J2000)	Flag T or R	z_s	Reference
	2.2	160.56779	-28.79252	T	...	
SPT-CL 1153-2137	1.1	178.36666	-21.63496	T	...	
	2.1	178.36552	-21.63623	T	...	
	3.1	178.37101	-21.63129	T	...	
SPT-CL 2023-5535	1.1	305.84005	-55.59827	T	...	
	1.2	305.84022	-55.59794	T	...	
	1.3	305.83922	-55.59571	T	...	
	1.4	305.83904	-55.59556	T	...	
	1.5	305.83520	-55.59748	R	...	
	2.1	305.83939	-55.59886	T	...	
	2.2	305.84001	-55.59691	T	...	
	2.3	305.83970	-55.59620	T	...	
	2.4	305.83846	-55.59512	T	...	
	2.5	305.83488	-55.59738	R	...	

Table B.1: Strong Lensing Constraints (cont'd).

SPT ID	Arc ID	R.A. (J2000)	Decl. (J2000)	Flag	z_s	Reference
SPT-CL 2025-5117	1.1	306.47335	-51.28831	T	...	
SPT-CL 2032-5627	1.1	308.05533	-56.43530	T	...	
SPT-CL 2108-4445	1.1	317.20165	-44.77001	T	...	
	1.2	317.20181	-44.76976	T	...	
	1.3	317.20203	-44.76923	T	...	
	2.1	317.20148	-44.77021	T	...	
	2.2	317.20182	-44.76962	T	...	
	2.3	317.20193	-44.76935	T	...	
SPT-CL 2112-4434	1.1	318.21976	-44.58528	T	...	
	1.2	318.22112	-44.58464	T	...	
	1.3	318.21889	-44.57966	T	...	
	1.4	318.20825	-44.58261	T	...	
	1.5	318.21751	-44.58230	R	...	
	2.1	318.22115	-44.57972	T	...	

Table B.1: Strong Lensing Constraints (cont'd).

SPT ID	Arc ID	R.A. (J2000)	Decl. (J2000)	Flag T or R	z_s	Reference
	2.2	318.21955	-44.57875	T	...	
	2.3	318.20923	-44.58096	T	...	
	2.4	318.21871	-44.58455	T	...	
	3.1	318.21855	-44.58118	T	...	
	3.2	318.21882	-44.58127	T	...	
	3.3	318.21950	-44.58218	T	...	
	3.4	318.21043	-44.58234	T	...	
	4.1	318.21478	-44.57874	T	...	
	4.2	318.21078	-44.58093	T	...	
	4.3	318.21608	-44.58465	T	...	
	4.4	318.22363	-44.58200	T	...	
	4.5	318.21655	-44.58234	R	...	
SPT-CL 2124-6124	1.1	321.15637	-61.40631	T	...	
	1.2	321.15700	-61.40632	T	...	

Table B.1: Strong Lensing Constraints (cont'd).

SPT ID	Arc ID	R.A. (J2000)	Decl. (J2000)	Flag T or R	z_s	Reference
	1.3	321.16229	-61.40794	T	...	
	2.1	321.15264	-61.40870	T	...	
	2.2	321.15426	-61.40935	T	...	
	2.3	321.16033	-61.41047	T	...	
SPT-CL 2130-6458	1.1	322.73702	-64.97561	T	...	
	1.2	322.73865	-64.97659	T	...	
	1.3	322.73953	-64.98027	T	...	
SPT-CL 2134-4109	1.1	323.52293	-41.15861	T	...	
	1.2	323.52348	-41.15910	T	...	
	1.3	323.53015	-41.15994	T	...	
	2.1	323.52282	-41.15854	T	...	
	2.2	323.52357	-41.15917	T	...	
	2.3	323.53013	-41.15995	T	...	
	3.1	323.53152	-41.15703	T	...	

Table B.1: Strong Lensing Constraints (cont'd).

SPT ID	Arc ID	R.A. (J2000)	Decl. (J2000)	Flag T or R	z_s	Reference
	3.2	323.52993	-41.15576	T	...	
SPT-CL 2138-6008	1.1	324.51531	-60.13267	T	...	
	1.2	324.51541	-60.13131	T	...	
	1.3	324.51510	-60.13039	T	...	
	1.4	324.51437	-60.12912	T	...	
	1.5	324.50847	-60.12588	T	...	
	2.1	324.50580	-60.13201	R	...	
	2.2	324.50505	-60.13200	R	...	
	2.3	324.49336	-60.12598	T	...	
	3.1	324.49769	-60.13452	T	...	
	3.2	324.49677	-60.13406	T	...	
	4.1	324.49699	-60.12931	T	...	
	4.2	324.49719	-60.12918	T	...	
	4.3	324.49853	-60.12829	T	...	

Table B.1: Strong Lensing Constraints (cont'd).

SPT ID	Arc ID	R.A. (J2000)	Decl. (J2000)	Flag T or R	z_s	Reference
SPT-CL 2244-3704	1.1	341.05395	-37.06916	T	...	
	1.2	341.05269	-37.06816	T	...	
	1.3	341.05100	-37.06376	T	...	
	2.1	341.05326	-37.06899	T	...	
	2.2	341.05315	-37.06892	T	...	
	3.1	341.05802	-37.06869	T	...	
	3.2	341.05673	-37.06550	T	...	
	3.3	341.05426	-37.06289	T	...	
	4.1	341.05330	-37.07037	T	...	
SPT-CL 2250-4808	4.2	341.05110	-37.06809	T	...	
	4.3	341.04984	-37.06465	T	...	
	1.1	342.68026	-48.14923	T	...	
	1.2	342.68187	-48.14846	T	...	
	1.3	342.68311	-48.14757	T	...	

Table B.1: Strong Lensing Constraints (cont'd).

SPT ID	Arc ID	R.A. (J2000)	Decl. (J2000)	Flag T or R	z_s	Reference
	2.1	342.67964	-48.14426	T	...	
	2.2	342.68035	-48.14310	T	...	
	2.3	342.68056	-48.14254	T	...	
SPT-CL 2254-4620	1.1	343.58053	-46.34315	T	...	
	1.2	343.58114	-46.34284	T	...	
	1.3	343.58186	-46.34262	T	...	
	1.4	343.58398	-46.34250	T	...	
	1.5	343.58585	-46.34297	T	...	
	1.6	343.58652	-46.34334	T	...	
SPT-CL 2256-2241	1.1	344.01033	-22.68315	T	...	
	1.2	344.01073	-22.68469	T	...	
	1.3	344.00896	-22.68854	T	...	
	2.1	344.01168	-22.68704	T	...	
	2.2	344.01190	-22.68634	T	...	

Table B.1: Strong Lensing Constraints (cont'd).

SPT ID	Arc ID	R.A. (J2000)	Decl. (J2000)	Flag	z_s	Reference
SPT-CL 2305-2248	1.1	346.29672	-22.82194	T	...	
	1.2	346.29235	-22.82147	T	...	
	1.3	346.29189	-22.82028	T	...	

R.A. and Decl. are the right ascension and declination of the identified arcs, respectively, Flag (T or R) indicates the tangential and radial arcs, respectively, and z_s is the spectroscopic redshifts of multiply-imaged lensed background sources and their reference. For more details see Section 5.4.

APPENDIX C

Analysis of Systematics from the Large Scale SPT Mass

Appendix of Chapter V

As mentioned in Section 5.4, the M_{500c} masses used in this analysis were computed using a fixed cosmology and best-fit scaling relations for the number count of SPT clusters. Bocquet et al. (2019) showed that when fully marginalizing over cosmology and scaling relations parameter uncertainties, the SPT cluster masses are less massive, compared to the mass estimates without these systematics taken into account. As the fully marginalized masses are not currently available for the complete sample of SPT clusters, we use the published M_{500c} without systematics. In this section, we use the simulations to estimate how a systematic overestimation of 20% in the large scale mass would affect the measurement of the concentration-mass relation.

For this test, we perform the identical procedure describe in Section 5.6.5, in which we validate the “observational” concentration measurement in the simulated SL fields against the full 3-D partical information, except here we use a large scale mass equal to $1.2 \times M_{500c}$. We measure a scatter of 33.7% between the concentration measured

for $1.2 \times M_{500c}$ and that inferred from the 3-D particle information; the scatter is similar to the scatter we measured in the main analysis. The bias we measure is -10.5% i.e., when the large scale mass is overestimated by $\sim 20\%$ the concentration is underestimated, but consistent with the “true” concentration within errors. For reference, the main analysis in Section 5.6.5 resulted in scatter of 38.0% and bias of 3.4% .

Next using the test concentration and overestimated mass, we fit the c-M relation following the procedure in Section 5.7.1. The results of the c-M fit parameters for this test using simulations are: $\alpha = 1.88 \pm 0.19$, $\beta = -0.75 \pm 0.21$, and $\gamma = -0.09 \pm 1.24$. We compare the results from this test and those presented in Section 5.7.1. We find that β and γ are consistent with those measured in the main analysis. A clear difference is observed between the normalization parameter α , with the test normalization being about 18% smaller than the one measured in the simulations, $\alpha = 1.88 \pm 0.19$ vs. 2.30 ± 0.21 , while their uncertainty is similar. This test demonstrates the effect that a systematic error in the large scale mass has on the normalization value of the c-M relation resulting in a normalization value which is smaller when no systematics are taken into account.

The latest work on one of the South Pole Telescope galaxy cluster samples include a mass estimation which fully marginalizes over cosmology and the scaling relations used to compute the SZ mass of galaxy clusters (Bocquet et al., 2019). The result of this work showed that the masses reported without taking into account this marginalization are systematically higher by about 20% . We expect that fully marginalized masses for all SPT clusters will be available in the near future. We intend to repeat the measurements presented in Section 5.7.3 using the updated masses, when these are available. In the meantime, we report that if a systematic 20% decrease is applied to all the SPT masses, repeating the analysis presented in Section 5.7.3 results in $\alpha = 2.77 \pm 0.15$, $\beta = -1.05 \pm 0.18$, and $\gamma = 0.10 \pm 0.44$.

APPENDIX D

Spectroscopic follow-up of SPT Strong Lensing Galaxy Clusters

In this appendix, I describe the multi-year spectroscopic follow-up program of South Pole Telescope strong lensing galaxy clusters. The program started in 2016A under PI: K. Sharon and I became the PI since 2019A. The program mainly uses the Low Dispersion Survey Spectrograph 3-C (LDSS3-C) instrument mounted on the Clay Magellan Telescope located at Las Campanas Observatory in the Atacama region of Chile. The program mainly used multi-slit masks to increase efficiency and target multiple objects at the same time, with the use of long-slits when the production of the multi-slits masks was not practical. The abstract of the latest observing semester is copied below.

Abstract

“We request to continue our program for spectroscopy of lensed arcs in strong lensing South Pole Telescope (SPT) clusters, selected via the Sunyaev-Zel’dovich (SZ) effect, in an effort to obtain the spectroscopic redshifts of these arcs from (primarily) emission features. SPT clusters have a well understood selection function, which

makes this subsample of strong-lensing, SZ-selected clusters the most potent probe we currently have for understanding the abundance and shapes of strong lensing dark matter halos. The projected masses of these clusters can be well constrained within the critical curves of the lensed arcs, which requires a robust measurement of the redshift of the giant arc. Strong lensing features have been identified in clusters from SPT follow-up ground and space based optical/IR imaging. PISCO imaging by collaborators and our large HST SNAP program have revealed dozens more strong lenses overall; our complementary spectroscopy with LDSS3 has so far been very successful every semester since 2015. Complementary NIR spectroscopy program using FIRE (Chicago time) has now occurred since 2018, targeting lensed sources for which the initial LDSS3 spectroscopy did not yield a redshift; the combined success rate is $> 90\%$. Due to the current COVID-19 pandemic, our program has encountered logistical challenges (e.g. no production of new multi-slit mask). We are planning accordingly to mitigate expected losses while achieving our observing goals for 2021A. The observations will be part of J. Remolina González’s PhD thesis, thesis prospectus attached.”

D.1 Work as PI of the Spectroscopic Follow-up Program

As the PI of this program since 2019, I led the preparatory work prior to each observing run, which was done with several collaborators at the University of Michigan, University of Chicago, and Argonne National Laboratory. The preparatory work includes identification of clusters for observation, identification of SL features, and, if needed, computation of a preliminary lens model. We designed multi-slit masks to target the lensing evidence as first priority, and cluster-member galaxies to be targeted by the remaining available slits. Finally, a detailed observing plan for each night and each run was developed, and contingency plans put in place to account for varying weather conditions and priorities.

I executed the observations during 9 of the observing runs. The COVID-19 world-wide pandemic resulted in cancellation of several observing run in 2020, and transition to remote observing once the observatory resumed limited operations.

All high-priority SPT SL clusters, which were identified up until 2021, were observed. Preliminary analysis of the spectra of the highest-priority targets (typically, the lensed features) took place during the observation, however since this preliminary analysis is rarely fully calibrated we do not report its results here. A full uniform reduction of the entire LDSS3–C SPT SL program is in progress, with results anticipated in Fall 2021.

D.2 Observation Records

I report the observational records of the spectroscopic program. This record is presented here as part of the legacy of this multi-year observational campaign, to provide a reference database, and to inform future work. As part of my work, I have kept track of the multi-object slit mask production and searched the archival database¹ for LDSS3–C and IMACS/GISMO to identify masks used on observing runs prior to my involvement in the project. Table D.1 lists for each observation the cluster ID, observing information (instrument, date, exposure time), and mask identifier. In addition, this table lists multi-object slit masks that are available at the observatory and have not been observed.

¹<http://masks.lco.cl/masks2/search/>

Table D.1: Strong Lensing South Pole Telescope Spectroscopic Program Record.

SPT ID	Instrument	Obs. Date MM/DD/YYYY	Exp. Time		Aperture	Aperture ID
			Exp.	× Min.		
SPT-CL 0000-5748
SPT-CL 0002-5557	LDSS3-C	09/26/2019	2 × 20	...	0002m55S	L1961401
	LDSS3-C	09/26/2019	2 × 20	...	0002m55S	L1961401
SPT-CL 0005-3751	LDSS3-C	12/30/2018	1 × 25	...	0005-37A	L18B2101
	LDSS3-C	09/27/2019	2 × 20	...	0005-37A	L18B2101
SPT-CL 0011-4614	LDSS3-C	06/08/2016	2 × 25	...	0011m46A	L1650201
SPT-CL 0014-3022	LDSS3-C	12/10/2017	3 × 20	...	a2744	L17B1501
SPT-CL 0025-4133
SPT-CL 0030-5213
SPT-CL 0040-4407
SPT-CL 0043-2037
SPT-CL 0048-5244	LDSS3-C	12/29/2018	2 × 25	...	0048-52A	L18B2101
SPT-CL 0048-6416	LDSS3-C	09/27/2019	2 × 20	...	0048-64	L1982201
SPT-CL 0049-2440	LDSS3-C	12/10/2017	2 × 20	...	0049-24A	L1783001

Table D.1: Strong Lensing South Pole Telescope Spectroscopic Program Record (cont'd).

SPT ID	Instrument	Obs. Date	Exp. Time	Aperture	Aperture ID
SPT-CL 0058-6145	LDSS3-C	09/22/2016	2 × 25	0058	L1551705
SPT-CL 0100-5359	LDSS3-C	09/28/2019	2 × 20	0100-53	L1990401
SPT-CL 0106-5355	LDSS3-C	09/11/2015	4 × 30	spt0106	L1562601
SPT-CL 0106-5943	LDSS3-C	12/29/2018	2 × 25	0106-53A	L18B2101
SPT-CL 0107-5833	LDSS3-C	09/23/2016	4 × 25	0107	L1551706
SPT-CL 0110-4445	LDSS3-C	09/21/2016	2 × 25	0110m45A	L1650202
SPT-CL 0114-4123	LDSS3-C	06/08/2016	2 × 25	0114m41A	L1650202
SPT-CL 0118-5156	LDSS3-C	09/22/2016	2 × 25	0118-51	L1961402
SPT-CL 0133-6434	LDSS3-C	09/23/2016	2 × 20	0133m64A	L1681701
SPT-CL 0138-2155	LDSS3-C	06/08/2016	2 × 25	LS-1.5c	...
SPT-CL 0142-5032	LDSS3-C	10/02/2019	1 × 20	0142m50A	L1650202
SPT-CL 0144-2214	LDSS3-C	0150-45	0150-45
SPT-CL 0150-4511	LDSS3-C	0150-45	0150-45	...	L1961403

Table D.1: Strong Lensing South Pole Telescope Spectroscopic Program Record (cont'd).

SPT ID	Instrument	Obs. Date MM/DD/YYYY	Exp. Time Exp. \times Min.	Aperture	Aperture ID
	LDSS3-C	10/22/2020	2 \times 20	0150-45	L1961403
SPT-CL 0151-3544	LDSS3-C	09/25/2017	2 \times 20	0151-35A	L1783001
SPT-CL 0151-5654	LDSS3-C	01/10/2018	2 \times 20	0151-56A	L17C2001
SPT-CL 0152-5303	LDSS3-C	12/10/2017	2 \times 20	0152-53A	L17B1201
SPT-CL 0154-4824	LDSS3-C	10/21/2020	3 \times 15	0154m48H	L1961404
SPT-CL 0159-3413
SPT-CL 0203-2017	LDSS3-C	09/27/2017	2 \times 25	0203_20A	L1783001
	LDSS3-C	12/30/2018	2 \times 25	0203-20A	L18B2101
SPT-CL 0205-5829
SPT-CL 0216-2609
SPT-CL 0216-4830	LDSS3-C	12/10/2017	2 \times 20	0216-48A	L1783001
SPT-CL 0218-3142	LDSS3-C	01/30/2017	2 \times 20	0218m31B	L1711902
	LDSS3-C	09/28/2017	2 \times 20	0218m31A	L1711902
	LDSS3-C	09/28/2017	2 \times 20	0218m31B	L1711902

Table D.1: Strong Lensing South Pole Telescope Spectroscopic Program Record (cont'd).

SPT ID	Instrument	Obs. Date MM/DD/YYYY	Exp. Time		Aperture	Aperture ID
			Exp.	× Min.		
SPT-CL 0219-4934	LDSS3-C		0219-49	L1990402
SPT-CL 0231-5403	LDSS3-C	10/02/2019	2 × 20		0231-54b	L1990401
SPT-CL 0232-4421	LDSS3-C	09/22/2016	2 × 25		0232m44A	L1681701
SPT-CL 0239-2455
SPT-CL 0240-5946	LDSS3-C	09/27/2019	2 × 20		0240-59	L1961405
SPT-CL 0242-4150
SPT-CL 0243-4833	GMOS
SPT-CL 0252-2100	LDSS3-C	09/27/2019	2 × 20		0252m21S	L1961406
SPT-CL 0254-6051	LDSS3-C		0254-60b	L1990402
SPT-CL 0257-2009
SPT-CL 0257-2209
SPT-CL 0304-4921
SPT-CL 0304-5404	LDSS3-C	10/22/2020	2 × 20		0304-54	L1953002
SPT-CL 0307-5042	GISMO	1/XX/2015	2 × 40		spt0307	G1510701

Table D.1: Strong Lensing South Pole Telescope Spectroscopic Program Record (cont'd).

SPT ID	Instrument	Obs. Date MM/DD/YYYY	Exp. Time Exp. \times Min.	Aperture	Aperture ID
SPT-CL 0307-6225	LDSS3-C	12/29/2018	2 \times 25	0307-62A	L18B2102
SPT-CL 0310-4647	LDSS3-C	10/22/2020	2 \times 20	0310-46	L1990403
SPT-CL 0315-2718
SPT-CL 0319-2244
SPT-CL 0319-3345	LDSS3-C	01/11/2018	4 \times 20	0319-33A	L17C2001
SPT-CL 0324-6236	LDSS3-C	01/10/2018	2 \times 20	0324-62A	L17C2001
SPT-CL 0328-2140	LDSS3-C	10/21/2020	2 \times 20	LS-1.25c	...
	LDSS3-C	10/21/2020	2 \times 10	LS-1.25c	...
SPT-CL 0330-5228	LDSS3-C	09/11/2015	4 \times 30	spt0330	L1562601
	LDSS3-C	09/11/2015	1 \times 25	spt0330	L1562601

SPT-CL 0333-5842
SPT-CL 0343-5518	LDSS3-C	09/28/2019	2 \times 20	0343-55	L1990404
SPT-CL 0348-2144

Table D.1: Strong Lensing South Pole Telescope Spectroscopic Program Record (cont'd).

SPT ID	Instrument	Obs. Date	Exp. Time	Aperture	Aperture ID
		MM/DD/YYYY	Exp. \times Min.		
SPT-CL 0348-4515
SPT-CL 0352-2644	LDSS3-C	09/28/2019	2 \times 15	0352-26	L1990404
SPT-CL 0352-5647	FIRE
SPT-CL 0354-3745	LDSS3-C	12/30/2018	2 \times 25	0354-37A	L18B2102
SPT-CL 0354-5904	0354-59b	L1990405
SPT-CL 0355-3634	LDSS3-C	09/25/2017	2 \times 20	0355-36A	L1783001
SPT-CL 0356-5337	LDSS3-C	01/09/2018	2 \times 20	0356-53B	L17C2001
	LDSS3-C	01/09/2018	2 \times 20	0356-53C	L17C2001
	LDSS3-C	0356-53A	L17C2001
	LDSS3-C	0356-53D	L17C2001
	LDSS3-C	0356m53	L1711902
SPT-CL 0357-4521	LDSS3-C	12/10/2017	3 \times 20	0357-45A	L17B1201
SPT-CL 0404-4418	LDSS3-C	09/28/2019	2 \times 16	0404-44	L1990405
SPT-CL 0406-4805	LDSS3-C	09/28/2019	2 \times 17	0406-48	L1990406

Table D.1: Strong Lensing South Pole Telescope Spectroscopic Program Record (cont'd).

SPT ID	Instrument	Obs. Date MM/DD/YYYY	Exp. Time Exp. \times Min.	Aperture	Aperture ID
SPT-CL 0411-2158	LDSS3-C	09/28/2019	2 \times 18	0411-21	L1982202
SPT-CL 0411-4819	GMOS
SPT-CL 0416-6359	GISMO	3/XX/2015	2 \times 20	spt0411	G1522101
SPT-CL 0417-4748	LDSS3-C	0416-63b	L1990406
SPT-CL 0420-3837	...	12/30/2018	2 \times 25	0417-47A	L18B2102
SPT-CL 0421-4845	LDSS3-C
SPT-CL 0440-4657	LDSS3-C	09/28/2019	1 \times 20	0421-48L	L1990408
SPT-CL 0441-4855	GISMO	10/01/2019	1 \times 20	0421-48L	L1990408
SPT-CL 0444-5603	LDSS3-C	09/23/2016	2 \times 25	0440m46A	L1681701
SPT-CL 0446-5849	LDSS3-C	3/XX/2015	2 \times 20	spt0441	G1522101
SPT-CL 0448-3020	GISMO	12/29/2018	2 \times 25	0441-48A	L18B2102
		12/10/2017	2 \times 20	0444-56A	L17B1201
		09/23/2016	2 \times 25	s0446-58	L1572201
		3/XX/2015	2 \times 20

Table D.1: Strong Lensing South Pole Telescope Spectroscopic Program Record (cont'd).

SPT ID	Instrument	Obs. Date MM/DD/YYYY	Exp. Time Exp. \times Min.	Aperture	Aperture ID
SPT-CL 0456-4906	LDSS3-C	09/26/2019	3 \times 20	0456-49	L1990407
SPT-CL 0502-6113	LDSS3-C	12/30/2018	2 \times 25	0502-61A	L18B2102
SPT-CL 0503-3553	LDSS3-C	01/01/2017	2 \times 20	LS-1.5c	...
	LDSS3-C	0503-35A	L17C2002
	LDSS3-C	0503m35	L1711902
SPT-CL 0504-2759
SPT-CL 0509-5342	GISMO	01/XX/2015	2 \times 30	spt0509	G1510701
SPT-CL 0512-3604	LDSS3-C	0512-36b	L1890301
SPT-CL 0512-3848	LDSS3-C	01/01/2017	2 \times 20	LS-1.5c	...
	LDSS3-C	01/30/2017	3 \times 20	0512m38A	L1711902
	LDSS3-C	01/30/2017	3 \times 20	0512m38B	L1711902
	LDSS3-C	09/02/2017	2 \times 20	0512-38A	L1783001
	LDSS3-C	01/09/2018	2 \times 20	0512-38C	L17C2007
	LDSS3-C	01/09/2018	2 \times 18	0512-38C	L17C2007

Table D.1: Strong Lensing South Pole Telescope Spectroscopic Program Record (cont'd).

SPT ID	Instrument	Obs. Date MM/DD/YYYY	Exp. Time Exp. \times Min.	Aperture	Aperture ID
	LDSS3-C	01/10/2018	4 \times 20	0512-38D	L17C2006
	LDSS3-C	01/23/2020	4 \times 20	0512-38	L2010801
SPT-CL 0516-6312
SPT-CL 0521-2754
SPT-CL 0521-5104
SPT-CL 0528-5300	LDSS3-C	09/27/2019	1 \times 12	0528-53	L1990408
	LDSS3-C	10/01/2019	2 \times 20	0528-53	L1990408
SPT-CL 0532-3701	LDSS3-C	09/26/2019	4 \times 20	0532-37	L1990409
SPT-CL 0535-4801	LDSS3-C	0535-48H	L1990409
SPT-CL 0537-6504
SPT-CL 0540-2127
SPT-CL 0540-5744	GISMO	3/XX/2015	1 \times 40	spt0540	G1522101
	GISMO	3/XX/2015	2 \times 30	spt0540	G1522101
	LDSS3-C	12/29/2018	2 \times 25	0540-57A	L18B2102

Table D.1: Strong Lensing South Pole Telescope Spectroscopic Program Record (cont'd).

SPT ID	Instrument	Obs. Date MM/DD/YYYY	Exp. Time Exp. \times Min.	Aperture	Aperture ID
SPT-CL 0544-3950	LDSS3-C	01/23/2020	2 \times 20	0544-39	L1990410
SPT-CL 0546-5345	GISMO	1/XX/2015	2 \times 40	spt0546	G1510701
SPT-CL 0549-6205	LDSS3-C	01/30/2017	3 \times 20	0549m62	L1711902
SPT-CL 0555-6406	LDSS3-C	01/23/2020	2 \times 20	0555-64	L1990411
SPT-CL 0556-5403
SPT-CL 0557-4113	LDSS3-C	12/10/2017	2 \times 20	0557-41A	L17B1201
SPT-CL 0600-2007
SPT-CL 0603-4714	LDSS3-C	01/11/2018	2 \times 20	0603-47A	L17C2005
SPT-CL 0615-5746	GISMO	1/XX/2015	3 \times 30	spt0615	G1510701
SPT-CL 0617-5507
SPT-CL 0643-4535
SPT-CL 0647-5828	LDSS3-C	09/23/2016	2 \times 25	0647m58A	L1681701
SPT-CL 0650-4503	LDSS3-C	01/23/2020	2 \times 20	0650-45	L1990412
SPT-CL 0650-4503	LDSS3-C	01/23/2020	1 \times 15	0650-45	L1990412

Table D.1: Strong Lensing South Pole Telescope Spectroscopic Program Record (cont'd).

SPT ID	Instrument	Obs. Date	Exp. Time	Aperture	Aperture ID
		MM/DD/YYYY	Exp. \times Min.		
SPT-CL 1000-3016	LDSS3-C	06/25/2019	2 \times 20	1000-30	L1961407
SPT-CL 1039-2502	LDSS3-C	06/29/2019	2 \times 20	1039-25	L1961408
SPT-CL 1042-2847	LDSS3-C	12/29/2018	2 \times 25	1042-28A	L18B2102
SPT-CL 1131-1955	LDSS3-C	06/07/2016	4 \times 25	a1300	L1650201
	LDSS3-C	06/08/2016	2 \times 25	a1300	L1650201
SPT-CL 1141-2127	LDSS3-C	06/27/2019	2 \times 20	1141-21	L1961409
	LDSS3-C	1141m21	L1711903
	LDSS3-C	1141-21A	L18B2103
	LDSS3-C	1141-21A	L17C2002
SPT-CL 1144-2835
SPT-CL 1153-2137	LDSS3-C	06/27/2019	2 \times 20	1153-21	L1961410
SPT-CL 1221-3010	LDSS3-C	06/26/2019	1 \times 20	1221-30	L1961411
SPT-CL 1223-3014	LDSS3-C	6/XX/2017	2 \times 20	LS-1.5c	...
SPT-CL 1238-2854	LDSS3-C	06/25/2019	2 \times 20	1238-28	L1961412

Table D.1: Strong Lensing South Pole Telescope Spectroscopic Program Record (cont'd).

SPT ID	Instrument	Obs. Date	Exp. Time		Aperture	Aperture ID
			MM/DD/YYYY	Exp. × Min.		
SPT-CL 1239-2915	LDSS3-C	01/30/2017	1 × 20	1239m29	L1711903	
	LDSS3-C	01/09/2018	2 × 20	1239-29B	L17C2003	
SPT-CL 1250-3010	LDSS3-C	06/27/2019	2 × 20	1250-30	L1961413	
SPT-CL 1256-2851	LDSS3-C	01/10/2018	2 × 20	1256-28A	L17C2002	
	LDSS3-C	01/10/2018	1 × 10	1256-28A	L17C2002	
SPT-CL 1259-1954	LDSS3-C	06/25/2019	2 × 20	1259m19S	L1961416	
SPT-CL 1315-28E	LDSS3-C	1315m28E	L1961417	
SPT-CL 1342-2442	
SPT-CL 2011-5725	LDSS3-C	06/07/2016	2 × 25	2011m57A	L1650201	
SPT-CL 2016-4954	
SPT-CL 2023-5535	LDSS3-C	10/02/2019	2 × 20	2023-55	L1953004	
SPT-CL 2025-5117	LDSS3-C	06/29/2019	2 × 20	2025-51	L1961419	
SPT-CL 2031-4037	IMACS	05/17/2015	4 × 40	spt2031a	...	
	IMACS	05/17/2015	1 × 20	spt2031a	...	

Table D.1: Strong Lensing South Pole Telescope Spectroscopic Program Record (cont'd).

SPT ID	Instrument	Obs. Date	Exp. Time	Aperture	Aperture ID
	IMACS	05/17/2015	2 × 40	spt2031b	...
	IMACS	05/27/2015	2 × 40	spt2031a	...
	IMACS	7/XX/2015	1 × 40	spt2031a	...
	IMACS	7/XX/2015	1 × 35	spt2031a	...
	IMACS	7/XX/2015	1 × 30	spt2031a	...

SPT-CL 2032-5627	LDSS3-C	06/25/2019	2 × 20	2032-56	L1961420
	LDSS3-C	10/02/2019	2 × 20	2032-56	L1961420
SPT-CL 2034-5936	LDSS3-C	11/17/2015	2 × 20	spt2034	L1562601
	LDSS3-C	6/XX/2017	4 × 20	LS-1.5c	...
	LDSS3-C	09/27/2019	2 × 20	2034-59	L1982203
SPT-CL 2050-4213
SPT-CL 2056-4405	LDSS3-C	06/07/2016	2 × 25	2056m44A	L1650202
SPT-CL 2106-5844

Table D.1: Strong Lensing South Pole Telescope Spectroscopic Program Record (cont'd).

SPT ID	Instrument	Obs. Date MM/DD/YYYY	Exp. Time Exp. \times Min.	Aperture	Aperture ID
SPT-CL 2108-4445	LDSS3-C	06/28/2019	2 \times 20	2108-44	L1961422
	LDSS3-C	09/27/2019	2 \times 20	2108-44	L1961422
SPT-CL 2110-5244	LDSS3-C	2110-52b	L1890301
SPT-CL 2112-4434	LDSS3-C	09/20/2016	3 \times 25	2112m44A	L1681701
	LDSS3-C	09/21/2016	3 \times 25	2112m44B	L1681701
SPT-CL 2124-6124	LDSS3-C	06/07/2016	1 \times 25	2124m61A	L1650201
	LDSS3-C	06/08/2016	2 \times 25	2124m61A	L1650201
SPT-CL 2130-6458	LDSS3-C	09/28/2019	2 \times 20	2130-64	L1953005
SPT-CL 2134-4109	LDSS3-C	06/28/2019	4 \times 20	2134-41	L1961425
	LDSS3-C	06/28/2019	2 \times 20	LS-1.5c	...
SPT-CL 2138-6008	IMACS	05/17/2015	2 \times 35	spt2138	...
	LDSS3-C	09/26/2019	2 \times 20	2138-60A	L1990413
	LDSS3-C	09/27/2019	2 \times 20	2138-60B	L1990414
	FIRE	9/XX/2018

Table D.1: Strong Lensing South Pole Telescope Spectroscopic Program Record (cont'd).

SPT ID	Instrument	Obs. Date	Exp. Time	Aperture	Aperture ID
		MM/DD/YYYY	Exp. \times Min.		
SPT-CL 2145-5644	IMACS	05/17/2015	3 \times 40	spt2145	...
	IMACS	05/17/2015	1 \times 30	spt2145	...
SPT-CL 2148-4843
SPT-CL 2203-5047	LDSS3-C	09/28/2019	2 \times 20	2203m50L	L1961427
SPT-CL 2214-4642	LDSS3-C	09/22/2016	4 \times 25	spt2214	L1572201
SPT-CL 2215-3537	LDSS3-C	06/25/2019	2 \times 20	2215m35E	L1961428
	LDSS3-C	2215m35L	L1961430
SPT-CL 2232-5959	GMOS
	IMACS	05/27/2015	2 \times 30	spt2232a	...
	IMACS	05/27/2015	2 \times 35	spt2232b	...
	IMACS	7/XX/2015	2 \times 20	spt2232b	...
SPT-CL 2236-4555	LDSS3-C	09/23/2016	4 \times 25	spt2236	L1572201
SPT-CL 2244-3704	LDSS3-C	06/25/2019	2 \times 20	2244-37	L1953006
	LDSS3-C	2244-37b	L1890301

Table D.1: Strong Lensing South Pole Telescope Spectroscopic Program Record (cont'd).

SPT ID	Instrument	Obs. Date MM/DD/YYYY	Exp. Time Exp. \times Min.	Aperture	Aperture ID
SPT-CL 2245-2113	LDSS3-C	6/XX/2017	1 \times 20	LS-1.5c	...
	LDSS3-C	09/25/2017	2 \times 20	2245-21A	L1783001
SPT-CL 2245-6206	LDSS3-C	2245-62b	L1990413
SPT-CL 2250-4808	LDSS3-C	10/21/2020	2 \times 20	LS-1.25c	...
	LDSS3-C	10/21/2020	2 \times 10	LS-1.25c	...
SPT-CL 2251-2247	2251m22S	L1961432
SPT-CL 2251-3323
SPT-CL 2254-4620	LDSS3-C	06/08/2016	3 \times 25	2254m46A	L1650202
SPT-CL 2256-2240	LDSS3-C	05/13/2021	2 \times 20	2256-22	L1961433
SPT-CL 2258-3447
SPT-CL 2300-4500	LDSS3-C	09/25/2017	2 \times 20	2300-45A	L1783002
SPT-CL 2305-2248	LDSS3-C	09/26/2019	2 \times 20	2305-22	L1961434
	LDSS3-C	2305-22b	L1890301
SPT-CL 2307-5440

Table D.1: Strong Lensing South Pole Telescope Spectroscopic Program Record (cont'd).

SPT ID	Instrument	Obs. Date	Exp. Time	Aperture	Aperture ID
		MM/DD/YYYY	Exp. \times Min.		
SPT-CL 2311-5522
SPT-CL 2325-4111	IMACS	05/27/2015	2 \times 40	spt2325	...
	IMACS	05/27/2015	1 \times 30	spt2325	...
	LDSS3-C	06/07/2016	4 \times 25	2325m41A	L1650201
	LDSS3-C	06/07/2016	4 \times 25	2325m41B	L1650202
	GMOS
SPT-CL 2331-5051	LDSS3-C	09/27/2019	2 \times 20	2331-50	L1990415
SPT-CL 2332-5053
SPT-CL 2332-5358
SPT-CL 2336-3205	2336-32A	L1783002
SPT-CL 2336-3210	2336-31A	L1783002
SPT-CL 2336-5352	LDSS3-C	09/25/2017	2 \times 20	2336-53A	L1783002
	LDSS3-C	2336-53B	L1783002

Table D.1: Strong Lensing South Pole Telescope Spectroscopic Program Record (cont'd).

SPT ID	Instrument	Obs. Date MM/DD/YYYY	Exp. Time Exp. \times Min.	Aperture	Aperture ID
SPT-CL 2337-5942	LDSS3-C	09/11/2015	3 \times 30	spt2337	L1562601
SPT-CL 2339-3555	LDSS3-C	09/27/2017	2 \times 25	2339-35A	L1783002
SPT-CL 2341-5724	LDSS3-C	12/29/2018	2 \times 25	2341-57A	L18B2103
SPT-CL 2342-5411	LDSS3-C	09/11/2015	3 \times 30	spt2342	L1562601
	LDSS3-C	09/26/2015	2 \times 20	spt2342	L1562601
	LDSS3-C	09/26/2015	1 \times 10	spt2342	L1562601
SPT-CL 2344-4243	LDSS3-C	09/21/2016	2 \times 25	2344m42A	L1650201
	LDSS3-C	2344-42A	L1892701
	LDSS3-C	2344-42B	L1892701
SPT-CL 2349-5113	LDSS3-C	09/20/2016	2 \times 29	2349m51A	L1681701
SPT-CL 2359-5009

Record of the strong lensing South Pole Telescope spectroscopic follow-up program. We report the SPT ID and the relevant observation records. The Aperture ID relates to the information of the mask name to be used in the LDSS3 mask database (<http://masks.lco.cl/masks2/search/>).

BIBLIOGRAPHY

BIBLIOGRAPHY

- Abazajian, K. N., Adelman-McCarthy, J. K., Agüeros, M. A., et al. 2009, *ApJS*, 182, 543
- Abbott, T. M. C., Abdalla, F. B., Allam, S., et al. 2018, *ApJS*, 239, 18
- Acebron, A., Jullo, E., Limousin, M., et al. 2017, *MNRAS*, 470, 1809
- Acebron, A., Cibirka, N., Zitrin, A., et al. 2018, *ApJ*, 858, 42
- Acebron, A., Alon, M., Zitrin, A., et al. 2019, *ApJ*, 874, 132
- Acebron, A., Zitrin, A., Coe, D., et al. 2020, *ApJ*, 898, 6
- Allam, S. S., Tucker, D. L., Lin, H., et al. 2007, *ApJ*, 662, L51
- Allen, S. W., Evrard, A. E., & Mantz, A. B. 2011, *Annual Review of Astronomy and Astrophysics*, 49, 409
- Allen, S. W., Rapetti, D. A., Schmidt, R. W., et al. 2008, *MNRAS*, 383, 879
- Allen, S. W., Schmidt, R. W., Fabian, A. C., & Ebeling, H. 2003, *MNRAS*, 342, 287
- Amendola, L., Appleby, S., Avgoustidis, A., et al. 2018, *Living Reviews in Relativity*, 21, 2
- Bartelmann, M. 2010, *Classical and Quantum Gravity*, 27, 233001
- Bartelmann, M., & Steinmetz, M. 1996, *MNRAS*, 283, 431
- Bayliss, M. B. 2012, *ApJ*, 744, 156
- Bayliss, M. B., Gladders, M. D., Oguri, M., et al. 2011a, *ApJ*, 727, L26
- Bayliss, M. B., Hennawi, J. F., Gladders, M. D., et al. 2011b, *ApJS*, 193, 8
- Bayliss, M. B., Johnson, T., Gladders, M. D., Sharon, K., & Oguri, M. 2014, *ApJ*, 783, 41
- Bayliss, M. B., Wuyts, E., Sharon, K., et al. 2010, *ApJ*, 720, 1559
- Bayliss, M. B., Ruel, J., Stubbs, C. W., et al. 2016, *ApJS*, 227, 3

- Belokurov, V., Evans, N. W., Moiseev, A., et al. 2007, *ApJ*, 671, L9
- Benson, B. A., Ade, P. A. R., Ahmed, Z., et al. 2014, in *Millimeter, Submillimeter, and Far-Infrared Detectors and Instrumentation for Astronomy VII*, Vol. 9153, 91531P
- Bertin, E., & Arnouts, S. 1996, *A&AS*, 117, 393
- Bertschinger, E. 1998, *Annual Review of Astronomy and Astrophysics*, 36, 599
- Bettinelli, M., Simioni, M., Aparicio, A., et al. 2016, *MNRAS*, 461, L67
- Bhattacharya, S., Habib, S., Heitmann, K., & Vikhlinin, A. 2013, *ApJ*, 766, 32
- Blanton, M. R., Bershadsky, M. A., Abolfathi, B., et al. 2017, *AJ*, 154, 28
- Bleem, L. E., Stalder, B., de Haan, T., et al. 2015, *The Astrophysical Journal Supplement Series*, 216, 27
- Bleem, L. E., Bocquet, S., Stalder, B., et al. 2020, *ApJS*, 247, 25
- Bocquet, S., Heitmann, K., Habib, S., et al. 2020, *ApJ*, 901, 5
- Bocquet, S., Dietrich, J. P., Schrabback, T., et al. 2019, *ApJ*, 878, 55
- Boldrin, M., Giocoli, C., Meneghetti, M., & Moscardini, L. 2012, *MNRAS*, 427, 3134
- Bom, C., Poh, J., Nord, B., Blanco-Valentin, M., & Dias, L. 2019, arXiv e-prints, arXiv:1911.06341
- Bonamigo, M., Despali, G., Limousin, M., et al. 2015, *MNRAS*, 449, 3171
- Bonilla, A., & Castillo, J. 2018, *Universe*, 4, 21
- Bradač, M., Allen, S. W., Treu, T., et al. 2008a, *ApJ*, 687, 959
- Bradač, M., Clowe, D., Gonzalez, A. H., et al. 2006, *ApJ*, 652, 937
- Bradač, M., Schrabback, T., Erben, T., et al. 2008b, *ApJ*, 681, 187
- Bradač, M., Treu, T., Applegate, D., et al. 2009, *ApJ*, 706, 1201
- Broadhurst, T., Benítez, N., Coe, D., et al. 2005, *ApJ*, 621, 53
- Broadhurst, T. J., & Barkana, R. 2008, *MNRAS*, 390, 1647
- Cañameras, R., Schuldt, S., Suyu, S. H., et al. 2020, *A&A*, 644, A163
- Caminha, G. B., Grillo, C., Rosati, P., et al. 2016, *A&A*, 587, A80
- . 2017, *A&A*, 600, A90
- Caminha, G. B., Rosati, P., Grillo, C., et al. 2019, *A&A*, 632, A36

- Cerny, C., Sharon, K., Andrade-Santos, F., et al. 2018, *ApJ*, 859, 159
- Chang, K., & Refsdal, S. 1979, *Nature*, 282, 561
- Child, H. L., Habib, S., Heitmann, K., et al. 2018, *ApJ*, 859, 55
- Chirivì, G., Suyu, S. H., Grillo, C., et al. 2018, *A&A*, 614, A8
- Cibirka, N., Acebron, A., Zitrin, A., et al. 2018, *ApJ*, 863, 145
- Clowe, D., Bradač, M., Gonzalez, A. H., et al. 2006, *ApJ*, 648, L109
- Coe, D., Zitrin, A., Carrasco, M., et al. 2013, *ApJ*, 762, 32
- Coe, D., Salmon, B., Bradač, M., et al. 2019, *ApJ*, 884, 85
- Corless, V. L., & King, L. J. 2009, *MNRAS*, 396, 315
- Dahle, H., Aghanim, N., Guennou, L., et al. 2016, *A&A*, 590, L4
- D’Aloisio, A., Natarajan, P., & Shapiro, P. R. 2014, *MNRAS*, 445, 3581
- De Boni, C., Ettori, S., Dolag, K., & Moscardini, L. 2013, *MNRAS*, 428, 2921
- de Haan, T., Benson, B. A., Bleem, L. E., et al. 2016, *ApJ*, 832, 95
- Despali, G., Giocoli, C., & Tormen, G. 2014, *MNRAS*, 443, 3208
- Diego, J. M., Broadhurst, T., Wong, J., et al. 2016, *MNRAS*, 459, 3447
- Diego, J. M., Protopapas, P., Sandvik, H. B., & Tegmark, M. 2005, *MNRAS*, 360, 477
- Diego, J. M., Tegmark, M., Protopapas, P., & Sandvik, H. B. 2007, *MNRAS*, 375, 958
- Diego, J. M., Kaiser, N., Broadhurst, T., et al. 2018, *ApJ*, 857, 25
- Diehl, H. T., Allam, S. S., Annis, J., et al. 2009, *ApJ*, 707, 686
- Doane, D. P. 1976, *The American Statistician*, 30, 181
- Duffy, A. R., Schaye, J., Kay, S. T., & Dalla Vecchia, C. 2008, *MNRAS*, 390, L64
- Dunkley, J., Komatsu, E., Nolta, M. R., et al. 2009, *The Astrophysical Journal Supplement Series*, 180, 306
- Dutton, A. A., & Macciò, A. V. 2014, *MNRAS*, 441, 3359
- Ebeling, H., Edge, A. C., Allen, S. W., et al. 2000, *MNRAS*, 318, 333
- Ebeling, H., Edge, A. C., Bohringer, H., et al. 1998, *MNRAS*, 301, 881

- Ebeling, H., Ma, C. J., Kneib, J. P., et al. 2009, *MNRAS*, 395, 1213
- Ebeling, H., Qi, J., & Richard, J. 2017, *MNRAS*, 471, 3305
- Einstein, A. 1911, *Annalen der Physik*, 340, 898
- Elíasdóttir, Á., Limousin, M., Richard, J., et al. 2007, arXiv e-prints, arXiv:0710.5636
- Ettori, S., Ghirardini, V., Eckert, D., et al. 2019, *A&A*, 621, A39
- Evrard, A. E., MacFarland, T. J., Couchman, H. M. P., et al. 2002, *ApJ*, 573, 7
- Fabian, A. C. 1991, *MNRAS*, 253, 29P
- Fitzgibbon, A. W., Pilu, M., & Fisher, R. B. 1996, in Proceedings of 13th International Conference on Pattern Recognition, Vol. 1, 253–257 vol.1
- Florian, M. K., Li, N., & Gladders, M. D. 2016, *ApJ*, 832, 168
- Foëx, G., Böhringer, H., & Chon, G. 2017, *A&A*, 606, A122
- Foreman-Mackey, D., Hogg, D. W., Lang, D., & Goodman, J. 2013, Publications of the Astronomical Society of the Pacific, 125, 306–312
- Fox, C., Mahler, G., Sharon, K., & Remolina González, J. D. 2021, arXiv e-prints, arXiv:2104.05585
- Frieman, J. A., Turner, M. S., & Huterer, D. 2008, Annual Review of Astronomy and Astrophysics, 46, 385
- Gifford, D., & Miller, C. J. 2013, *ApJ*, 768, L32
- Giocoli, C., Meneghetti, M., Metcalf, R. B., Ettori, S., & Moscardini, L. 2014, *MNRAS*, 440, 1899
- Gladders, M. D., & Yee, H. K. C. 2000, *AJ*, 120, 2148
- Gladders, M. D., Yee, H. K. C., Majumdar, S., et al. 2007, *ApJ*, 655, 128
- Golse, G., & Kneib, J. P. 2002, *A&A*, 390, 821
- Gonzaga, S., Hack, W., Fruchter, A., & Mack, J. 2012, The DrizzlePac Handbook (Baltimore: STScI)
- Gonzalez, A. H., Stanford, S. A., Brodwin, M., et al. 2012, *ApJ*, 753, 163
- Gonzalez, E. J., Chalela, M., Jauzac, M., et al. 2020, *MNRAS*, 494, 349
- Gralla, M. B., Sharon, K., Gladders, M. D., et al. 2011, *ApJ*, 737, 74
- Graur, O., Rodney, S. A., Maoz, D., et al. 2014, *ApJ*, 783, 28

- Habib, S., Pope, A., Finkel, H., et al. 2016, *J. New Ast.*, 42, 49
- Halkola, A., Hildebrandt, H., Schrabback, T., et al. 2008, *A&A*, 481, 65
- Harvey, D., Robertson, A., Massey, R., & McCarthy, I. G. 2019, *MNRAS*, 488, 1572
- Heitmann, K., Finkel, H., Pope, A., et al. 2019, *ApJS*, 245, 16
- Heitmann, K., Frontiere, N., Rangel, E., et al. 2021, *ApJS*, 252, 19
- Heneka, C., Rapetti, D., Cataneo, M., et al. 2018, *MNRAS*, 473, 3882
- Hennawi, J. F., Gladders, M. D., Oguri, M., et al. 2008, *AJ*, 135, 664
- Hilbert, S., White, S. D. M., Hartlap, J., & Schneider, P. 2007, *MNRAS*, 382, 121
- . 2008, *MNRAS*, 386, 1845
- Hilton, M., Hasselfield, M., Sifón, C., et al. 2018, The Astrophysical Journal Supplement Series, 235, 20
- Hoekstra, H., Bartelmann, M., Dahle, H., et al. 2013, *Space Sci. Rev.*, 177, 75
- Hsu, L.-Y., Ebeling, H., & Richard, J. 2013, *MNRAS*, 429, 833
- Hu, W. 2003, *Phys. Rev. D*, 67, 081304
- Hu, W., & Kravtsov, A. V. 2003, *ApJ*, 584, 702
- Huang, K.-H., Lemaux, B. C., Schmidt, K. B., et al. 2016, *ApJ*, 823, L14
- Huang, N., Bleem, L. E., Stalder, B., et al. 2020, *AJ*, 159, 110
- Huang, X., Storfer, C., Gu, A., et al. 2021, *ApJ*, 909, 27
- Huterer, D., & Shafer, D. L. 2018, Reports on Progress in Physics, 81, 016901
- Ishigaki, M., Kawamata, R., Ouchi, M., et al. 2015, *ApJ*, 799, 12
- Jacobs, C., Collett, T., Glazebrook, K., et al. 2019, *ApJS*, 243, 17
- Jauzac, M., Klein, B., Kneib, J.-P., et al. 2020, arXiv e-prints, arXiv:2006.10700
- Jauzac, M., Richard, J., Jullo, E., et al. 2015, *MNRAS*, 452, 1437
- Jauzac, M., Richard, J., Limousin, M., et al. 2016, *MNRAS*, 457, 2029
- Jenkins, A., Frenk, C. S., White, S. D. M., et al. 2001, *MNRAS*, 321, 372
- Johnson, T. L. 2018, PhD thesis, University of Michigan, Horace H. Rackham School of Graduate Studies
- Johnson, T. L., & Sharon, K. 2016, *ApJ*, 832, 82

- Johnson, T. L., Sharon, K., Bayliss, M. B., et al. 2014, *ApJ*, 797, 48
- Johnson, T. L., Sharon, K., Gladders, M. D., et al. 2017a, *ApJ*, 843, 78
- Johnson, T. L., Rigby, J. R., Sharon, K., et al. 2017b, *ApJ*, 843, L21
- Jullo, E., & Kneib, J. P. 2009, *MNRAS*, 395, 1319
- Jullo, E., Kneib, J. P., Limousin, M., et al. 2007, *New Journal of Physics*, 9, 447
- Karman, W., Caputi, K. I., Caminha, G. B., et al. 2017, *A&A*, 599, A28
- Kawamata, R., Ishigaki, M., Shimasaku, K., et al. 2018, *ApJ*, 855, 4
- Kawamata, R., Oguri, M., Ishigaki, M., Shimasaku, K., & Ouchi, M. 2016, *ApJ*, 819, 114
- Keeton, C. R. 2010, *General Relativity and Gravitation*, 42, 2151
- Khedekar, S., & Majumdar, S. 2013, *Journal of Cosmology and Astro-Particle Physics*, 2013, 030
- Khullar, G., Gozman, K., Lin, J. J., et al. 2021, *ApJ*, 906, 107
- Killedar, M., Borgani, S., Fabjan, D., et al. 2018, *MNRAS*, 473, 1736
- Kneib, J. P., Ellis, R. S., Smail, I., Couch, W. J., & Sharples, R. M. 1996, *ApJ*, 471, 643
- Kneib, J.-P., & Natarajan, P. 2011, *Astronomy and Astrophysics Review*, 19, 47
- Kochanek, C. S. 2006, *Strong Gravitational Lensing* (Berlin, Heidelberg: Springer Berlin Heidelberg), 91–268
- Koester, B. P., Gladders, M. D., Hennawi, J. F., et al. 2010, *ApJ*, 723, L73
- Koester, B. P., McKay, T. A., Annis, J., et al. 2007, *ApJ*, 660, 239
- Komatsu, E., Smith, K. M., Dunkley, J., et al. 2011, *The Astrophysical Journal Supplement Series*, 192, 18
- Kubo, J. M., Allam, S. S., Drabek, E., et al. 2010, *ApJ*, 724, L137
- Lagattuta, D. J., Richard, J., Bauer, F. E., et al. 2019, *MNRAS*, 485, 3738
- Laureijs, R., Amiaux, J., Arduini, S., et al. 2011, *ArXiv e-prints*, arXiv:1110.3193
- Levenberg, K. 1944, *Quarterly of Applied Mathematics*, 2, 164–168
- Li, N., Gladders, M. D., Rangel, E. M., et al. 2016, *ApJ*, 828, 54
- Li, N., Gladders, M. D., Heitmann, K., et al. 2019, *ApJ*, 878, 122

- Liddle, A. R. 2007, *MNRAS*, 377, L74
- Liesenborgs, J., De Rijcke, S., & Dejonghe, H. 2006, *MNRAS*, 367, 1209
- Limousin, M., Ebeling, H., Ma, C. J., et al. 2010, *MNRAS*, 405, 777
- Limousin, M., Richard, J., Jullo, E., et al. 2016, *A&A*, 588, A99
- Lotz, J. M., Koekemoer, A., Coe, D., et al. 2017, *ApJ*, 837, 97
- LSST Science Collaboration, Abell, P. A., Allison, J., et al. 2009, arXiv e-prints, arXiv:0912.0201
- LSST Science Collaboration, Marshall, P., Anguita, T., et al. 2017, ArXiv e-prints, arXiv:1708.04058
- Mahler, G., Richard, J., Clément, B., et al. 2018, *MNRAS*, 473, 663
- Mahler, G., Sharon, K., Fox, C., et al. 2019, *ApJ*, 873, 96
- Mahler, G., Sharon, K., Gladders, M. D., et al. 2020, *ApJ*, 894, 150
- Mainali, R., Stark, D. P., Tang, M., et al. 2020, *MNRAS*, 494, 719
- Mantz, A., Allen, S. W., Rapetti, D., & Ebeling, H. 2010, *MNRAS*, 406, 1759
- Mantz, A. B., Allen, S. W., Morris, R. G., et al. 2014, *MNRAS*, 440, 2077
- . 2015, *MNRAS*, 449, 199
- Mantz, A. B., Allen, S. W., Morris, R. G., & von der Linden, A. 2018, *MNRAS*, 473, 3072
- Marquardt, D. W. 1963, *Journal of the Society for Industrial and Applied Mathematics*, 11, 431
- Marriage, T. A., Acquaviva, V., Ade, P. A. R., et al. 2011, *ApJ*, 737, 61
- McCarthy, I. G., Schaye, J., Bird, S., & Le Brun, A. M. C. 2017, *MNRAS*, 465, 2936
- McCully, C., Keeton, C. R., Wong, K. C., & Zabludoff, A. I. 2014, *MNRAS*, 443, 3631
- Meneghetti, M., Bartelmann, M., Dahle, H., & Limousin, M. 2013, *Space Sci. Rev.*, 177, 31
- Meneghetti, M., Bartelmann, M., & Moscardini, L. 2003, *MNRAS*, 346, 67
- Meneghetti, M., Rasia, E., Merten, J., et al. 2010, *A&A*, 514, A93
- Meneghetti, M., Melchior, P., Grazian, A., et al. 2008, *A&A*, 482, 403

- Meneghetti, M., Rasia, E., Vega, J., et al. 2014, *ApJ*, 797, 34
- Meneghetti, M., Natarajan, P., Coe, D., et al. 2017, *MNRAS*, 472, 3177
- Merten, J., Meneghetti, M., Postman, M., et al. 2015, *ApJ*, 806, 4
- Mittal, A., de Bernardis, F., & Niemack, M. D. 2018, *Journal of Cosmology and Astro-Particle Physics*, 2018, 032
- Mohammed, I., Liesenborgs, J., Saha, P., & Williams, L. L. R. 2014, *MNRAS*, 439, 2651
- Molino, A., Benítez, N., Ascaso, B., et al. 2017, *MNRAS*, 470, 95
- Morgan, R., Nord, B., Birrer, S., Lin, J., & Poh, J. 2021, *The Journal of Open Source Software*, 6, 2854
- Motl, P. M., Hallman, E. J., Burns, J. O., & Norman, M. L. 2005, *ApJ*, 623, L63
- Narayan, R., & Bartelmann, M. 1996, ArXiv e-prints, astro
- Navarro, J. F., Frenk, C. S., & White, S. D. M. 1996, *ApJ*, 462, 563
- . 1997, *ApJ*, 490, 493
- Newman, A. B., Treu, T., Ellis, R. S., & Sand, D. J. 2011, *ApJ*, 728, L39
- Newman, A. B., Treu, T., Ellis, R. S., et al. 2013, *ApJ*, 765, 24
- Newville, M., Stensitzki, T., Allen, D. B., & Ingargiola, A. 2014, LM-FIT: Non-Linear Least-Square Minimization and Curve-Fitting for Python, doi:10.5281/zenodo.11813
- Niemiec, A., Jauzac, M., Jullo, E., et al. 2020, *MNRAS*, 493, 3331
- Nord, B., Buckley-Geer, E., Lin, H., et al. 2016, *ApJ*, 827, 51
- . 2020, *MNRAS*, 494, 1308
- Ofek, E. O., Seitz, S., & Klein, F. 2008, *MNRAS*, 389, 311
- Oguri, M. 2006, *MNRAS*, 367, 1241
- . 2010, *PASJ*, 62, 1017
- Oguri, M., Bayliss, M. B., Dahle, H., et al. 2012, *MNRAS*, 420, 3213
- Oguri, M., & Blandford, R. D. 2009, *MNRAS*, 392, 930
- Oguri, M., & Hamana, T. 2011, *MNRAS*, 414, 1851

- Okabe, N., Takada, M., Umetsu, K., Futamase, T., & Smith, G. P. 2010, *PASJ*, 62, 811
- Pardo, K., Desmond, H., & Ferreira, P. G. 2019, *Phys. Rev. D*, 100, 123006
- Paterno-Mahler, R., Sharon, K., Coe, D., et al. 2018, *ApJ*, 863, 154
- Pearson, J., Li, N., & Dye, S. 2019, *MNRAS*, 488, 991
- Peng, C. Y., Ho, L. C., Impey, C. D., & Rix, H.-W. 2002, *AJ*, 124, 266
- . 2010, *AJ*, 139, 2097
- Perlmutter, S., Aldering, G., Goldhaber, G., et al. 1999, *ApJ*, 517, 565
- Petrillo, C. E., Tortora, C., Chatterjee, S., et al. 2017, *MNRAS*, 472, 1129
- Pillepich, A., Reiprich, T. H., Porciani, C., Borm, K., & Merloni, A. 2018, *MNRAS*, 481, 613
- Pirzkal, N., Viana, A., & Rajan, A. 2010, The WFC3 IR 'Blobs', Space Telescope WFC Instrument Science Report
- Planck Collaboration, Ade, P. A. R., Aghanim, N., et al. 2016, *A&A*, 594, A27
- Porcas, R. W., Booth, R. S., Browne, I. W. A., Walsh, D., & Wilkinson, P. N. 1979, *Nature*, 282, 385
- Postman, M., Coe, D., Benítez, N., et al. 2012, *ApJS*, 199, 25
- Prada, F., Klypin, A. A., Cuesta, A. J., Betancort-Rijo, J. E., & Primack, J. 2012, *MNRAS*, 423, 3018
- Pratt, G. W., Arnaud, M., Biviano, A., et al. 2019, *Space Sci. Rev.*, 215, 25
- Priewe, J., Williams, L. L. R., Liesenborgs, J., Coe, D., & Rodney, S. A. 2017, *MNRAS*, 465, 1030
- Puchwein, E., & Hilbert, S. 2009, *MNRAS*, 398, 1298
- Raney, C. A., Keeton, C. R., & Brennan, S. 2020a, *MNRAS*, 492, 503
- Raney, C. A., Keeton, C. R., Brennan, S., & Fan, H. 2020b, *MNRAS*, 494, 4771
- Rangel, E., Li, N., Habib, S., et al. 2016, in 2016 IEEE International Conference on Cluster Computing (CLUSTER), 30–39
- Ravindranath, S., & Ho, L. C. 2002, *ApJ*, 577, 133
- Reichardt, C. L., Stalder, B., Bleem, L. E., et al. 2013, *ApJ*, 763, 127

- Remolina González, J. D., Sharon, K., Li, N., et al. 2021a, arXiv e-prints, arXiv:2102.06351
- Remolina González, J. D., Sharon, K., & Mahler, G. 2018, *ApJ*, 863, 60
- Remolina González, J. D., Sharon, K., Reed, B., et al. 2020, *ApJ*, 902, 44
- Remolina González, J. D., Sharon, K., Mahler, G., et al. 2021b, arXiv e-prints, arXiv:2104.03883
- Richard, J., Kneib, J.-P., Ebeling, H., et al. 2011, *MNRAS*, 414, L31
- Richard, J., Claeysens, A., Lagattuta, D. J., et al. 2020, arXiv e-prints, arXiv:2009.09784
- Riess, A. G., Filippenko, A. V., Challis, P., et al. 1998, *AJ*, 116, 1009
- Rigby, J. R., Bayliss, M. B., Sharon, K., et al. 2018, *AJ*, 155, 104
- Robertson, A., Harvey, D., Massey, R., et al. 2019, *MNRAS*, 488, 3646
- Robertson, A., Massey, R., & Eke, V. 2017, *MNRAS*, 467, 4719
- Rozo, E., Wechsler, R. H., Rykoff, E. S., et al. 2010, *ApJ*, 708, 645
- Rykoff, E. S., Rozo, E., Busha, M. T., et al. 2014, *ApJ*, 785, 104
- Rykoff, E. S., Rozo, E., Hollowood, D., et al. 2016, *ApJS*, 224, 1
- Sagunski, L., Gad-Nasr, S., Colquhoun, B., Robertson, A., & Tulin, S. 2021, *J. Cosmol. Astropart. Phys.*, 2021, 024
- Salmon, B., Coe, D., Bradley, L., et al. 2018, *ApJ*, 864, L22
- . 2020, *ApJ*, 889, 189
- Schneider, P. 2006, Introduction to Gravitational Lensing and Cosmology (Berlin, Heidelberg: Springer Berlin Heidelberg), 1–89
- Schneider, P. 2006, in Saas-Fee Advanced Course 33: Gravitational Lensing: Strong, Weak and Micro, ed. G. Meylan, P. Jetzer, P. North, P. Schneider, C. S. Kochanek, & J. Wambsganss, 269–451
- Schwarz, G. 1978, *Annals of Statistics*, 6, 461
- Sebesta, K., Williams, L. L. R., Liesenborgs, J., Medezinski, E., & Okabe, N. 2019, *MNRAS*, 488, 3251
- Sereno, M., Giocoli, C., Ettori, S., & Moscardini, L. 2015, *MNRAS*, 449, 2024
- Sharon, K., Gladders, M. D., Rigby, J. R., et al. 2012, *ApJ*, 746, 161

Sharon, K., Gladders, M. D., Marrone, D. P., et al. 2015, *ApJ*, 814, 21

Sharon, K., Bayliss, M. B., Dahle, H., et al. 2017, *ApJ*, 835, 5

—. 2020, *ApJS*, 247, 12

Shin, T., Adhikari, S., Baxter, E. J., et al. 2019, *MNRAS*, 487, 2900

Sifón, C., Menanteau, F., Hasselfield, M., et al. 2013, *ApJ*, 772, 25

Smith, G. P., Kneib, J.-P., Ebeling, H., Czoske, O., & Smail, I. 2001, *ApJ*, 552, 493

Smith, G. P., Kneib, J.-P., Smail, I., et al. 2005, *MNRAS*, 359, 417

Stark, D. P., Auger, M., Belokurov, V., et al. 2013, *MNRAS*, 436, 1040

Strait, V., Bradač, M., Hoag, A., et al. 2018, *ApJ*, 868, 129

Strait, V., Bradač, M., Coe, D., et al. 2020, *ApJ*, 888, 124

Sunyaev, R. A., & Zeldovich, I. B. 1980, *Annual Review of Astronomy and Astrophysics*, 18, 537

Sunyaev, R. A., & Zeldovich, Y. B. 1970, *Ap&SS*, 7, 3

—. 1972, *Comments on Astrophysics and Space Physics*, 4, 173

Umetsu, K., & Diemer, B. 2017, *ApJ*, 836, 231

Vega-Ferrero, J., Diego, J. M., & Bernstein, G. M. 2019, *MNRAS*, 486, 5414

Verdugo, T., Motta, V., Muñoz, R. P., et al. 2011, *A&A*, 527, A124

Vikhlinin, A., Burenin, R. A., Ebeling, H., et al. 2009, *ApJ*, 692, 1033

Walsh, D., Carswell, R. F., & Weymann, R. J. 1979, *Nature*, 279, 381

Wambsganss, J., Bode, P., & Ostriker, J. P. 2004, *ApJ*, 606, L93

Wambsganss, J., Ostriker, J. P., & Bode, P. 2008, *ApJ*, 676, 753

Wang, J., & White, S. D. M. 2009, *MNRAS*, 396, 709

Werner, N., Churazov, E., Finoguenov, A., et al. 2007, *A&A*, 474, 707

Weymann, R. J., Chaffee, F. H., J., Davis, M., et al. 1979, *ApJ*, 233, L43

Williamson, R., Benson, B. A., High, F. W., et al. 2011, *ApJ*, 738, 139

Yee, H. K. C., & Ellingson, E. 2003, *ApJ*, 585, 215

Zitrin, A., Broadhurst, T., Umetsu, K., et al. 2009, *MNRAS*, 396, 1985

- Zitrin, A., Rosati, P., Nonino, M., et al. 2012, *ApJ*, 749, 97
- Zitrin, A., Zheng, W., Broadhurst, T., et al. 2014, *ApJ*, 793, L12
- Zitrin, A., Fabris, A., Merten, J., et al. 2015, *ApJ*, 801, 44
- Zwicky, F. 1933, *Helvetica Physica Acta*, 6, 110
- . 1937, *Physical Review*, 51, 290